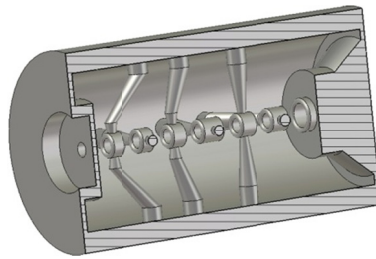


RF Acceleration of Intense Laser Generated Proton Bunches

Dissertation zur Erlangung
des Doktorgrades der Naturwissenschaften



vorgelegt beim Fachbereich Physik
der Johann Wolfgang Goethe-Universität
in Frankfurt am Main

von

MSc. Phys. ALI ALMOMANI

geboren in Irbid Jordanien

Frankfurt am Main 2012

D30

vom Fachbereich Physik

der Johann Wolfgang Goethe-Universität als Dissertation angenommen.

Dekan: Prof. Dr. Michael Huth

Erster Gutachter: Prof. Dr. Ulrich Ratzinger

Zweiter Gutachter: Prof. Dr. Ingo Hofmann

Datum der Disputation:

DEDICATION

To

My Parents Mohammad and Fathia

and

My lovely wife Suha

*“It doesn't matter how beautiful your theory
is, it doesn't matter how smart you are.
If it doesn't agree with experiment, it's
wrong”*

Richard P. Feynman

ZUSAMMENFASSUNG

Die Erzeugung intensiver Protonenstrahlung durch Wechselwirkung gepulster, scharf fokussierter Laserstrahlen mit dünnen Folien ist ein sehr aktuelles Forschungsgebiet. Die Technik der „Chirped Pulse Amplification CPA“ ermöglicht fokussierte Strahlungsdichten bis zu 10^{21} W/cm². Damit kann die Emission von Protonenpulsen aus der Rückseite der getroffenen Folie mit Teilchenenergien bis zu mehreren 10 MeV erreicht werden. Es läuft dabei der Mechanismus der „Target Normal Sheath Acceleration TNSA“ ab, wobei hochenergetische Elektronen aus der Rückseite der Folie austreten und dabei ein hohes elektrisches Feld von bis zu 10^{12} V/m zwischen Folie und Elektronenwolke aufbauen.

In diesem Feld werden in der Folienoberfläche adsorbierte Protonen ionisiert, aus der Folie gelöst und beschleunigt.

An dem PHELIX – Laser bei GSI Darmstadt wurden bis zu 1.5×10^{13} Protonen pro Puls bei Energien bis zu 30 MeV nachgewiesen. Bei der im weiteren verwendeten Referenzenergie waren innerhalb eines Energiefensters von ± 0.5 MeV mehr als 10^{10} Protonen enthalten (Abb. 1).

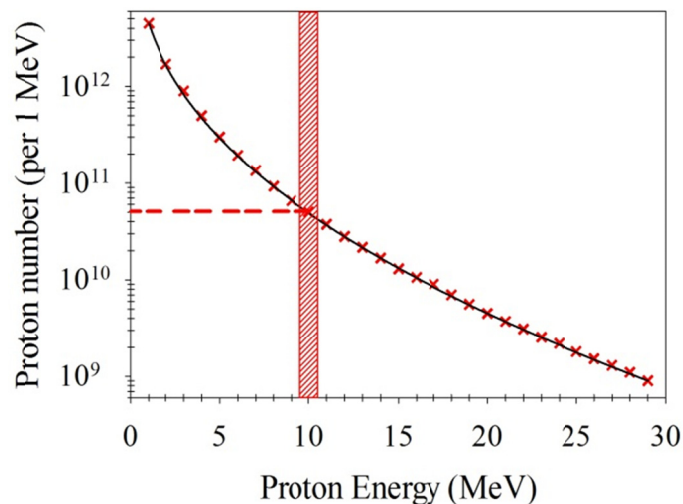


Abb. 1: In PHELIX – Experimenten erhaltenes Protonenspektrum. Die Protonenzahl fällt exponentiell mit der Energie ab. Mehr als 10^{10} Protonen sind im Energiefenster $10 \text{ MeV} \pm 0.5 \text{ MeV}$ enthalten (Mitteilung von M. Roth und V. Bagnoud).

Die emittierte Protonenstrahlung weist einen großen Divergenzwinkel von $\pm 23^\circ$ bei 10 MeV. Aufgrund der attraktiven Eigenschaften kann diese lasergetriebene Ionenquelle in manchen Fällen eine interessante Alternative zu herkömmlichen Protonenbeschleunigerkonzepten am

Niederenergieende sein. Außerdem erscheint die Kombination der lasergetriebenen Quelle mit einem konventionellen Hochfrequenzlinearbeschleuniger interessant.

Aufgrund der erreichten Strahlenergien kann direkt in einen Driftröhrenbeschleuniger eingeschossen werden. Hochspannungsterminals und Radiofrequenzquadrupole üblicher Aufbauten werden somit hinfällig. Eine derartige Kopplung wurde bereits früher angedacht (Einschuss in einen Alvarez – Driftröhrenbeschleuniger) aber noch nie verwirklicht.

In der vorliegenden Arbeit wird der Einschuss eines laserbeschleunigten 10 MeV Protonenbunches in einen Driftröhrenbeschleuniger vom CH – Typ untersucht, welcher gegenwärtig am IAP Frankfurt entwickelt wird. Diese Struktur zeichnet sich durch hohe Effizienz bei den gegebenen Strahlenergien aus. Am Einschuss wird ein 18 T Solenoid zur Fokussierung benutzt.

Transport durch den Solenoiden

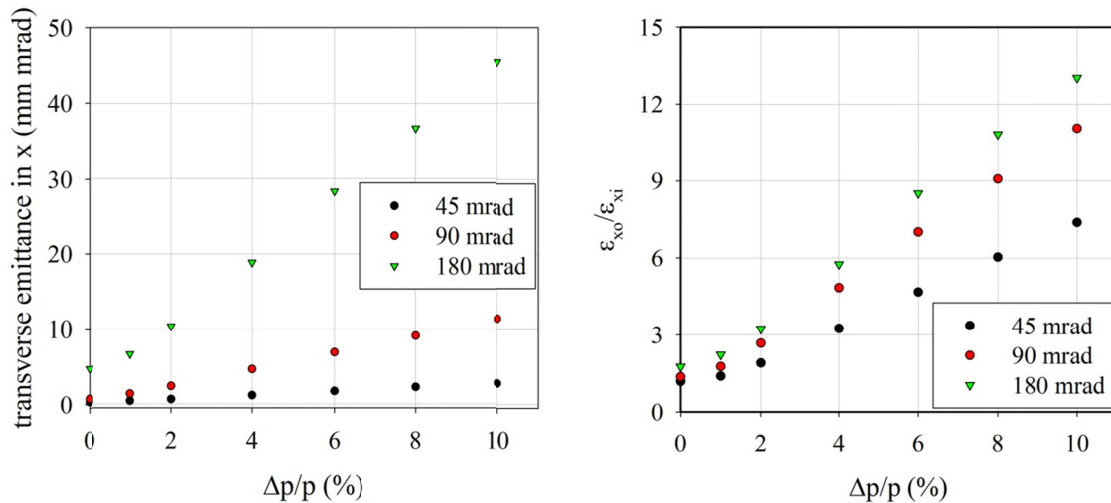


Abb. 2: Resultierende rms – Emittanzwerte in $x - x'$ in Abhängigkeit der Impulsunschärfe $\Delta p/p$ (links); Verhältnis von Eingangs- zu Ausgangs- rms – Emittanz in $x - x'$ in Abhängigkeit von $\Delta p/p$ (rechts) bei verschiedenen Strahlöffnungswinkeln am Ende der 210 mm langen Transportstrecke durch den Solenoiden.

Chromatische und geometrische Aberrationen entlang des Niederenergietransports von der erzeugenden Folie bis zum Einschuss in den Linearbeschleuniger wurden im Vorfeld detailliert untersucht (Abb. 2).

Besonders interessant war die Untersuchung der auftretenden Raumladungskräfte entlang dieser Anpassstrecke. Hierzu wurde einmal die volle Raumladung der im Energieintervall 10

± 0.5 MeV enthaltenen Protonen zugelassen, um die bewirkte Coulombexplosion quantitativ zu erfassen. Danach wurde der realistischere Fall eines mit Elektronen zunächst vollständig raumladungskompensierten Bunches simuliert.

Es konnte gezeigt werden, dass das Solenoidfeld zu einer ausgeprägten Ladungstrennung zwischen Protonen und Elektronen führt. Die Auswirkungen auf das Emittanzwachstum wurden quantitativ untersucht.

Abb. 3 zeigt, dass sich Elektronen- und Protonenverteilung bereits nach 25 ps sichtbar unterscheiden, die Elektronen erzeugen ein ausgeprägtes negatives Raumladungspotential in Achsennähe, da das Randfeld des Solenoiden dort eine erhöhte Elektronendichte herbeiführt.

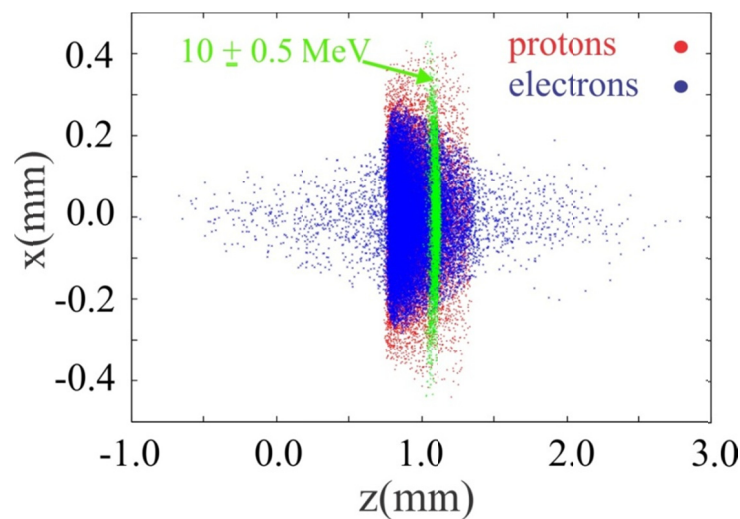


Abb. 3: $z - x$ Projektion der Teilchenverteilungen nach 25 ps. Man erkennt bereits die relativ ungehindert divergent weiterlaufenden Protonen im Gegensatz zu den Elektronen, welche durch die Solenoidrandfelder zur Achse abgelenkt werden und infolge des entstehenden, negativen Raumladungspotentials entlang der Strahlachse beschleunigt werden.

Im Weiteren bewirkt die achsennahe Elektronenkonzentration eine lokale Überfokussierung des Protonenstrahls, wie die Abb. 4 zeigt.

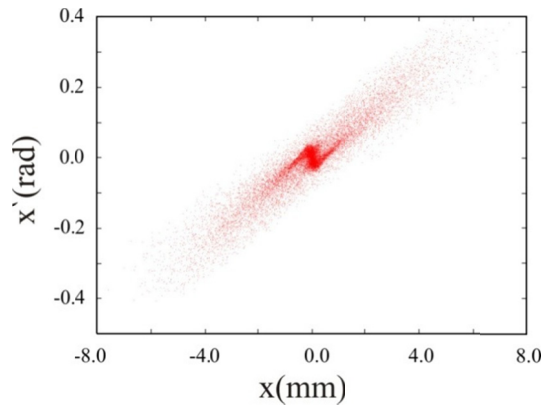


Abb. 4: $x - x'$ Phasenraumprojektion beim Eintritt in den Solenoiden. Hier sind Protonen zwischen 5 und 15 MeV enthalten. Der niederenergetische Protonenanteil ist im dichten Kern der Verteilung überproportional vertreten.

Bei der Ankunft am Linearbeschleunigereingang zeigt die simulierte Strahlverteilung schließlich Emittanzwerte, welche die Akzeptanz voll ausfüllen. Es war ein wesentliches Ergebnis der Arbeit, die Emittanzproblematik des lasergenerierten Strahls bzgl. der Anpassung an einen Linearbeschleuniger aufzuzeigen. Aufgrund der hohen Protonenstrahlenergie beim Erzeugungsprozess ist es nicht trivial, mit den Emittanzwerten konventionell erzeugter Strahlen zu konkurrieren.

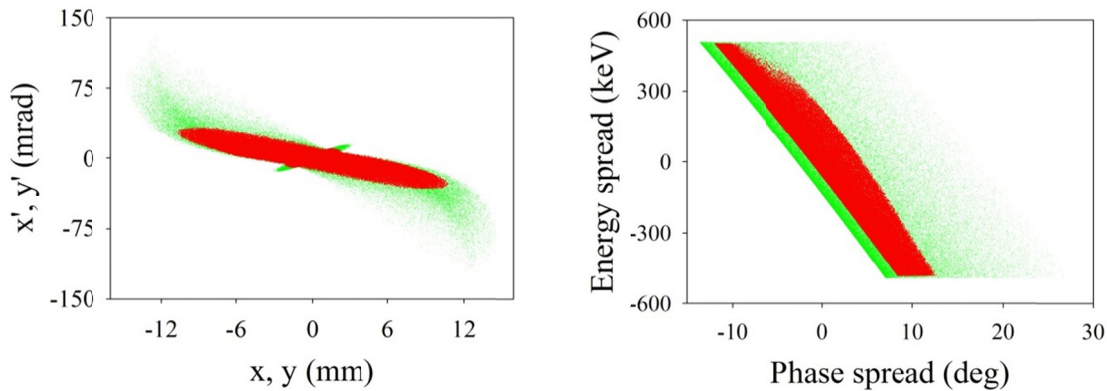


Abb. 5: In grün sind die simulierten Teilchenverteilungen am Linac-Einschuss im Energiebereich $10 \text{ MeV} \pm 0.5 \text{ MeV}$ gezeigt. In rot ist der Akzeptanzbereich des Linac dargestellt.

Linearbeschleunigerauslegung

Die Auslegung des Linearbeschleunigers wurde auf Basis der „Cross Bar H-Type“ CH – Struktur vorangetrieben.

Zur teilchenoptischen Auslegung wurde zunächst eine künstlich erzeugte Teilchenverteilung mit einer zu 500 mA äquivalenten Teilchenzahl verwendet. In diese Struktur wurde dann der entsprechend obiger Beschreibung simulierte, lasererzeugte Teilchenpuls eingeschossen und bis zum Ende gerechnet. Schließlich wurde die Struktur mit Hilfe dieses Pulses optimiert bzgl. der resultierenden Strahleigenschaften.

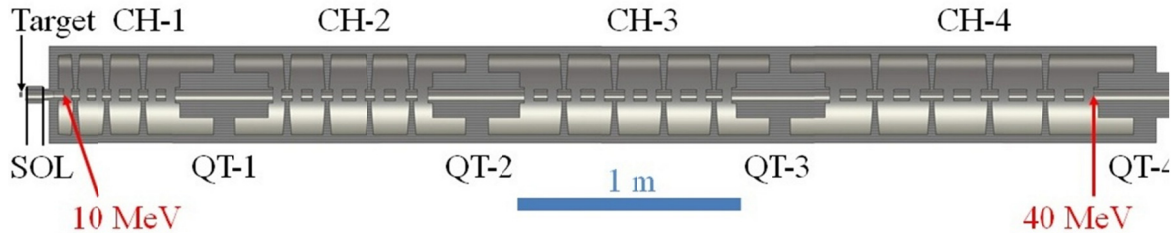


Abb. 6: Längsschnitt durch den konzipierten CH – Linac. Am Eingang erkennt man den Solenoiden zur Fokussierung des Strahls auf den Linac-Eingang.

Der Linac besteht aus 4 Kavitäten, die Spaltzahlen liegen zwischen sieben und zehn, bedingt durch die transversale Strahldynamik: Zwischen den Kavitäten sitzt jeweils ein Quadrupoltriplett mit begrenzter Apertur. Innerhalb von 5.1 m wird der Strahl von 10 MeV auf 40 MeV beschleunigt. Alle effektiven Spaltspannungen liegen nahe bei 1 MV, die Beschleunigungsgradienten liegen zwischen 7 und 12.6 MV/m. Folgende Ergebnisse resultierten von den strahldynamischen Untersuchungen:

1 – *Angepasster Fall*: Die Strahlparameter der künstlich erzeugten Verteilung sind in Tab. 1 zusammengefasst. Die Simulation zeigte 100% Transmission.

Tab. 1: Normierte rms- Emittanzwerte bei 500mA äquivalentem Strahlstrom

Emittanz	Eingang	Ausgang
Transversal/ mm mrad	x: 3.85	4.08
	y: 3.85	4.06
Longitudinal/ keV ns	5.37	6.68

Die rms- Emittanzzuwächse sind entlang des Linac weniger als 25% longitudinal und weniger als 6 % transversal. Die Emittanzwerte am Einschuss sind allerdings vergleichsweise groß gewählt. Dies war als Vorbereitung auf den lasererzeugten Strahl auch notwendig.

Die transversalen und longitudinalen 90,99 und 100 % Strahlenveloppen bei 500 mA äquivalentem Strahlstrom zeigt Abb. 7. Die Quadrupolgradienten reichen dabei bis zu

50.5 T/m bei einem Aperturradius von 25 mm. Dies ist nur noch mit Kobalt – basiertem Material zu erreichen.

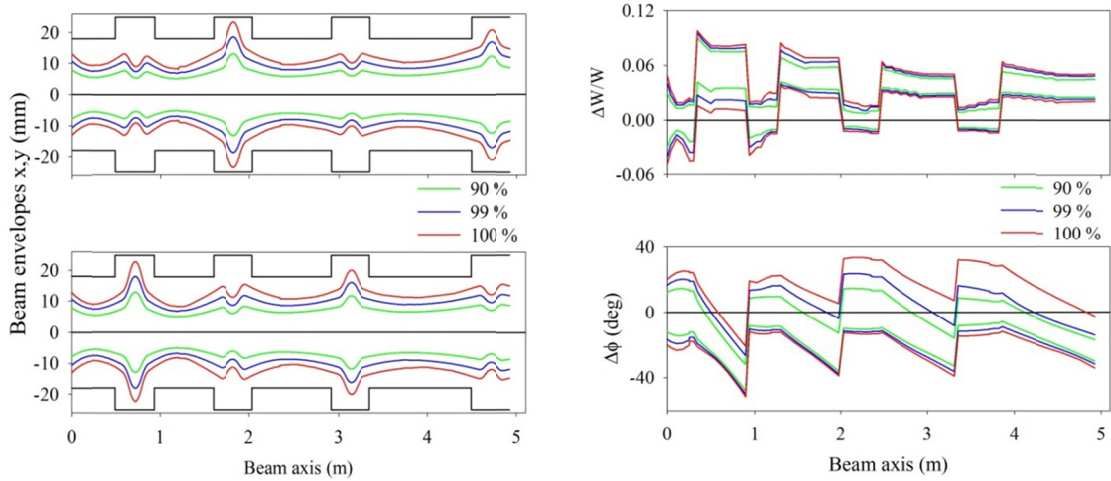


Abb. 7: Transversale (links) und longitudinale (rechts) 90%, 99% und 100% Einhüllende bei 500 mA äquivalentem Strahlstrom. Die schwarzen Berandungslinien deuten grob den Aperturverlauf an.

Die zweidimensionalen Phasenraumverteilungen am Ein- und Ausgang sind in Abb. 8 gezeigt. Man sieht deutlich, dass die Raumladung sich bei der gewählten Auslegung hauptsächlich in der longitudinalen Ebene auswirkt.

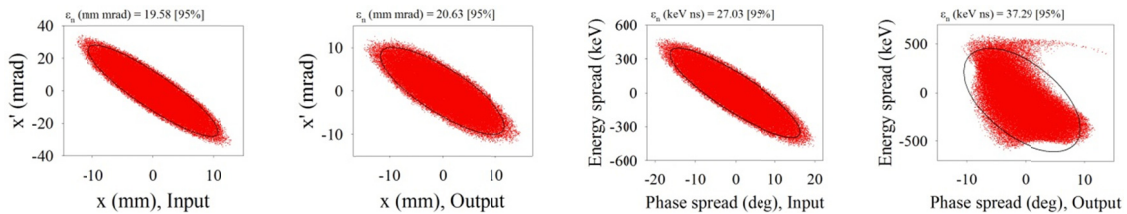


Abb. 8: Transversale (links) und longitudinale (rechts) Teilchenverteilungen am Ein- und Ausgang des Linac bei 500 mA Strahlstrom. Mit eingetragen sind die norm. Emittanzwerte der dargestellten 95 % Ellipsen.

2 – Laserbeschleunigter Strahl: Die in Abb. 5 dargestellte Teilchenverteilung (nur die in rot gezeichnete Untermenge) wird nun in den Linac eingeschossen, und die Linsenparameter entsprechend optimiert. Zunächst ist festzustellen, dass der akzeptierte Teilstrahl mit Energien zwischen 9.5 MeV und 10.5 MeV nur noch einem äquivalenten Strahlstrom von 216 mA entspricht. Die wesentlichen Strahlparameter des verlustfrei beschleunigten Strahls sind in Tabelle 2 angegeben.

Tab. 2: Norm. rms- Emittanzwerte des laserbeschleunigten Strahls am Ein- und Ausgang des Linac, äquivalenter Strahlstrom 216 mA.

Emittanz	Eingang	Ausgang
Transversal/ mm mrad	x: 2.89	3.06
	y: 2.89	3.33
Longitudinal/ keV ns	3.42	6.86

In diesem Fall ergeben sich rms – Emittanzzuwächse von 100 % longitudinal und 16 % transversal. Trotz des deutlich geringeren Strahlstroms sind die Emittanzzuwächse also deutlich größer als im angepassten Fall, was insbesondere an der deformierten Eingangsemittanz liegen dürfte (Abb. 5, rechts).

Die in diesem Fall mit 20000 Makroteilchen erhaltenen Ausgangsemittanzen sind in Abb. 9 dargestellt.

Die erhaltenen Verteilungen wären für eine weitere Beschleunigung oder für den Einschuss in ein Synchrotron geeignet, allerdings sollte die longitudinale Strahlführung weiter verbessert werden.

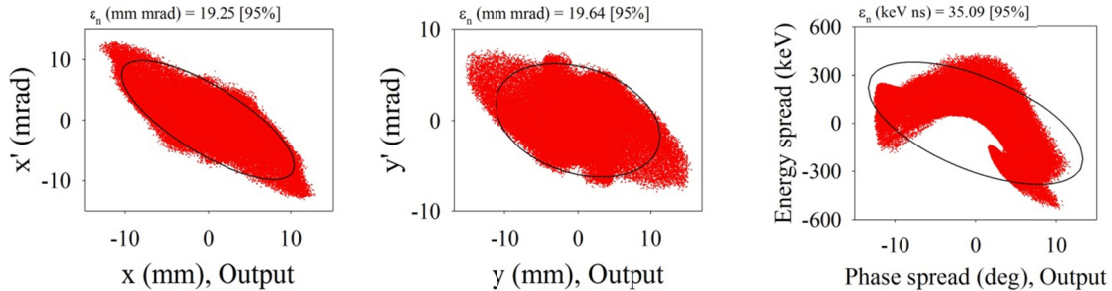


Abb. 9: 40 MeV - Ausgangsverteilungen im Fall des laserbeschleunigten Strahlpulses entsprechend Abb. 5

Ein großer Vorteil der Beschleunigung einzelner Hochstromeimpulse aus lasergetriebenen Ionenquellen ist, dass die aufgenommene Strahlleistung aus der gespeicherten Feldenergie der einzelnen Kavitäten entnommen werden kann. Bei längeren Bunchfolgen muss dagegen der Hochfrequenzverstärker die Strahlleistung zusätzlich aufbringen und damit entsprechend leistungsstärker ausgelegt werden. Es wurde abgeschätzt, dass Einzelpulse mit bis zu 2×10^{11} Protonen auf diese Weise beschleunigt werden könnten, ohne die Spannungsamplitude dabei um mehr als 1 % zu senken.

Ein weiterer wichtiger Aspekt sind die in den Linac eingeschossenen Teilchen, welche nicht in die Akzeptanz passen und auf die Wände treffen. Hier sollte durch Blenden am Linac-Eingang möglichst viel Intensität im Vorfeld abgetrennt werden. Ansonsten ist dieser Aspekt zweifelsfrei nur durch ein Strahlexperiment zu klären, welches innerhalb der LIGHT – Kollaboration und durch weitere Fördermittel realisiert werden soll (Abb. 10).

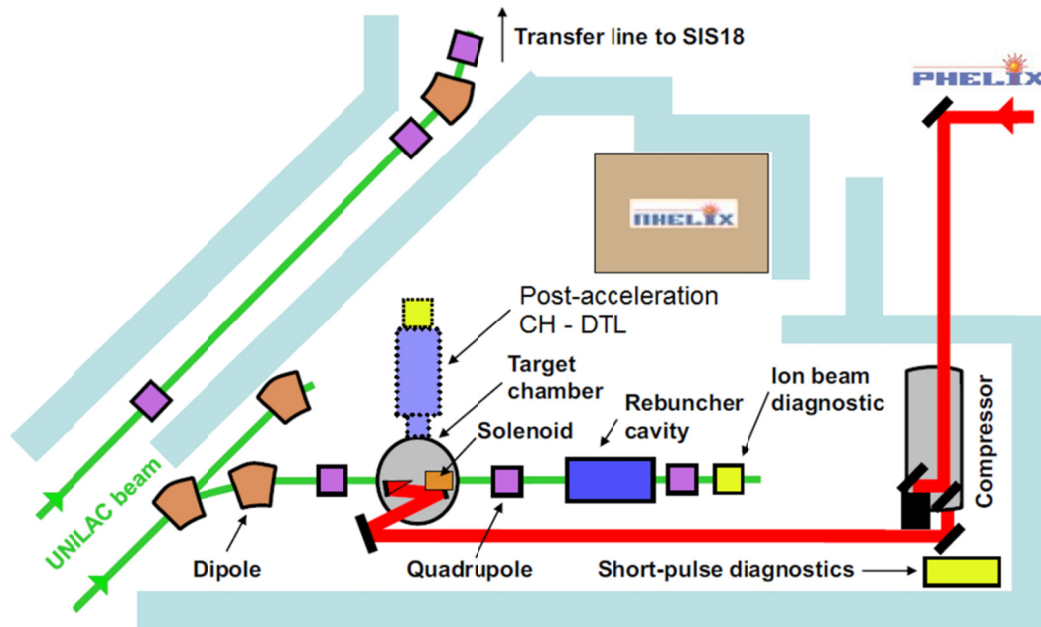


Abb.10: Die Experimentierplätze Z4 and Z6 in der GSI-Unilac – Experimentierhalle. Die in Planung befindliche CH – Kavität kann mit PHELIX – erzeugten Strahlpulsen getestet werden.

Detaillierte Auslegung der ersten Kavität des CH – Linac

Mit Hilfe des Programms MWS der Fa. CST zur Berechnung elektromagnetischer Feldverteilungen in Kavitäten wurde die erst Linac- Kavität ausgelegt und die Spaltgeometrie sowie die Feldverteilungen in Einklang mit den Parametern der strahldynamischen Untersuchungen gebracht. Die Driftröhrenaufhängungen (Stems) wurden so geformt, dass speziell an den Tankenden die gewünschte Spaltspannungsamplitude erreicht wurde, bei möglichst kurzer Gesamtlänge der Kavität (Abb. 11 und 12). Die Beschleunigungsgradienten wurden sehr hoch gewählt, um genügend starke longitudinale Strahlfokussierung zu erhalten. In genaueren Untersuchungen wurde gezeigt, dass die Felder um etwa 25 % gesenkt werden können, ohne signifikante Strahlverschlechterungen zu erhalten.

Eine Auftragung der höchsten Oberflächenfelder entlang achsenparalleler Pfade knapp innerhalb des Außenradius der Driftröhren zeigt einen Verlauf wie in Abb. 13 dargestellt. Die Spitzen für den Nominalfall entsprechen bis zu 94 MV/m und sind damit an der technischen Grenze.

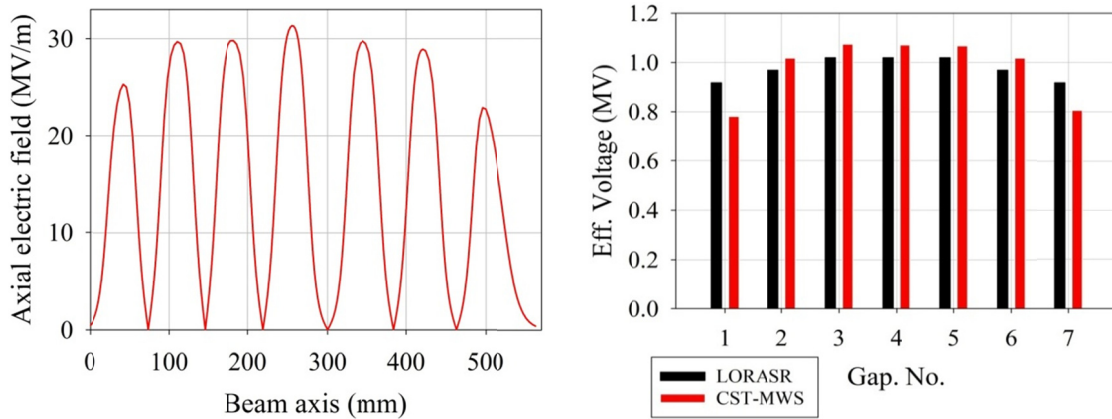


Abb. 11: Die mit MWS simulierte Feldverteilung entlang der Strahlachse (links) sowie der Vergleich von gewünschter und simulierter Spaltspannungsverteilung (rechts)

Tab. 3: Die wichtigsten Parameter der ersten CH - Kavität

Spaltzahl	7
Frequenz (MHz)	325.2
Energiebereich (MeV)	10.05 – 16.09
Verlustleistung (MW)	1.92
Q_0 – Wert	13289
Eff. Shuntimpedanz ($M\Omega/m$)	45.7
Beschleunigungsgradient (MV/m)	12.6
Aperturdurchmesser (mm)	30

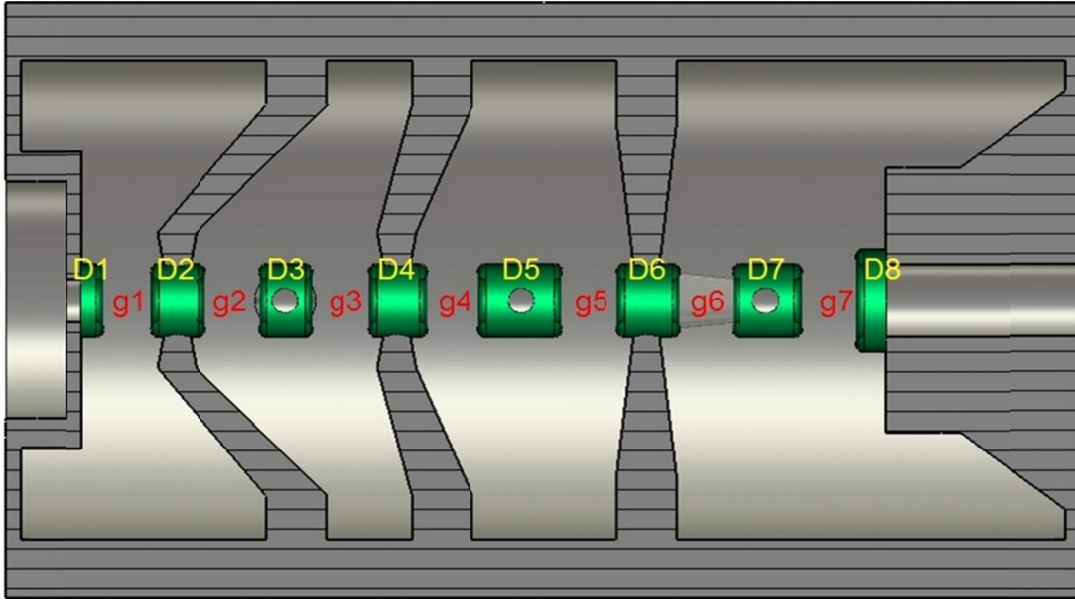


Abb. 12: Skizze der ersten CH – Kavität mit gekröpften Stems und resonanten Endgeometrien.

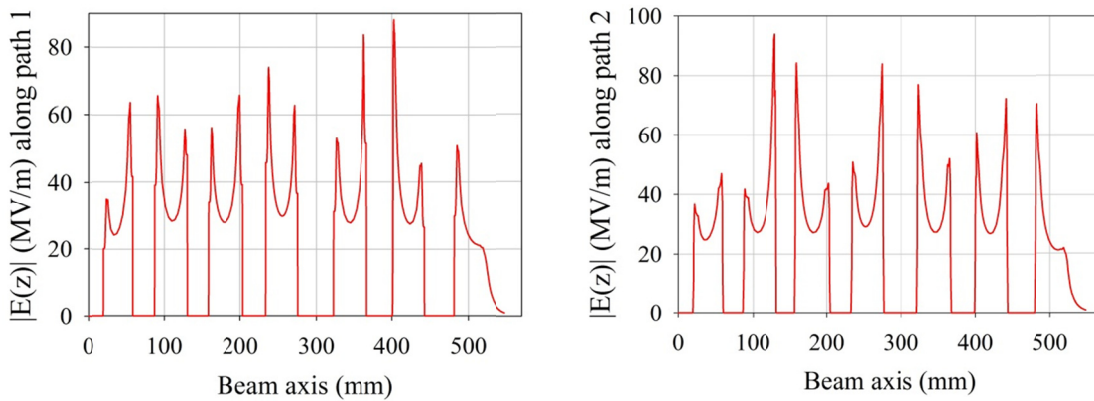


Abb. 13: Darstellung der auftretenden Oberflächenfeldmaxima in der xz - und yz - Ebene. Die Wegpfade laufen dabei parallel zur Strahlachse in einem Abstand geringfügig unterhalb des äußeren Driftröhrenradius.

Ausblick

Lasererzeugte Protonenstrahlen zeigen interessante Eigenschaften, welche eine Kopplung mit Linearbeschleunigern ermöglichen. Insbesondere Anwendungen für intensive Einzelpulse könnten hiermit optimal bedient werden. Wichtig für solche Ziele ist allerdings eine erhebliche Steigerung der Laserpulswiederhol frequenzen sowie eine hohe Puls- zu Pulsstabilität. Die Strahltransportstrecken für lasererzeugte Teilchenstrahlen sind sehr anspruchsvoll – wegen der hohen Erzeugungsdichte der Strahlpulse und der komplexen Verteilung im Phasenraum. Der in dieser Arbeit eingeschlagene Weg einer möglichst kurzen Anpassstrecke an einen Linac erscheint vielversprechend und wird weiter verfolgt.

TABLE OF CONTENTS

Zusammenfassung.....	V
Chapter 1: Introduction	1
1.1 Overview	1
1.2 Thesis Structure	4
Chapter 2: Laser – Accelerated Protons: A New Particle Source for the Conventional Accelerators	7
2.1 Laser – Plasma Interaction	7
2.1.1 <i>Electrons Interaction with Laser</i>	8
2.1.2 <i>Ponderomotive Force</i>	9
2.1.3 <i>Laser Propagation in the Plasma</i>	12
2.1.4 <i>Electron Acceleration and Transport</i>	13
2.2 Laser – Proton Acceleration	14
2.2.1 <i>Target Normal Sheath Acceleration – TNSA</i>	15
2.2.2 <i>Proton Beam Expansion</i>	16
2.3 Application of Laser – Accelerated Protons	18
2.3.1 <i>A new particle Source for Conventional Accelerators</i>	19
2.3.2 <i>Isochronic Heating</i>	19
2.3.3 <i>Medical Applications</i>	20
Chapter 3: Experimental Setup for Laser – Proton Acceleration	23
3.1 PHELIX Laser Facility.....	24
3.2 Radio Chromic Films	26
3.3 Proton Beam Parameter.....	29
Chapter 4: Tracking of Laser – Accelerated Protons through a Pulsed Magnetic Solenoid	35
4.1 LASIN Code.....	36
4.2 Pulsed Magnetic Solenoid.....	36
4.3 Simulations without Space Charge	38
4.3.1 <i>Chromatic and Geometric Aberrations</i>	38
4.3.2 <i>Proton Bunch Transported through the Solenoid</i>	45
4.4 Simulations with Space Charge.....	46

4.4.1 <i>Proton Bunch Tracking (without electrons)</i>	47
4.4.2 <i>Two Species (Proton Bunch with Electrons)</i>	52
Chapter 5: RF Linacs with H-type Cavities	65
5.1 RF Linacs Parameters.....	65
5.2 Beam Dynamics in Linac	69
5.2.1 <i>Longitudinal Particle Dynamic</i>	71
5.2.2 <i>Transverse Beam Dynamics</i>	73
5.3 H- type Cavities.....	75
5.3.1 <i>Interdigital H-type DTL (IH-DTL)</i>	78
5.3.2 <i>Crossbar H-type DTL (CH-DTL)</i>	80
5.4 KONUS Beam Dynamics and LORASR Code.....	83
5.5 Superconducting CH – DTL	88
Chapter 6: Development and Matching of a Dedicated CH- Linac for Intense Laser – Accelerated Proton Bunches.....	91
6.1 Dedicated CH – linac Design for Laser- Accelerated Proton Bunch	92
6.1.1 <i>Matched Beam Case</i>	95
6.1.2 <i>Laser- Accelerated Beam Case</i>	97
6.2 Linac Designs for Reduced Voltage Gain.....	101
6.3 Limitation of Voltage Drop Tolerance.....	104
6.4 RF Power Budget for a Single Bunch Operation	110
Chapter 7: The First Cavity of the Dedicated DTL for Laser Proton Acceleration	113
7.1 Optimization of the First CH – Cavity	113
7.2 Surface Field Distribution	124
Chapter 8: Conclusion and Outlook	131
Bibliography	135
List of Figures.....	151
List of Tables	160
Acknowledgement	161
Curriculum Vitae	165

CHAPTER 1

INTRODUCTION

1.1 Overview

The construction of the early particle accelerators was motivated by nuclear physics [1]. In 1932, J. Cockroft and E. Walton performed the first artificial nuclear reaction with a proton beam using a dc particle accelerator [2].

Due to the limitations of dc voltage the main acceleration is provided nowadays by RadioFrequency RF accelerators.

In 1927 Wideröe built the first RF linear accelerator by applying a time – alternating voltage to a sequence of drift tubes [3]. This inspired E. Lawrence to invent the cyclotron in the following year [4].

The development progress in this field was focused on accelerating the particles to highest energies. At the same time, a good beam quality (brilliance) was needed – especially in case of colliding beam experiments. For example in the Large Hadron Collider LHC [5], the proton beam will be accelerated to energies of 7 *TeV* with about 10^{11} particles per bunch.

On the other hand, the accelerator size and costs become quite high. Because of that, the new research in accelerator physics is aiming on developing new approaches and concepts to overcome these constraints.

The interactions of the high – power lasers with solid targets are capable of accelerating ions to energies in the *MeV* – range (ten to several tens on *MeV* in case of protons) [6-35].

The invention of Chirped Pulse Amplification CPA in 1985 by Strickland and Mourou [36] opened the way for increasing the power of laser pulses. After the implementation of CPA technology in modern laser facilities, one can achieve high energy laser systems with ultra – short ultra – intense laser pulses with intensities approaching 10^{21} *W/cm²* [37-40]. The unavoidable laser pre-pulse with an intensity of the order 10^{12} *W/cm²* is high enough to ionize the target and to create plasma [7-8, 10, 18, 20, 25, 27, 41-48]. The main laser pulse will interact with the plasma on the target front side. Beyond intensities of 10^{18} *W/cm²*, the motion

of electrons in the plasma is treated fully relativistic. In case of protons, the corresponding intensity for relativistic motion exceeds 10^{24} W/cm^2 .

Through the interaction between the laser and the plasma, a part of the laser energy is converted into electron kinetic energy resulting in electrons with energies in the MeV – range [49]. These electrons are transported to the target rear side and form a huge electric field of the order TV/m due to charge separation [8-9, 24-25, 43, 50]. This field will be high enough to ionize the atoms on the rear side and to accelerate the ions to energies in the MeV – range (several tens of MeV for protons) [6-35]. The process of ion acceleration is called Target Normal Sheath Acceleration TNSA [6-10, 18, 25, 43, 50-56]. Figure 1.1 shows the development in laser – focused intensities and corresponding maximum ion energies extracted [33].

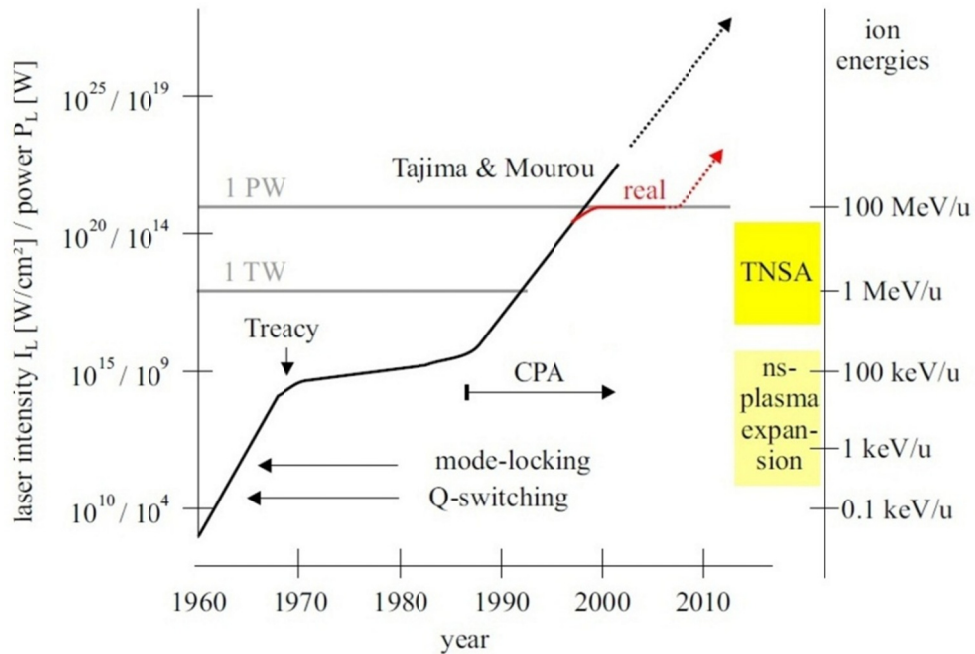


Figure 1.1: Development in laser – focused power density and laser power (left axis) and corresponding maximum ion energies (right axis) during the years. The solid black curve is taken from Tajima and Mourou [57-58]. This trend should be corrected (red line) because the threshold 1 PW laser intensity was not overcome since the first realization at Lawrence Livermore Laboratory. The yellow rectangle shows the current TNSA – regime [Courtesy of J. Schreiber, ref. 33].

The laser – accelerated protons (TNSA) possess interesting features in terms of energy, emittance and proton number per bunch which make them “promising attractive” to conventional proton sources [20, 41, 59-64].

In contrast to conventional accelerators, they can achieve considerably higher peak currents at beam energies of ten to several tens of MeV [7-8, 10, 18, 42-43, 65] when compared to state of the art injectors like single ended dc accelerators or RFQ’s [66-67].

The laser – proton source injector is capable of producing a single proton bunch, but on the other hand such an injector will have a very low duty factor.

The important topic for further acceleration of the laser – accelerated proton bunch is the matching into the acceptance of the succeeding RF accelerator [19, 41, 48, 59, 68-71].

Several projects are proposed in this field, LIGHT (**L**aser **I**on **G**eneration, **H**andling and **T**ransport) at GSI Darmstadt is one of them [68-69, 72-73]. The LIGHT project is developing laser accelerated proton beams, beam transport, and injection into a conventional accelerator.

This kind of hybrid proton accelerator will benefit from the interesting features of a laser based source and from the flexibility of RF based accelerator structures.

Due to the available energies, drift tube linacs are the most adequate choice for this purpose. The injection of laser – accelerated protons into a conventional drift tube linac DTL was discussed in the literature earlier [19, 59, 68-71].

The demonstration of focusing a laser – accelerated 10 MeV proton bunch by a pulsed 18 T magnetic solenoid into a linac structure is the subject of this thesis. H-type drift tube accelerators [74-76] seem well suited to accept beam bunches like generated by lasers. A **C**rossbar **H**-type (CH) structure is suggested because of its high acceleration gradient, β -range, mechanical robustness, and high shunt impedance [74-76] at the relevant injection energies. The motivation for such a combination is to deliver single beam bunches with acceptable emittance values and at extremely high particle number per bunch.

The results from PHELIX laser experiments and from simulations performed by the Warp code [20, 22, 40, 48, 77-78] show, that there are some restrictions with respect to a post acceleration of the generated bunches.

For example at PHELIX experiments performed in 2008, protons with energies up to 30 MeV and a total yield of 10^{13} protons were observed [20, 22, 40, 78]. The proton spectrum is characterized by a large divergence ($\pm 23^\circ$ at 10 MeV). This divergence decreases with increasing energies down to $\pm 8^\circ$ at 29 MeV as shown in Figure 1.2.

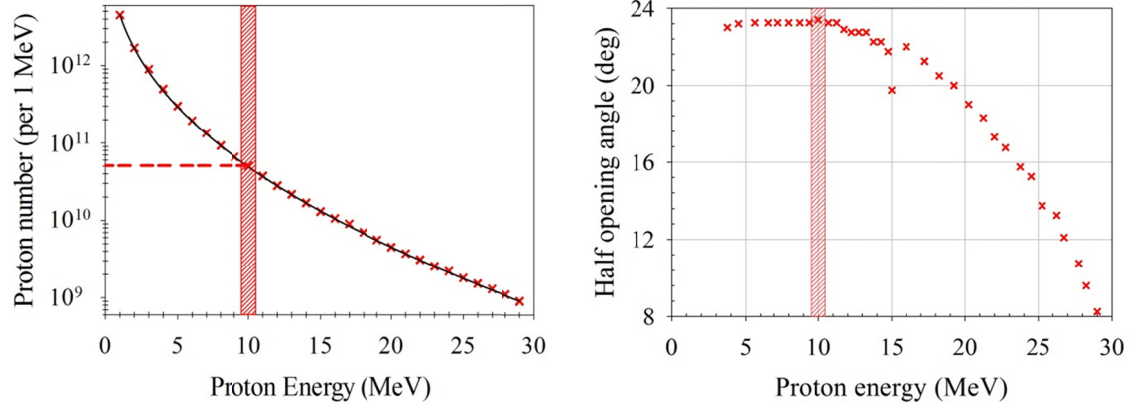


Figure 1.2: Dependence of differential particle yield (left) and half opening angle (right) from the proton energy at TNSA experiments with PHELIX (Courtesy of M. Roth and V. Bagnoud).

The main aim of this work is to find the matching tools from the laser accelerated – protons at the target position to the injection point into the CH – DTL.

1.2 Thesis Structure

The thesis is structured in 8 chapters.

In chapter 2 an overview on the interaction of the laser with the solid target will be given. Then a general discussion about the laser – plasma interaction follows, including the laser propagation in the plasma. The electron acceleration and transport will be discussed briefly. In section 2.2 the laser – proton acceleration mechanism “Target Normal Sheath Acceleration” will be explained. Finally, an overview on optional applications of laser – accelerated protons (ions) will be addressed.

Chapter 3 is discussing the tracking of laser – accelerated protons through a pulsed magnetic solenoid. In this chapter, the higher order aberrations in the solenoid like chromatic and spherical (geometric) aberrations are investigated in detail. Space charge effects caused by the solenoid will be studied. Here two cases are described: The proton bunch tracking at full space charge from the starting point and the completely neutralized bunch starting at the

target position. In the second, more realistic case, the space charge force is identically zero at the target position ($t = 0$) and starts growing due to charge separation between electrons and protons while passing the magnetic solenoid field.

The simulations in this chapter were performed using LSAIN code, which was developed at IAP – Frankfurt by Dr. Martin Droba.

The experimental setup for laser – proton acceleration will be shown in chapter 4. The results of one experiment carried out at PHELIX (**P**etawatt **H**igh **E**nergy **L**aser for heavy **I**on **eX**periments) will be summarized in section 4.3.

In chapter 5 an introduction on RF linacs including the beam dynamics will be given. The H-type cavities (CH- and IH- DTL) are discussed in section 5.3. The KONUS beam dynamics is explained in section 5.4.

Chapter 6 is describing the matching of laser – accelerated protons into a dedicated CH – linac. The beam dynamics in longitudinal and transversal planes through the structure are investigated in detail. After designing a CH linac suited to accept the high bunch current from the TNSA – process a bunch particle distribution as resulting from beam simulations along the matching section was tracked through the linac.

In chapter 7, the simulations of CST - MicroWave Studio will be presented. The optimization of the drift tube, gap and stem geometries for the first cavity in the dedicated DTL will be shown. Tuning of the electric and magnetic fields distributions inside the cavity was performed. Section 7.2 shows the investigations on the surface electric fields for the CH – DTL.

Chapter 8 contains the main results, conclusions and the outlook on experimental activities.

CHAPTER 2

LASER – ACCELERATED PROTONS: A NEW PARTICLE SOURCE FOR CONVENTIONAL ACCELERATORS

The interactions of the ultra-short ultra-intense laser pulses with solid targets create novel states of matter [13, 16, 43, 50, 79-97]. In the process of Chirped Pulse Amplification (CPA) disturbing effects like Amplified Spontaneous Emission (ASE) promote the formation of laser pre-pulses which are intense enough to ionize the target and to create a pre-plasma [7-8, 10, 18, 20, 25, 27, 41-48]. The main laser pulse interacts with the pre-plasma on the target front side. The laser pulses with intensities exceeding 10^{18}W/cm^2 have a corresponding electric field of the order TV/m [8-9, 24-25, 43, 50]. This field is an order of magnitude larger than the electric field of a hydrogen atom. Because of their small masses the main interaction happens between the laser and electrons which are accelerated to velocities close to speed of light. Thus, the relativistic electron mass will increase and the laser magnetic field comes into play and the relativistic effects define the electron motion. At these intensities, different absorption mechanisms of laser energy are introduced in the plasma where a large fraction of the laser energy is converted into kinetic energy of electrons. Hence, the electrons with energies in the MeV- range are transported through the target and then leave the rear side, forming a dense electron cloud [16, 98-100]. The charge separation of the electrons from the remaining target creates a strong electric field which is able to accelerate the ions (mainly protons) from the rear target surface to kinetic energies in MeV – range.

2.1 Laser – Plasma Interaction

In order to understand the interaction between the laser and plasma, it will be worth to study the case of single electron in the electromagnetic waves. The electric and magnetic fields are given as the solution of Maxwell's equations. For linearly polarized laser propagating in the z- direction, \mathbf{E} and \mathbf{B} are given as

$$\mathbf{E}(\mathbf{r}, t) = E_0 \mathbf{e}_x \exp[i(kz - \omega_L t)] \quad (2.1)$$

$$\mathbf{B}(\mathbf{r}, t) = E_0 \mathbf{e}_y \exp[i(kz - \omega_L t)] \quad (2.2)$$

where E_0 and B_0 are the laser electric and magnetic field amplitudes, respectively with $B_0 = E_0/c$, ω_L the laser angular frequency, k the laser propagation vector, t the time, c speed of light and $\mathbf{e}_{x,y}$ the unit vectors defining the orthogonality of \mathbf{E} and \mathbf{B} with the propagation vector \mathbf{k} .

The energy flux density (energy per unit area, per unit time) transported by the fields is given by the Poynting vector \mathbf{S}

$$\mathbf{S} = \frac{1}{\mu_0} \mathbf{E} \times \mathbf{B} \quad (2.3)$$

where μ_0 is the permeability of the vacuum.

The laser intensity is defined as the average power per unit area transported by an electromagnetic wave over the fast oscillations of the laser field

$$I = \langle |\mathbf{S}| \rangle = \frac{1}{2} \varepsilon_0 c E_0^2 \quad (2.4)$$

where ε_0 is the permittivity of the vacuum.

A laser pulse with intensity 10^{19} W/cm² has a corresponding electric field amplitude of $E_0 \approx 9$ TV/m. Using the relation $B_0 = E_0/c$, the corresponding magnetic field amplitude $B_0 \approx 30$ kT.

2.1.1 Electron – Laser Interaction

The motion of a single electron in free space in presence of the laser can be described by the Lorentz force. The equation of motion can be written as

$$\frac{d\mathbf{p}}{dt} = \frac{d}{dt}(\gamma m_e \mathbf{v}) = -e(\mathbf{E} + \mathbf{v} \times \mathbf{B}) \quad (2.5)$$

where \mathbf{p} and \mathbf{v} are the electron momentum and velocity, respectively. $\gamma = 1/\sqrt{1 - \beta^2} = \sqrt{1 + p^2/m_e^2 c^4}$ is the relativistic factor, $\beta = v/c$ is the normalized velocity, e and m_e is the charge and the rest mass of electron, respectively.

For non-relativistic motion ($v \ll c$), the $\mathbf{v} \times \mathbf{B}$ –term can be neglected and electron motion is defined by the electric field term. The solution of equation (2.5) leads to a harmonic oscillation in x- direction with the maximum oscillation velocity

$$v_{osc} = \frac{eE_0}{m_e \omega_L} \quad (2.6)$$

At intensities higher than 10^{18} W/cm², the motion becomes relativistic. In order to differentiate between different motion regimes, the dimensionless electric field amplitude a_0 is introduced as the ratio of maximum oscillation velocity in equation (2.6) to speed of light

$$a_0 = \frac{eE_0}{m_e \omega_L c} \quad (2.7)$$

Hence, the corresponding electric and magnetic field amplitudes can be defined in terms of a_0 as

$$E_0 = \frac{m_e \omega_L c}{e} a_0 = \frac{a_0}{\lambda_L [\mu m]} \cdot 3.2 \times 10^{12} V/m \quad (2.8)$$

$$B_0 = \frac{m_e \omega_L}{e} a_0 = \frac{a_0}{\lambda_L [\mu m]} \cdot 1.07 \times 10^4 T \quad (2.9)$$

and the intensity given by

$$I = \frac{1}{2} \varepsilon_0 c E_0^2 = \frac{a_0^2}{\lambda_L^2 [\mu m^2]} \cdot 1.37 \times 10^{18} W/cm^2 \quad (2.10)$$

In the classical, non-relativistic regime $a_0 \ll 1$, the electron motion is dominated by the electric field as mentioned above. The magnetic field force $F = qvB$ leads to a forward drift of the electron motion in z- direction. The corresponding velocity is

$$\mathbf{v}_D = \frac{a_0^2}{4 + a_0^2} c \mathbf{e}_z \quad (2.11)$$

Nevertheless, at the end of the laser pulse the electron velocity is zero despite the electron has changed his position. Hence, the electron does not gain energy from laser, which is known as the Lawson-Woodward theorem [101]. For $a_0 \approx 1$ the electron velocity approaches the speed of light, and the motion must be treated fully relativistic. The ultra-relativistic regime is defined in case $a_0 \gg 1$.

2.1.2 Ponderomotive Force

Up to this point, the problem was restricted to a laser plane wave. While in reality, the laser is focused to a focal spot diameter of several μm resulting in a varying transverse intensity profile which could be, for example, Gaussian.

Hence, the laser intensity decreases with increasing distance from the axis. This will lead to a displacement of the electron during the first half-cycle into the region of lower intensity. At its new position, the electron experiences a weaker laser field whose electric field is not able to return the electron to its initial position during the second half-cycle of the laser oscillation. Thus, the electron drifts towards the lower intensity regions with a finite velocity.

The force driving the electron to lower intensity region is called the ponderomotive force [102-108]. It was derived in 1957 by Boot and Harvie [102], who showed that charged particles of either sign will experience acceleration towards the position of least electric field strength [109-110]. For a single electron, the ponderomotive force is given by [102, 104, 108]

$$\mathcal{F}_p = -\frac{e^2}{4m_e\omega_L^2}\nabla(\mathbf{E}\cdot\mathbf{E}^*) \quad (2.12)$$

As soon as the electron velocity approaches the speed of light, the Lorentz force acting on the electron due to the magnetic field cannot be neglected anymore. The $\mathbf{v}\times\mathbf{B}$ force pushes the electron into the forward direction (see equation (2.11)). In this case, the relativistic correction on the ponderomotive force has been obtained by Bauer et al. [104]

$$\mathcal{F}_p = -\frac{c^2}{\gamma}\left[\nabla m_{eff} + \frac{\gamma-1}{v_0^2}(\mathbf{v}_0\cdot\nabla m_{eff})\mathbf{v}_0\right] \quad (2.13)$$

where m_{eff} the space and time dependent effective mass is given by

$$m_{eff} = \left(1 + \frac{e^2\mathbf{A}\cdot\mathbf{A}^*}{2m_e^2c^2}\right)^{1/2} = \bar{\gamma} \quad (2.14)$$

where \mathbf{A} the magnetic vector potential and the cycle- averaged gamma function $\bar{\gamma} = \sqrt{1 + a_0^2/2}$ [111] for a linearly polarized laser.

The solution of equation (2.13) is very complicated and has to be done numerically which is not a topic in this thesis.

Up to this point, only the interaction of a single electron with the laser field is described. In comparison with electrons, ions have much higher rest mass. Protons for example, as the lightest ion ($m_p = 1836 m_e$), have the relativistic threshold not at $a_0 = 1$ but at $a_{0,p} = 1836$. Using equations (2.8 – 2.10) and by replacing the electron mass by the proton one gets

$$E_0 = \frac{a_{0,p}}{\lambda_L[\mu m]} \cdot 5.9 \times 10^{15} V/m \quad (2.15)$$

$$B_0 = \frac{a_{0,p}}{\lambda_L[\mu m]} \cdot 1.9 \times 10^7 T \quad (2.16)$$

$$I = \frac{a_{0,p}^2}{\lambda_L^2[\mu m^2]} \cdot 4.6 \times 10^{24} W/cm^2 \quad (2.17)$$

where $a_{0,p}$ denotes the dimensionless electric field amplitude in the proton case.

A required intensity of $> 10^{24} W/cm^2$ is far beyond the present laser development. With intensities available today ($I_L = 10^{18} - 10^{21} W/cm^2$, $\lambda_L \approx 1 \mu m$) the ions hardly move in the laser electric field and they are assumed to form an immobile, positively charged background.

The averaged kinetic energy W_p which electrons gain during one laser cycle, can be obtained by calculating the ponderomotive potential U_p via $\mathcal{F}_p = -m_e \nabla U_p$, which leads to W_p . The resulting equation for the energy gain by the relativistic ponderomotive potential is

$$W_p = (\bar{\gamma} - 1)m_e c^2 \quad (2.18)$$

Equation 2.18 can be expressed in terms of measurable laser parameters or with the dimensionless electric field amplitude as [104-105, 112-114]

$$\begin{aligned} W_p = k_B T_e &= m_e c^2 \left(\sqrt{1 + \frac{I_L [10^{18} W/cm^2] \lambda_L^2 [\mu m^2]}{2.74}} - 1 \right) \\ &= m_e c^2 \left(\sqrt{1 + \frac{a_0^2}{2}} - 1 \right) \end{aligned} \quad (2.19)$$

where $I_L [10^{18} W/cm^2]$ is the laser intensity given in units of $10^{18} W/cm^2$, λ_L the laser wave length given in μm units, k_B the Boltzmann constant and T_e the electron temperature.

For a laser intensity of $5 \times 10^{19} W/cm^2$ at $\lambda_L = 1.054 \mu m$, one gets for protons $W_p^p = 2.81 keV$ and for electrons $W_p^e = 1.85 MeV$.

2.1.3 Laser Propagation in the Plasma

Up to this point, the study focuses on the interaction of the laser with a single electron. But in reality, the laser interacts with all plasma electrons.

An important length for quasi-neutral plasma is the Debye length λ_D [115]

$$\lambda_D = \sqrt{\frac{\epsilon_0 k_B T_e}{n_e e^2}} \quad (2.20)$$

where n_e and T_e are the electron density and electron temperature, respectively.

The electrons will oscillate with the electron plasma frequency ω_p [115]

$$\omega_p = \sqrt{\frac{n_e e^2}{\epsilon_0 m_e \bar{\gamma}}} \quad (2.21)$$

Hence, the laser can propagate in the plasma as long as its frequency ω_L exceeds the plasma frequency ω_p . The refractive index n_p can be defined in terms of ω_p and ω_L as [115]

$$n_p = \sqrt{1 - \frac{\omega_p^2}{\omega_L^2}} \quad (2.22)$$

For $\omega_L < \omega_p$ the refractive index becomes imaginary, which means that the laser can propagate up to the point where $\omega_L = \omega_p$. At this point, one can define the critical density, n_c as the electron density where the laser pulse is reflected by the plasma

$$n_c = \frac{\epsilon_0 \omega_L^2 m_e \bar{\gamma}}{e^2} \quad (2.23)$$

Figure 2.1 shows the interaction process between the laser and a solid target. The laser pulse propagates through the pre-plasma up to the point where the electrons reach the critical density.

Because of the ponderomotive force, the plasma electrons are pushed radially from the high intensity area near the axis towards lower intensities. This will change the radial electron density profile. Hence, this profile works as a convex lens for the laser beam. This effect is called the relativistic self-focusing [116-117].

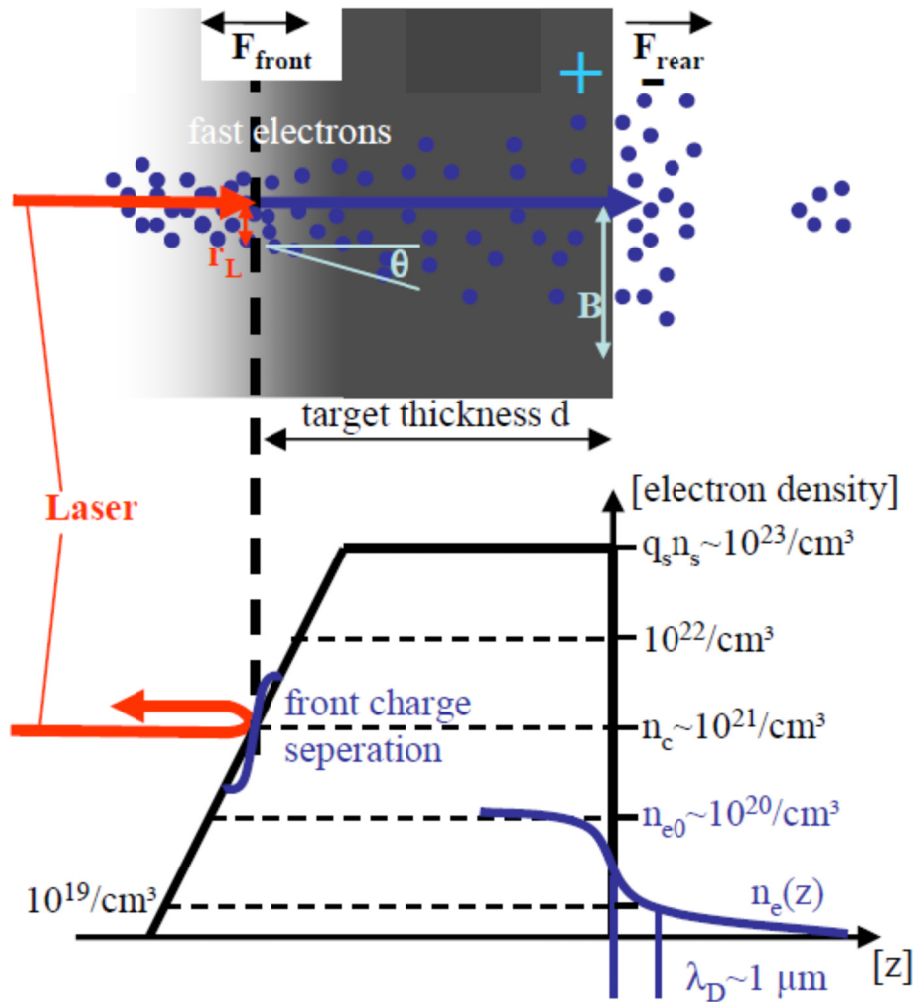


Figure 2.1: Scheme of the interaction between the laser and solid target. The laser pulse with focal spot radius r_L hits a target of thickness d resulting in a pre-plasma on the target front side. The laser propagates through the plasma until it reaches a position where the electrons have its critical density n_c . At that density the plasma has a zero refractive index and the laser will be reflected [Courtesy of J. Schreiber, ref. 33].

2.1.4 Electron Acceleration and Transport

In the laser-plasma interaction, the ions do not gain the energy directly from the laser but indirectly by the accelerated electrons as will be discussed in the next section. So, the electron acceleration up to MeV-range and the transport through the target to the rear side is very important because it will define the accelerated proton bunch parameters as well and its quality.

Assuming that, as shown in Figure 2.1, the laser accelerated electrons propagate through the target of thickness d with an opening angle θ , which can be calculated as $\tan^2 \theta = 2/(\bar{\gamma} - 1)$ [118-121], the electron bunch radius B at the rear side can be written as [33]

$$B = r_L + d \cdot \tan \theta \quad (2.24)$$

where r_L the laser focal spot radius.

The number N_e of laser accelerated electrons in dependence from the laser energy E_L is given by introducing the conversion efficiency coefficient η defined by [32]

$$N_e = \frac{\eta E_L}{k_B T_e} \quad (2.25)$$

where $k_B T_e$ is the mean electron energy given by equation 2.19.

The initial electron density n_{e0} can be estimated as

$$n_{e0} = \frac{N_e}{c \tau_L \pi B^2} \quad (2.26)$$

where τ_L the laser pulse duration, and B as given by (2.24).

A detailed study on the dependence of the conversion efficiency on laser intensities and target properties can be found in Refs. [7-9, 21, 90, 122-126]. Several experiments worldwide show a dependence of η on the laser intensity according to [126]

$$\eta = 1.2 \cdot 10^{-15} \times I_L^{0.74} \quad (2.27)$$

where I_L given in W/cm^2 .

For example, the laser pulse at PHELIX experiments [78] has an energy (after the compressor) of about $108 J$ and a duration of $700 fs$ and was focused by a copper parabola mirror to a focal spot area of $54 \pi \mu m^2$, resulting in $4.5 \times 10^{19} W/cm^2$. The predicted conversion efficiency is about 45% and the total number of electrons can be estimated by equations (2.19) and (2.25) to be 1.6×10^{14} , where the laser wave length $\lambda_L = 1.054 \mu m$.

2.2 Laser – Proton Acceleration

The acceleration of ions directly with the laser is not possible with intensities available today. As mentioned in the previous section (Equations 2.15 – 2.17), this becomes possible for laser

intensities above $10^{24} W/cm^2$. Instead, electrons are used in an intermediate step to transfer energy from the laser pulse to protons.

In this work, the ion acceleration from the rear side of a solid target will be discussed. Due to the laser intensities as well as to target parameters at PHELIX laser experiments, the Target Normal Sheath Acceleration mechanism – TNSA [6-10, 18, 25, 50] will occur. In the following section, this process will be explained in detail.

Radiation Pressure Acceleration (RPA) [51, 127-130] is another mechanism where the protons can be accelerated up to energies in the GeV - range. In this process a circularly polarized laser is needed, which is not the case in PHELIX. Because of that the RPA – mechanism is not discussed in this thesis.

2.2.1 Target Normal Sheath Acceleration – TNSA

In the previous section 2.1.4 the transport of accelerated electrons, though a solid target, was explained. These electrons are reaching the rear side of the target and some of them can escape leaving the target positively charged. The emitted electrons are trapped by Coulomb forces and form an electron sheath cloud. Hence, the charge separation between target and electron cloud will form a strong electric field estimated by

$$E_0 = \frac{k_B T_e}{e \lambda_D} \quad (2.28)$$

The typical value for λ_D is a few μm [11]. Therefore, this electric field is in the same strength order of the laser field itself (TV/m) which will be strong enough to ionize the atoms on the rear side of the target and to accelerate the protons to energies in the MeV to several tens of MeV – range.

Because of the protons are the lightest ions, it will be easy to ionize first. The electric field lines are pointed normally to the target rear surface, resulting in the ion acceleration in the same direction, therefore this acceleration mechanism is called Target Normal Sheath Acceleration. Figure 2.2 shows a schematic for TNSA process [25]. This process was observed by different groups [6-10, 18, 25, 43, 50-56]. After that, several experiments were demonstrated on the proton acceleration with energies up to $70 MeV$ [37] and heavier ions with energies up to $7 MeV/nucleon$ [11, 131].

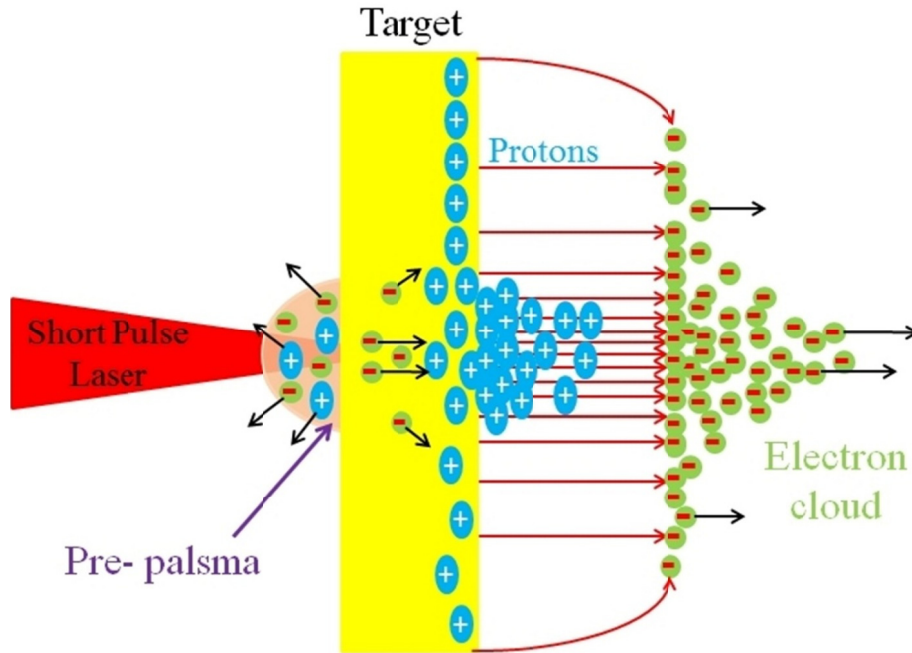


Figure 2.2: Scheme of the Target Normal Sheath Acceleration TNSA mechanism. The laser pulse is focused on the front side of the target and interacts with the pre-plasma generated by unavoidable laser pre-pulse. The laser energy is converted to the plasma electrons resulting in electrons with kinetic energy in MeV – range. These electrons are accelerated and transported through the solid target and it reaches the rear side and some of them can escape leaving the target positively charged. The charge separation between the electron sheath and the target will form a huge electrostatic field of order TV/m which is high enough to ionize the atoms at the target rear side and accelerate the protons (ions) to energies in MeV – range.

The proton beam quality generated by TNSA is highly dependent in the laser parameters, target material and initial proton radius. In this process, the protons are generated with a high intensity yield of order $10^{12} - 10^{13}$, low initial emittance values, wide energy spread and large angular divergence [6-13, 16-21, 23-24, 43, 56, 60-64, 78, 81-82, 88, 132-146]. The proton beam parameters can be improved by different cleaning procedures of the target rear side like coating [11], resistivity heating [13] and laser ablation [81].

2.2.2 Proton Beam Expansion

After the discovery of TNSA, different models are used to explain the plasma expansion at the target rear side. Patrick Mora [132] described the plasma expansion in vacuum with an isothermal model, where the plasma does not cool through expansion.

When the plasma expands in vacuum, the electrons transfer energy to the protons through the Coulomb interaction. Finally, electrons are co- moving with the protons resulting in a neutral plasma.

This model [132] expects an exponential proton spectrum where the number of protons per unit energy dN/dE_p can be expressed as

$$\frac{dN}{dE_p} = \frac{n_{i0} c_s \tau_{acc}}{\sqrt{2k_B T_e E_p}} \exp\left(-\sqrt{\frac{2E_p}{k_B T_e}}\right) \quad (2.29)$$

Where $c_s = \sqrt{k_B T_e / m_p}$ the ion – acoustic velocity, $n_{i0} = n_{e0}$ the initial proton density and τ_{acc} the proton acceleration time which can be estimated by the laser pulse duration as

$$\tau_{acc} = 1.3 \times \tau_L \quad (2.30)$$

The maximum energy that can be gained in the isothermal model is given by

$$E_{max} = 2k_B T_e \left[\ln t_p + (t_p^2 + 1)^{1/2} \right]^2 \quad (2.31)$$

where $t_p = \omega_{pp} \tau_{acc} / \sqrt{2 \exp(1)}$ the normalized acceleration time and $\omega_{pp} = \sqrt{e^2 n_{p0} / \bar{\gamma} m_p \epsilon_0}$ the proton plasma frequency.

Notice that, the electron density profile has a Gaussian – radial distribution which was shown in the measurements [61]. Hence, the protons accelerated in the direction normal to the electron density gradient result in different proton energies. The central part is accelerated more than the protons on the edge. The proton bunch radii as well as the emission angles are energy dependent.

Figure 2.3 shows the results of one experiment at PHELIX. Obviously one can see the exponential energy spectrum of the protons (Figure 2.3, left), the opening angle being highly dependent on proton energy (Figure 2.3, right).

Proton spectra are characterized by a large divergence at low energies. This divergence is found to be decreased with increasing proton energy (Figure 2.3, right). The emission radius of the protons at the target position is also decreased with increasing energy (see Figure 2.4) [15-16, 18, 24, 61-63, 78-79, 95, 147-148].

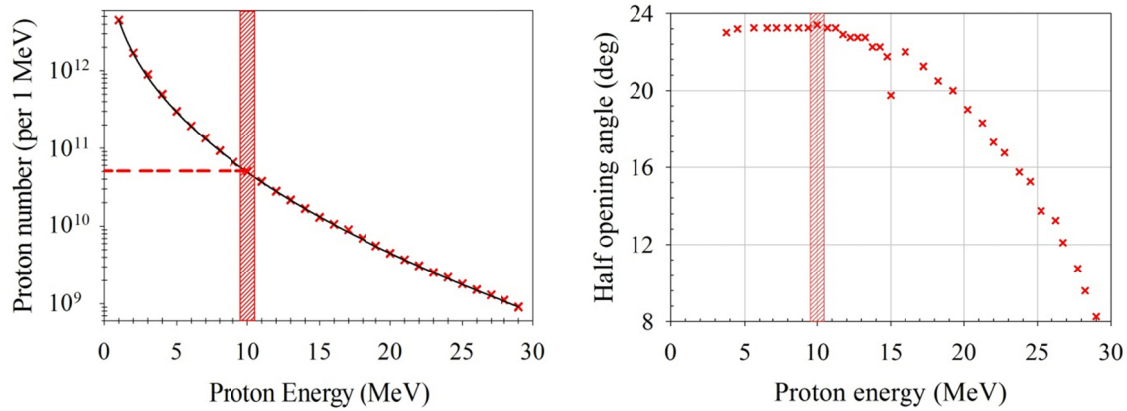


Figure 2.3: Dependence of differential particle yield (left) and half opening angle (right) on proton energy generated in PHLIX laser experiments (Courtesy of M. Roth and V. Bagnoud).

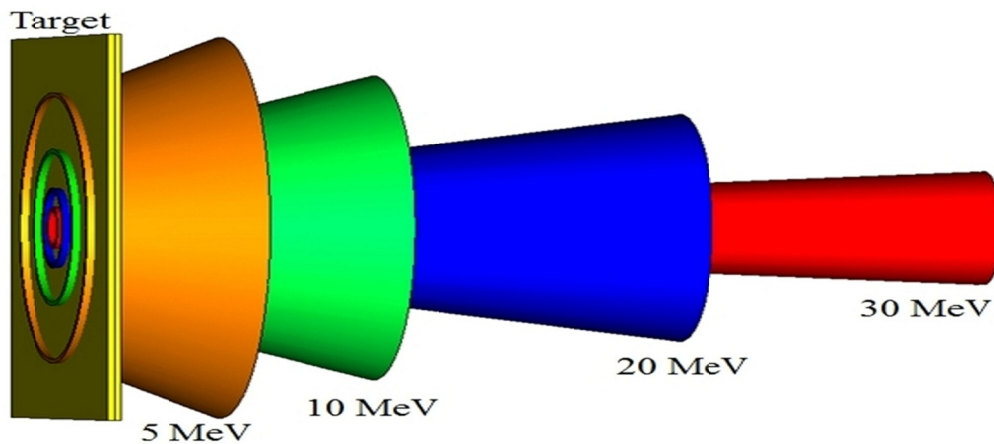


Figure 2.4: The laser – accelerated proton envelopes for different proton energies. This sketch is showing the dependence of source size and envelope divergence at proton energies generated by laser. For increasing proton energy the generated proton source radius and the divergence is decreasing.

2.3 Application of Laser – Accelerated Protons

Experimental results from the laser acceleration of proton achieved energies of ten to several tens of *MeV*. The unique features of the accelerated protons, like small emittance values and high yields up to 10^{13} protons per shot open new research areas. Since the first acceleration experiments, several laboratories are working not only on developing high quality proton beam, but also on controlling them for easy use in other applications.

The main topic in this work is concerned about using the laser acceleration protons as an alternative for particle proton source for conventional accelerators [19, 41, 48, 59, 68-71,

149-153]. Other options on using these protons are still investigated in wide researcher areas like in medicine [51, 154-166].

In the following, an overview on the application of laser accelerated protons (ions) will be addressed briefly.

2.3.1 A new particle Source for Conventional Accelerators

The unique features of laser – accelerated protons could be useful for accelerator technology [41, 59, 149-153]. The laser technique can deliver proton beams at energies of ten to several tens of MeV – far above energies delivered by RFQ's [66-67], which are the current linac front end technology. The important topic for further acceleration of proton bunch is the matching into the acceptance of an RF accelerator. The e RFQ is no more efficient at energies beyond $10 MeV$.

With respect to the transit energies, direct matching into drift tube linacs are the most adequate choice. A Crossbar **H**-type (**CH**) structure is suggested as the linac part.

The matching problem from the target into the CH- structure by a magnetic pulsed solenoid will be explained in detail in the following chapters 3 and 6.

2.3.2 Isochronic Heating

Isochronic heating means heating at constant volume. It is the way to produce a Warm Dense Matter (WDM) with a solid state density at a temperature of several tens of eV [167]. The WDM is very important in astrophysics to understand the interior planets such as Uranus and Neptune [22, 167]. Production of a matter at solid state density heated normally with a temperature $> 10^6 K$ is challenging. The laser – accelerated protons with short pulse duration may be used for this purpose [22, 167-168]. The characteristic behavior of the protons deposition energy in matter is shown in Figure 2.5.

The proton loses its energy uniformly in the matter up to the point of Bragg peak where the proton comes to rest. Hence, the target located in the plateau region allows to achieve an almost uniform temperature.

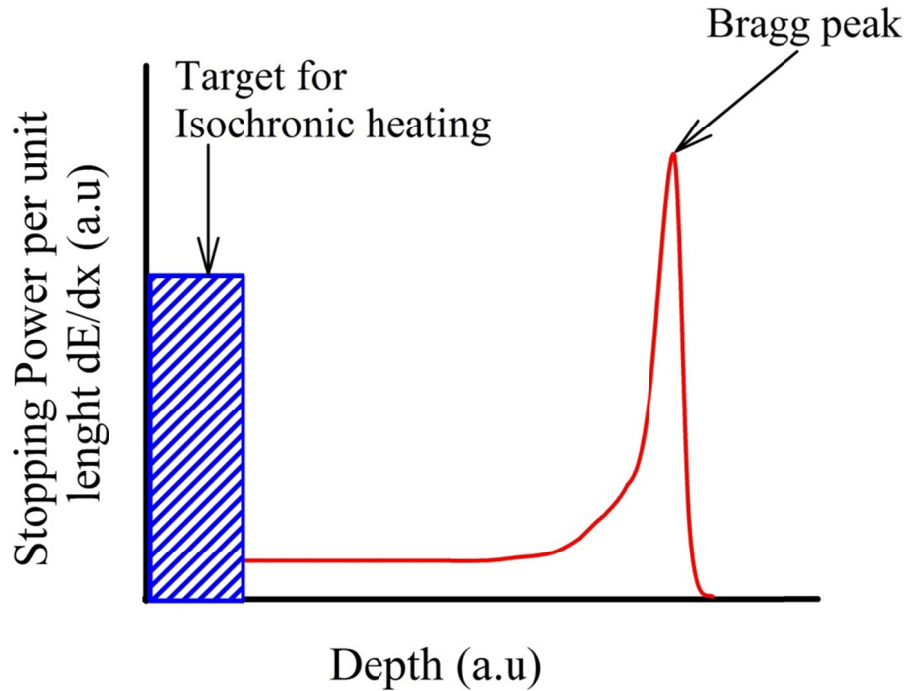


Figure 2.5: The proton loses its energy uniformly in the matter up to the point of the Bragg peak where the proton comes to rest. In the isochronic heating, the target is located in the plateau region which leads to an almost uniform temperature.

2.3.3 Medical Applications

The laser – accelerated protons (ions) can be used in medical applications especially in radiography and cancer therapy [51, 154-158].

a. Radio – Isotope for Positron Emission Tomography (PET)

The positron emission tomography is a nuclear medicine techniques that produces a three dimensional image [169]. The system detects a pair of gamma rays emitted indirectly by a positron – emitter radionuclide (tracer). In order to protect the patient from dispensable dose, the life time of the β^+ emitter needs to be short. Several radionuclides are used in PET like ^{11}C and ^{18}F . The production of these radionuclides are done by (p, n) or (p, α) reactions. The production of ^{11}C and ^{18}F using laser – accelerated protons seems possible [159-163].

b. Ion Radiotherapy

The irradiation of a tumor inside the patient by X – ray, γ – ray and electrons could kill the healthy cell because of the loss of a high fraction of energy along their paths in the

body. While in the ion therapy, it will be possible to deposit the ion energy in a well localized area within the tumor. Protons with energies ranging from 70 MeV – 250 MeV and carbon ions with energies up to 430 MeV per nucleon are used [51]. The Heidelberg Ion beam Therapy (HIT) is one of the modern facilities located in Germany [170]. The cost of the ion therapy facility is about 100 million Euros. The new developments in lasers predicted that in the coming years one can laser accelerate protons or even carbon ions to energies of several hundreds of MeV and up to GeV. Hence, laser ion acceleration might be able to compete with conventional accelerators in the ion therapy facilities [51, 154-157, 164-166]. The hope is that this might not only reduce the cost of construction of such a facility but also make the device more compact [155, 164].

Other applications for laser accelerated protons may open in nuclear physics [131, 171] and in fast ignition [172-175], especially.

CHAPTER 3

EXPERIMENTAL SETUP FOR LASER – PROTON ACCELERATION

After the invention of Chirped Pulse Amplification (CPA) technology in modern laser facilities [36], one can achieve focused intensities up to 10^{22} W/cm^2 . Under these conditions, intense protons are accelerated normally from the rear surface of the solid target with the TNSA process discussed in Chapter 2.

In the scope of this work, the PHELIX (Petawatt High Energy Laser for heavy Ion eXperiments) laser system [40, 176-177] will be used to accelerate the protons to energies in MeV – range.

The typical experimental setup for the laser – proton acceleration at PHELIX can be shown in Figure 3.1 [32, 78].

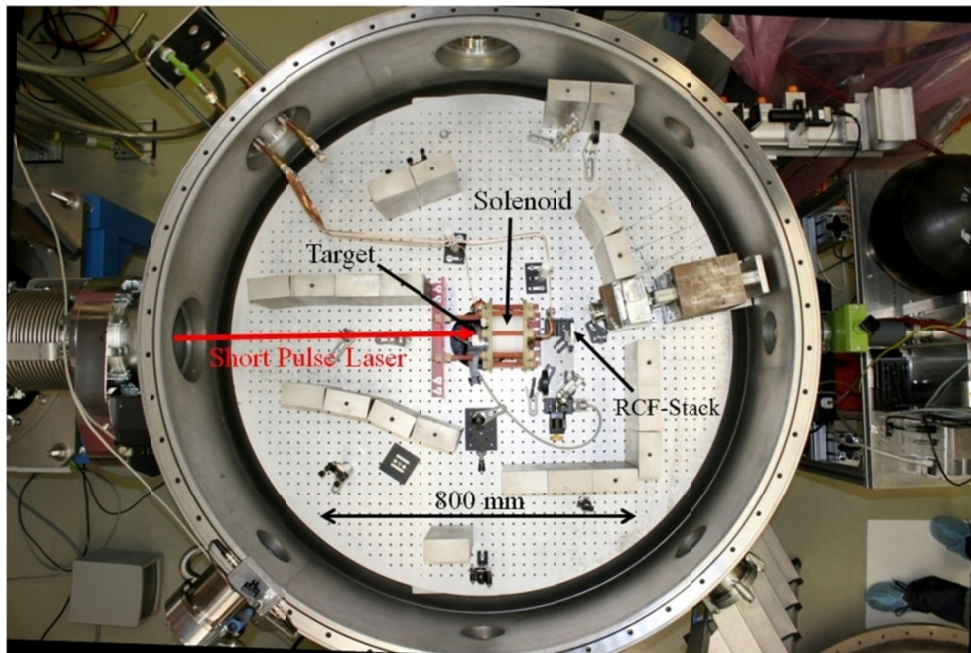


Figure 3.1: Experimental setup for the laser – proton acceleration at PHELIX [Courtesy of Knut Harres , the same as shown in ref. 78].

In this chapter, an overview of the PHELIX facility will be presented in the next section. For proton detection, a high resolution detector Gafchromic Radiochromic film (RCF) [178] is used. This will be the topic of section 3.2. Finally, the results of an experiment performed at PHELIX will be presented in section 3.3.

3.1 PHELIX Laser Facility

The PHELIX laser system is one of the most powerful lasers in the world. It is located at the GSI Helmholtzzentrum für Schwerionenforschung in Darmstadt, Germany (see Figure 3.2).

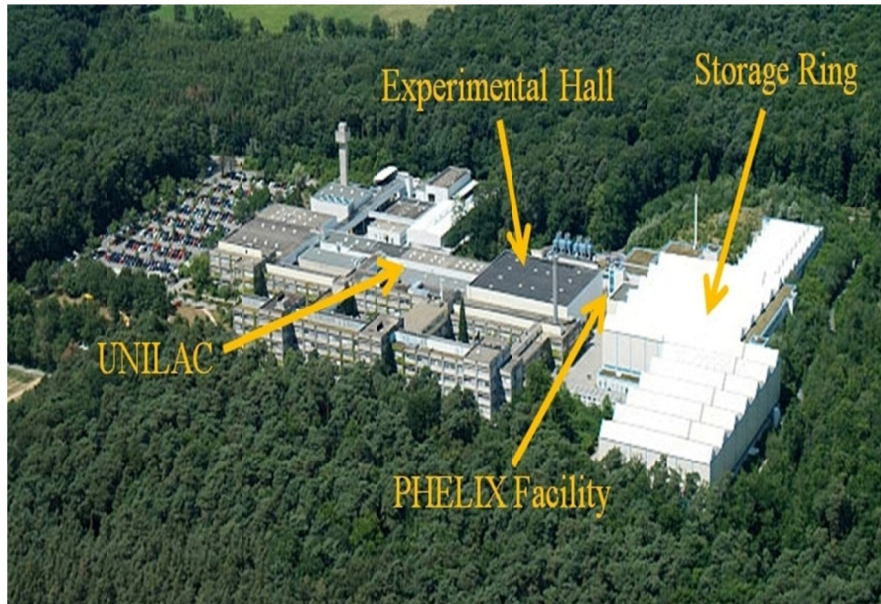


Figure 3.2: Schematic for the PHELIX laser facility and the accelerator chain in GSI.

PHELIX is a Nd: glass laser system and was built in cooperation with Lawrence Livermore National Laboratory LLNL in the USA and Commissariat à l'Énergie Atomique CEA in France. Figure 3.3 shows the schematic overview of the PHELIX facility [40].

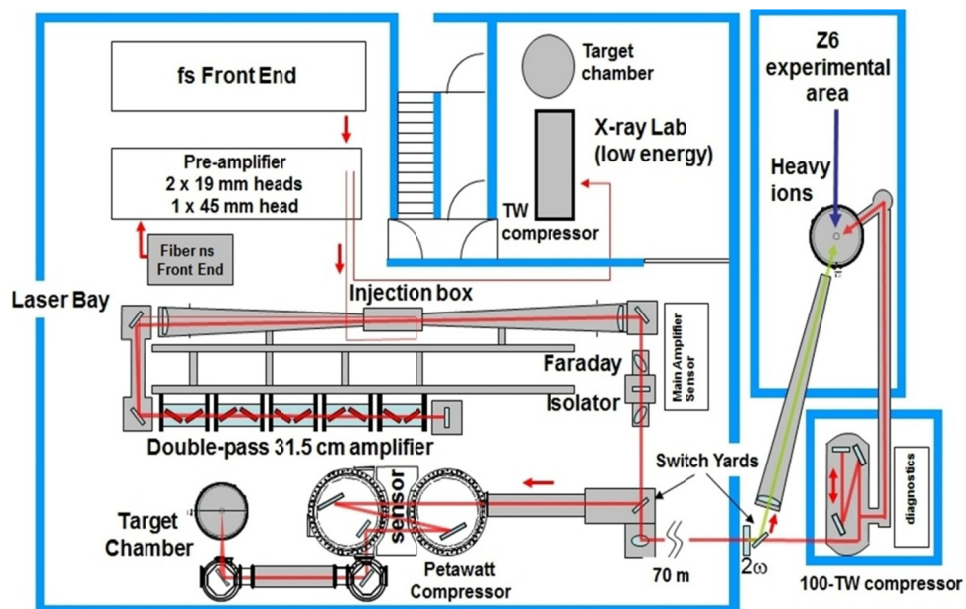


Figure 3.3: Schematic of the PHELIX laser system (Courtesy of V.Bagnoud).

Two operational modes are available at PHELIX; the long pulse mode with pulse duration ranging from 700 ps to 20 ns and short pulse mode with a pulse duration ranging from 500 fs to 20 ps. The main parameters for each mode are summarized in Table 3.1 [40].

Table 3.1: Present operational parameters of the PHELIX laser system for long pulses and for short pulses operations [40].

Parameter	Long pulse	Short pulse
Pulse duration	0.7 – 20 ns	0.5 – 20 ps
Energy	0.3 – 1 kJ	120 J
Maximum intensity	10^{16} W/cm ²	10^{20} W/cm ²
Repetition rate at max. power	1 shot every 90 min	1 shot every 90 min
Contrast	50 dB	60 dB

For laser – proton acceleration, the short pulse mode is used in order to achieve the high intensities.

In the short pulse mode, the femtosecond front – end laser oscillator is used to generate the short pulses with durations of 100 fs and with energies around 40 nJ at 76 MHz repetition rate. The pulse can be stretched by orders of magnitude up to 2.3 ns (FWHM) in the pulse stretcher. The stretched pulse is then amplified by two titanium – doped sapphire regenerative amplifiers with a repetition rate of 10 Hz. The output energy after the amplifier will be typically 30 mJ. After that, the pulse is injected into several glass–based amplifiers having a final energy of about 160 J. Finally, the pulse will be re-compressed to pulse durations of < 1 ps in a vacuum tank to avoid nonlinear interaction of the pulse in air.

The efficiency of the compressor is about 90% [78], resulting in the final laser energy at the target chamber about 130 J.

This process described above was invented in 1985 by D. Strickland and G. Mourou [36, 179] and is called the Chirped Pulse Amplification (CPA). The schematic for this process is shown in Figure 3.4.

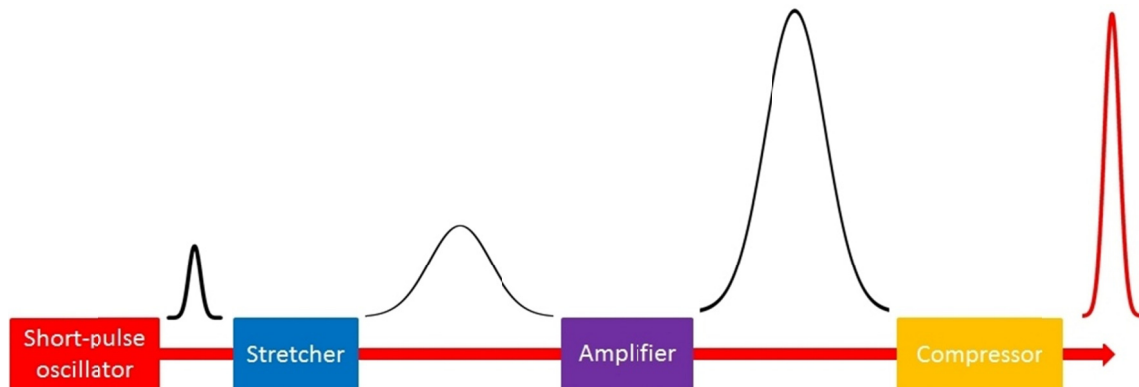


Figure 3.4: Schematic for the Chirped Pulse Amplification (CPA) process.

Due to the heating up of the optical components and to the cooling time of the main amplifier, the repetition rate of PHELIX is limited to one shot per 90 min [40].

In order to generate protons, the incident laser pulse is focused on the target by a copper parabola mirror on a beam spot of several μm radius only. The target material consists of metallic foils like gold, copper,...etc. with a thickness ranging from several μm up to tens of μm . The laser-accelerated protons can be measured by several methods like with a Magnetic Spectrometer [126, 180-183], a Thomson Parabola [11, 26, 50, 84, 184], CR-39 [50, 185] and with Radiochromic films [20, 32, 34, 78].

The Radiochromic films (RCF) are common in use because of their suitability for the reconstruction of the laser-accelerated protons with high resolution [20, 32, 34, 78, 80, 186-188]. For more details about the other methods see references [20, 32, 34].

3.2 Radio Chromic Films

The laser-accelerated protons can be detected with a high-sensitivity *Gafchromic* radiochromic film (RCF) detector [20, 32, 34, 78, 189] by resolving the dose distribution in two dimensions.

Different RCF films of types HD-810, HS and MD-55 [190] are common in use for this purpose [20, 32, 34, 78]. Figure 3.5 shows the configuration layers and the composition of these films. The chemical compositions of each layer as well as the densities are summarized in table 4.2 [32, 34, 190].

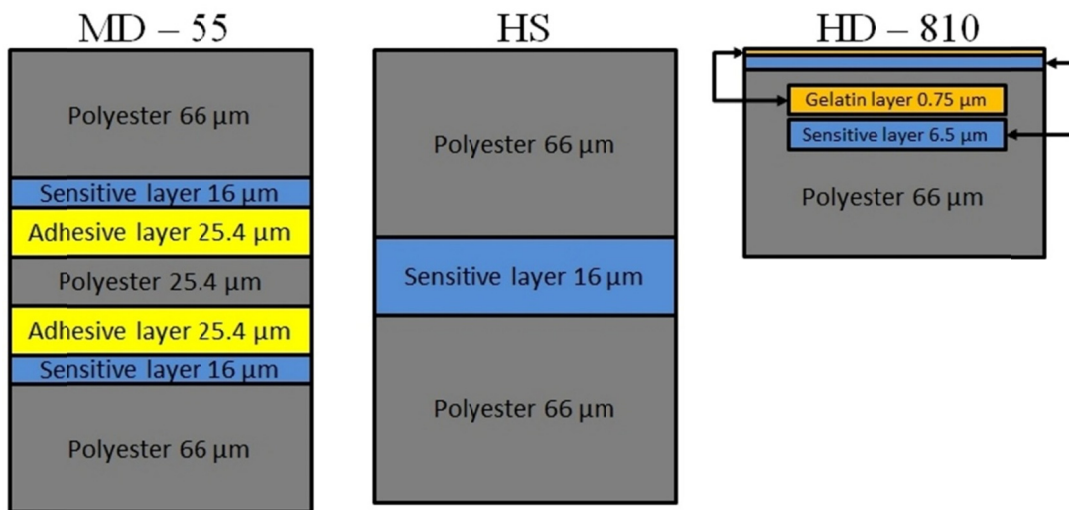


Figure 3.5: Layer configuration of Radiochromic film of types MD-55, HD-810 and HS. The color codes in Figure 4.5 and Table 4.2 are identical.

Table 3.2: Chemical composition and density of Gafchromic Radiochromic films.

	density (g/cm ³)	C (%)	H (%)	O (%)	N (%)
Polyester	1.35	45.44	36.36	18.20	0.00
Sensitive layer	1.08	29.14	56.80	7.12	6.94
Adhesive	1.20	33.33	57.14	9.53	0.00
Gelatin coating	1.20	22.61	53.52	11.12	12.75

The dosimetry film is sensitive for an ionizing dose like provided by accelerated protons. After the interaction, the film color changes from transparent to different shades of blue, depending on the amount of dose absorbed in the film by polymerization [191].

Hence, it depends on the total number of protons passing the film and their energies.

The RCF films have been calibrated for protons by Hey et al., with a micro-densitometer [84, 192]. At PHELIX the transmission film scanner Microtek ArtixScan 1800f was used to scan the films resulting in the same accuracy as micro-densitometers [34]. The scanner was calibrated with a grey scale wedge [34, 193]. This allows converting the film information to an optical density.

The deposited energy E_{dep} of protons in each film is calculated by the SRIM code [194]. Figure 3.6 shows calibration curves for three different RCF films [20, 34]. The results in Figure 3.6 can be approximated by a non-linear exponential function [34]

$$E_{dep} = \exp\left(\sum_i a_i \cdot D^{b_i}\right) \quad (3.1)$$

where E_{dep} is the deposition energy in KeV/mm^2 , D is the optical density, a and b are constant fitting parameters, having different values for different film types.

For more details about this technique see the PhD dissertations of F. Nürnberg and M. Schollmeier [32, 34].

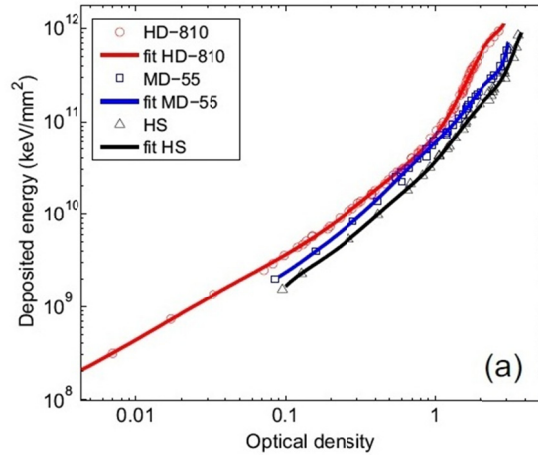


Figure 3.6: Calibration curves for the deposited energy versus the optical density for the radiochromic film types HD-810, MD-55 and HS [PhD thesis of F. Nürnberg ref 34].

The stopping power of the proton dE/dx in the material depends on the proton initial energy and on the material density. Figure 3.7 shows a SRIM calculation for different proton energies penetrating a HD-810. When the proton enters each layer, the energy loss is changed. At the end of each trace, the energy loss peaks at the Bragg-peak.

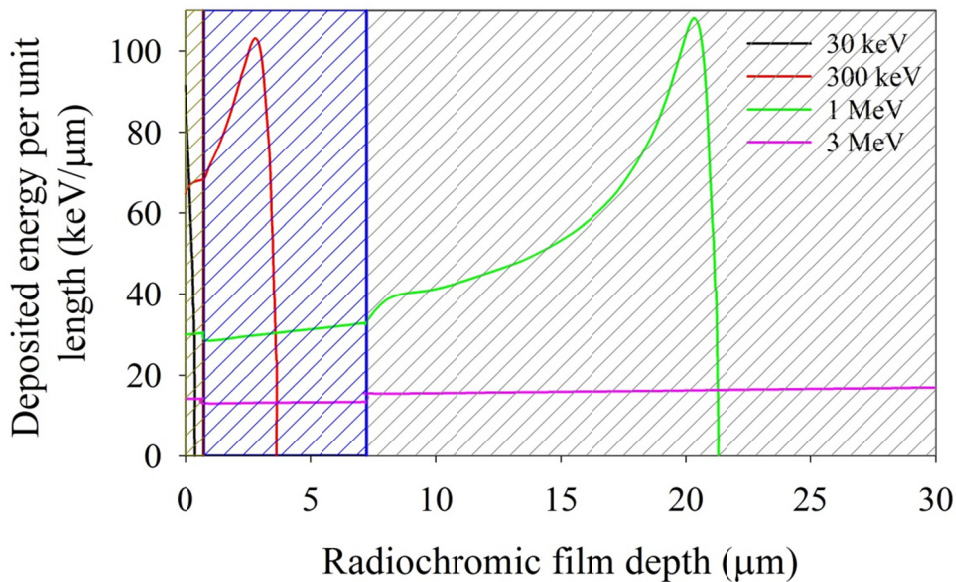


Figure 3.7: The proton energy deposited per unit length in radiochromic film type HD-810 for four different initial energies as calculated with SRIM 2006 (the Stopping and Range of Ions in Matter). The marked areas from left to right are correspondence to different layers in RCF from left to right: gelatin coating (dark yellow), sensitive layer (blue) and polyester (dark gray).

3.3 Method of Determining Proton Beam Parameters

Several PHELIX experiments were performed to generate intense protons with energies of several MeV up to tens of MeV [22, 40, 48, 78, 176].

One of these experiments which was done in January 2011 as a part of LIGHT (Laser Ion Generation Handling and Transport) project [68-69, 72-73] will be described in some detail. The results are published in references [69, 73].

It should be noted that, the experimental results given in reference 34 (see Figures 4.21 – 4.22) are used to investigate the post-acceleration by a CH-DTL (Chapter 6).

In these experiments, a 7.8 J laser pulse of about 700fs duration was focused by a copper parabola mirror on a beam spot of about $100\mu m^2$ (FWHM) as shown in Figure 3.8. This results in a power intensity of about $1 \times 10^{19} W/cm^2$. A gold target of thickness $10 \mu m$ was used.

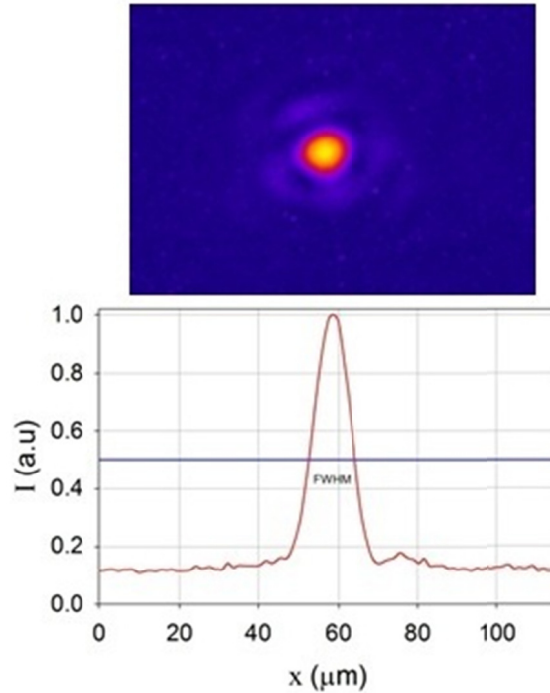


Figure 3.8: Intensity distribution of the laser focal spot focused by a parabola mirror. The full width at half maximum (FWHM) dimensions of the spot are $10\mu m \times 10\mu m$.

The film detector in stack configuration consisted of three HD-810 films followed by another three MD-55 films. Due to the high sensitivity of RCF films to the ionizing radiation, an

Aluminum layer with a thickness $14 \mu\text{m}$ was inserted before the first HD-810 film. Figure 3.9 shows the RCF stack configuration which is used to analyze proton beams.

Protons with higher energies penetrate the first film and will be completely stopped in one of the following films. Hence, each film is characterized by a certain proton energy range.

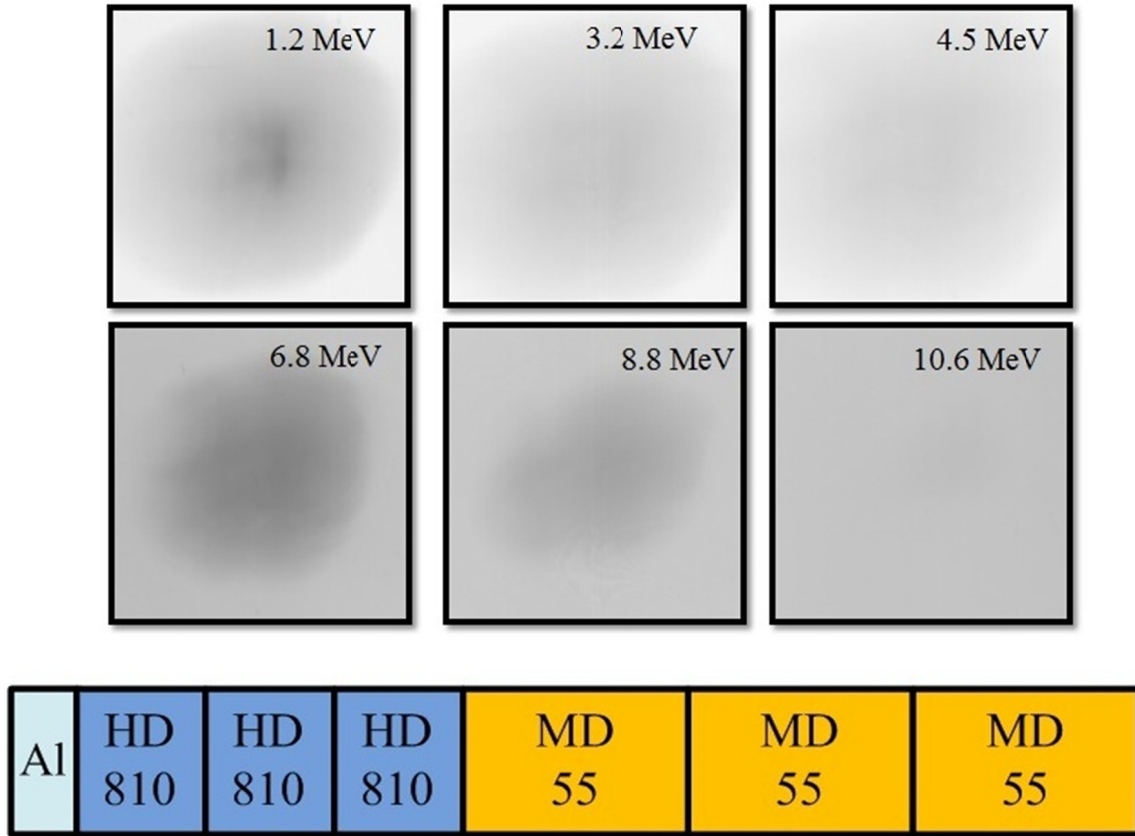


Figure 3.9: Radiochromic film stack (three films of HD-810 type followed by another three films of MD-55 type) exposed by a laser – accelerated proton beam at PHELIX experiment. A gold target of thickness $10 \mu\text{m}$ was exposed to a laser intensity of about 10^{19} W/cm^2 resulting in protons with 10.6 MeV maximum energy. The stack was positioned 31 mm behind of the target. The energy value on the top right of each film corresponds to the proton Bragg peak energy.

The energy value written on each film represents the Bragg-peak energy (see Figure 3.10).

Since the RCF film is a two-dimensional detector in space [34], the beam divergence can be calculated by knowing the distance between the target and the RCF-stack, which is 37 mm . Figure 3.11 shows the angular divergence of the proton beam at different energies. The opening angle is decreased with increasing energy. This behavior was seen not only in this experiment, but also in earlier PHELIX experiments [34, 40, 78].

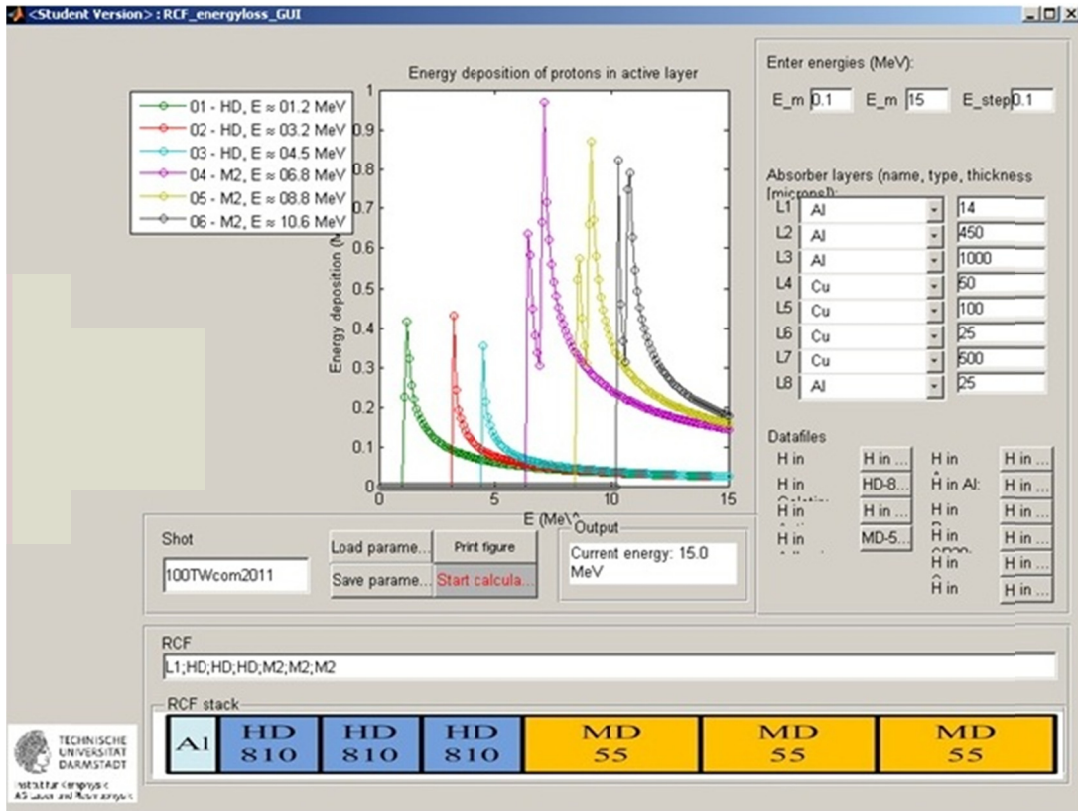


Figure 3.10: Screenshot of the graphical user interface running in MATLAB program for the reconstruction of the proton spectrum, written by the working group of M. Roth from Institut für Kernphysik, Technische Universität Darmstadt (Courtesy of S. Busold).

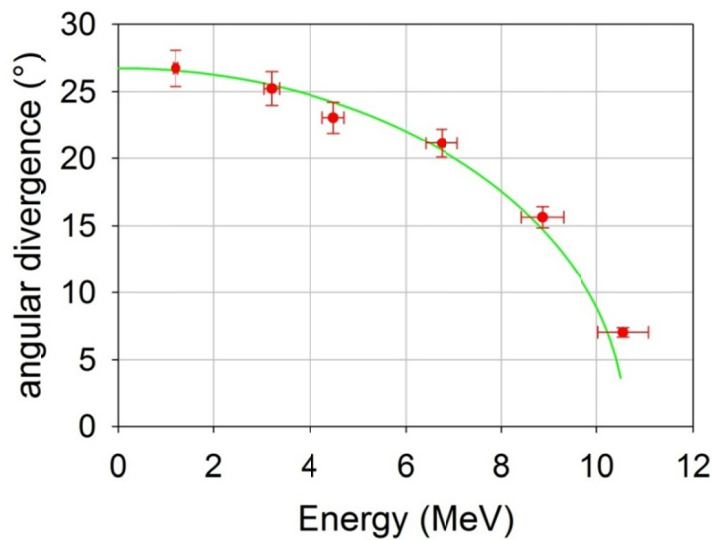


Figure 3.11: The dependence of the half opening angular divergence of the PHELIX proton beam on the proton energy.

As mentioned before, protons deposit a part of their energy in all penetrated layers. This fraction is varying from one layer to another. So the total deposited energy in a specific film can be calculated by integration over the whole spectrum

$$E_{total} = \int \frac{dN(E')}{dE} \times E_{loss}(E') dE' \quad (3.2)$$

where dN/dE is the number of proton detected per energy interval, and $E_{loss}(E')$ the energy loss of a proton with energy E' in a given layer.

Each layer need to be de – convolved by the nonlinear detector response function to calculate the particle spectrum dN/dE . This can be done by a convolution with an assumed function for dN/dE .

Recent publications have shown that the particle spectrum dN/dE has an exponential behavior [20, 32, 34, 40, 48, 126]. Assuming an isothermal, quasi-neutral plasma expansion as given by Fuchs et al. [126] the particle spectrum can be written as

$$\frac{dN}{dE} = \frac{N_0}{\sqrt{2Ek_B T}} \times \exp\left(-\sqrt{\frac{2E}{k_B T}}\right) \quad (3.3)$$

With the particle spectrum function dN/dE and the E_{loss} as calculated by the SRIM-code, the total deposited energy is calculated for each RCF layer. The energy deposited by all protons in MeV as a function of the proton energy is shown in Figure 3.12.

The integral in equation 3.2 is solved numerically. The parameters N_0 and $k_B T$ are iteratively determined by minimizing of the root mean square deviation [34]. For the proton beam in this experiment, the best fit function is given by equation 3.3 where the fit parameters are $N_0 = 4.6 \times 10^{11}$ and $k_B T = 0.61 MeV$.

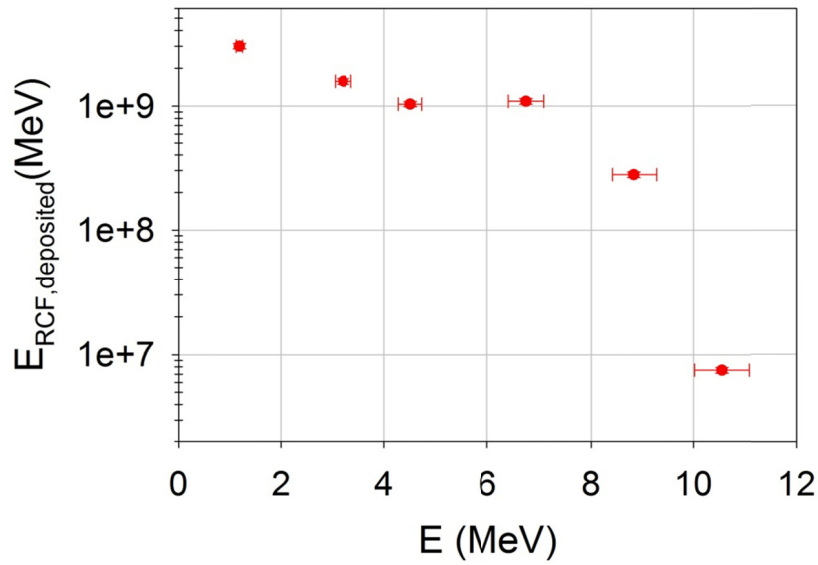


Figure 3.12: The calculated energy deposited of the measured data in the RCF stack (Courtesy of S. Busold).

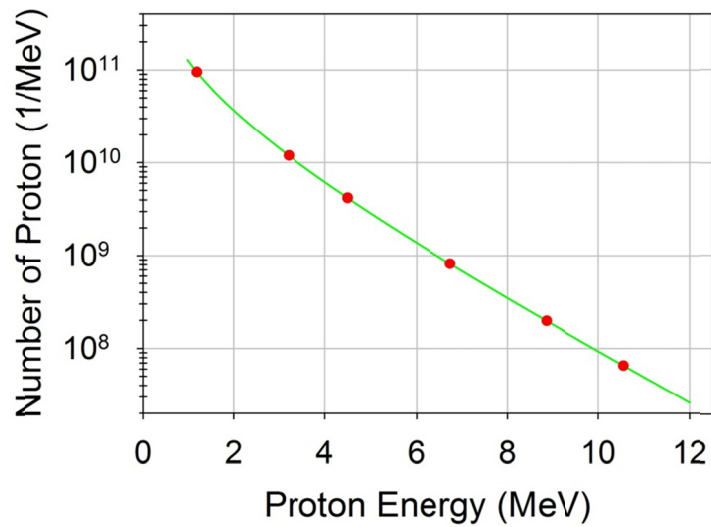


Figure 3.13: Dependence of differential particle yield on energy for PHELIX experiment by solving the integral in equation 4.2 numerically using equation 3.3.

CHAPTER 4

TRACKING OF LASER – ACCELERATED PROTONS THROUGH A PULSED MAGNETIC SOLENOID

The unique features of laser – accelerated protons make them attractive for study. Possible applications of these generated and accelerated protons require a collimated beam with well-defined energy and divergence.

Due to the fact that the protons are generated with a large divergence and as the transversal acceptance of accelerators is limited, focusing elements (lenses) must be designed properly to match the beam into the linac.

The impact of the electric field compared to the magnetic field can be estimated by the relation $\mathbf{E} = v\mathbf{B}$. Hence, a magnetic field strength of 18 T at $\beta \cong 0.15$ (about 10 MeV proton kinetic energy) is equivalent to $E = 7.8 \times 10^8\text{ V/m}$. This value of the electric field is far above the technical limits. Thus, for laser – accelerated proton collimation, magnetic lenses will be used. The focusing elements could be quadrupole or solenoid.

Different options were suggested and demonstrated for focusing and transporting laser – accelerated protons [19, 34, 48, 70-71, 151, 195-198].

Due to highly divergent protons, most of them were lost when a quadrupole transport channel was used. Thus, the quadrupole element was found not to be convenient for this problem (see for example refs. 32, 195).

In order to catch the laser – accelerated protons, a pulsed magnetic solenoid is used as the first focusing element, with fields as high as 20 T theoretically [19, 22, 71, 78, 196-198]. In the following, the protons with energy around 10 MeV are selected from the TNSA proton spectrum for further acceleration to higher energies by an RF linac (see chapter 6). They required field strengths up to 20 T theoretically for collimation [19, 71, 196-198] (see the next sections).

It is shown that, the pulsed magnetic solenoid is able to match the laser accelerated protons into the linac structure (CH – DTL) [19, 71, 196-198].

The particle simulations through the solenoid starting at the target position and ending at the linac entrance were done by a new 3D code – LASIN (LASer INjection) [199]. This code, which was developed at IAP – Frankfurt by Dr. Martin Droba, is used for multi – particle tracking through the solenoidal magnetic field including fringing fields.

4.1 LASIN Code

The LASIN- code is a 3D code, developed for multi-species (electrons, protons and ions) beam tracking through a solenoidal magnetic field with high space charge forces and at rapidly varying geometric bunch dimensions. The tracking in longitudinal and transversal planes can be adapted depending on the initial bunch parameters. The magnetic field is calculated by the Biot- Savart solver using a numerical integration scheme from a given distribution of current elements. At every exact particle position at a given time step, the corresponding magnetic field \mathbf{B} is calculated accordingly.

In case of space charge forces, the charge density is integrated on a cylindrical mesh from a particle distribution by PIC (Particle- In- Cell) techniques [200]. Afterwards, the Poisson equation is solved numerically by the iteration method BiCGSTAB (Bi-Conjugate Gradient Method- STABILized) [201] on the mesh resulting in the potential distribution. For the tracking algorithm the electric field is interpolated at the particle position.

A symplectic middle step scheme [202] in Cartesian coordinates is used to follow the particle motion in given fields.

The code is implemented at the Frankfurt Center for Scientific Computing CSC cluster [203] by fully exploiting the parallel processing capabilities. Typically, 50 processors and up to 10^7 macroparticles are used in proton tracking simulations from the target (TNSA – Protons) to the linac accelerating structure (CH – DTL in this work). For optimization purposes and memory requirement a reduction of the sparse format of stored vectors and matrices is used.

4.2 Pulsed Magnetic Solenoid

The magnetic solenoid consists of radial and axial magnetic fields with cylindrical symmetry around the beam axis [204]. Since the magnetic field is constant during the passage of the particle bunch, the particles don't change their energy.

As the particles cross the fringing field of the solenoid, the Lorentz force $q \cdot v_z \times B_r$ will act azimuthally. The resulting velocity v_θ will lead to a radial force when the particles cross B_z inside the solenoid. This radial force will focus the particles towards the axis [204].

In order to collimate the protons with energy $10 \text{ MeV} \pm \Delta E$, a pulsed magnetic solenoid with 33 circular windings having an inner diameter of 44 mm, an outer diameter of 76 mm and a total length of 72 mm is used [19, 71, 196-198]. The solenoid parameters are shown in Figure 4.1. The distance between target and solenoid entrance was set to 15 mm in order to catch as many protons as possible and corresponds to the performed experiments.

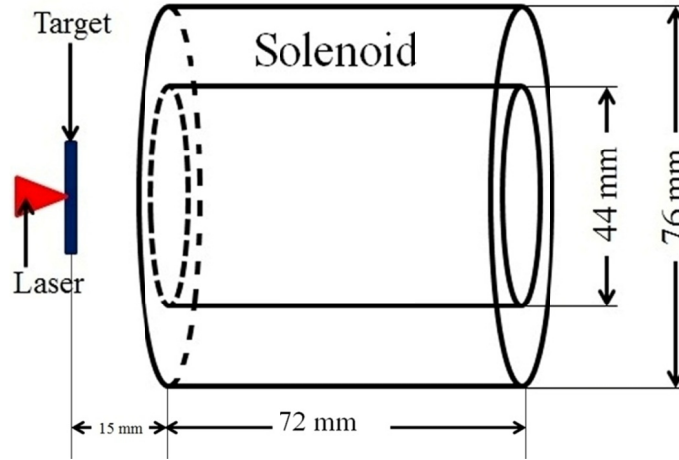


Figure 4.1: A schematic view of the laser target and the focusing solenoid. The geometrical parameters of the solenoid were indicated.

The 10 MeV proton bunch in this work needs a magnetic field level of about 20 T theoretically in order to focus directly into the CH – DTL at a distance of about 210 mm from the target. The solenoidal field extension along z is shown in Figure 4.2. The cyan lines represent the geometrical size of the solenoid while the brown line represents the TNSA target position. The magnetic field in the target area is about 6 T (Figure 4.2, left), which means that the protons (and the co- moving electrons) are produced in a relatively high magnetic field. That means, the hard edge solenoid approximation is insufficient for our study and the effect of fringing fields must be taken into account as it was done in this study. The particle tracking (without space charge) immediately behind of the target is performed in the time domain with time steps of 10^{-11} s, typically. This corresponds to steps in space of about 440 μm along the drift axis. In case of space charge studies, the time steps are adapted to whether the electrons are included (the time step is about 10^{-14} s) or not included (the time step can vary from 10^{-13} to 10^{-12} s depending on the electric field level). Simulation tools for a wide range of particle energies will be shown in chapter 4.4. where space charge is included.

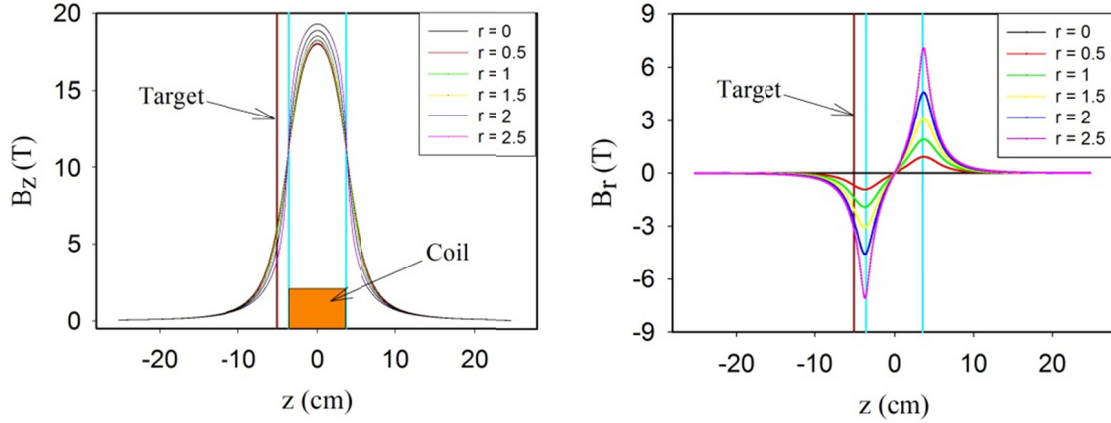


Figure 4.2: Longitudinal (left) and transverse (right) components of the solenoidal field along the axis for different radii in cm; the geometric length of the solenoid (cyan lines) as well as the target position (brown line) are marked.

4.3 Simulations without Space Charge

Beam dynamics simulations through the pulsed magnetic solenoid for a proton bunch with energies of 10 MeV $\pm \Delta E$ are described in the following.

The 4D Kapchinski-Vladimirski (KV) distribution [205] was generated as a very first particle distribution for the simulations. At the beginning, the beam dynamics simulations were performed without space charge. The main goal was a check of chromatic and geometric effects taking into account higher order aberration. The impact of their effect on the proton tracking through the magnetic solenoid was investigated.

4.3.1 Chromatic and Geometric Aberrations

In the paraxial approximation [204, 206], the equations of motion are derived by keeping only the linear terms in r, r' . The lenses treated in this approximation are considered as ideal ones (optically thin lens).

In practice, magnetic solenoids are not perfect focusing devices, and other nonlinear effects cause imperfections or aberrations. These aberrations enlarge the beam spot. The important ones are spherical (geometrical) and chromatic aberrations. The spherical aberration (Figure 4.3) is a geometrical aberration and arises from third-order terms ($r^3, r^2 r', \dots$) [204, 206].

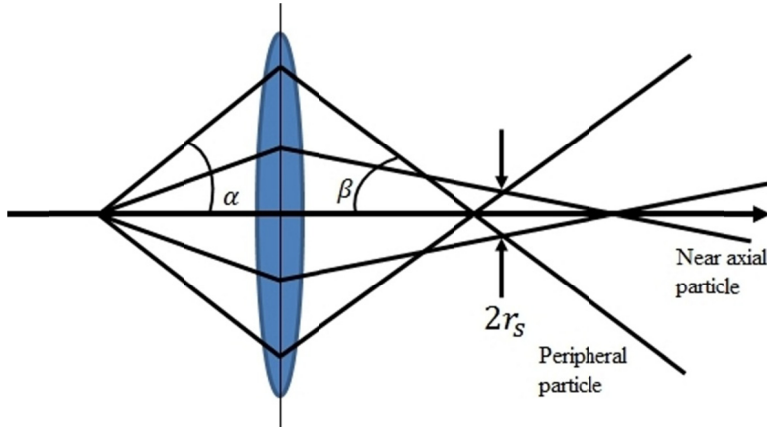


Figure 4.3: Spherical aberration. The lens focuses the particles far from the axis more strongly than the particles near the axis.

Spherical aberration appears because the focusing action on the ions far from the axis is stronger. The spherical aberrations result in a waist with a radius r_s given by [204, 206]

$$r_s \approx \frac{1}{4} C_s \beta^3 \quad (4.1)$$

where C_s is the spherical aberration coefficient, which depends on lens geometry and the initial conditions. The angle of convergence β depends on the initial divergence (opening angle) α and on the beam diameter in the solenoid.

Chromatic aberrations (Figure 4.4) are due to the spread in kinetic energy that is inherent in any beam. In contrast to the spherical aberration, the chromatic aberration does not imply any nonlinear terms in the trajectory equations [204, 206].

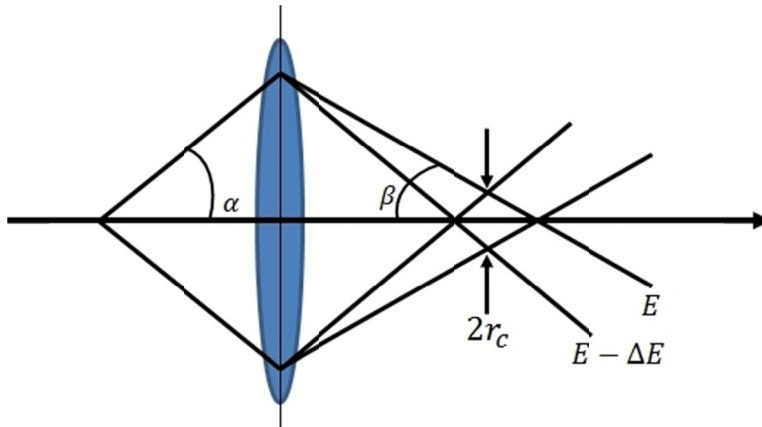


Figure 4.4: Chromatic aberration. The lens focuses the particles with higher energies less than the particles with lower energies.

Due to the fact that the focal length depends on the momentum, particles with different momentum (or energy) are focused at different distances from the lens.

Hence, particles with lower energies are bent more and therefore focused at shorter distances from the lens. This effect results in an enlargement of the beam radius behind the lens, which is given by [204, 206]

$$r_c = C_c \beta \frac{\Delta p}{p} \quad (4.2)$$

where C_c is the chromatic aberration coefficient, β the angle of convergence and $\Delta p/p = \Delta E/2E$ the momentum spread.

For the pulsed magnetic solenoid from previous section, the chromatic and spherical aberrations were investigated in detail [68, 198]. The beam dynamics simulations were performed for proton beams with varied input transverse divergence (opening angle). Three different cases were analyzed for $\alpha : \pm 45$ mrad, ± 90 mrad and ± 180 mrad. For each case different momentum spreads up to $\pm 10\%$ are used. These simulations are made at negligible space charge conditions.

For a given solenoid and spot radius, one can use eq. 4.2 to scale the chromatic emittance ϵ_c as

$$\epsilon_c = C_c \beta^2 \frac{\Delta p}{p} \quad (4.3)$$

For small input emittance values ϵ_i , ϵ_c can dominate and will become the effective emittance ϵ_o as can be seen in Figures 4.5. The magnetic field level at 210 mm behind of the target is below 1% of the maximum field. Thus, the resulting emittance at that position depends on the momentum spread as well as on the initial beam divergence, α .

In Figure 4.5, the impact of the chromatic and spherical effects at that position can be seen, where three different cases for the beam divergence are plotted.

The predicted linear behavior in eq. 4.3 is confirmed for a momentum spread larger than 2% for both planes x and y . At vanishing momentum spread, the relative emittance growth is caused by spherical aberrations only. This can be seen in Figures 4.5, right ($\Delta p/p < 2\%$).

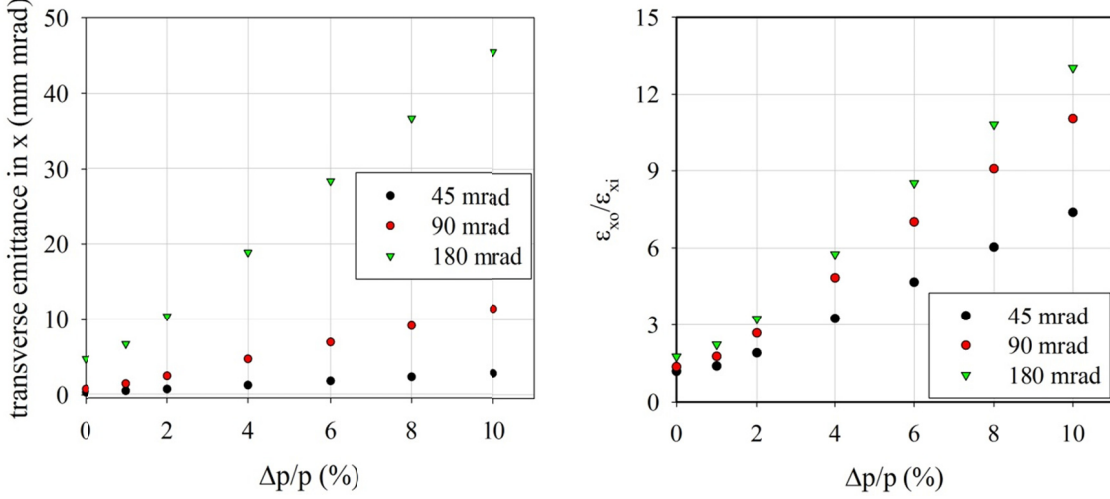


Figure 4.5: Output rms – emittance values in $x - x'$ versus $\Delta p/p$ (left) output to the input rms – emittance ratio in $x - x'$ versus $\Delta p/p$ (right) at a position 210 mm behind of the target, in dependent from the initial divergence α .

With absence of spherical aberrations, the ratio of the output emittance to the input one for mono energetic beam should be one. This is not the situation in our simulation; the ratio of the output to the input emittance at the same momentum spread is varying with input divergence which is due to the spherical effect only (see Figure 4.5, right and Figure 4.6).

To clarify the chromatic effect, the input and output phase space distributions $x - x'$ are plotted for three different momentum spreads at $\alpha = \pm 90$ mrad input divergence (see Figure 4.7). In this part, an absolute transverse emittance of $5.4\pi \text{ mm} \cdot \text{mrad}$ ($\epsilon_{rms} = 1.36 \text{ mm} \cdot \text{mrad}$) was used as the input emittance for different momentum spreads. For $\Delta p/p = 0\%$, the in rms-emittance is purely due to the spherical aberration and this is equal to $0.35 \text{ mm} \cdot \text{mrad}$. Therefore, in order to get the net growth or contribution due to chromatic aberration in the other two cases ($\Delta p/p = 4\%$ and 10%), one should subtract the contribution of geometric aberration ($\{\epsilon_{rms,o} - \epsilon_{rms,i}\}_{at \Delta p/p=0\%} = 0.35 \text{ mm} \cdot \text{mrad}$) from the output rms-emittance. It becomes obvious that, the effective enlargement in the output-distribution for $\Delta p/p = 4\%$ and 10% is very good in agreement with of eq. 4.3. Hence,

$$\frac{\epsilon_{c(\Delta p/p=10\%)}}{\epsilon_{c(\Delta p/p=4\%)}} \underset{\text{simulation}}{=} \frac{11.64 - 0.35}{4.87 - 0.35} \underset{\text{eq.3.3}}{\approx} \frac{10\%}{4\%} = 2.5 \quad (4.4)$$

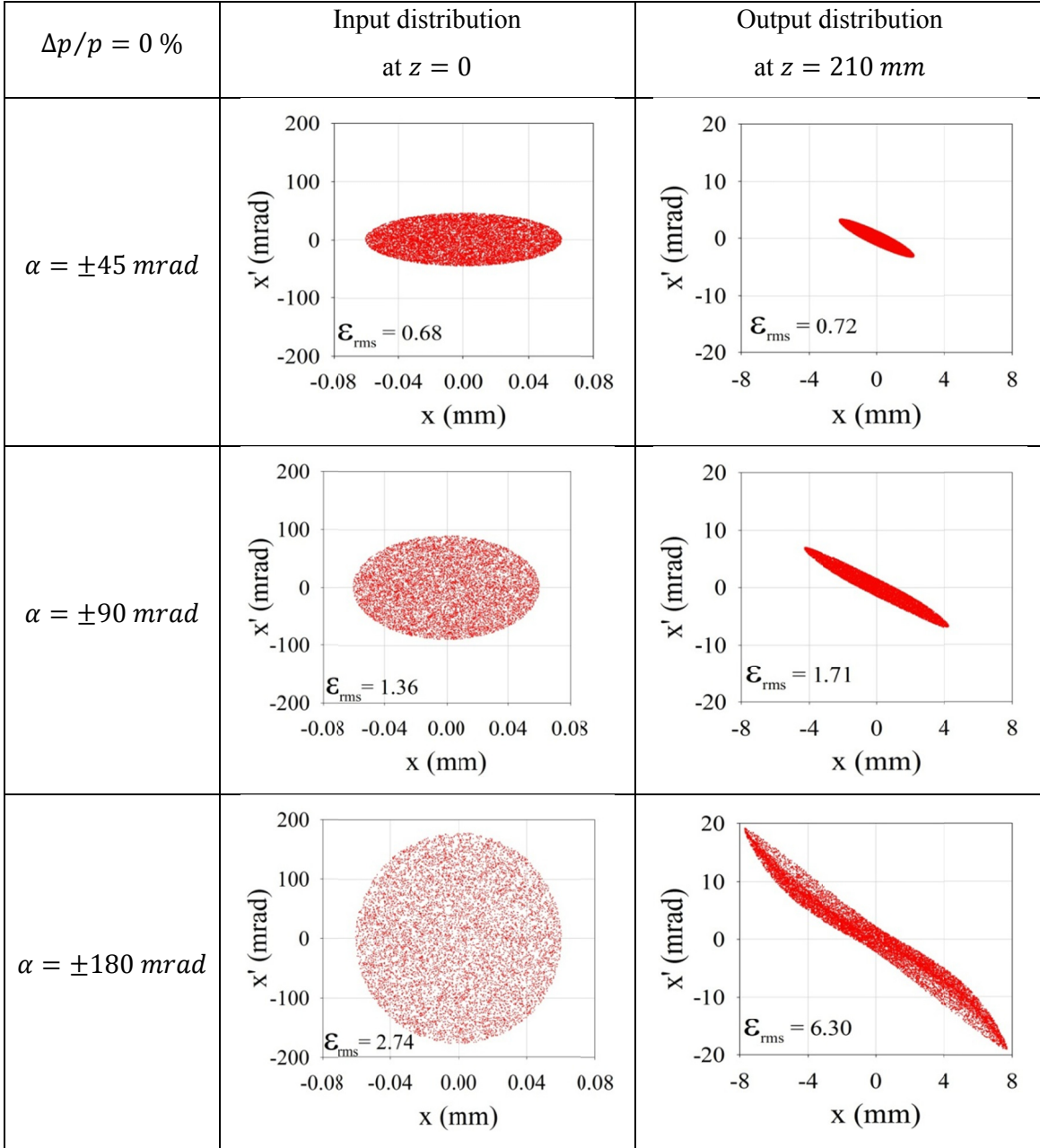


Figure 4.6: Input and output particle distributions in $x - x'$ for different opening angles with $\Delta p/p = 0\%$.

It was proven that in the presented simulations with the LASIN code, the non-paraxial effects were included. Thus, the geometric aberration will lead to the s-shaped distortion of output distribution even for a mono-energetic beam (Figure 4.7).

To explain how the s-shaped distortion is formed, the evolution of $x - x'$ output distribution for $\alpha = 180\text{ mrad}$ and $\Delta p/p = 0\%$ are shown at different z - positions (Figure 4.8).

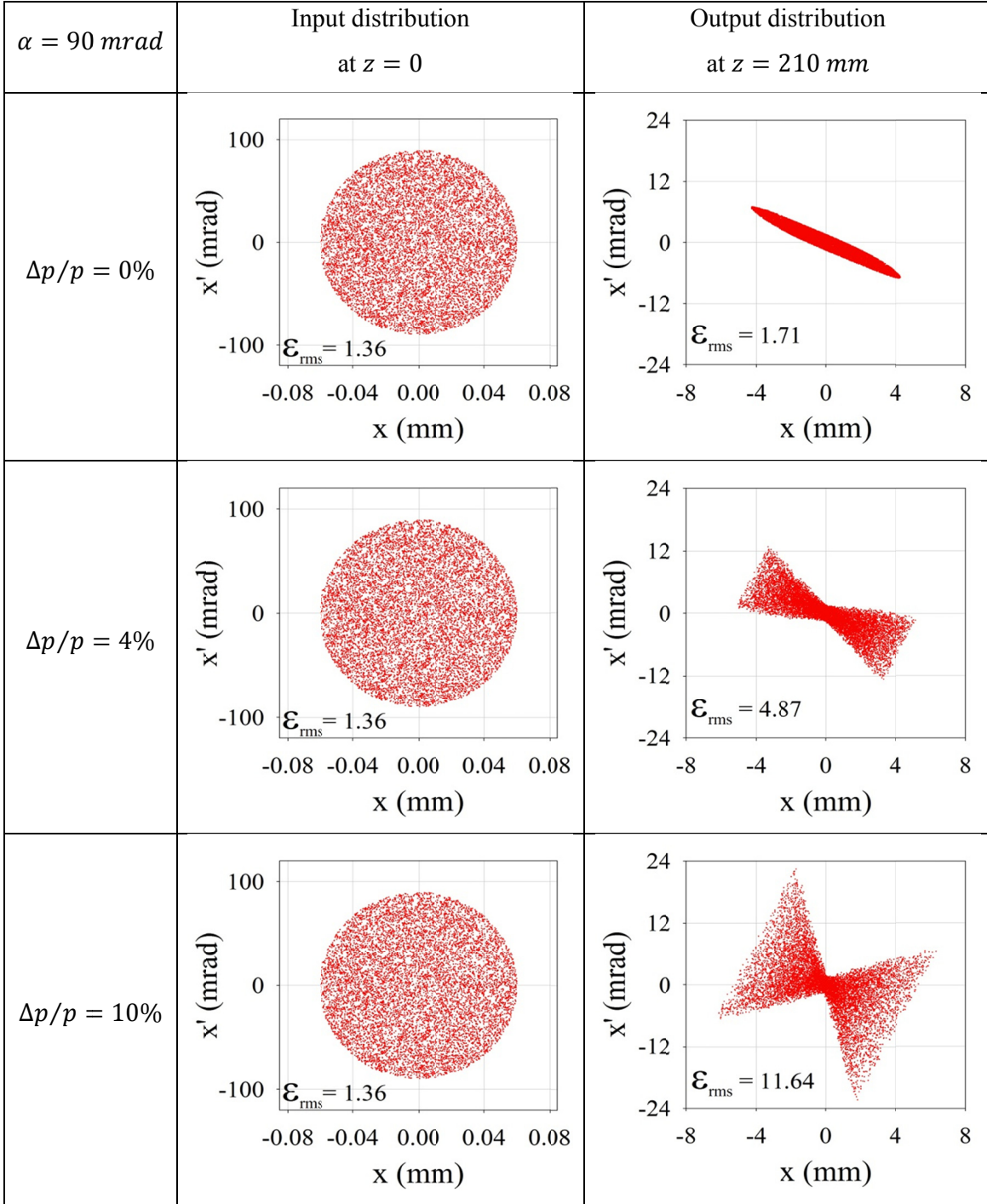


Figure 4.7: Input and output particle distributions in $x - x'$ for different momentum spreads $\Delta p/p$ with 90 mrad opening angle.

To analyze the emittance behavior along the solenoid it is necessary to follow the rms – “canonical” emittance $\epsilon_{cano.}$, this means to replace the mechanical momentum by the canonical momentum ($\mathbf{P}_{canonical} = \mathbf{P}_{mechanical} + q \cdot \mathbf{A}$ where $\mathbf{P}_{mechanical}$ is the mechanical momentum $\mathbf{P}_{mechanical} = m\mathbf{v}$ and \mathbf{A} is the vector potential).

The root-mean-square (rms-) emittance is defined as

$$\varepsilon_{rms} = \left(\overline{x^2 \cdot x'^2} - (\overline{xx'})^2 \right)^{1/2} \quad (4.5)$$

where $x' = p_x/p_z$.

The common definition of rms-emittance (mechanical) and the “canonical rms- emittance” can be defined as in eq. 4.5 but x' definition is different;

$$x' = \begin{cases} p_x/p_z & \text{Mechanical emittance} \\ p_{x,cano.}/p_{z,cano.} = (p_x + qA_x)/(p_z + qA_z) & \text{Canonical emittance} \end{cases} \quad (4.6)$$

Thus, $\varepsilon_{cano.}$ is growing while the protons are crossing the solenoid (see Figure 4.9).

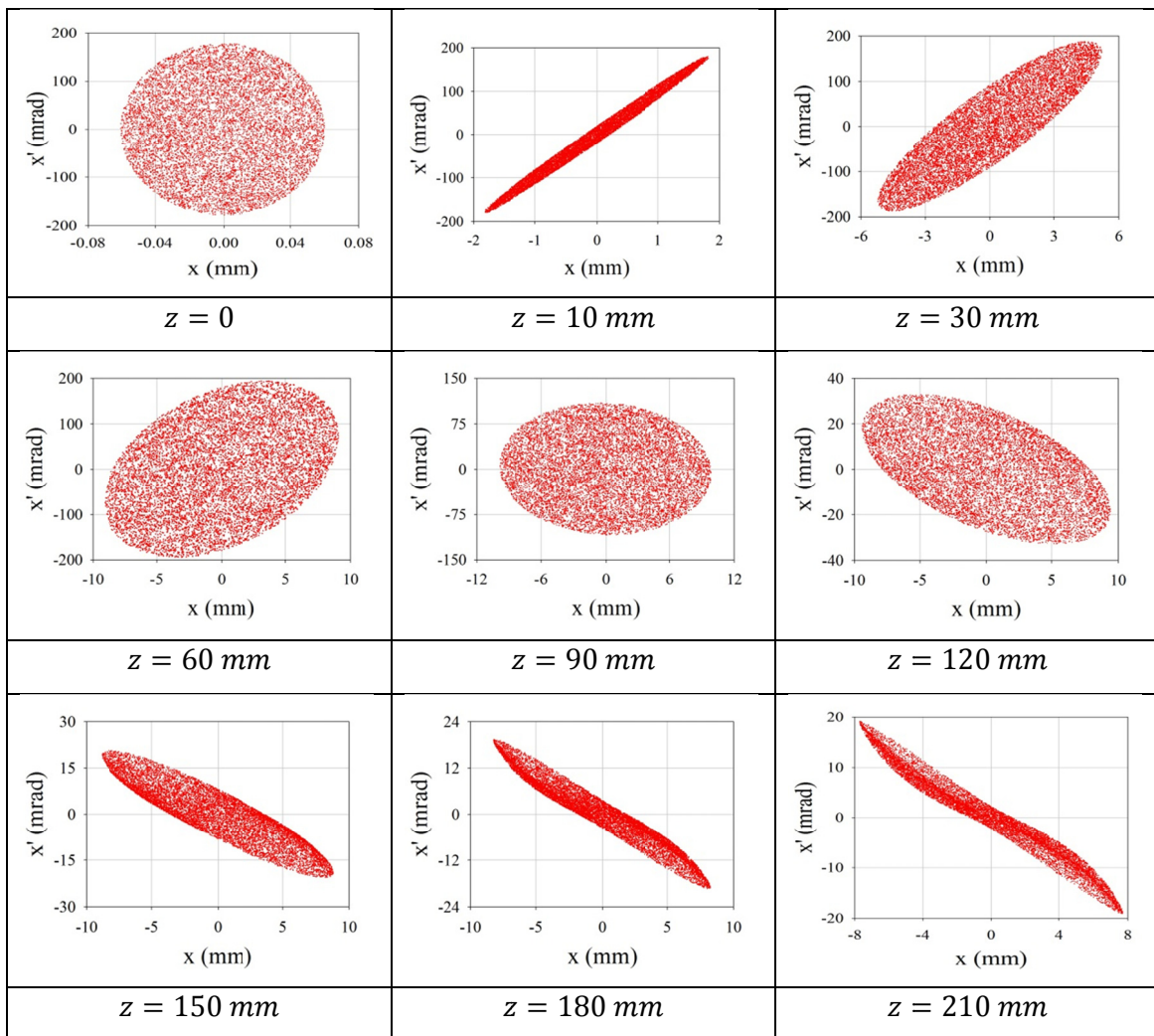


Figure 4.8: The evolution of $x - x'$ distribution for $x = 180 \text{ mrad}$ and $\Delta p/p = 0\%$ at different positions. The s – shaped deformation at the last position is mainly due to the spherical aberration.

With absence of any aberrations and space charge forces, the canonical emittance should be conserved. In the case discussed in Figure 4.9, the particles are generated without energy spread to have no contribution of chromatic aberrations. Thus, the growth in transverse canonical emittance, which is happened mainly in the solenoid, is due to the spherical aberration.

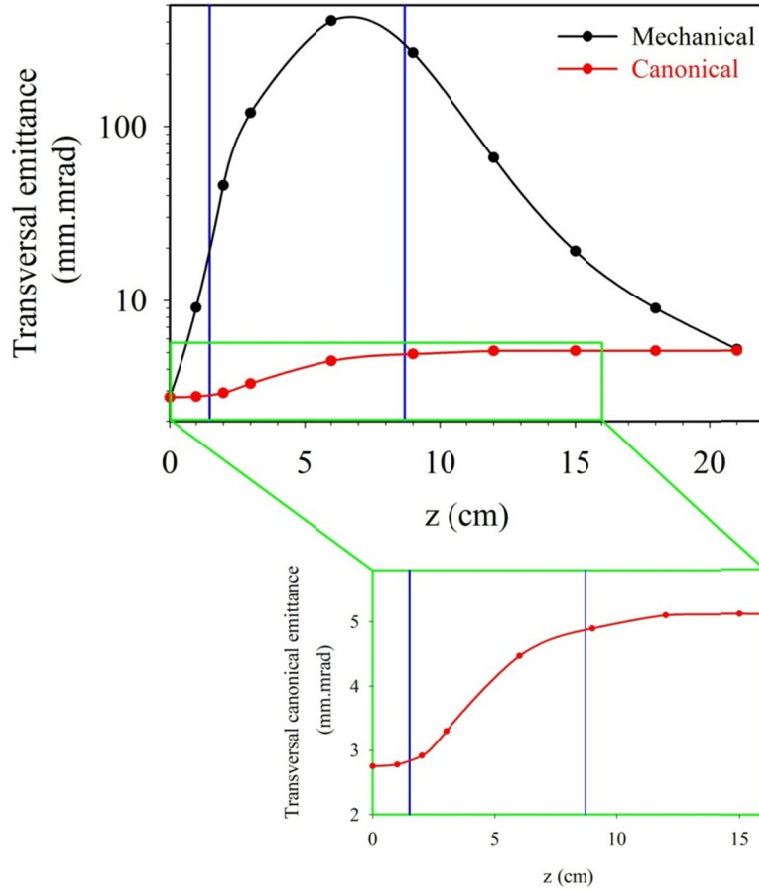


Figure 4.9: Canonical (red) and mechanical (black) emittance evolutions on the z – axis for $\Delta p/p = 0\%$. The smooth growth in the canonical emittance is an impact of the spherical effect. Both evolutions are ended at the same values where the magnetic field is reduced down to less than 1%. The geometric length of the solenoid (blue lines) is marked.

4.3.2 Proton Bunch Transported through the Solenoid

The tracking of the proton beam through the magnetic solenoid up to 210 mm behind the target was investigated with variable initial parameters in detail. Beam Envelopes in x for different opening angles ($\alpha = \pm 45$ mrad, ± 90 and ± 180 mrad, with mono-energetic beam) are shown by Figure 4.10, left.

The maximum beam radius was below 10 mm, even for the 180 mrad case. Since the laser accelerated protons are generated with a large momentum spread, the beam envelopes for different momentum spreads: $\Delta p/p = 0\%$, 4% and 10% with $\alpha = 45$ mrad are investigated and results are shown in Figure 4.10, right.

Hence, the main difference in envelope for different momentum spread can be seen along the 123 mm long drift behind the solenoid. This behavior is due to different exit angles at the solenoid exit.

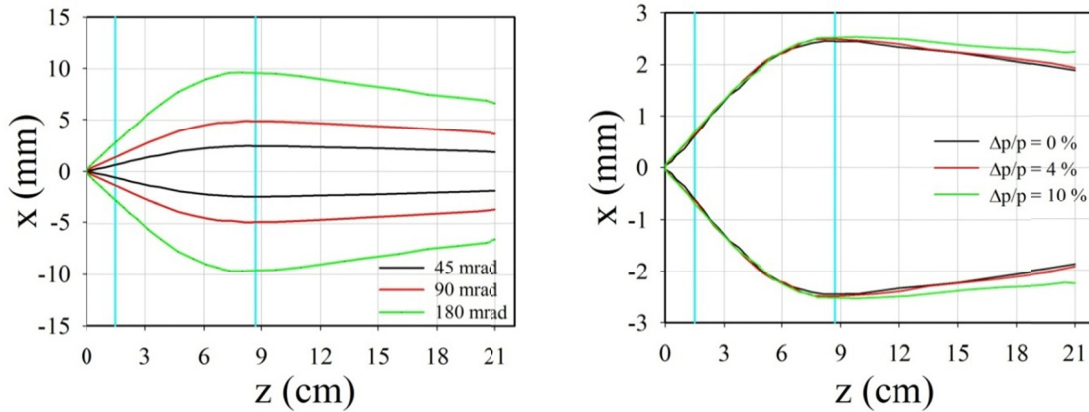


Figure 4.10: The beam envelopes of a proton beam in x for different opening angles at $\Delta p/p = 0\%$ (left) and for different momentum spreads at $\alpha = \pm 45$ mrad (right), the geometrical length of the solenoid is marked in cyan lines.

4.4 Simulations with Space Charge

The effect of space charge forces on the beam dynamics of a single proton bunch generated by laser was investigated in detail. The laser – accelerated proton bunch is generated together with co-moving electrons [32, 34, 61, 77].

In order to understand this problem, the study was divided in two parts; the first part concentrates on the pure proton bunch starting with a bunch length of 500 fs from a 60 μm radius spot. It was aimed to transport the proton bunch through the solenoid, including the Coulomb explosion effect in the first millimeters. But in reality, the protons generated by the TNSA mechanism are expected to be space charge neutralized to a high degree by the co-moving electrons, which are generated together with the protons at the target rear side [32, 34, 61, 77]. This will be the topic of part two.

4.4.1 Proton Bunch Tracking (without electrons)

In order to estimate the space charge force on a single proton bunch transported through the solenoid without electrons, the following case was simulated: 10^{10} protons of energies $10 \text{ MeV} \pm 0.5 \text{ MeV}$ within a bunch length of 500 fs are assumed. The parameters of the proton bunch used in these simulations are summarized in Table 4.1. In this simple model, the influence of the great majority of about 10^{13} protons over all energies in the bunch (see Figure 4.11) as well as the electrons were neglected.

Table 4.1: Starting conditions of the proton bunch at the target position.

Energy Band	$10 \text{ MeV} \pm 0.5 \text{ MeV}$
Beam Diameter	$120 \mu\text{m} *$
Bunch Length	$500 \text{ fs} *$
Divergence	$\pm 1 \text{ mrad}$
Emittance	$0.06 \pi \text{ mm} \cdot \text{mrad}$
Normalized Emittance	$0.028 \text{ mm} \cdot \text{mrad}$
Proton Number	10^{10} protons

* The value was chosen depending on the expected value from TNSA.

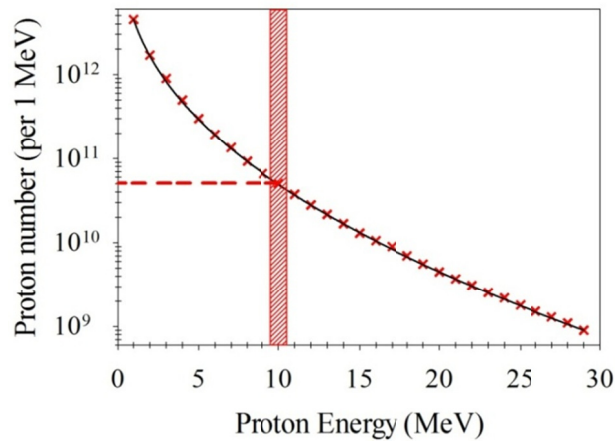


Figure 4.11: Proton spectrum measured at PHELIX experiments. The proton number per unit energy is showing an exponential by decreasing curve. 10^{10} protons can be detected in the energy band of $10 \text{ MeV} \pm 0.5 \text{ MeV}$ (Courtesy of M. Roth and V. Bagnoud, [40]).

The complete bunch transport from the target position along the z-axis was done in two steps; the first step was extended up to 1.6 mm (bunch center) behind of the target and along the beam axis in order to examine the Coulomb explosion and the second step was pursued up to about 210 mm (bunch center) along the beam axis as discussed below.

4.4.1.a Coulomb Explosion

The simulations for this section were started with a uniform ellipsoidal distribution with $\pm 1 \text{ mrad}$ as the initial divergence of the beam in transverse planes (Figures 4.12 left). Hence, in order to study pure space charge effects the protons were generated almost in parallel with the beam axis. The mesh size was adapted by choosing the time step to be 10^{-13} s .

Due to the enormous space charge forces with an extreme electric field resulting in an electric potential of about 1 MV in the bunch center, the bunch starts quickly to expand with transforming the electrostatic potential energy to kinetic energy [207]. The bunch reached a divergence of about $\pm 150 \text{ mrad}$ after 1.6 mm behind the target (Figure 4.12, right) while the beam potential decreased to the 72 kV level [207].

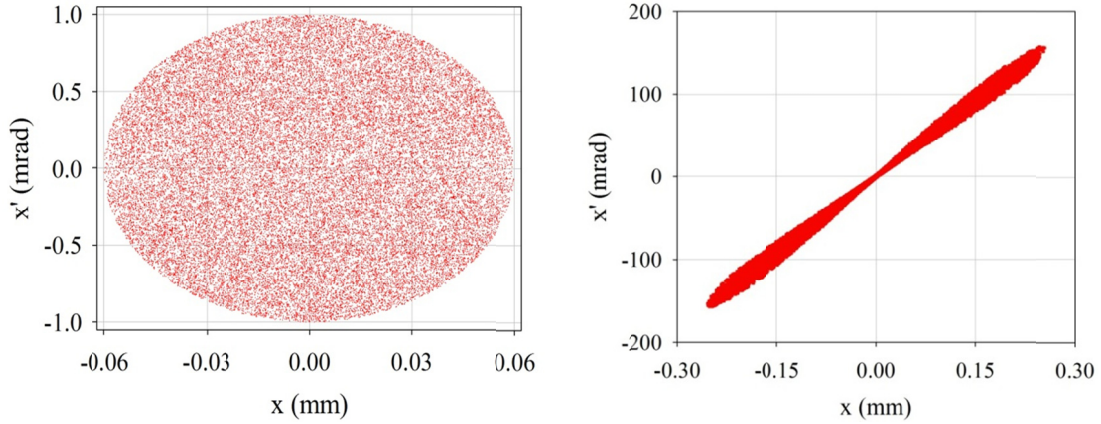


Figure 4.12: Input and output distribution in $x - x'$ at the target positions (left) and after the Coulomb explosion at $z = 1.6 \text{ mm}$ (right).

Besides this divergence, the energy spread of the bunch was also increased and it reached $\pm 40 \%$ at the end (Figure 4.13).

Additionally as a second effect of higher energy spread, the initial transversal phase space distribution is transformed to the “Propeller – like” form (See Figure 4.12, right)

The relation between bunch widths Δx and Δz was investigated and it was fitted to be linear with a slope of 1.37 (Figure 4.14), where Δx and Δz are the bunch widths in x and z , respectively.

In Figure 4.14, the linear behavior is no more valid for $z < 0.25 \text{ mm}$. This nonlinear behavior is mainly due to the Coulomb explosion.

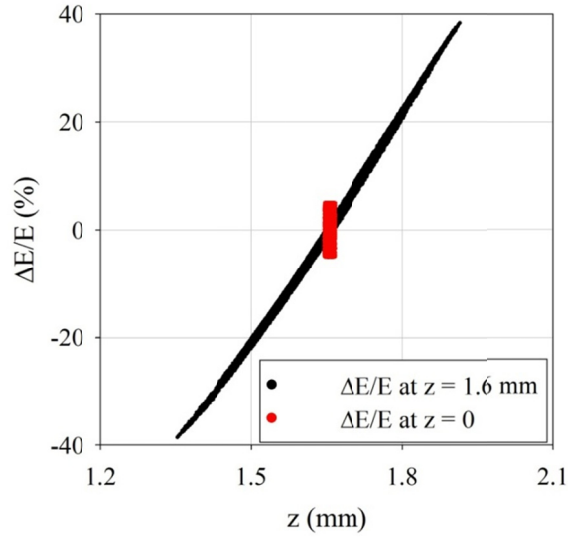


Figure 4.13: Input and output energy spread distributions in the proton bunch at the target position (red) and after the Coulomb explosion at $z = 1.6$ mm (black).

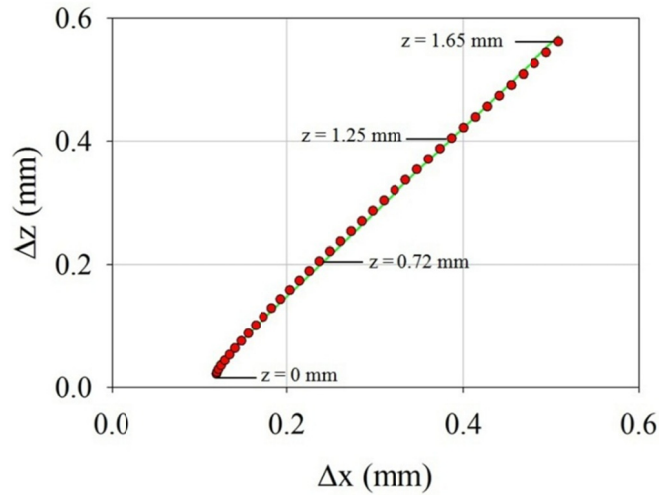


Figure 4.14: The relation between the bunch diameters in x (or y) and z at different positions. The non – linear behavior around $z = 0$ is mainly due to the Coulomb explosion. Starting conditions like given in table 4.1 and mirror effects of the target are not included.

The ratio of bunch widths $\Delta x/\Delta z$ is shown in Figure 4.15 as a function of z . At the initial point the ratio was about 5.45, after that it was decreased rapidly and reached 1.0 at $z = 1.03$ mm. This means that our initial ellipsoid became a sphere due to the space charge forces. Thus, the longitudinal space charge forces in z are initially much bigger than the transversal ones in x and y .

Figure 4.16 shows the bunch evolution at different z position. Hence, the rapidly beam expansion can be seen easily by comparing the first bunch at $z = 0$ and the last one (in blue) at $z = 1.6 \text{ mm}$.

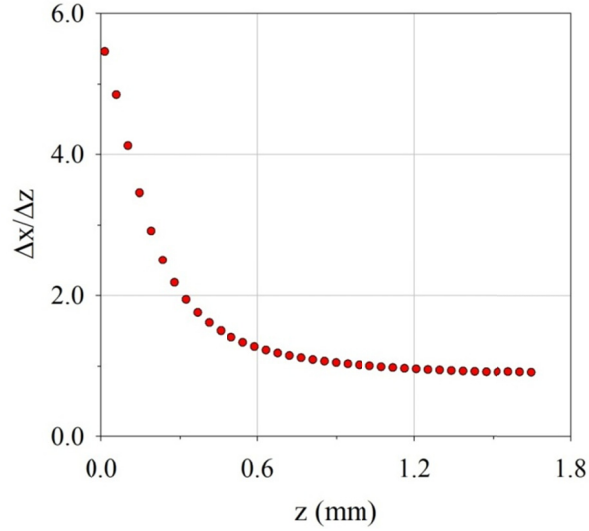


Figure 4.15: The ratio of bunch widths $\Delta x / \Delta z$ at different z positions. The initial ellipsoid distribution was expanded longitudinally more than transversally due to the bigger space charge forces in z and it becomes a sphere after the end of Coulomb's explosion.

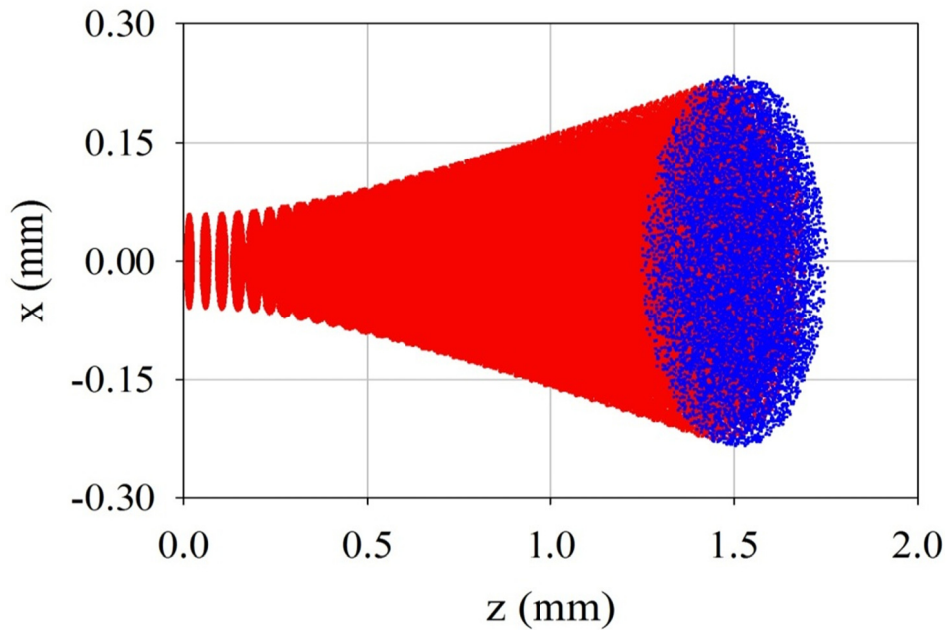


Figure 4.16: The proton bunch at different positions, where the initial bunch at $z = 0$ is expanding in all directions especially in z - direction where it is about 22 times larger finally.

4.4.1b Transport of the Proton Bunch behind the Solenoid

After the space charge explosion along the first millimeters, discussed in the previous section, the proton bunch was transported through the focusing magnetic solenoid with its fringing fields.

Due to the Coulomb's explosion, the proton bunch has an energy spread of about $\pm 40\%$ and an angular divergence up to $\pm 150\text{ mrad}$. Due to the chromatic aberration explained in section 4.3.1, particles with different energies are focused at different positions (Figure 4.17). Due to the energy spread ($10 \pm 4\text{ MeV}$), the transported proton bunch has a wide spread in longitudinal z direction reaching about 88.6 mm at 210 mm (bunch center) from the target.

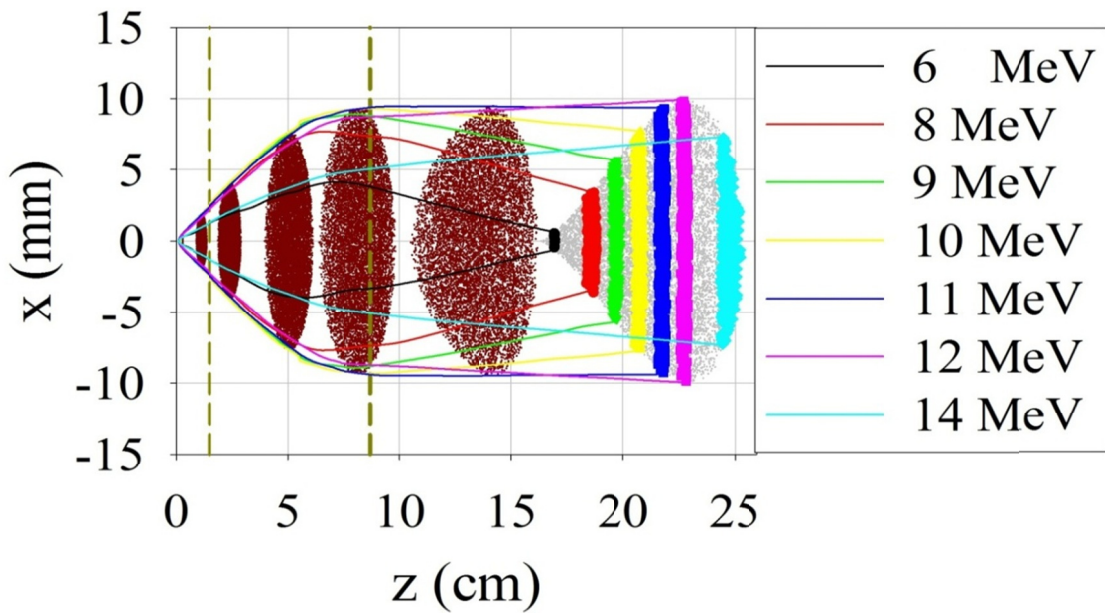


Figure 4.17: Bunch shapes in x - z projection at different positions along the beam axis. Additionally, the beam envelopes with their correlated proton energies at the last position are color coded. The dashed dark green lines show the geometrical length of the solenoid.

Figure 4.18 shows the $x - x'$ output distribution in phase space with “bow tie” shape. In comparing the results in Figure 4.18 with Figure 4.7, it is clear that the main influence is given by space charge induced chromatic aberrations. Due to large angular divergence, the spherical aberrations are contributing.

In conclusion, these simulations show that already the space charge forces of one permille of bunch particles with energies of $10\text{ MeV} \pm 0.5\text{ MeV}$ is sufficient to cause a large beam divergence up to $\pm 150\text{ mrad}$ as well as a large additional energy spread of $\pm 4\text{ MeV}$ ($\pm 40\%$ along the drift of 210 mm through the magnetic solenoid).

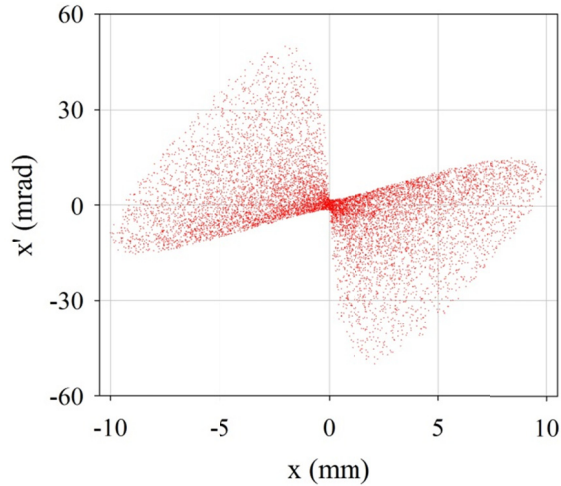


Figure 4.18: Output distribution in $x - x'$ of the proton bunch at the last position which is extended from $z = 16.3$ cm to $z = 25.2$ cm (see Figure 4.16).

By choosing an extreme case where the bunch contains only protons, it was possible to estimate the effect of space charge on the beam dynamics when the bunch is exposed to full space charge. But in reality the protons are generated with an initial divergence, and additionally with co-moving electrons which will reduce and modify the space charge effect. This is described in the next section

4.4.2 Two Species (Proton Bunch with Electrons)

The proton bunches are expected to be space charge neutralized to a high degree behind the target foil in the absence of magnetic fields [77]. Before we start to discuss the effect of co-moving electrons on the beam dynamics of a single proton bunch, the impact of the magnetic field on the proton and electron bunches along the first millimeters is studied.

Figure 4.19 shows a detail view of the laser target, the focusing magnetic solenoid and the drift to the rf linac. The longitudinal axis is marked in mm and in ps time of flight for a 10 MeV on axis protons. The effective range of LASIN and LORASR code based simulations in space charge case are indicated.

Since the target is located 15 mm from the entrance of the magnetic solenoid, the protons and electrons are generated in the fringing field of the solenoid. The field level at the target position is more than 6 T.

Because of a neutralized beam in the beginning, the beam potential starts at zero. Thus, no space charge forces exist at this point. Due to the difference in mass between protons and electrons, their response to the magnetic field is quite different.

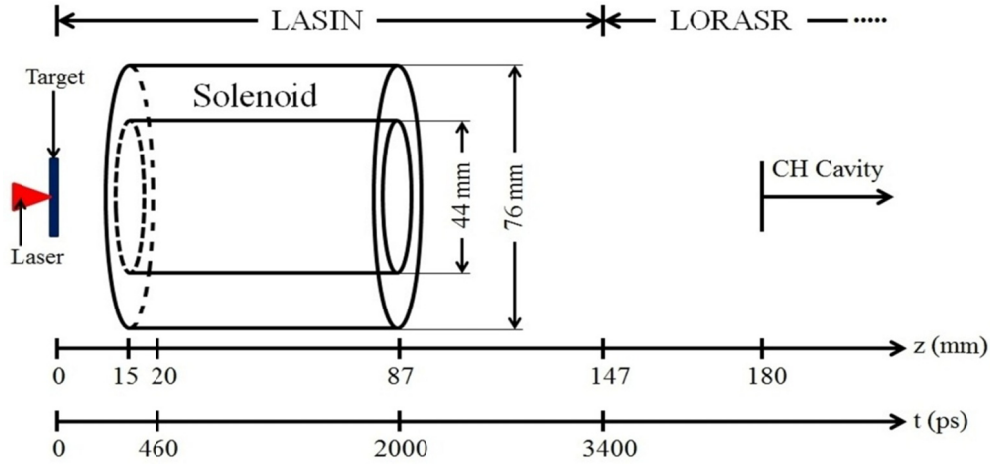


Figure 4.19: Schematic view of the laser target, the focusing solenoid and the drift to the rf linac. The longitudinal axis is marked in mm and in ps time of flight for a 10 MeV on axis proton. Additionally, the range of LASIN and LORASR code based simulations in space charge case (protons with the co-moving electrons) are indicated.

The gyroradius (Lamor radius) r_g is given by [204]

$$r_g = \frac{mv_{\perp}}{|q|B} \quad (4.5)$$

where m the mass of charged particle, q the charge of the particle and v_{\perp} the velocity component perpendicular to the direction of the magnetic field B .

In the fringing field area, the divergent particles have different v_{\perp} , moreover the magnetic field will have different strengths and directions.

For electrons, the charge-to-mass ratio is much bigger compared with protons; the motion can be described by a decreasing helix. The electrons are focused strongly towards the axis following the magnetic field lines and gyrating around them.

Due to the focusing process, the axial electron density increases and forms a negative on axis potential. As a result, space charge forces occur because of more and more differing distributions between electrons and protons in space. Part of electrons will be accelerated in the forward direction and others will slow down.

Finally, it should be noted that the solenoid field can act like a magnetic mirror [115] and reflect electrons in case of large initial divergence (conservation of the adiabatic constant μ , μ being the magnetic momentum of gyrating potential [115]). The reflection condition in terms of the magnetic field levels is given as

$$\sin^2 \theta = \frac{B_{min}}{B_{max}} \quad (4.6)$$

where θ defines the cone loss. Particles with initial divergence larger than θ will be reflected backwards to the lower field region. B_{min} is the field level at the starting point, B_{max} is the field level in the solenoid mid-plane.

For the target – solenoid array as shown in Figure 4.19 θ corresponds to about 35° .

Figure 4.20 shows the evolution of a neutralized bunch from electrons and protons at different positions during the first millimeters. Here, a uniform KV – distribution was assumed for both – electron and proton distributions. The magnetic field levels are shown in the top right corner. The impact of magnetic field on electrons is much bigger than on protons. Here, it easily can be seen that the electrons are accelerated in forward and opposite directions.

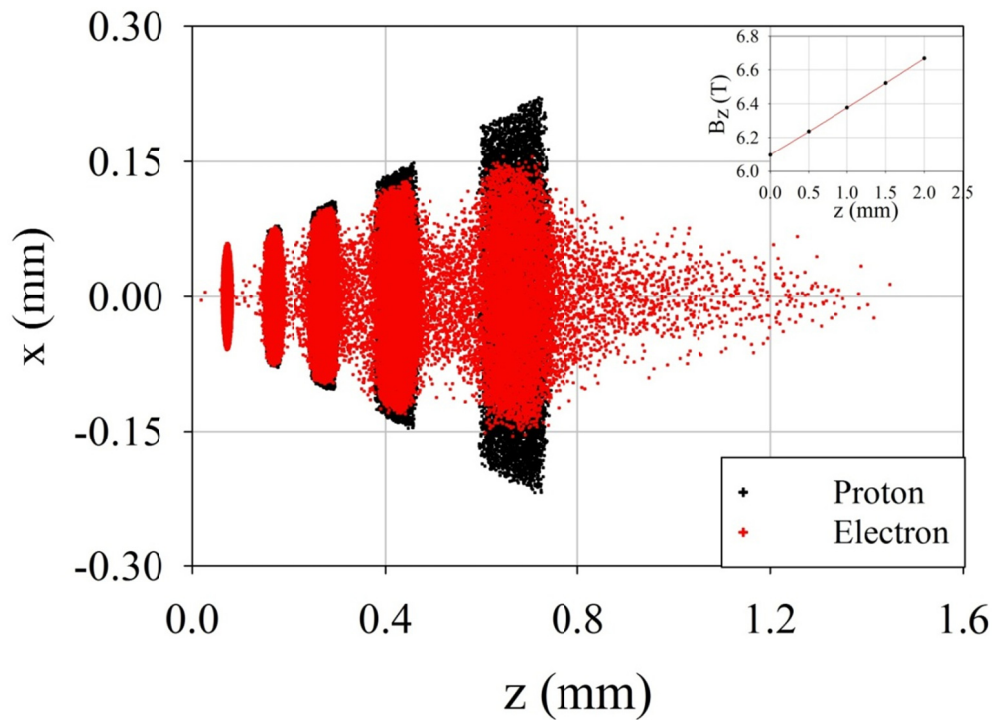


Figure 4.20: The evolution of a neutralized bunch propagating along the z – axis towards the magnetic solenoid. The bunch starts with 100 % neutralization between protons and electrons. The impact of the magnetic field on the electron is much bigger than on protons. The magnetic field level at the starting point was more than 6 T, reaching a maximum of 18 T in the solenoid.

Besides the mesh resolution close to the target, details of the initial proton and electron distributions in phase space have to be chosen properly. Especially, the huge electric fields caused by charge separation in the presence of the solenoid field were limiting the choice of the mesh cell dimensions. Moreover, Courant stability criteria for numerical explicit schemes require that $v \times \Delta t_{\text{mesh}} < \Delta z_{\text{mesh}}$, resulting in a small time step. Due to the fact, that the maximum occurring electric field is a dynamical variable, several preliminary test simulations were needed to find an optimum mesh setting. The total internal energy (potential plus kinetic energy of all particles) was calculated as a control parameter to check conservation properties and to distinguish between numerical and physical effects.

These preliminary simulation checks and an optimum use of the available cluster capabilities resulted in the following strategy, which divides the transport line into 4 sections a) – d), simulated by LASIN.

The tracking of the proton bunch through the pulsed magnetic solenoid with the presence of co-moving electrons is described in the following [198].

a) Initial Particle Distribution and Transport 0 – 10 ps.

In the following, an isothermal expansion model (drifting particles) during the first 10 ps with starting from a radial Gaussian 2σ density distribution was assumed.

The input parameters for the initial distribution as well as their dependence on the proton energy were chosen according to the simulated and measured data in the PHELIX laser experiments [34]. Figures 4.21 – 4.22 summarize these data.

The input parameter “initial source radius” was varied from $180 \mu\text{m}$ at 5 MeV to $70 \mu\text{m}$ at 15 MeV continuously. The angular divergence is decreased with increasing proton energy. The angle of divergence was varied from about 400 mrad at 5 MeV to 140 mrad at 15 MeV (24° to 8°).

An initial energy spectrum as large as $10 \text{ MeV} \pm 5 \text{ MeV}$ was assumed now in the simulations: This is already 10 times larger than the energy band of $10 \text{ MeV} \pm 0.5 \text{ MeV}$, which is adequate for injection into the rf linac finally. Within the chosen energy range $10 \text{ MeV} \pm 5 \text{ MeV}$, the particle distribution is chosen according to the measured energy spectrum as shown in Figure 4.11.

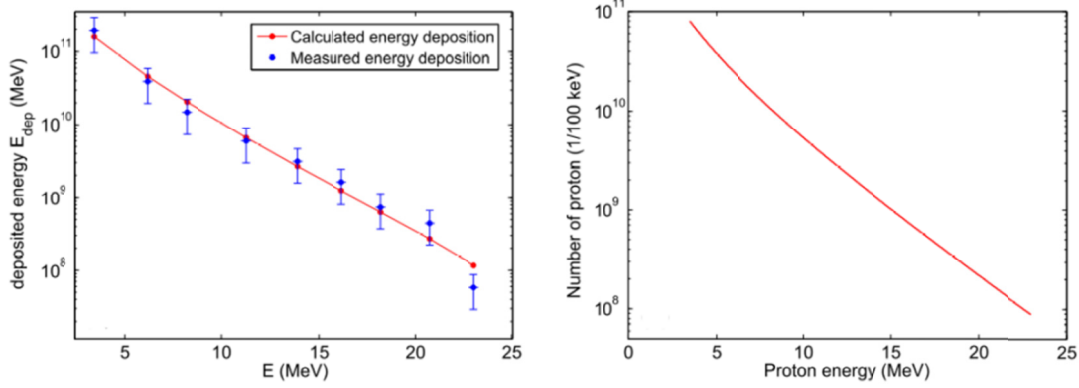


Figure 4.21: The measured energy deposition of protons in RCF films compared with the calculations using equation $\int (dN(E')/dE) \times E_{\text{loss}}(E')dE'$ (left). The fit shows the number of protons per energy interval. Equation $dN/dE = (N_0/\sqrt{2Ek_B T}) \times \exp(-\sqrt{2E/k_B T})$ was used to get the plot on the right [PhD thesis of F. Nürnberg ref. 34].

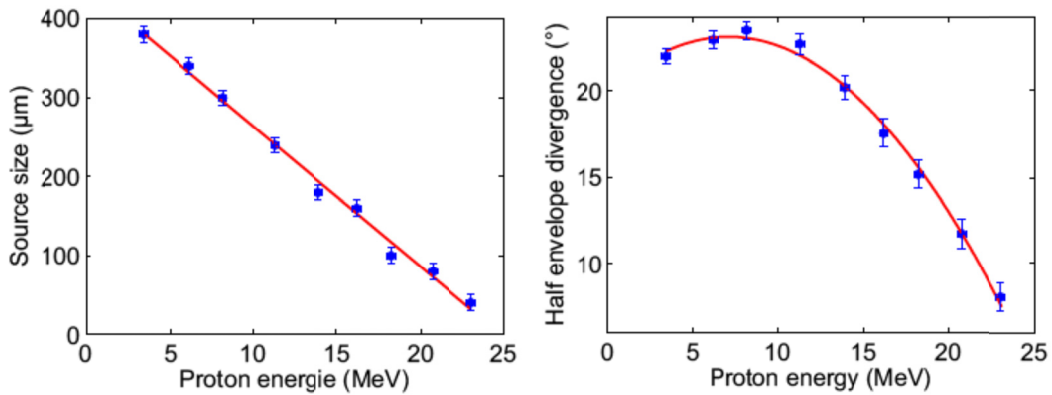


Figure 4.22: Proton beam parameters of the PHELIX data used in the LASIN simulations where the blue dots (■) are referring to the experimental data and (—) is the fitted function [PhD thesis of F. Nürnberg ref. 34].

The particles with low energy below 5 MeV were truncated due to the limited maximum macro-particle number 10^7 and their expected small interaction with the $10 \text{ MeV} \pm 0.5 \text{ MeV}$ proton fraction of interest for post-acceleration. The protons with an energy larger than 15 MeV are truncated for the same reason.

Electrons were chosen co-moving with the protons with 100% space charge compensation at the starting position.

b) Transport 10 – 40 ps.

During the first 10 ps, the proton and electron bunches expand to convenient dimensions for the simulation in LASIN. The starting distribution for the energy band $10 \text{ MeV} \pm 0.5 \text{ MeV}$ is

shown in Figure 4.23. The corresponding position of the particles after 40 ps is about $400\ \mu\text{m}$ behind the target.

The density profile of the protons in the transverse planes is distributed as Gaussian (See Figure 4.24).

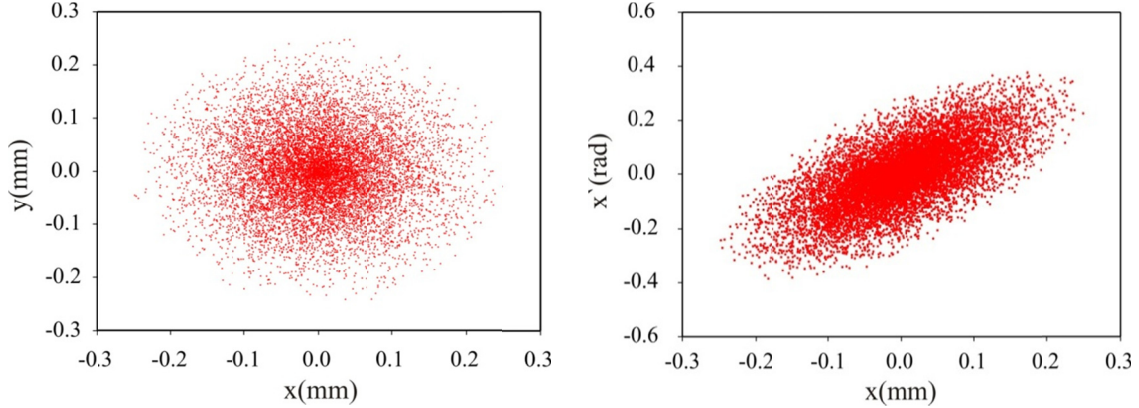


Figure 4.23: The $x - y$ - (left) and $x - x'$ - (right) projections of the $10\text{ MeV} \pm 0.5\text{ MeV}$ fraction of a simulated proton pulse after 10 ps ; $\varepsilon_{rms} = 6.56\text{ mm} \cdot \text{mrad}$.

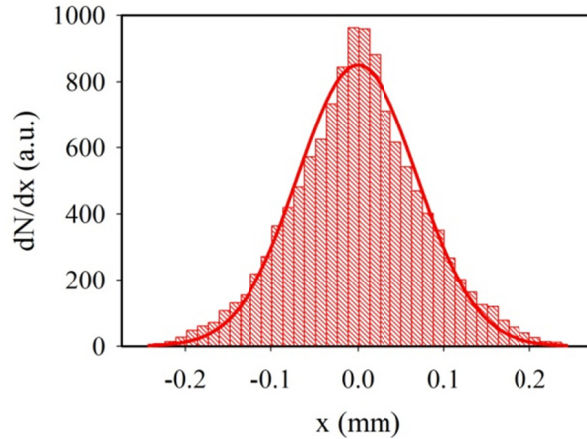


Figure 4.24: Transversal density profile distribution of the macroparticle from Figure 4.23, left.

The initial cylindrical mesh has the dimensions $\Delta r = 4\ \mu\text{m}$, $\Delta z = 2\ \mu\text{m}$, $\Delta\phi = 0.21\text{ rad}$ and the time step $\Delta t = 2.5 \times 10^{-14}\text{ s}$. Due to the fringing field of the focusing magnetic solenoid in the target region, electrons are transversally focused and cannot expand transversally in x and y . On contrary, the protons with their large transversal momentum can expand radially. The proton density decreases while the electron density stays almost unchanged near the beam axis (Figure 4.25).

Due to the charge separation and fringing fields, the electron on axis density is increased, which leads to arising negative on axis potential, reaching about -40 kV after 40 ps . Figure 4.26 shows the longitudinal and transversal on axis potential.

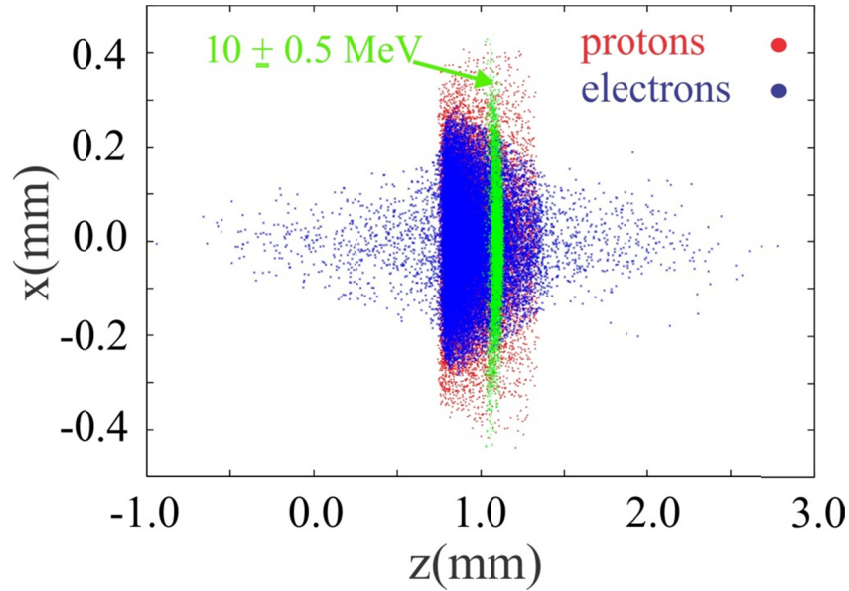


Figure 4.25: $z - x$ projection of the particle distributions after 25 ps . The action of the magnetic solenoid fringing field is seen already.

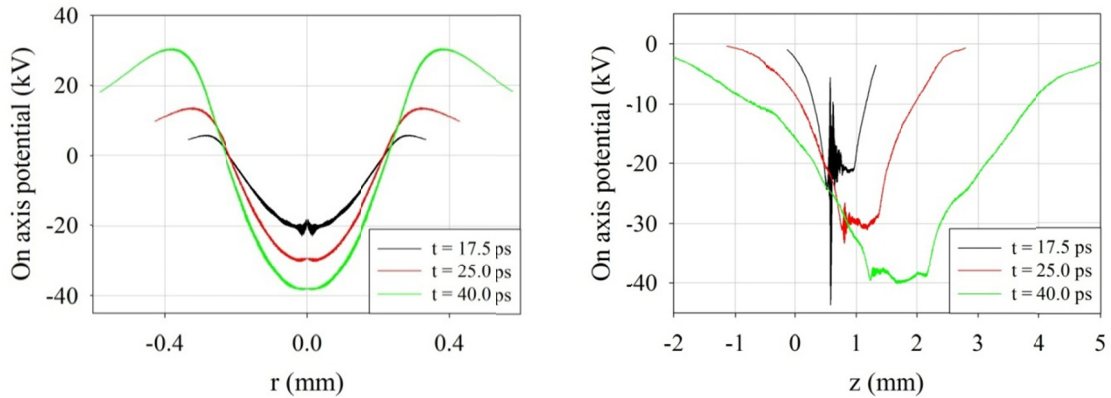


Figure 4.26: Potential curves in transversal (left) and longitudinal (right) directions at three different positions along z . At $t = 40\text{ ps}$, the space charge potential is reaching a maximum.

As a consequence, the electrons can escape and are accelerated in forward and backward directions. Subsequently, the potential drops down and electrostatic energy is converted to the kinetic energy of the particles. The rapid thermalisation process of the longitudinal electron distribution along the magnetic field was observed. Generally this fact is demonstrated by the potential behavior as shown in Figure 4.26. An occurring plasma oscillation at $t = 17.5\text{ ps}$

(Figures 4.26 – 4.27) is almost damped at $t = 40$ ps. For comparison, at a typical electron density of 10^{21} m^{-3} the plasma frequency has an oscillation period of 2 ps. The potential at $t = 40$ ps is reaching almost constant values along the z -axis within the propagating proton bunch

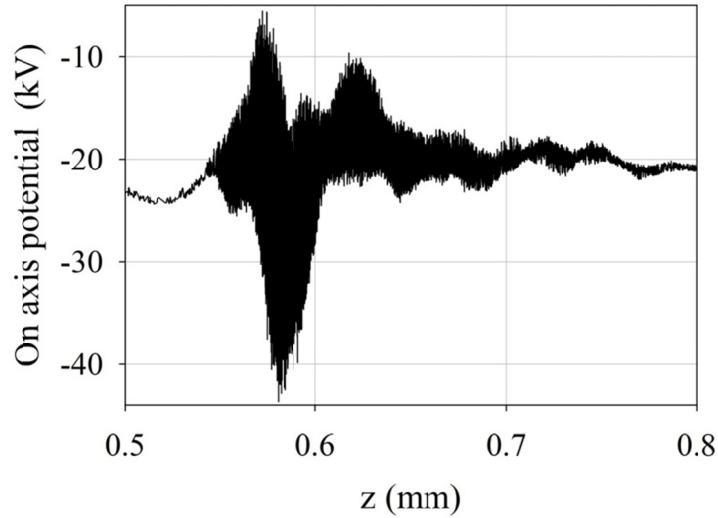


Figure 4.27: Detail of the potential curve (from Figure 4.26) after 17.5 ps in the longitudinal direction. The plasma oscillation has a higher potential fluctuation at lower z – positions, where the simulated particle density reaches its maximum.

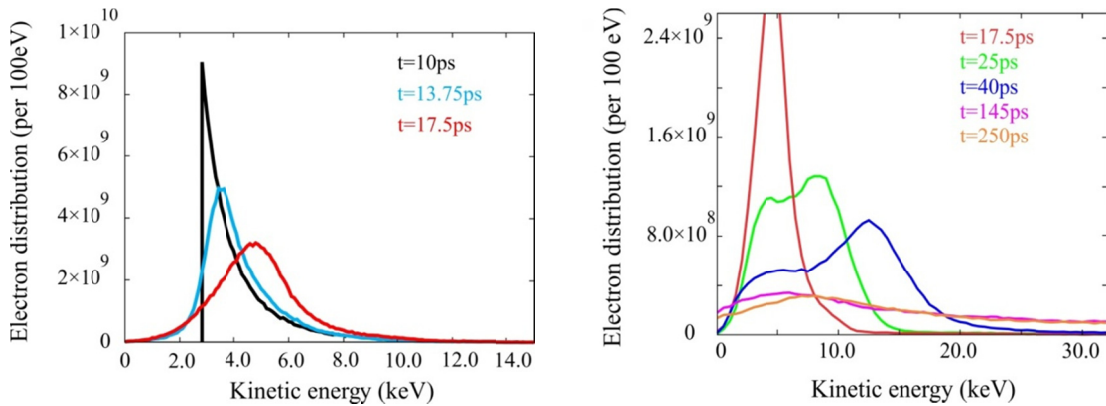


Figure 4.28: Time evolution of the electron energy distribution at different time steps. The right picture has different scaling.

The electron kinetic energy distribution (Figure 4.28, left) is changed to the Maxwellian form.

After the propagation time $t = 25$ ps some of electrons start to escape from the proton bunch and are accelerated to high energies in both directions along the z -axis. Two peaks are now evident in the distribution function (Figure 4.28, right). The proton kinetic energy distribution stays unchanged within the same time scale (first 40 ps, see Figure 4.33). However it was

found that, the growing potential energy as caused by the charge separation, is actually converted from the initial transversal kinetic proton energy. The growing pronounced charge separation is stimulated by the big initial beam divergence. The overall energy conservation is not violated on the 10^{-4} level.

c) Transport 40 – 460 ps.

Because of the relaxing space charge forces, the cylindrical mesh could be adapted to have dimensions $\Delta r = 45 \mu\text{m}, \Delta z = 45 \mu\text{m}, \Delta\phi = 0.21 \text{ rad}$ with the time step $\Delta t = 3.5 \times 10^{-13} \text{ s}$. The small time step is due to the high gyration frequency in the magnetic field.

The proton pulse expands transversally in radius; however, the expansion is slower than in the case of a single specie transport as discussed in section 4.4.1. At the end of the discussed time span ($t = 460 \text{ ps}$) the proton bunch propagated up to the position around 2 cm behind the target (Figure 4.29, position inside of the solenoid) and the electric potential is relaxing slowly towards zero on axis.

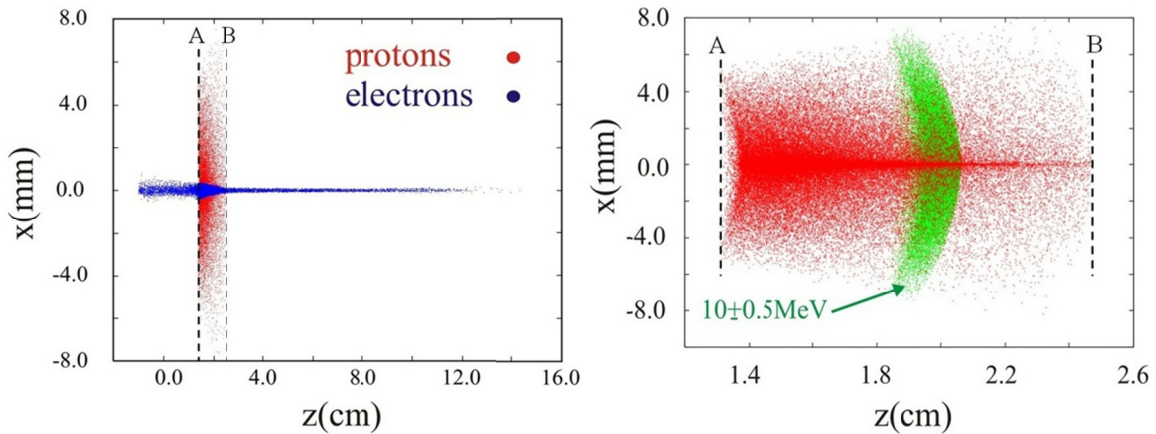


Figure 4.29: Proton (red) and electron (blue) distribution in z-x plane after 460 ps. Electrons are accelerated axially by their own potential. The detail AB containing the whole proton distribution is shown in detail (right). The green marked area corresponds to the protons with $10 \text{ MeV} \pm 0.5 \text{ MeV}$.

An electron influence on the proton distribution could be clearly demonstrated in the $x - x'$ phase space projection for the whole energy spectrum $10 \text{ MeV} \pm 0.5 \text{ MeV}$ (Figure 4.30):

The central part of the proton distribution ($r < 500 \mu\text{m}$) is strongly focused due to the pronounced radial focusing force of the electrons close to the beam axis. Consequently, the slope of the core – distribution in phase space differs strongly from the protons at larger radii, which just experienced the drift into the edge field of the solenoid so far.

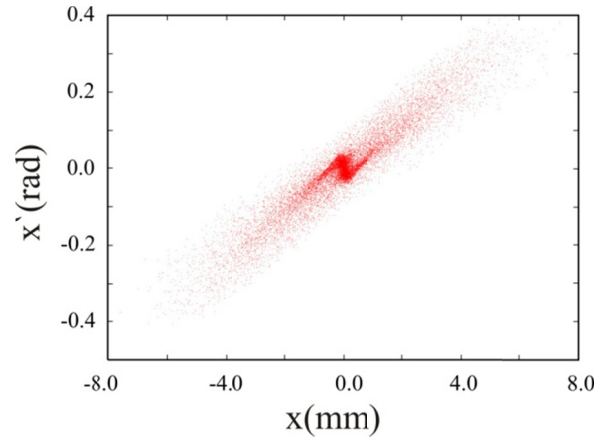


Figure 4.30: The $x - x'$ phase space projection of the transported proton spectrum with $10 \text{ MeV} \pm 5 \text{ MeV}$ at 460 ps .

The peaked central proton distribution, with about 30 % of all macroparticles concentrated within a radius of $500 \mu\text{m}$ is composed of all proton energies. This is also demonstrated for the energy of interest $10 \text{ MeV} \pm 0.5 \text{ MeV}$. The transversal proton distribution has no more a Gaussian shape and is peaked on the axis (See Figure 4.31).

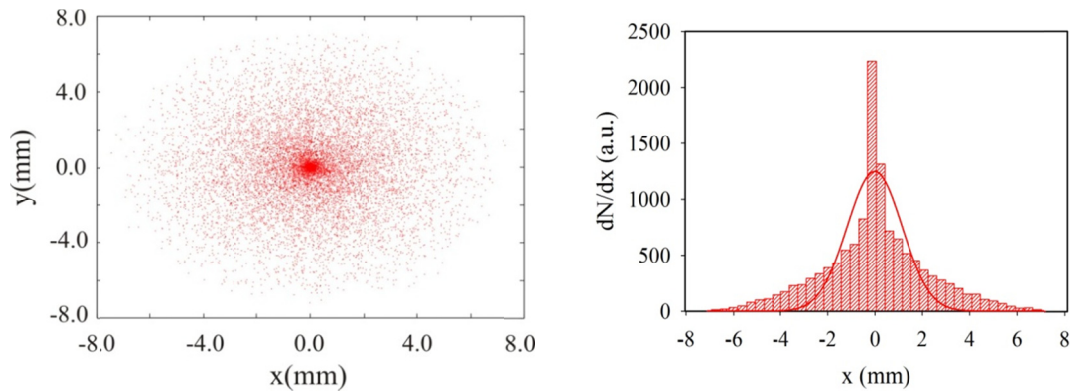


Figure 4.31: Transversal proton distribution for the energy band $10 \text{ MeV} \pm 0.5 \text{ MeV}$ after 460 ps .

The phase space distribution $x - x'$ has a central core in a focus (almost parallel beam) and an outside defocused part ($\pm 350 \text{ mrad}$ divergence) at radii up to $\pm 7 \text{ mm}$ (See Figure 4.32).

The proton kinetic energy spectrum after 460 is only slightly changed, mainly within the lower energy side (Figure 4.33). The longitudinal proton bunch position after 460 ps is just at the entrance of the solenoid.

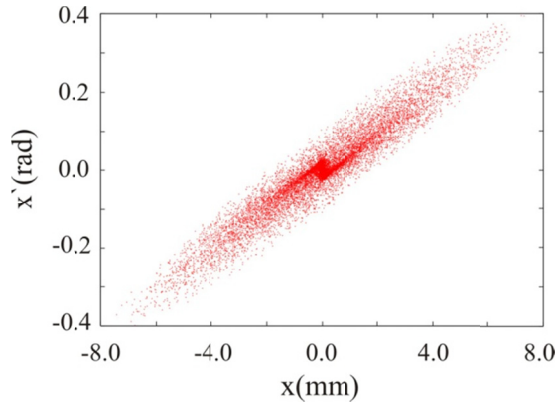


Figure 4.32: Proton distribution $x - x'$ for the energy band $10 \text{ MeV} \pm 0.5 \text{ MeV}$ after 460 ps . The local influence of co-moving on axis electrons is seen at $|x| < 0.5 \text{ mm}$.

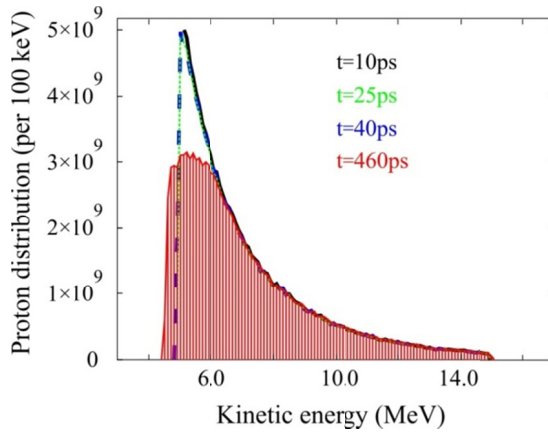


Figure 4.33: Proton spectral distribution development within the first 460 ps . The shape is changing mainly at low energy end.

d) Transport $460 \text{ ps} - 3.4 \text{ ns}$.

In the following simulation through the solenoid the influence of co-moving electrons was neglected because the electron and proton phase spaces are well separated now (see Figure 4.29): The maximum radial electric field at $t = 460 \text{ ps}$ reached about 10^7 V/m level at $500 \mu\text{m}$ radius. This corresponds to the equilibrium between magnetic and electric focusing forces in case of the proton distribution.

After 460 ps the focusing electric forces due to the electron distribution will be further reduced and the magnetic force becomes dominant.

No more additional proton accumulation on axis is possible and the proton distribution will show the cyclotron motion.

The radial electric force due to the electron column reached about 10^6 V/m level in the outer part ($r > 1$ mm) of the proton distribution and its contribution is then decreasing proportional to $1/r$ outside. Estimating the momentum transfer to the proton distribution after 460 ps down along the whole solenoid results in angular corrections below the 1% level.

The other reason to stop the electrons is because of an impractically long run – time of the numerical simulations with electrons which took more than 4000 hours.

The time step was set to $\Delta t = 2.5 \times 10^{-11}$ s and mesh cells to $\Delta z = 1$ mm, $\Delta r = 88$ μ m.

The resulting proton distribution as described in section 4.4.2.c is now transported along the remaining length of the solenoid and up to $t = 3.4$ ns. This corresponds to a drift of 60 mm behind the solenoid for the 10 MeV protons.

Due to its individual orientation at the solenoid exit, the inner 30% core (compare Figure 4.30) will further diverge along the drift while the outer beam fraction is approaching the waist (Figure 3.34).

In Figure 4.34, the low energy proton fraction is concentrated on the left, approaching a waist, while the high energy protons on the right show a central, focused core caused by the electrons in the early stage of beam motion as described in section 3.4.2.c. The distribution of the particles with $10 \text{ MeV} \pm 0.5 \text{ MeV}$ clearly shows the dominance of the chromatic aberration as discussed in section 4.3.1 and displayed in Figure 4.7.

A maximum beam potential of + 14 kV after the propagation time of 3.4 ns was reached on the beam axis at position $z = 11$ cm. The potential level of about 4 kV was detected for the energies of interest around 10 MeV at the same moment at $z = 15$ cm. It has to be noted that this potential is now acting on protons only.

To have a full view for the particles motion in phase space, the longitudinal particle distribution for the whole proton spectrum ($10 \text{ MeV} \pm 5 \text{ MeV}$) is shown in Figure 4.35, left.

The particles in red are represented to the protons with energies $10 \text{ MeV} \pm 0.5 \text{ MeV}$. This can be seen in detail in Figure 4.35, right.

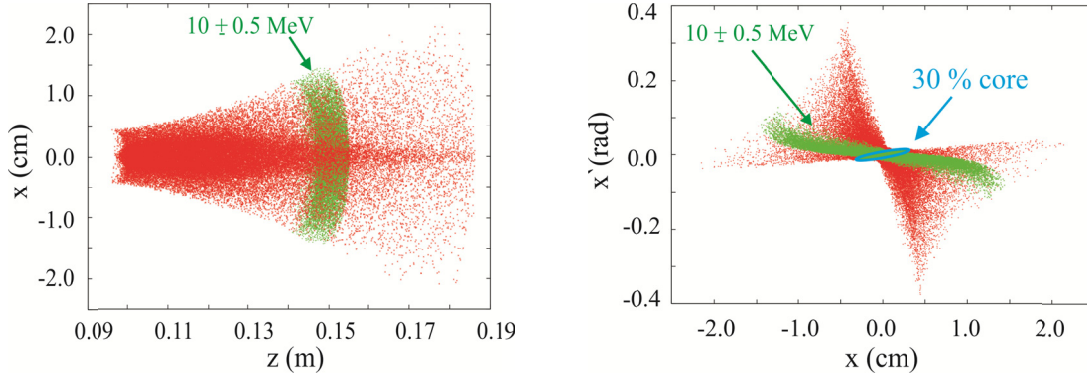


Figure 4.34: (Left) $z - x$ proton pulse distribution after solenoid and followed by a 6 cm drift. The low energy part is near to the focal spot. (Right) $x - x'$ distribution for the same propagation time $t = 3.4$ ns. Green marked area corresponds to the energy of interest (see also Figure 6.6 for more detailed view).

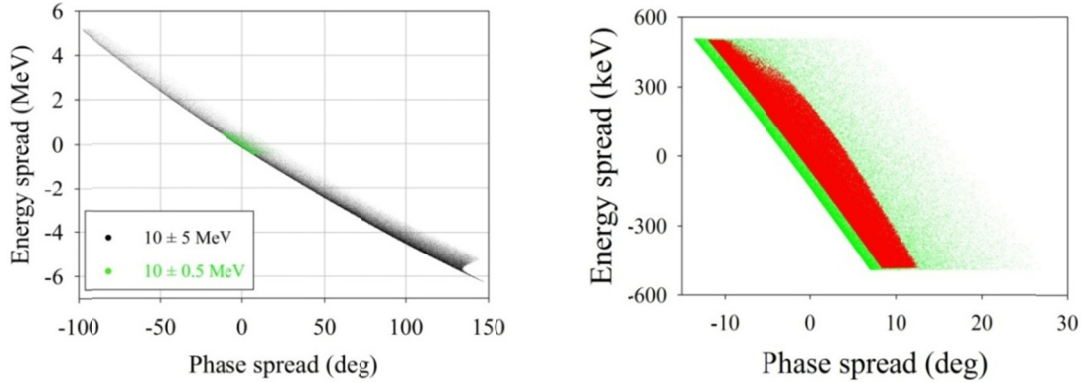


Figure 4.35: Longitudinal particle distribution of laser generated protons 60 mm behind the solenoid with energies $10 \text{ MeV} \pm 5 \text{ MeV}$ (left). Green marked area corresponds to protons within energy of interest $10 \text{ MeV} \pm 0.5 \text{ MeV}$, which is shown in detail at right. The red marked area corresponds to the accepted particle distribution fall within the CH – DTL acceptance and used for post-acceleration study. The vertical axis of right picture has different unit.

The simulations with LASIN end at this point and the fractional distribution (green marked area, Figure 4.34) was adapted as input distribution for the following linac post-acceleration. This distribution was adjusted to the LORASR code format. The relative transverse and longitudinal rms – emittance growth could be calculated as the ratio between the output to the input rms values and it was about 10 times at the end of the solenoid transport ($\epsilon_{rms,out}/\epsilon_{rms,in} \approx 10$).

The matching and injection of the proton bunch within energy band will be discussed in detail. This will be the topic of chapter 6.

CHAPTER 5

RF LINACS WITH H-TYPE CAVITIES

5.1 RF Linac Parameters

A particle accelerator transfers energy to the particles by applying an electric field. In the RF linacs, the particles are accelerated along a linear path by time – dependent electromagnetic fields. One of the main advantages of a linac is its ability for producing high intensity and high energy particle beams. Figure 5.1 shows a block diagram of an RF linac with its main components. An RF power system (Klystron) feeds the accelerating cavities with the needed energy for acceleration. For efficient transmission, the cavities are vacuumed to the $10^{-7} - 10^{-9}$ hPa level.

Due to the losses in the cavity walls, a cooling system is needed (water for normal conducting cavities and liquid helium for superconducting cavities).

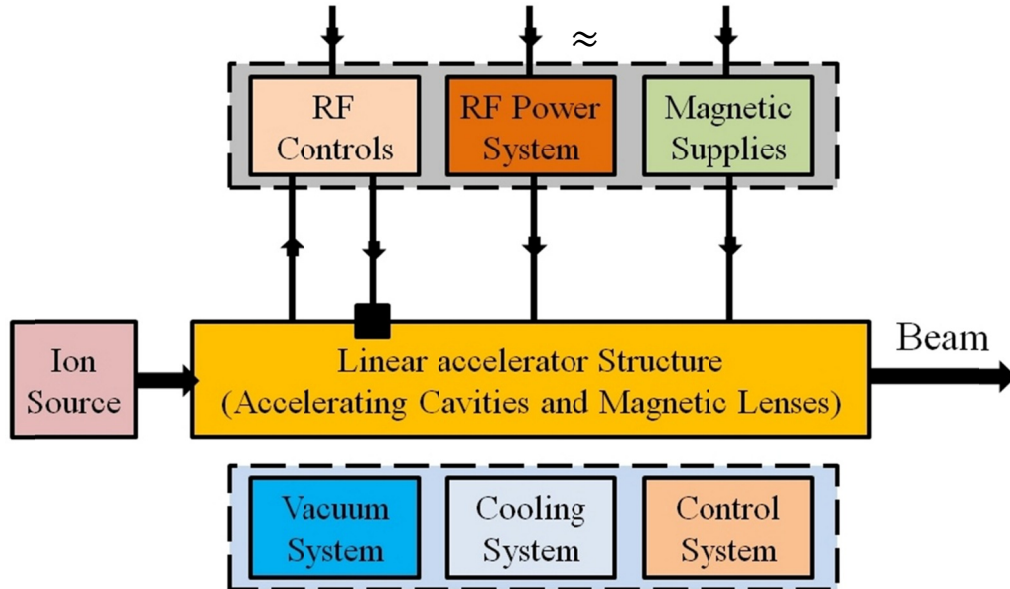


Figure 5.1: Basic block diagram of an RF linear accelerator showing its main components.

Hence, the energy can be transferred to a particle from an EM standing wave in an RF cavity. The axial electric field along the beam axis is given by

$$\mathbf{E}_z(z, t) = E_0(z)\cos(\omega t(z)) \quad (5.1)$$

where $t(z) = \int_0^z \frac{dz}{v(z)}$, the time needed by a particle of velocity $v(z)$ to arrive at position z .

Figure 5.2 shows an accelerating gap of length g , and its on axis field distribution. The field is confined within a distance $L > g$.

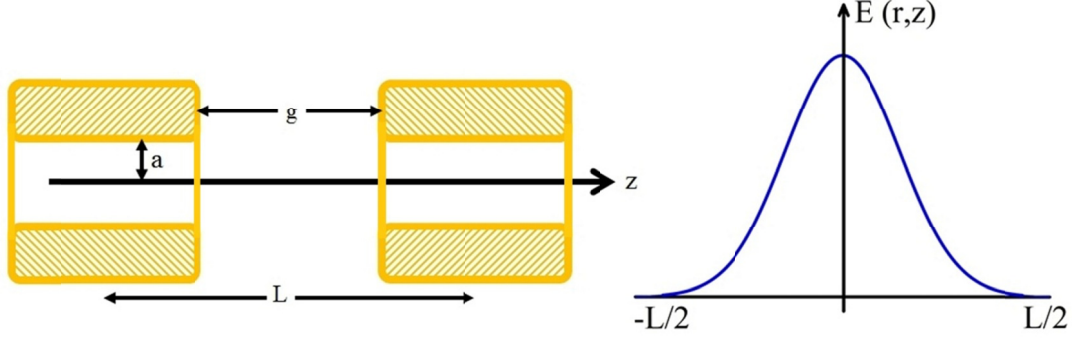


Figure 5.2: Schematic of the geometry (left) and the electric field distribution (right) for an accelerating gap. The length L is standing for the gap effective length where the field distribution is confined within $\pm L/2$ as shown in right of the Figure.

The energy gain of a charged particle with a charge q crossing the gap is

$$\Delta W = q \int_{-\frac{L}{2}}^{\frac{L}{2}} E_0(z) \cos(\omega t(z) + \phi) dz \quad (5.2)$$

Eq. (5.2) can be written in the form

$$\Delta W = qV_0 T \cos\phi \quad (5.3)$$

where $V_0 = \int_{-\frac{L}{2}}^{\frac{L}{2}} E_0(z) dz$ is the gap voltage amplitude along the beam axis, and T is called transit-time factor [207], which represents the ratio of energy gain caused by the sinusoidal RF field to dc voltage of amplitude $V_0 \cos\phi$.

The transit-time factor along the beam axis is defined as [208]

$$T = \frac{\int_{-\frac{L}{2}}^{\frac{L}{2}} E_0(z) \cos \omega t(z) dz}{\int_{-\frac{L}{2}}^{\frac{L}{2}} E_0(z) dz} \quad (5.4)$$

For efficient acceleration in linac, the particle beam must be bunched as shown in Figure 5.3. These bunched may be separated by one or more RF periods.

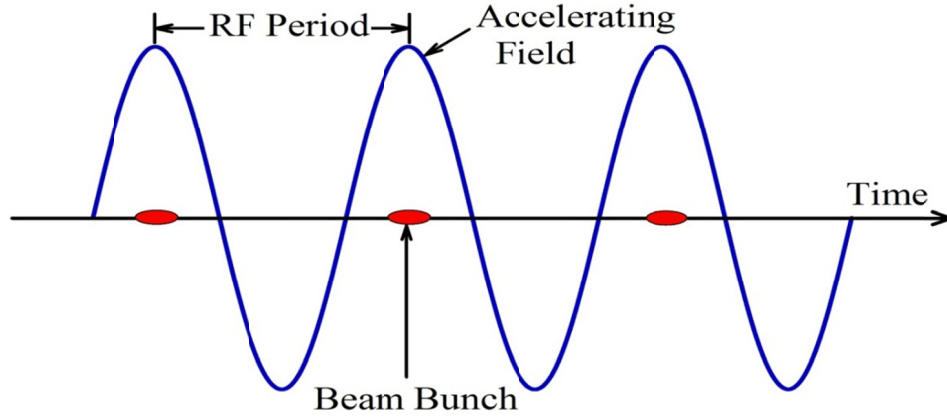


Figure 5.3: Beam bunches in an RF linac for efficient acceleration. The bunches are separated longitudinally by one or more RF periods.

The accelerating cavity is characterized by several parameters, regarding the rf and beam properties.

The first quantity is called the quality factor Q , which is defined by the bandwidth of the resonance frequency. In terms of the energy stored in the cavity W and the dissipative power P , Q can be expressed as

$$Q = \frac{\omega W}{P} \quad (5.5)$$

where ω is the angular resonance frequency.

The definition in equation (5.5) refers to the unloaded cavity which means the reflected power is not included. Hence, the loaded Q-value, Q_l is defined as

$$\frac{1}{Q_l} = \frac{1}{Q} + \frac{1}{Q_{ext}} \quad (5.6)$$

$$Q_{ext} = \frac{\omega W}{P_{ext}} \quad (5.7)$$

where Q_{ext} is the external Q-value, and P_{ext} is the power dissipated in the external load [207].

It is also convenient to define the shunt impedance per unit length, Z . The shunt impedance per unit length measures the effectiveness of producing an axial voltage V_0 for a given dissipated power per unit lengths. Hence, Z can be expressed as

$$Z = \frac{V_0^2}{P \cdot L} = \frac{E_0^2}{P/L} \quad (5.8)$$

In an accelerating cavity, it is aimed to maximize the energy gain per dissipated power. The maximum energy gain is calculated by equation (5.3) for $\Phi = 0$, $\Delta W_{\max} = qV_0T$. In comparison with equation (5.8) one can define a maximum effective voltage for a given dissipated power per unit length as the effective shunt impedance per unit length, Z_{eff} .

$$Z_{eff} = ZT^2 = \left[\frac{\Delta W_{\max}}{q} \right]^2 \frac{1}{P \cdot L} = \frac{[V_0T]^2}{P \cdot L} = \frac{(E_0T)^2}{P/L} \quad (5.9)$$

The units of shunt impedance per unit length and the effective shunt impedance per unit length are $M\Omega/m$.

In the design of normal conducting cavities, one aims to choose the optimum geometry to maximize the effective shunt impedance per unit length. Hence, this leads to maximize the energy gain for a given dissipated power in a given length.

The ratio of effective shunt impedance to the quality factor, is another useful parameter

$$\frac{Z_{eff}}{Q} = \frac{[V_0T]^2}{\omega W} \quad (5.10)$$

This parameter depends only on the cavity geometry and is independent of the power losses. Z_{eff}/Q measures the acceleration efficiency per stored energy at a given frequency.

The power delivered to the beam P_B is calculated as

$$P_B = I \Delta W / q \quad (5.11)$$

where I the beam current, and ΔW is the energy given through the acceleration.

The total power is the sum of beam power and the loss power

$$P_T = P + P_B \quad (5.12)$$

The beam power to total power efficiency is measured by the beam loading parameter,

$$\epsilon_s = \frac{P_B}{P_T} \quad (5.13)$$

The efficiency of the acceleration increases with increasing beam current, up to the current limit of a given structure.

Finally, the dependence of RF parameters mentioned previously, on the operating frequency can be summarized as [208]:

$$P \propto \begin{cases} f^{-\frac{1}{2}} & \text{normal conducting NC} \\ f & \text{super conducting SC} \end{cases} \quad (5.14)$$

$$Q \propto \begin{cases} f^{-\frac{1}{2}} & \text{NC} \\ f^{-2} & \text{SC} \end{cases} \quad (5.15)$$

$$ZT^2 \propto \begin{cases} f^{\frac{1}{2}} & \text{NC} \\ f^{-1} & \text{SC} \end{cases} \quad (5.16)$$

$$\frac{ZT^2}{Q} \propto \begin{cases} f & \text{NC} \\ f & \text{SC} \end{cases} \quad (5.17)$$

Notice that, ZT^2/Q has the same dependency on operating frequency for both normal and superconducting, which is another evidence that ZT^2/Q is independent of the surface properties.

In these scaling's it is assumed that the frequency shift is provided by a scaling of the cavity geometry: Size $\sim 1/f$.

5.2 Beam Dynamics in a Linac

The energy gain of a particle in an RF gap is given by equation (5.3)

$$\Delta W = qV_0 T \cos\phi \quad (5.3)$$

The value of ϕ at which the cavity is designed to operate is called the synchronous phase, ϕ_s . A particle arriving at each gap center with synchronous phase will gain the right amount of energy to maintain synchronism with the field, this particle is called the synchronous particle.

Synchronous phase points $-90^\circ < \phi_s < 0^\circ$ are stable points because particles arriving earlier than the synchronous particle gain less energy, and particles arriving later will gain more

energy, as shown in Figure 5.4. Hence, the particles near by the synchronous particle oscillate around the stable phase point.

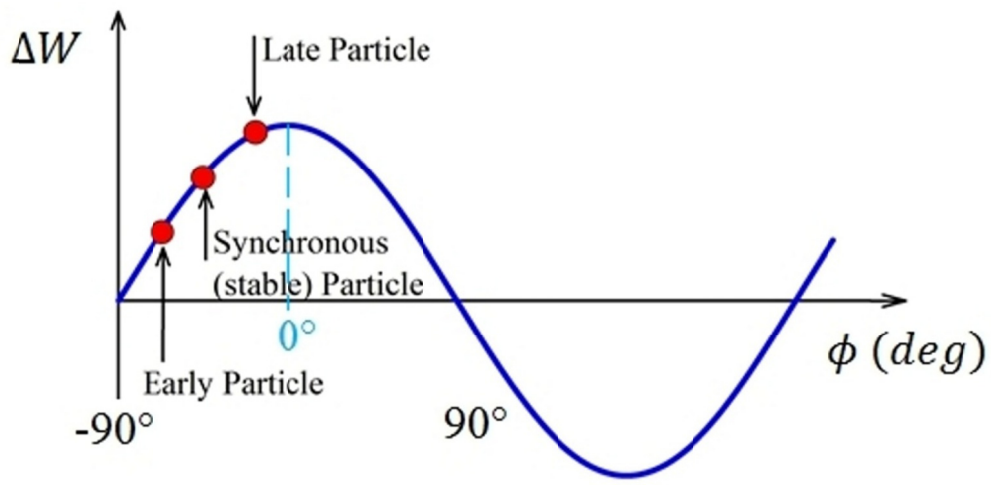


Figure 5.4: Longitudinal focusing is provided by choosing the right phase of the synchronous particle relative to the accelerating wave crest. The synchronous phase point is the stable point because particles arrive earlier than the synchronous particle gain less energy and particles arrive later will gain more energy.

Nevertheless, through the acceleration, an off-axis particle in a gap will experience radial forces (see Figure 5.5). These forces will work as defocusing forces in case of longitudinally focusing synchronous phases.

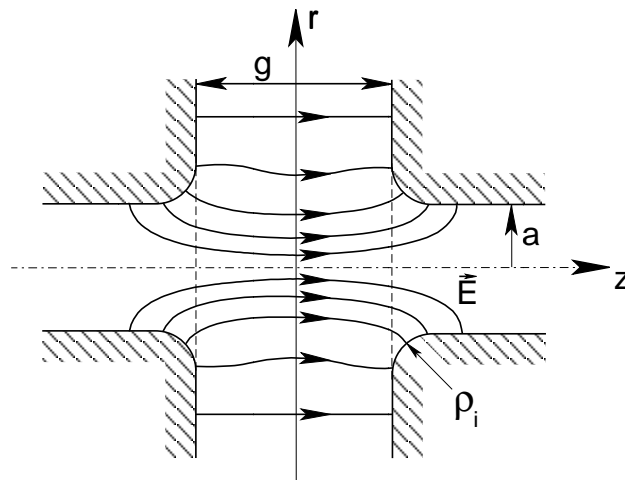


Figure 5.5: Accelerating field lines in an accelerating gap of length g . The off-axis particles in the gap experience radial forces. These forces work like focusing forces in the first half of the gap and as defocusing forces in the second half (Courtesy of U. Ratzinger).

5.2.1 Longitudinal Particle Dynamic

The acceleration of particle bunches in a linac is done by a series of accelerating cells (see Figure 5.6), consisting of drift tubes separated by accelerating gaps. It is assumed in a first order calculation that, the normalized velocity β_{n-1} is constant when the bunch passes from gap center $n-1$ to gap center n . The energy gain in a single gap is assumed to be small against the particle energy.

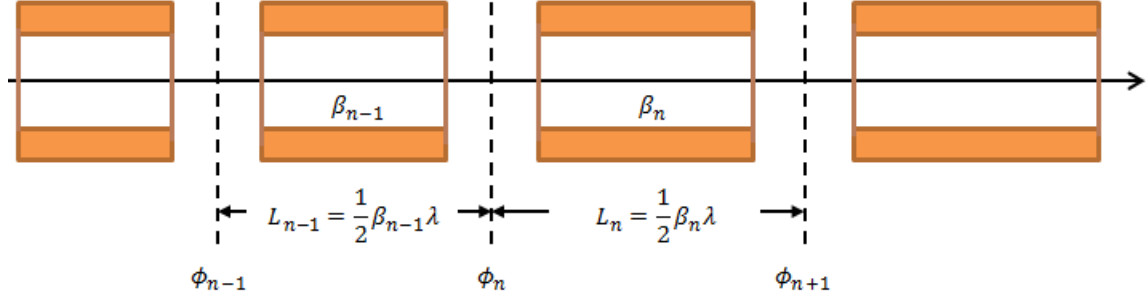


Figure 5.6: A series of accelerating cells describing the longitudinal motion. These cells are consisting of drift tubes separated by accelerating gaps.

The phase, energy and velocity of the synchronous particle in the n^{th} gap express as $\phi_{s,n}$, $W_{s,n}$ and $\beta_{s,n}$, respectively. In similar way, for an arbitrary particle in the same gap one can express its phase, energy and velocity as ϕ_n , W_n and β_n , respectively.

To investigate the motion of particles in phases and energies, it is assumed that the synchronous particle arrive each gap in the correct phase. Hence, the motion in a $\beta\lambda/2$ structure (π -mode) will be investigated.

The particles in the accelerated beam bunch will perform the so – called synchrotron oscillations around the synchronous particle.

These oscillations can be described by the energy and phase difference between an arbitrary particle in the bunch and the synchronous particle ($\Delta W_{i,s} = W_i - W_s$, $\Delta\phi_{i,s} = \phi_i - \phi_s$).

The variation of $\Delta W_{i,s}$ and $\Delta\phi_{i,s}$ along the beam axis s is given as [208]

$$\gamma_s^3 \beta_s^3 \frac{d(\phi - \phi_s)}{ds} = -2\pi \frac{W - W_s}{mc^2 \lambda} \quad (5.18)$$

$$\frac{d(W - W_s)}{ds} = qE_0 T (\cos \phi - \cos \phi_s) \quad (5.19)$$

By differentiate eq. (5.24) and substitute eq. (5.25), one gets a second-order non-linear differential equation for the longitudinal motion, which can be simplified by assuming a slow rate acceleration to

$$\gamma_s^2 \beta_s^2 \frac{d^2(\phi - \phi_s)}{ds^2} = -2\pi \frac{qE_0 T}{mc^2 \lambda} (\cos \phi - \cos \phi_s) \quad (5.20)$$

By using the following notation

$$w = \delta\gamma = \frac{W - W_s}{mc^2}, A = \frac{2\pi}{\beta_s^3 \gamma_s^3 \lambda} \text{ and } B = \frac{qE_0 T}{mc^2} \quad (5.21)$$

With the help of equation (5.20) and equations (5.21), one can obtain

$$\frac{Aw^2}{2} + B(\sin \phi - \phi \cos \phi_s) = \text{const} = H_\phi \quad (5.22)$$

where H_ϕ is a constant and can identify as the Hamiltonian (total energy): the first term is the kinetic energy and the second one is the potential energy.

Thus, the potential energy V_ϕ can be expressed as

$$V_\phi = B(\sin \phi - \phi \cos \phi_s) \quad (5.23)$$

For $-\pi \leq \phi_s \leq 0$, V_ϕ has a potential well (as can be seen in Figure 5.8). The acceleration happens for $-\frac{\pi}{2} \leq \phi_s \leq \frac{\pi}{2}$, thus the stable acceleration occurs for $-\frac{\pi}{2} \leq \phi_s \leq 0$.

The potential V_ϕ has the maximum at $\phi = -\phi_s$, therefore $\phi' = 0$ and $w = 0$.

One can rewrite equation 5.32, by defining the constant H_ϕ at $\phi = \phi_s$, as

$$\frac{Aw^2}{2} + B(\sin \phi - \phi \cos \phi_s) = -B[\sin \phi_s - \phi_s \cos \phi_s] \quad (5.24)$$

Equation (5.24) represents the separatrix equation which separates the longitudinal phase space into a stable and an unstable region.

The maximum particle energy on the separatrix occurs at $\phi = \phi_s$. Hence, solving the equation of separatrix at $\phi = \phi_s$ leads to

$$w_{max} = \frac{W - W_s}{mc^2} = \sqrt{\frac{2qE_s T \beta_s^3 \gamma_s^3 \lambda}{\pi mc^2} (\phi_s \cos \phi_s - \sin \phi_s)} \quad (5.25)$$

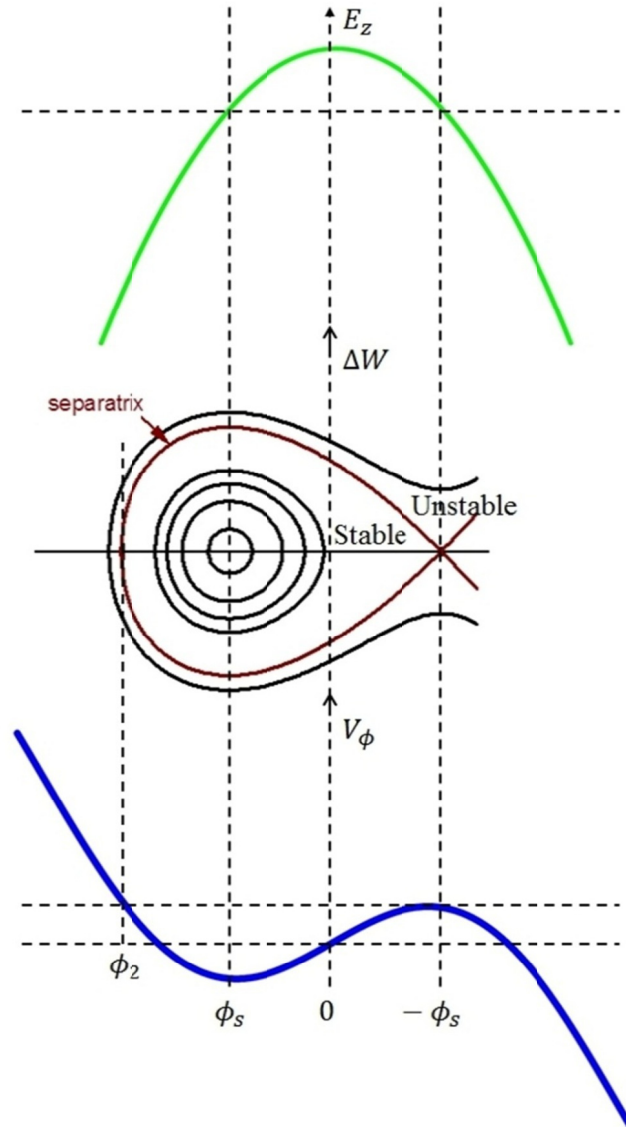


Figure 5.7: At the top, the accelerating electric field E_z is shown as a function of the phase ϕ ; the synchronous phase ϕ_s is shown as a negative value. Thus, the longitudinal potential V_ϕ has its minimum at $\phi = \phi_s$ as shown in the bottom. The particle trajectories in the longitudinal phase space are shown in the middle. Here, the separatrix is dividing the motion in the longitudinal phase space into a stable (inside the separatrix) and unstable (outside the separatrix) area.

5.2.2 Transverse Beam Dynamics

The off-axis particles experience radial electric forces. For longitudinal stability ϕ_s must be negative, this means the majority of particles experience higher fields in the second half gap

resulting in a net defocusing force. This defocusing force appears as soon as there is a net focusing longitudinal force.

The Maxwell's equations in cylindrical coordinates with azimuthal symmetry and with absence of charge and current sources in the gap can be written as

$$\nabla \cdot \mathbf{E} = 0 \quad \rightarrow \quad \frac{1}{r} \frac{\partial(rE_r)}{\partial r} + \frac{\partial E_z}{\partial z} = 0 \quad (5.26)$$

$$\nabla \times \mathbf{B} = \frac{1}{c^2} \frac{\partial \mathbf{E}}{\partial t} \quad \left\{ \begin{array}{l} (\nabla \times \mathbf{B})_z = \frac{1}{c^2} \frac{\partial E_z}{\partial t} \rightarrow \frac{1}{r} \frac{\partial(rB_\theta)}{\partial r} = \frac{1}{c^2} \frac{\partial E_z}{\partial t} \quad z - \text{component} \\ (\nabla \times \mathbf{B})_r = \frac{1}{c^2} \frac{\partial E_r}{\partial t} \rightarrow -\frac{\partial B_\theta}{\partial z} = \frac{1}{c^2} \frac{\partial E_r}{\partial t} \quad r - \text{component} \end{array} \right. \quad (5.27)$$

$$\nabla \times \mathbf{E} = -\frac{\partial \mathbf{B}}{\partial t} \quad \rightarrow \quad \frac{\partial E_r}{\partial z} - \frac{\partial E_z}{\partial r} = -\frac{\partial B_\theta}{\partial t} \quad (5.28)$$

Notice that, only E_z and E_r are non-zero field components.

Assuming that near the axis E_z is independent of r , equations (5.26) and (5.27) can be integrated to have

$$E_r = -\frac{r}{2} \frac{\partial E_z}{\partial t} \quad (5.30)$$

and

$$B_\theta = -\frac{r}{2c^2} \frac{\partial E_z}{\partial t} \quad (5.31)$$

Hence, the radial momentum component near the axis is

$$\Delta p_r = \int_{-\frac{L}{2}}^{\frac{L}{2}} q(E_r - \beta c B_\theta) \frac{dz}{\beta c} \quad (5.32)$$

where dt replaced by $dz/\beta c$ and $v_z = \beta c$.

Using equations (5.30) and (5.31) to substitute into equation (5.29), we get

$$\Delta p_r = -\frac{q}{2} \int_{-\frac{L}{2}}^{\frac{L}{2}} r \left(\frac{\partial E_z}{\partial z} + \frac{\beta}{c} \frac{\partial E_z}{\partial t} \right) \frac{dz}{dt} \quad (5.33)$$

To simplify equation (5.33), it is useful to use

$$\frac{dE_z}{dz} = \frac{\partial E_z}{\partial z} + \frac{1}{\beta c} \frac{\partial E_z}{\partial t} \quad (5.34)$$

The electric field E_z near the axis looks like

$$E_z = E_0 \cos(\omega t + \phi) \quad (5.35)$$

Now, one can use equations (5.34) and (5.35) and the definition of T to get

$$\Delta p_r = -\frac{q\pi E_0 T L \sin\phi}{\gamma^2 \beta^2 \lambda c} r \quad (5.36)$$

In case of $\phi = \phi_s$ we obtain

$$\Delta p_r = -\frac{q\pi E_0 T L \sin\phi_s}{\gamma^2 \beta^2 \lambda c} r \quad (5.37)$$

In the previous section, the longitudinal stable motion is happened when $-\frac{\pi}{2} \leq \phi_s \leq 0$, but this leads to defocus the beam.

In conclusion, the phase stable acceleration which happened for $-\frac{\pi}{2} \leq \phi_s \leq 0$, giving a positive RF deflection.

In order to compensate this rf defocusing in the linac, it is needed to use a focusing devices like magnetic lenses. The quadrupole lenses are the most common.

In Alvarez structure, the quadrupoles are inserted within the drift tubes. This will reduce the RF efficiency of the cavity. In order to overcome this problem, one option was to invent a new structure with a lake of internal focusing element in the RF cavity.

The focusing elements are installed between the cavities. H-type cavity is an example on this structure.

5.3 H- type Cavities

H-type cavities are characterized by the direction of the RF magnetic field, which is parallel and antiparallel with respect to the beam axis [74-76, 209-214]. Closed field loops are provided by connecting field lines with opposite orientation at the cavity ends. These cavities are operating in transverse-electric (TE)-mode structure (known also as H-mode).

Solving the Maxwell equations in a cylindrical cavity of radius R and length L lead to [213]

$$H_{z(m,n,l)} = H_0 J_m(k_c r) \cos m\phi \cdot \sin k_z z \quad (5.38)$$

$$H_{\phi(m,n,l)} = \frac{H_0 \cdot k_z \cdot m}{k_c^2} \cdot \frac{1}{r} \cdot J_m(k_c r) \cdot \sin m\phi \cdot \cos k_z z \quad (5.39)$$

$$H_r(m,n,l) = \frac{H_0 \cdot k_z}{k_c} J'_m(k_c r) \cos m\phi \cdot \cos k_z z \quad (5.40)$$

$$E_{\phi(m,n,l)} = \frac{H_0 \cdot Z_0 \cdot k}{k_c} \cdot J'_m(k_c r) \cdot \cos m\phi \cdot \sin k_z z \quad (5.41)$$

$$E_r(m,n,l) = \frac{H_0 \cdot Z_0 \cdot k \cdot m}{k_c^2} J_m(k_c r) \cdot \sin m\phi \cdot \sin k_z z \quad (5.42)$$

where J_m is the Bessel's function of order m , J'_m is the first derivative of the Bessel's function and (m, n, l) are integers defining the excited mode.

The wave number k , k_z and k_c are defining as

$$k^2 = k_c^2 + k_z^2 \quad (5.43)$$

$$k_z = \frac{l \cdot \pi}{L} \quad l = 0, 1, 2 \quad (5.44)$$

$$k_c = \frac{x'_{mn}}{R} \quad (5.45)$$

where x'_{mn} is the n th zero of J'_m .

The H-type structures have excellent properties which make them attractive for low and medium β – acceleration. The RF efficiency, beam quality and operation reliability are the main aspects in any linac structure. The H-type shows excellent behavior in these aspects. Table 5.1 shows the comparison between the Alvarez-DTL and H-type structure.

Table 5.1: A comparison between Alvarez drift tube linac and H – type DTL.

Structure	Alvarez	H-type
Field mode	TM	TE
Structure mode	2π	π
Frequency range [MHz]	100 – 400	30 – 800
Period length	$\beta\lambda$	$\beta\lambda/2$
β - range	≤ 0.5	≤ 0.5
Max. accelerating gradient [MV/m]	4	10.7 for IH [215]
Availability*	RT	RT & SC

* This refers to the material type where RT and SC stand for room temperature (normal conductor) and Superconducting, respectively.

The capability to reduce the capacitance between the drift tubes was used in H-type DTL's. This will lead to an increase of the shunt impedance (see Figure 5.8) [212-213]. At the same time, high field gradients (up to 10 MV/m in IH-DTL [215]) can be reached. A schematic of a H-type linac structure period applying the KONUS – beam dynamics [74-76, 211-214] is shown in Figure 5.9. A brief description of the KONUS – beam dynamics will be given in section 5.4.

A sequence of drift tubes without focusing elements is used. The focusing quadrupoles (usually triplets) are installed at the end of each accelerating drift tube section. The other quantities that characterize this design in comparison with other structure are the high mechanical robustness and a very efficient cooling [74-76, 210-213]. Figure 5.10 shows the versions of RFQ's and DTL's for the H_{110} -mode and H_{210} -mode [210].

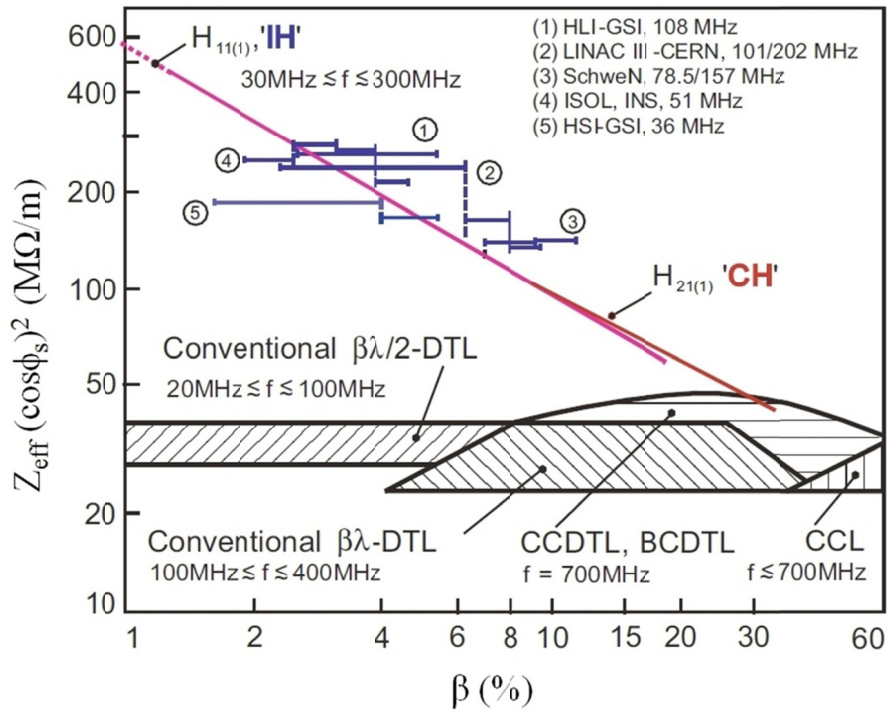


Figure 5.8: Effective shunt impedance for different rf structures including the transit time factor T and the synchronous phase ϕ as a function of the particle velocity $\beta = v/c$. The black horizontal bars represent some existing IH-DTLs and the red bars represent the expected shunt impedance of the rt CH cavities for the GSI-FAIR 70 MeV, 70 mA proton linac (Courtesy of U. Ratzinger and R. Tiede).

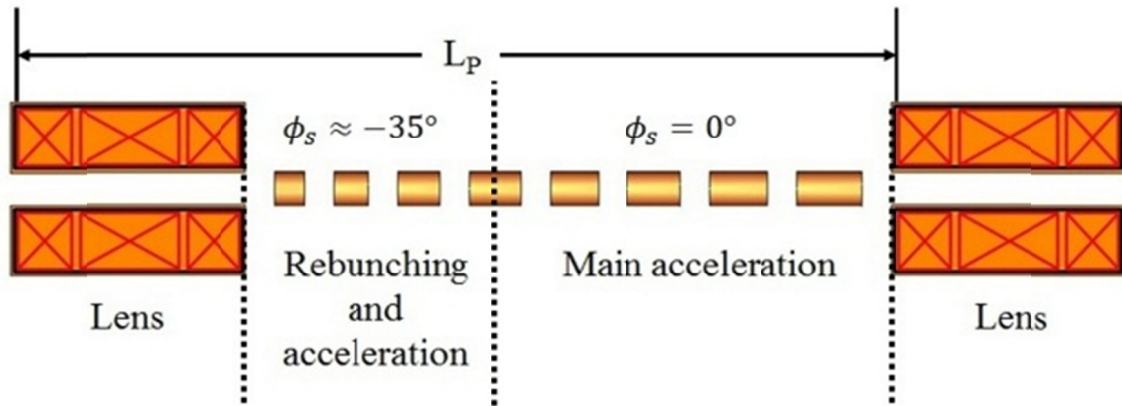


Figure 5.9: A scheme of the H-DTL, showing the separated function principle KONUS – beam dynamics with respect to acceleration and beam focusing.

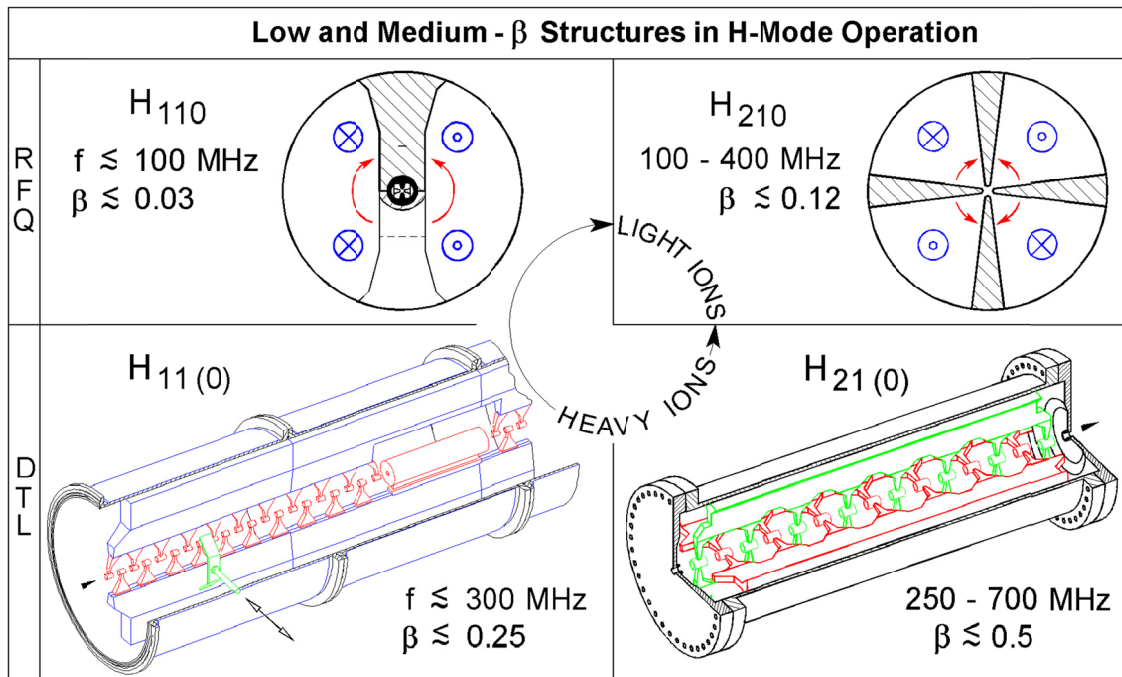


Figure 5.10: The H – mode structure family. The main direction of the magnetic RF field is oriented parallel or antiparallel with respect to the beam axis (Courtesy of U. Ratzinger).

5.3.1 Interdigital H-type DTL (IH-DTL)

The Interdigital H-type drift tube structure (IH, H_{110} -mode) was pointed out as a solution for proton acceleration up to 30 MeV by J.P. Blewett in the CERN Symposium in 1956 [216].

After that, several improvements and developments were achieved in H-type linacs in different projects [74-76, 210-213, 217-231].

The empty H-mode cavity is excited in the H_{111} -mode. Hence, the longitudinal electric field E_z is zero and the acceleration is provided by the drift tube structure [74-76, 209-210, 213], as can be seen in Figure 5.11.

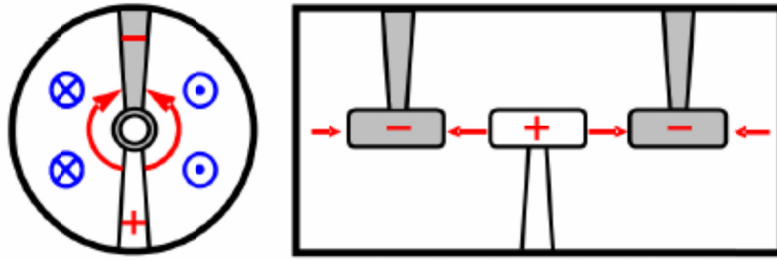


Figure 5.11: Scheme of an Interdigital H-mode structure (IH) showing the electric field lines in red and the magnetic field lines in blue (Courtesy of R. Tiede).

The resonance frequency for empty H-type cavities is given by

$$f_{H_{mnl}} = \frac{\omega_{mnl}}{2\pi} = c * \sqrt{\left(\frac{x'_{mn}}{2\pi R}\right)^2 + \left(\frac{l}{2L}\right)^2} \quad (5.61)$$

where c the speed of light, x'_{mn} the zeros of the derivative of the Bessel functions J'_m (for IH: $x'_{11} = 1.841$, and for CH: $x'_{21} = 3.054$ [210]), L and R are the length and radius of a cylindrical cavity, respectively.

For example, the IH-DTL cavity no. 2 for the CERN-LINAC3 [210, 213, 215] is shown in Figure 5.12 and has a length of 1.43m and a radius of 173 mm.

The resonance frequency for the empty cylinder is 570.46 MHz compared with the measured operating frequency of 202.56 MHz, which is less than 36% of the corresponding value. Hence, this reduction is due to the extra capacitance between the drift tubes.

For a resonance frequency higher than 300 MHz, the dimensions of an IH structure will be too small and it will not be possible to make a realistic design. Thus, the crossbar H-type (CH-DTL) structure can be used at higher frequencies.

IH - Cavity, $H_{11(0)}$, 202 MHz

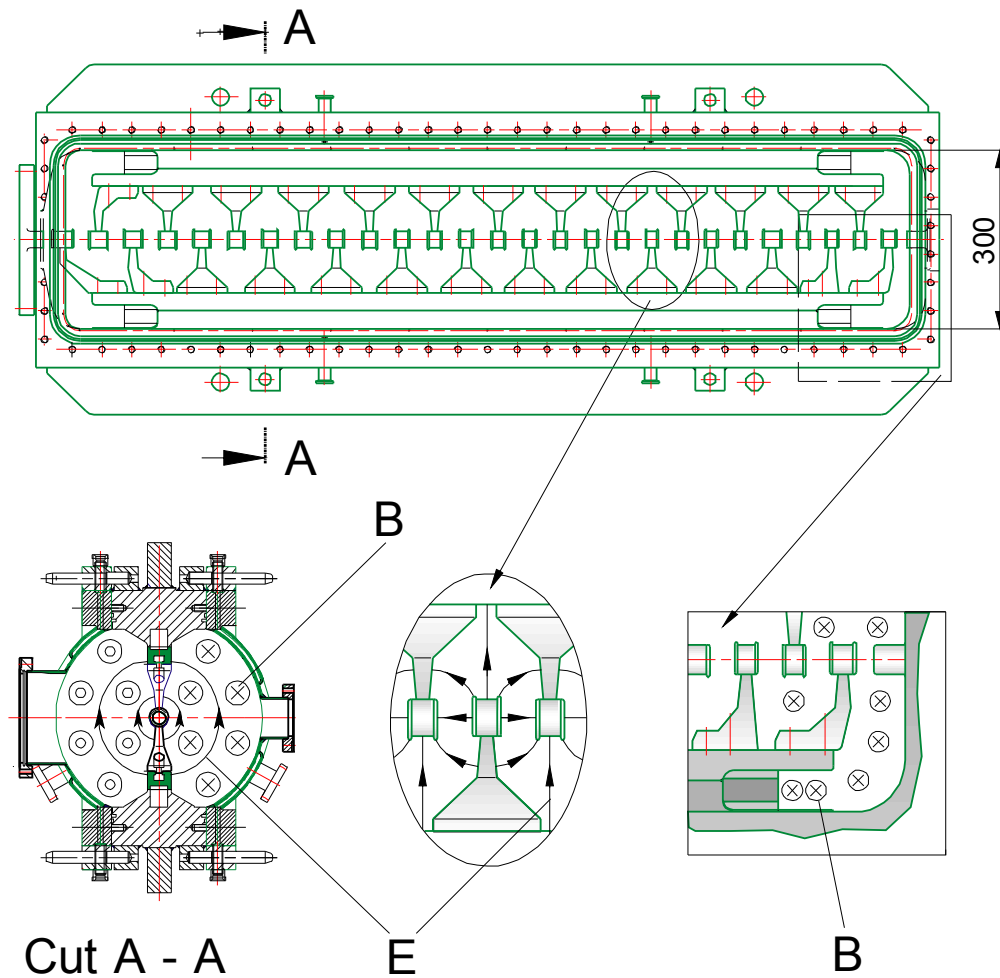


Figure 5.12: IH – DTL for the CERN LINAC 3 lead injector showing a detail of the electric and magnetic field distributions inside the cavity (Courtesy of U. Ratzinger).

5.3.2 Crossbar H-type DTL (CH-DTL)

For frequencies > 250 MHz, the dimensions of the IH are too small and in terms of mechanical construction the cavity design is not attractive. So, one can consider to excite higher H-modes, H_{n10} .

H_{mn} – modes show higher frequencies at a given tank radius for higher m . On the other hand, the structure gets more complex. The H_{21} – mode with two stems per drift tube seems to be attractive for medium β – profiles. The cavity operated in this mode is called a Crossbar H-type structure (CH-DTL) [74-76, 210, 212-214, 227]. In this mode, the operation frequency can reach up to 800 MHz [210, 212-213].

In the CH-DTL, the orientation of each two neighboring stems at 90° is responsible for the mechanical robustness of the structure, and it generates the accelerating electric field (Figure 5.13). This configuration makes the cavity easy to cool by water. Therefore, the CH-structure is a good option for high duty factor or cw applications.

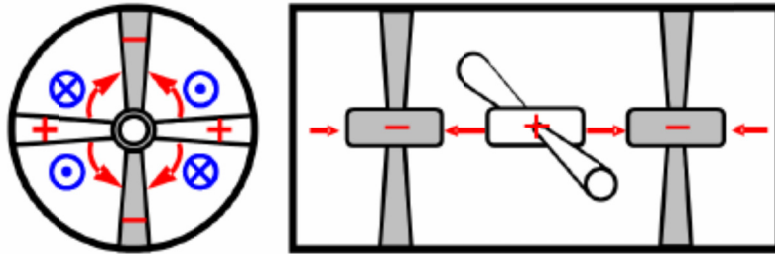


Figure 5.13: Schematic diagram of a Crossbar H-mode structure (CH) showing the electric field lines in red and the magnetic field lines in blue (Courtesy of R. Tiede).

The proton injector for the FAIR facility [76, 232-234] (Facility for Antiprotons and Ion Research) is based on the CH-DTL [76, 235-236]. Figure 5.14 shows the accelerator chain of GSI and of the FAIR facility.

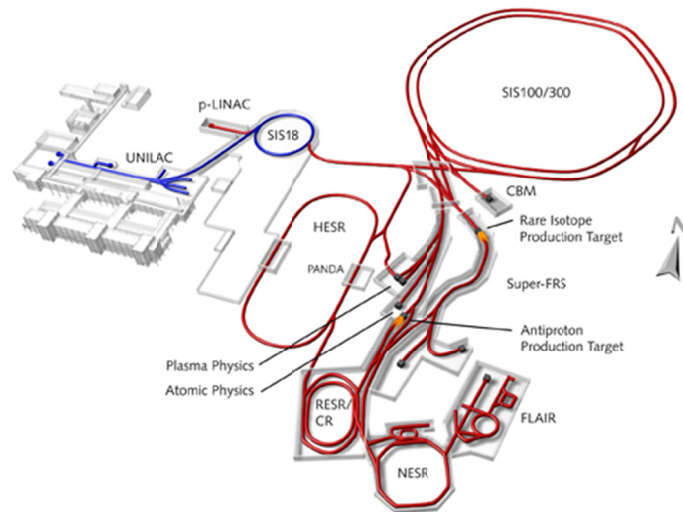


Figure 5.14: Schematic for the accelerator chain in GSI and FAIR facility [214].

The proton linac for the FAIR project will be the first linac based on CH-structures. Six CH modules are needed to accelerate a 70 mA proton bunch from 3 MV to the final energy of 70 MeV, where the beam is injected into the SIS18 [76, 214, 235, 237-238].

The first room temperature CH cavity is under construction at IAP-Frankfurt [76, 214, 235, 237, 239-240]. This cavity consists of 27 gaps within two sections coupled by a coupling cell containing a triplet quadrupole. It will accelerate the proton beam from 11.7 to 24.3 MeV within 2.8 m inner length (Figure 5.15).

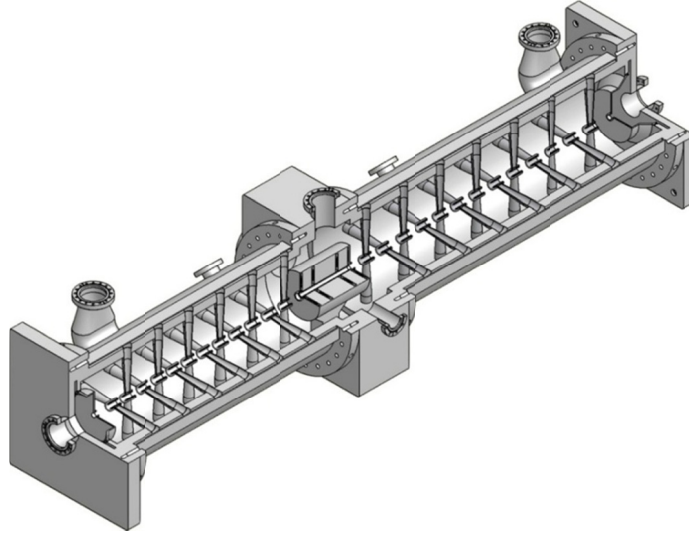


Figure 5.15: 3D view on the second coupled CH – cavity for the FAIR proton injector. This cavity consists of 27 gaps within two sections coupled by a triplet quadrupole and accelerates the proton beam from 11.7 to 24.3 MeV within 2.8 m inner length (Courtesy of R. Brodhage).

The main parameters of the coupled CH-prototype are summarized in table 5.2 [76].

Table 5.2: The main parameters of the second CH cavity of the FAIR proton injector.

No. of Gaps	27
Frequency (MHz)	325.2
Energy Range (MeV)	11.7 - 24.4
Beam Loading (kW)	882.6
Heat Loss (MW)	1.35
Total Power (MW)	2.2
Q ₀ -Value	15300
Effective Shunt Impedance (MΩ/m)	60
Average E ₀ T (MV/m)	5.8 – 6.4
Kilpatrick Factor	2.0
Coupling Constant (%)	0.3
No. of Plungers	11
Beam Aperture (mm)	20
Inner Total Length (mm)	3000

5.4 KONUS Beam Dynamics and LORASR Code

In section 5.2 it was shown that, in conventional DTL's the synchronous phase of an accelerating gap should be negative for a longitudinal stable motion. This causes a defocusing in transverse direction and therefore additional focusing elements are housed in the drift tubes. This will limit the achievable accelerating gradient and reduce the shunt impedance.

An alternative focusing scheme proposed by U. Ratzinger to solve this problem, was the KONUS (Kombinierte Null grad Struktur – Combined Zero Degree Structure) beam dynamics concept [74-76, 211-214, 241]. The main idea of the KONUS beam dynamics is to apply the 0° synchronous phase in the accelerating gap to maximize the acceleration efficiency, and thus minimize the defocusing in transverse planes.

Figure 5.16 shows a comparison between the particle trajectories in longitudinal phase space at different values of the synchronous phase $\phi_s = -30^\circ, -90^\circ$ and 0° . Obviously, at $\phi_s = 0^\circ$ the separatrix does not exist (shrinks to zero) and full field will be used for acceleration. Figure 5.17 explains the difference to the KONUS structure.

In the absence of a separatrix, the quasi stable area in longitudinal phase space which can be used by KONUS is marked with dark arrows in Figure 5.18 [213].

The KONUS period consists of three sections with different purposes (see Figures 5.9, 5.19). These sections are

- 1- A transverse focusing magnetic lens (a quadrupole triplet in case of room temperature cavity or a solenoid in case of superconducting cavity).
- 2- A short rebunching section with a negative synchronous phase for longitudinal matching.
- 3- A main acceleration section with a multi – cell 0° - synchronous phase.

The main acceleration section in KONUS beam dynamics is defined by a zero degree synchronous particle, the beam is injected to this section with a surplus in energy against the synchronous particle.

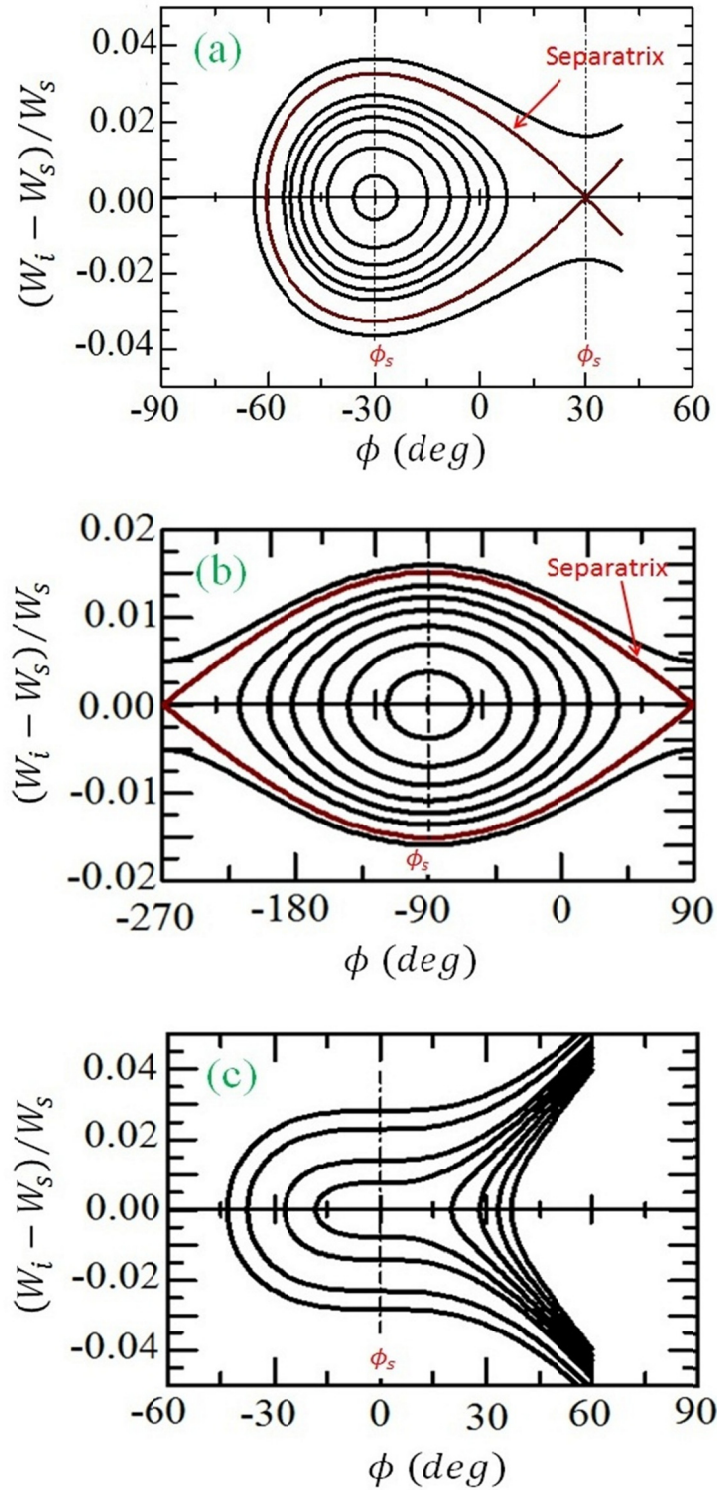


Figure 5.16: Particle trajectories in longitudinal phase space at different values of synchronous phase $\phi_s = -30^\circ$ (a), -90° (b) and 0° (c) (Courtesy of R. Tiede).

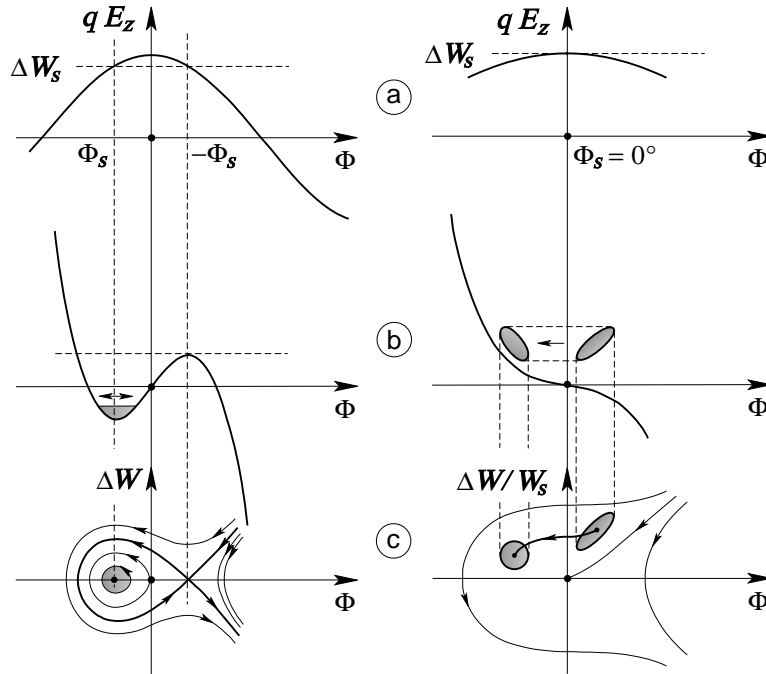


Figure 5.17: Comparison of the longitudinal particle motion at two synchronous phase values; a negative synchronous phase (left) and zero synchronous phase (right). The accelerating field is shown as a cosine function of the phase (a), the longitudinal potential well (b) and the longitudinal phase – space trajectories are shown in (c) (Courtesy of U. Ratzinger).

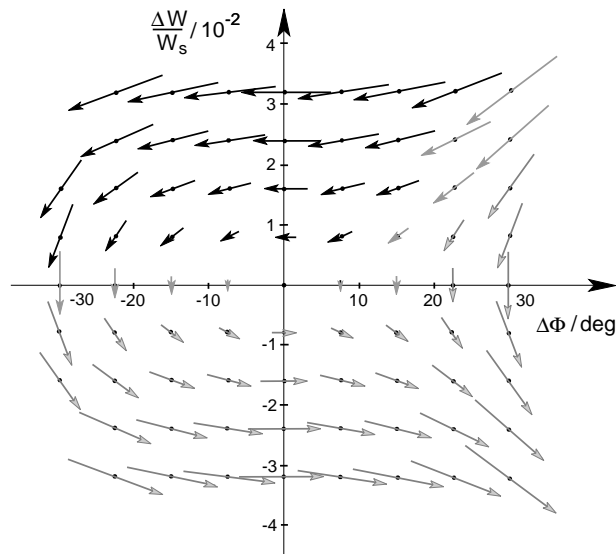
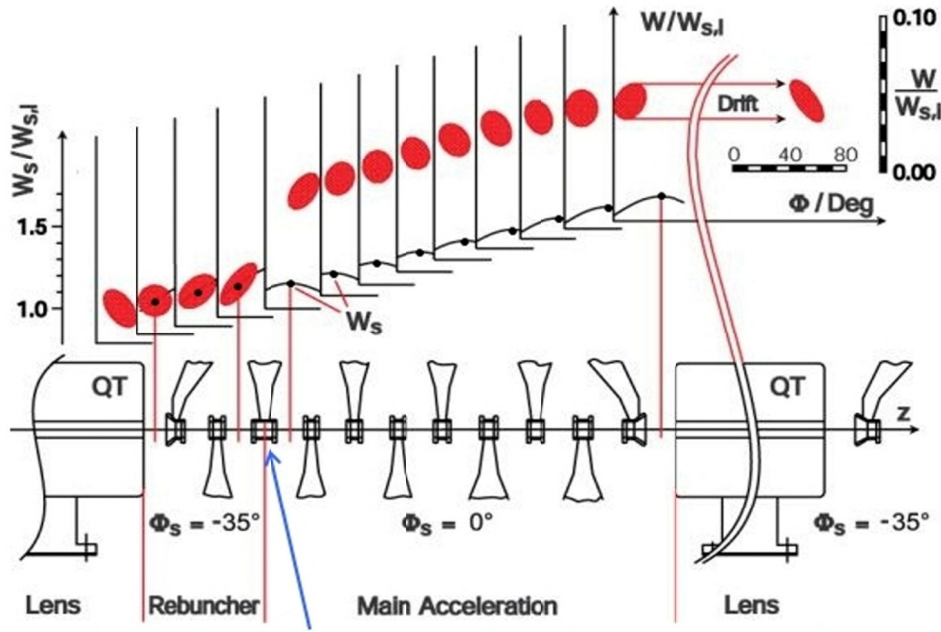


Figure 5.18: Flowchart of single particle motion in the longitudinal phase space for $\phi_s = 0^\circ$. Stable area in longitudinal phase space which can be used by KONUS is marked with dark arrows (Courtesy of U. Ratzinger).



Phase shift at transition: rebunching $\rightarrow 0^\circ$ section

Figure 5.19: Schematic of the KONUS period showing its main sections; focusing magnetic lenses, rebuncher sections with a negative synchronous phase and main acceleration section with a zero synchronous phase. On the top, the bunch motions in phase space reflecting the KONUS beam dynamics (Courtesy of U. Ratzinger).

The motion in the longitudinal phase space will be counterclockwise. The longitudinal by stable motion occurs mainly along the second quadrant. Hence, before the bunch would enter the third quadrant, the drift tube structure is ended and followed by a focusing triplet quadrupole for a focusing in transverse planes.

After that, in order to avoid longitudinal defocusing and to rebunch the beam, the focusing element followed by a short rebuncher section with a negative synchronous phase.

The KONUS beam dynamics is designed by using of the LORASR code [74, 2132, 241]. LORASR (Longitudinale und Radiale Strahldynamikrechnungen mit Raumladung) was invented in Munich and further developed at GSI and IAP Frankfurt University. It is especially suited for accelerator designs of the $\beta\lambda/2$ – type involving slim drift tubes which carry no focusing elements. The space charge solver routine was also implemented in this code [213, 241]. A full description of the LORASR code can be found in references [213, 241].

The IH cavity of the GSI HLI injector was the first one applying this beam dynamics with the three structure sections as explained before. The longitudinal and transversal beam envelopes along the cavity are shown in Figure 5.20.

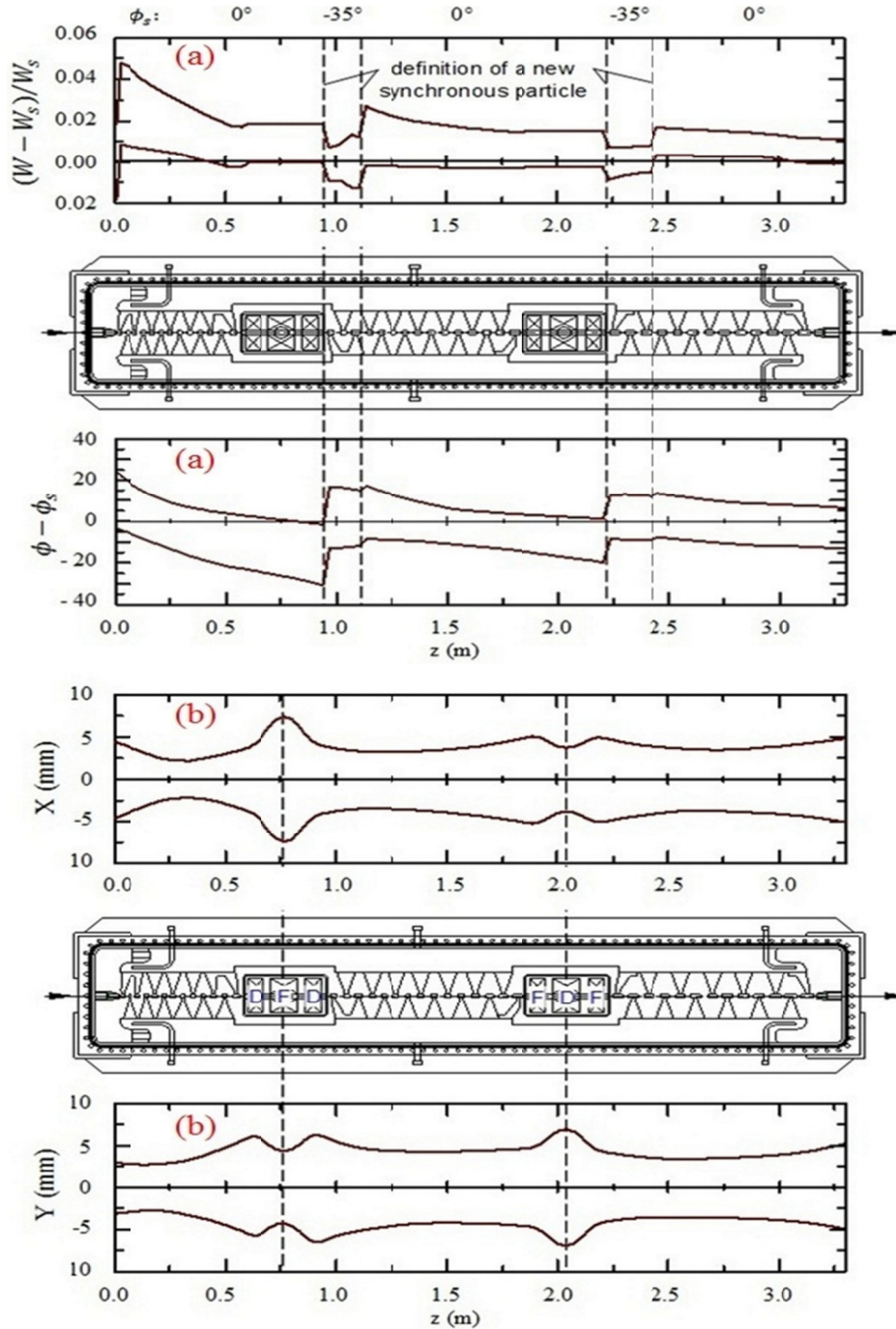


Figure 5.20: The beam envelopes in longitudinal (a) and transversal (b) planes along the IH-DTL cavity of the GSI HLI injector. The plots reflect the KONUS beam dynamics (Courtesy of R. Tiede).

5.5 Superconducting CH – DTL

Different types of superconducting cavities for low and medium energy $\beta < 0.5$ have been developed for ion and proton accelerators. Several projects like EUROTRANS [242], IFIMF [225, 243], RIA [244], SPIRAL-2 [245] and TRASCO [246] require high duty cycles or cw operational mode. The higher reliability and low operational cost make the superconducting option favorable compared to room temperature versions.

Many types of superconducting cavities have been developed for recent projects. But there are still many attempts worldwide to improve the low and medium β – structures.

The design of the superconducting CH-structure [212, 247-253] was motivated by the aim to create an efficient low β – multi-cell structure.

The geometry of a superconducting CH-cavity is quite different from the room temperature CH cavity to reduce the electric and magnetic peak fields [249, 251].

In the superconducting CH the surface magnetic field must be reduced to minimize the surface current. If the magnetic field is reaching its critical value a quench will happen [253].

Figure 5.21 shows the first superconducting CH-DTL. A 360 MHz superconducting CH-DTL has been developed at IAP Frankfurt and was fabricated at ACCEL Company [212, 251]. The cavity is designed for low energy protons $\beta < 0.1$ with 19 cells. This cavity has a length of 105 cm and diameter of 28 cm, and it was fabricated from 2 mm thick bulk niobium sheets (RRR=250)[212, 247]. Many cryogenic tests have been performed at IAP-Frankfurt University since 2005 [74, 212].

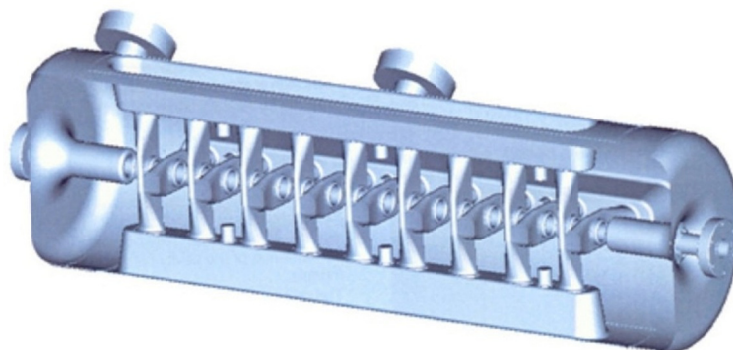


Figure 5.21: Superconducting CH – DTL (Courtesy of U. Ratzinger).

The maximum acceleration gradient which has been measured for this cavity is 7 MV/m between end gaps as shown in Figure 5.22. This corresponds to an effective accelerating

voltage of 5.6 MV and to a peak surface electric field of 36 MV/m. The Q -value at low field level was about 8×10^8 which gives a surface resistance of 88 n Ω [248].

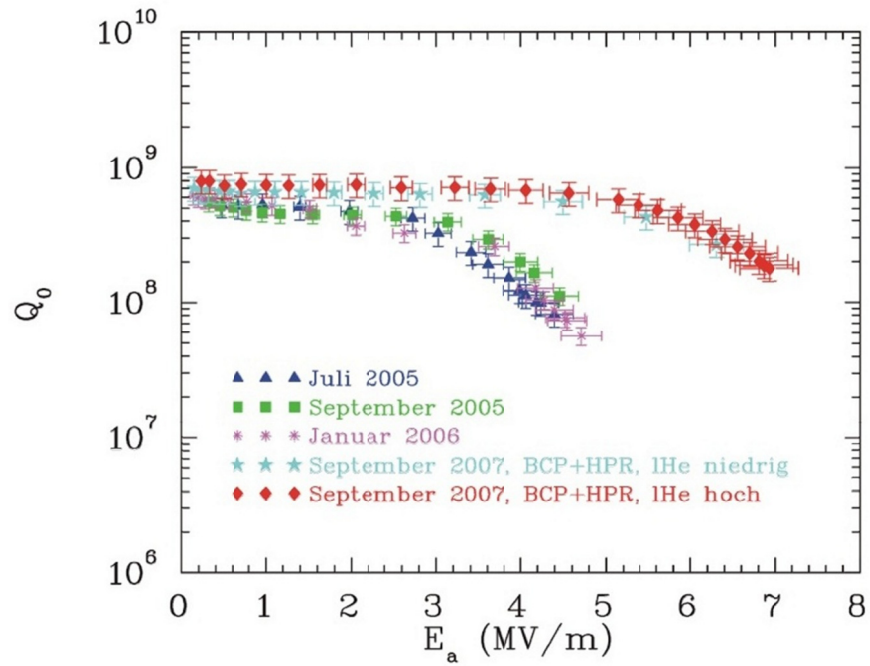


Figure 5.22: Dependence of the measured quality factor – Q_0 for the superconducting CH – DTL on the accelerating field gradient E_a (Courtesy of H. Podlech).

CHAPTER 6

DEVELOPMENT AND MATCHING OF A DEDICATED CH- LINAC FOR INTENSE LASER – ACCELERATED PROTON BUNCHES

Laser – accelerated protons possess interesting properties in terms of energy, emittance and proton number per bunch which make them competitive to conventional proton sources in some cases. The important topic for a further acceleration of these protons is the matching into the acceptance of a conventional RF accelerator. This kind of hybrid proton accelerator will benefit from the interesting features of the laser based source and from the flexibility of RF based accelerator structure.

Such a combination will give us the chance for a further acceleration and control of the laser – accelerated protons by conventional accelerator structures which adapt the beam to fulfill the required parameters for different applications.

Due to the available energies, drift tube linacs are the most adequate choice for this purpose. The coupling between laser – accelerated protons and a conventional drift tube linac – DTL was discussed and studied numerically [19, 48, 59, 69-71, 151, 254]. In this work, a crossbar H-type (CH) structure is suggested as the linac structure [196-198].

The laser generated proton bunch is expected to have small emittance values initially when compared to conventional accelerators, at an extremely high proton number per bunch. To compare the beam dynamics in each bunch with conventional bunch trains, one has to take the beam current resulting from a cw linac operation with all rf buckets filled with the same particle number. The resulting equivalent beam current to be used for beam dynamics calculations is then

$$\bar{I}_b = N_p \cdot f \cdot e \quad (6.1)$$

For example, in our case 10^{10} protons in the laser generated bunch can be detected in the energy band $10 \text{ MeV} \pm 0.5 \text{ MeV}$. These protons will be injected into a 325 MHz CH-DTL, the corresponding averaged beam current corresponds then to $\bar{I}_b = 520 \text{ mA}$. This may be

compared to 100 mA beam current which is state of the art in conventional injector techniques.

Ref [59, 254] is an early publication about the RF post-acceleration topic: A 7 MeV laser generated proton pulse is matched by a 1.8 m long matching section with five quadrupoles to a 6 m long 7 MV Alvarez type DTL.

In the present work, the capabilities of a CH – linac for the post-acceleration of laser generated proton pulses are investigated [71, 196, 198].

6.1 Dedicated CH – linac Design for Laser- Accelerated Proton Bunch

The proton bunch generated by the laser has unique features in terms of emittance and proton number per bunch. In chapter 3, it was shown that the protons located in the energy band $10 \text{ MeV} \pm 0.5 \text{ MeV}$ are quite affected by the co-moving electrons. Due to the large beam divergence and high space charge forces, it was finally not possible to accept all protons in the desired energy band. The acceptance of the CH- DTL was chosen large enough to fit to the laser generated bunch and to limit the further emittance growth along the rf linac.

The layout of the CH – DTL (Figure 6.1) was performed in two main steps [198]. At first a 500 mA equivalent beam current design was developed. In a second step, this linac layout was used to simulate the acceleration of the laser generated bunch.

Indeed, the initial beam emittance values of the laser – accelerated protons are smaller than the values for conventional linacs, but as a consequence the space charge forces become much bigger (chapter 3.4). It is shown in the following that the beam emittance of the laser – accelerated bunch in front of the linac was too big for full transmission.

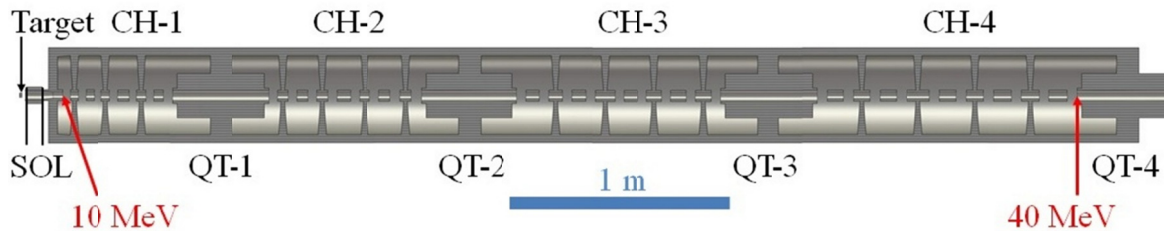


Figure 6.1: 3D view on the proposed CH- DTL consisting of four RF- cavities separated by triplet quadrupoles. In front of the first cavity, the pulsed solenoid is located and the distance between the end edge of the solenoid and the center of the first gap is 103 mm.

The bunch transport from the target position up to the CH- DTL entrance through the pulsed magnetic solenoid was simulated using the LASIN code (chapter 3). The following beam dynamics studies for longitudinal and transverse planes along the linac were performed by the LORASR code.

This design consists of four CH-DTL cavities with gap numbers varying from 7 to 10 gaps and operating at 325 MHz . It will accelerate up to 10^{10} protons per bunch from 10 MeV to 40 MeV. The cavities consist of 34 gaps within a total length of about 5.1 m and the average accelerating gradient per cavity varies from 7.00 MV/m to 12.61 MV/m. The high field gradient in the first cavity (12.61 MV/m) is attractive in order to compensate the space charge forces at 10 MeV energy. Hence, in order to get a robust longitudinal bunch focusing and to prevent beam losses, high gap voltages of typically 1 MV are applied. The drift tube aperture diameter is 30 mm along the central part of each cavity and up to 36 mm close to the lenses. The lens aperture diameter is 50 mm.

The calculated effective gap voltage distribution along the CH- structure is roughly uniform within each section and has the minimum near the quadrupoles. It was varied from 0.92 MV to 1.08 MV per gap. The voltage distribution along the CH- DTL cavities is shown in Figure 6.2.

Table 6.1 summarizes the geometry of each cell in the cavities. This includes the gap length, drift tube length, voltage and cell period.

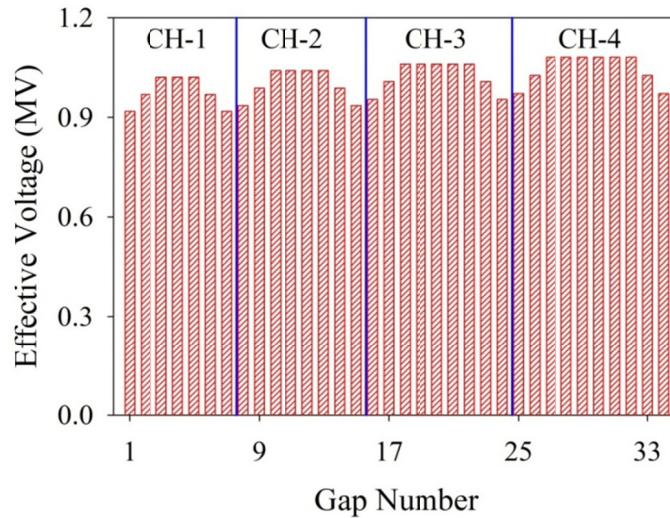


Figure 6.2: Simulated effective gap voltage along the CH structure, the voltage near the quadrupoles is minimized.

Table 6.1: A summary for each cell period structure in all cavities of the CH – DTL.

Period Cell (cm)	Drift Tube No.	Tube Length (cm)	Gap No.	Gap Length (cm)	Voltage (MV)	TTF
CH – 1						
4.01*	1	2.41	1	3.20	0.918	0.838
6.91	2	3.65	2	3.31	0.969	0.840
7.15	3	3.78	3	3.43	1.020	0.840
7.39	4	3.91	4	3.53	1.020	0.840
9.10	5	5.68	5	3.31	1.020	0.837
7.68	6	4.23	6	3.60	0.969	0.839
7.95	7	4.22	7	3.87	0.918	0.844
CH – 2						
47.24**	8	43.34	8	3.92	0.936	0.846
8.60	9	4.64	9	4.01	0.988	0.847
8.80	10	4.79	10	4.00	1.040	0.853
8.99	11	4.89	11	4.21	1.040	0.844
11.16	12	7.01	12	4.09	1.040	0.858
9.22	13	4.98	13	4.39	1.040	0.846
9.46	14	4.96	14	4.62	0.988	0.839
9.68	15	5.00	15	4.74	0.936	0.836
CH – 3						
47.24**	16	42.27	16	5.19	0.954	0.813
10.23	17	5.31	17	4.65	1.007	0.854
10.40	18	6.02	18	4.12	1.060	0.887
10.57	19	6.35	19	4.33	1.060	0.878
13.02	20	8.84	20	4.04	1.060	0.897
10.72	21	6.65	21	4.11	1.060	0.898
10.93	22	6.83	22	4.08	1.060	0.902
11.13	23	7.07	23	4.04	1.007	0.906
11.32	24	7.24	24	4.10	0.954	0.905
CH – 4						
47.24**	25	43.19	25	4.00	0.972	0.915
11.82	26	7.80	26	4.05	1.026	0.915
11.96	27	7.88	27	4.13	1.080	0.914
12.11	28	8.00	28	4.08	1.080	0.916
14.86	29	10.88	29	3.88	1.080	0.926
12.21	30	8.30	30	3.94	1.080	0.926
12.39	31	8.43	31	3.99	1.080	0.926
12.57	32	8.54	32	4.05	1.080	0.926
12.74	33	8.63	33	4.17	1.026	0.924
12.90	34	8.80	34	4.02	0.972	0.931
47.23**	35	45.22				

* Entrance drift to the first gap center.

** Drift across the quadrupole triplets.

Due to the fact that the transverse focusing period is much larger than in a conventional FODO structure, and in order to avoid beam losses, the length of the first cavity was limited to 7 gaps only.

Two injected beam distributions were analyzed for this design: The matched case which is a numerically generated waterbag distribution with rms – emittance values close to the linac acceptance (compare aperture filling in Figure 6.4), and the laser accelerated case with a proton distribution as simulated in chapter 3.4.2.

6.1.1 Matched Beam Case

The matched beam parameters at 500 mA equivalent beam current are summarized in Table 6.2, where the input values are given 40 mm in front of the first gap center (corresponding to $z = 147$ mm in Figure 3.1). The 6D-water bag distribution, which is defined in the LORASR code, is used as an initial distribution. The particles were accelerated to the exit without any losses.

Table 6.2: Normalized rms- emittance values for the input and output distribution with 500 mA beam current.

Emittance	Input	Output
Transverse/ $mm \cdot mrad$	x: 3.85	4.08
	y: 3.85	4.06
Longitudinal/ $keV \cdot ns$	5.37	6.68

The rms- emittance growth rates along the linac are less than 25 % in longitudinal plane and less than 6% in the transverse planes as shown in Figure 6.3.

The transverse and longitudinal 90,99 and 100 % beam envelopes at 500 mA equivalent beam current can be seen in Figure 6.4. The 100 % beam envelope is reaching more than 90% of the aperture in the second triplet lens. The magnetic field gradients of the quadrupoles are ranging up to $50.5 T/m$ at quadrupole aperture radii of 25 mm, which can be reached with cobalt based cores (Vacoflux 50 for example).

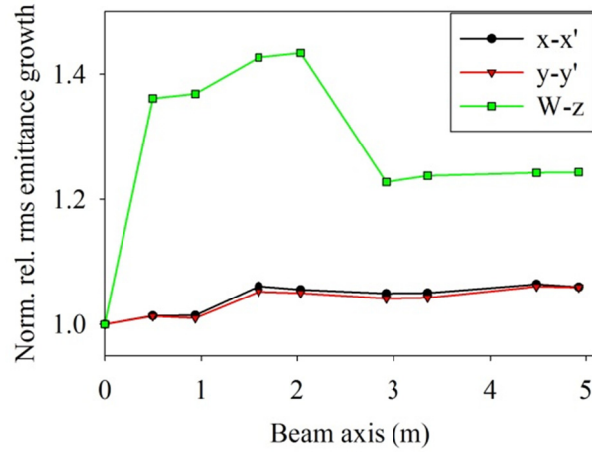


Figure 6.3: Normalized relative rms- emittance growth for the matched case.

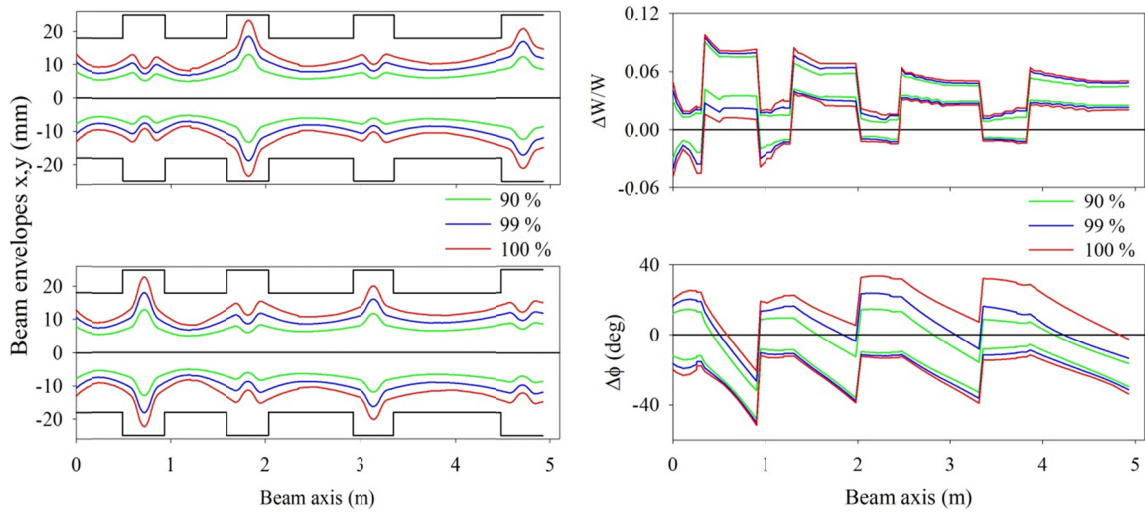


Figure 6.4: Transverse (left) and longitudinal (right) 90%, 99% and 100% envelopes at 500 mA beam current. $\Delta W/W$ and $\Delta\phi$ – plots are showing details of the KONUS – beam dynamics design. Black lines in the left plot indicate the aperture.

The particle distribution at entrance and exit in transverse and longitudinal planes are shown in Figure 6.5 for 10^6 macro-particles.

These simulations allow estimating the capability of the CH- structure for high current beams.

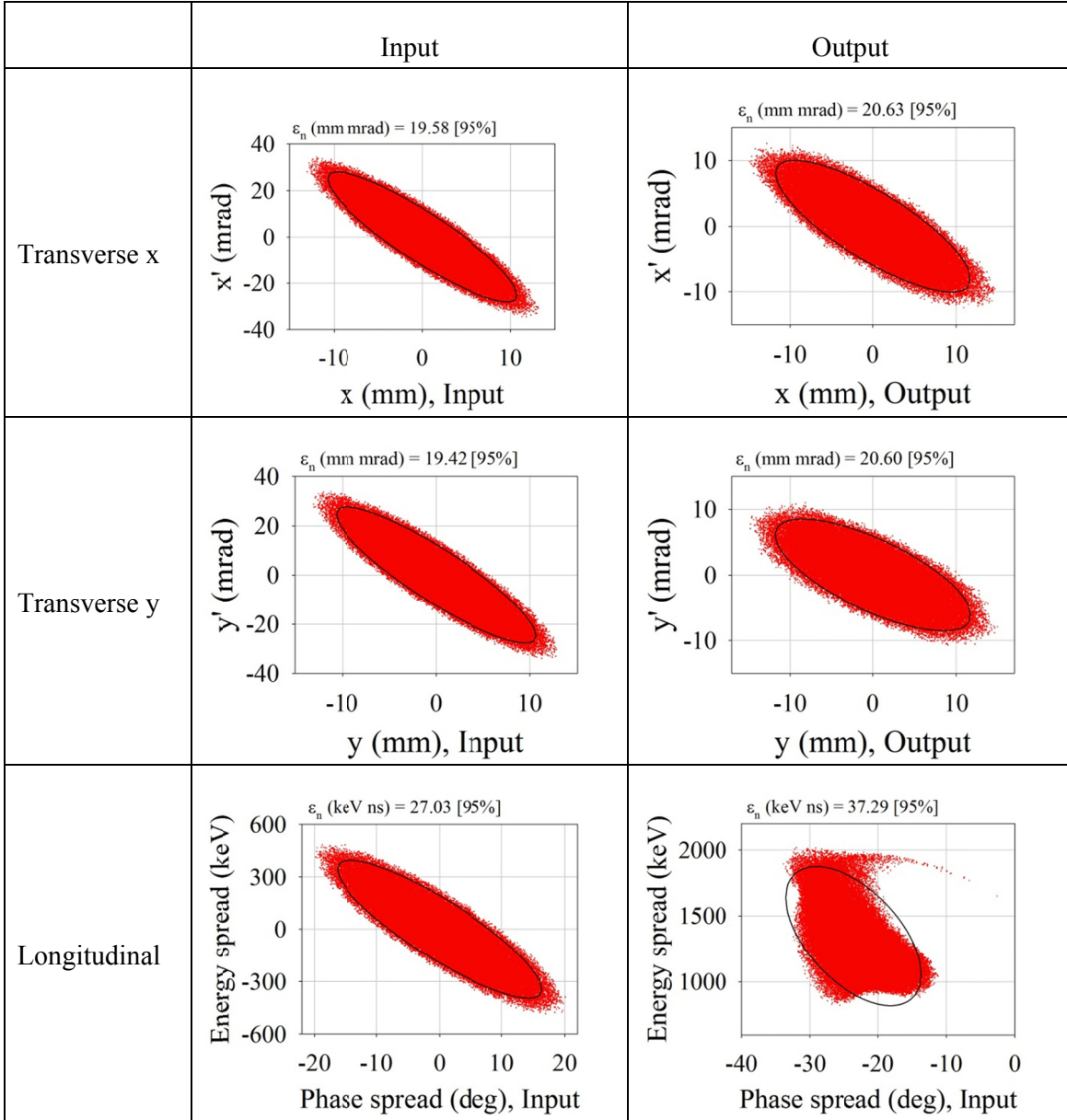


Figure 6.5: Transverse (top and middle) and longitudinal (bottom) particle distributions at entrance and exit of the CH-DTL section at 500 mA equivalent beam current. The input and output energies of the CH – DTL were 10 MeV and 40 MeV, respectively. Normalized emittance values are relevant for the plotted 95% ellipses.

6.1.2 Laser- Accelerated Beam Case

The laser generated proton bunch was simulated by LASIN along the pulsed magnetic solenoid (section 3.4.2) and down to a position 40 mm in front of the first DTL gap. After that, the particle distribution is reduced to an energy band $10 \text{ MeV} \pm 0.5 \text{ MeV}$ corresponding to the DTL acceptance. 6×10^9 protons are contained in this bunch, corresponding to a linac

equivalent current of 300 mA, and plotted in green in Figure 6.6. Due to the phase space distribution in $x - x'$ and $y - y'$ where a part of the protons is focused and the other part is defocused and due to the large angular divergence which is reaching up to 130 mrad , it was not possible to accept the whole distribution. In longitudinal phase space the proton bunch has a wide phase spread reaching about $\pm 20^\circ$. But due to the acceptance in transverse planes, this spread was reduced to about $\pm 12^\circ$.

In Figure 6.6 green particles correspond to the laser generated distribution with energies $10 \text{ MeV} \pm 0.5 \text{ MeV}$, while the red particles fall into the simulated transverse DTL acceptance as derived from the matched beam case in section 6.1.1. In consequence, only 72% of the total number (as shown in green) is accepted by the DTL. The other particles are truncated at that position with respect to the beam simulations.

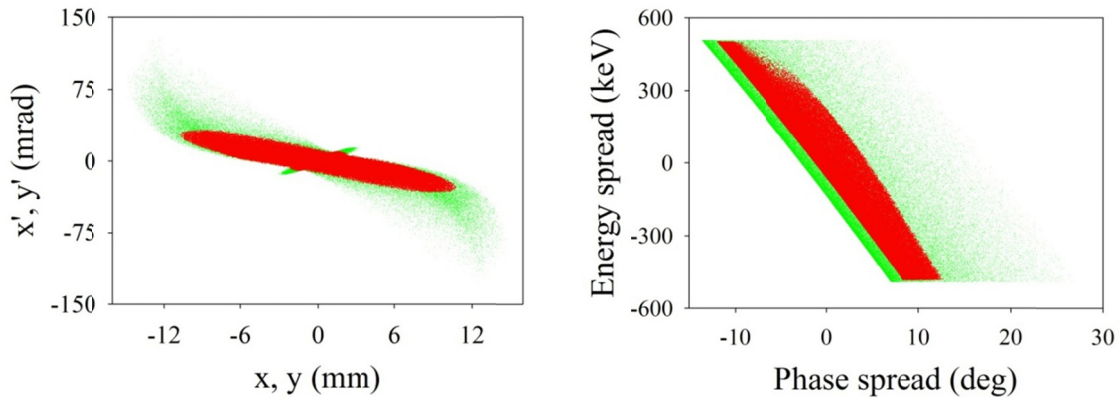


Figure 6.6: Laser generated particle distribution in transversal (left) and longitudinal (right) planes at the DTL – entrance within an energy range $10 \text{ MeV} \pm 0.5 \text{ MeV}$ in green (identical with Figure 3.37, right). The red 72% subsets of the particle distribution fall within the transverse CH – DTL acceptance area and are used for DTL beam dynamics simulations.

The beam parameters for this subset of delivered particles are summarized in Table 6.3.

Table 6.3: Normalized rms- emittance values for the input and output distribution for the laser accelerated case (216 mA equivalent beam current).

Emittance	Input	Output
Transverse/ $\text{mm} \cdot \text{mrad}$	x: 2.89	3.06
	y: 2.89	3.33
Longitudinal/ $\text{keV} \cdot \text{ns}$	3.42	6.86

All remaining particles were accelerated to the exit without any further losses along the CH-DTL.

The resulting normalized rms- emittance growth rates of 100% in longitudinal plane and less than 16% in each transverse plane are shown in Figure 6.7.

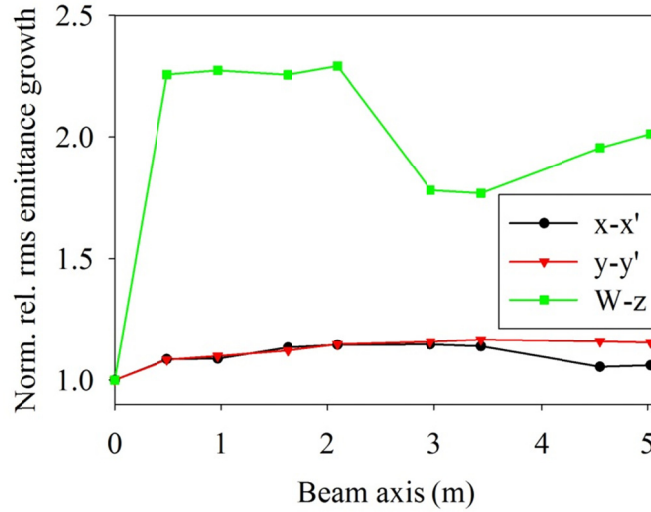


Figure 6.7: Normalized relative rms- emittance growth rates along the linac for the laser generated proton case.

By comparing with the matched case, it becomes clear, that the deformed longitudinal input emittance in the laser generated distribution is a disadvantage: The longitudinal growth rate is even bigger than in the matched case, although the proton number in the beam is 43% only.

The transverse and longitudinal 90,99 and 100% envelopes can be seen in Figure 6.8. The optimized magnetic field gradients of the quadrupoles are ranging up to $50.8 T/m$ at quadrupole aperture radii of 25 mm.

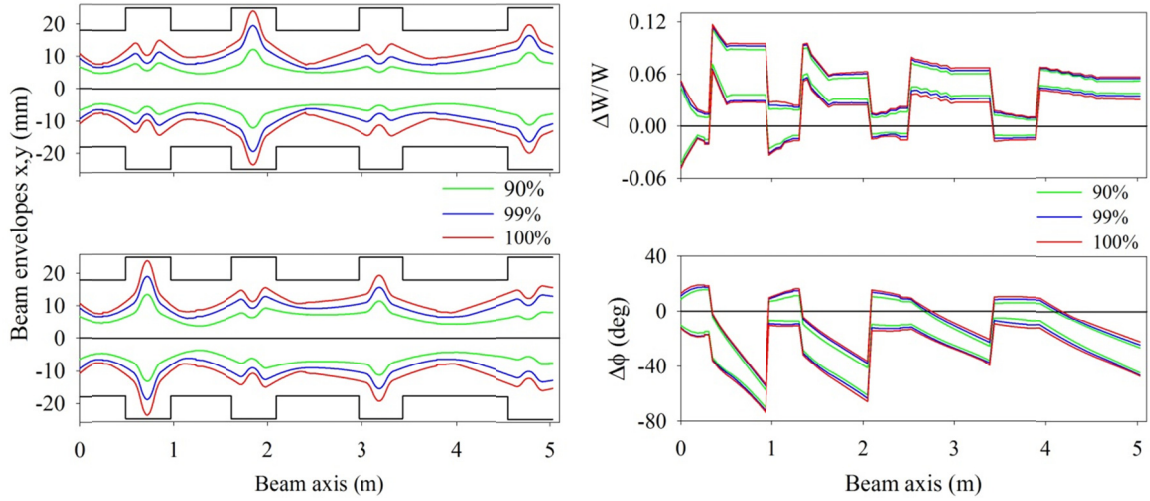


Figure 6.8: Transverse (left) and longitudinal (right) 90%, 99% and 100% beam envelopes starting at 6 cm behind of the solenoid. Black lines in the left plot indicate the aperture.

The particle distribution at the entrance and exit in transverse and longitudinal planes are shown in Figure 6.9 for 200000 macro-particles, respectively.

These distributions are valid for further rf acceleration at acceptable loss rates, as the duty cycle for this kind of injector will stay very low.

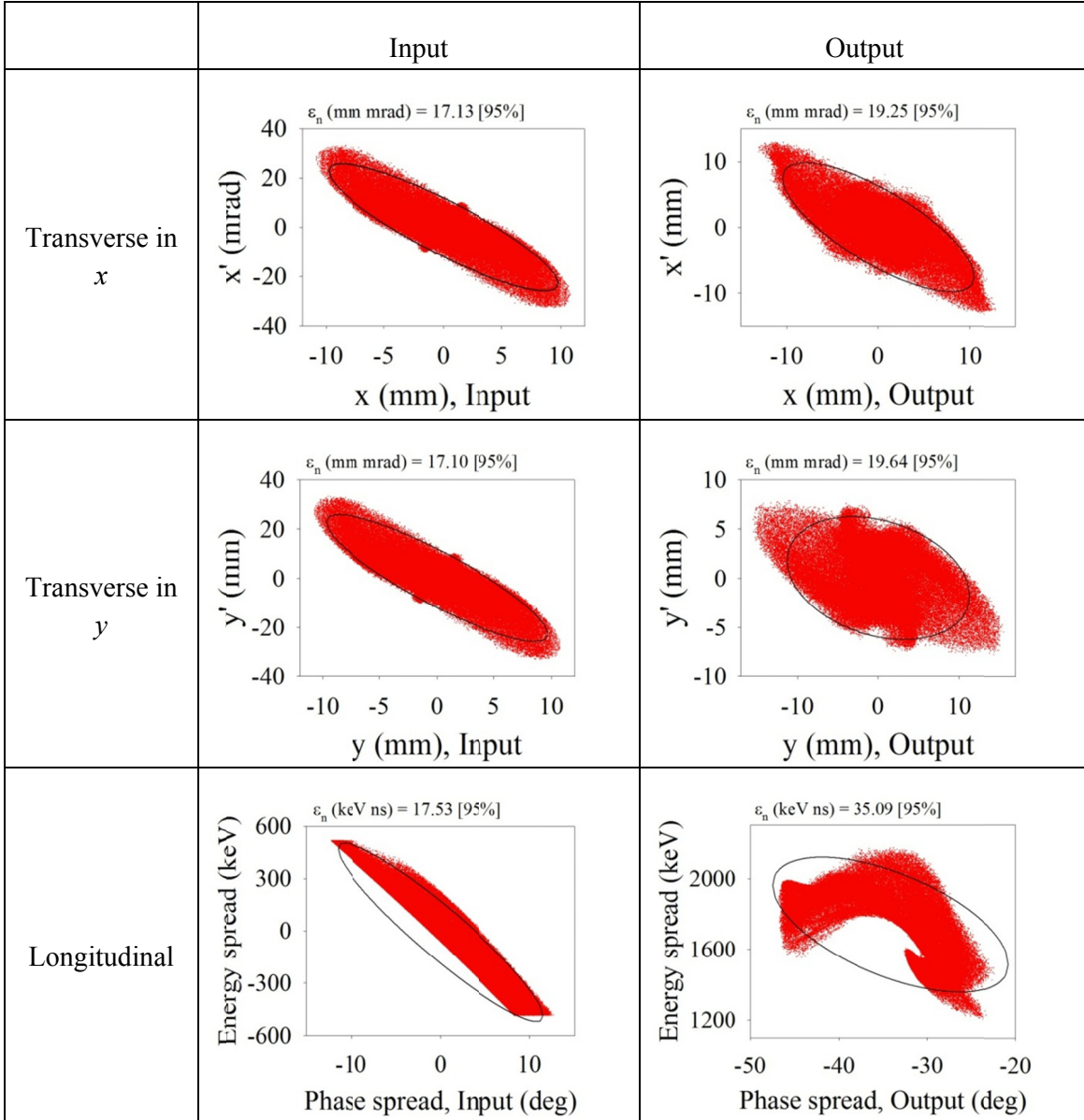


Figure 6.9: Transverse (top and middle) and longitudinal (bottom) particle distributions at entrance (6 cm behind the solenoid) and exit of the CH-DTL structure. The input and output energies of the CH – DTL were 10 MeV and 40 MeV, respectively. Normalized emittance values are relevant for the plotted 95% ellipses.

6.2 Linac Designs for Reduced Voltage Gain

In the previous section, the dedicated CH – cavity was demonstrated to accelerate the proton bunch from 10 MeV up to 40.03 MeV with four CH – cavities. The accelerating gradient V_0 per cavity varies from 7.00 to 12.61 MV/m. This high accelerating gradient especially in the

first cavity was chosen in order to handle the huge space charge and to prevent beam losses. A gap voltage of about 1 MV was applied at all gaps.

10^{10} protons per bunch are expected to be delivered by TNSA in the energy band of 10 $MeV \pm 0.5 MeV$. This number is equivalent to 520 mA averaged beam current in a linac if all buckets are filled with the same number.

The high gap voltage will increase the power losses and have a high risk of sparking. It could be reduced by a certain percentage, without a serious reduction of beam quality. This is described now.

The accelerating gap voltage was investigated for three different cases. The first case is the one explained in section 6.1.1 where the proton bunch is accelerated from 10 MeV up to 40.03 MeV . In the second case, the accelerating gradient was reduced to 75%. Hence, the proton bunch will be accelerated up to 32.53 MeV .

A 50% reduction in accelerating gradient which will accelerate the bunch up to 25.02 MeV in the third case.

For each case, the transmission and longitudinal emittance growth was evaluated at different beam currents up to 2 A .

For the first and second cases, where the accelerating gradient was V_0 and $0.75V_0$, the resulting 100% transmission up to 1 A was approved (see Figures 6.10 and 6.11). While in the third case, 100% transmission is valid up to 400 mA only. Beyond this point, the transmission starts to decrease with increasing beam current as shown in Figure 6.12.

At 500 mA beam current, the longitudinal emittance growth is slightly different between V_0 and $0.75V_0$ case, but quite different for the $0.5V_0$ case. Table 6.4 shows a comparison between the different cases at different beam current.

As a result, a 25% reduction of the gap voltages for a 500 mA beam current layout seems reasonable. This gives then effective gap voltages of around 750 kV which gives a good safety margin against sparking at the envisaged, that rf phase operation.

With respect to longitudinal rms – emittance growth, the factor is increasing from 1.23 (nominal case) to 1.31.

In further investigations to be done, it will be tried to reduce the voltage against the nominal case in the very first cavity. The others will then get longer gaps.

By that technique, the voltage gain of the nominal case should be conserved, while reducing the risk of sparking.

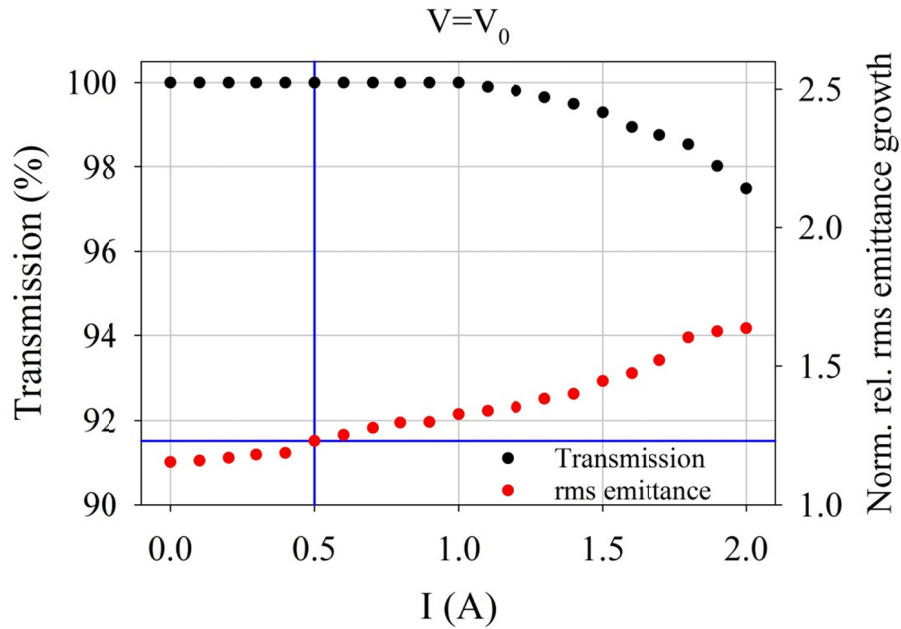


Figure 6.10: The dependence of transmission and normalized relative longitudinal rms-emittance growth on the beam current in case of acceleration the proton bunch from 10 – 40 MeV within a total length of about 5.1 m (nominal case).

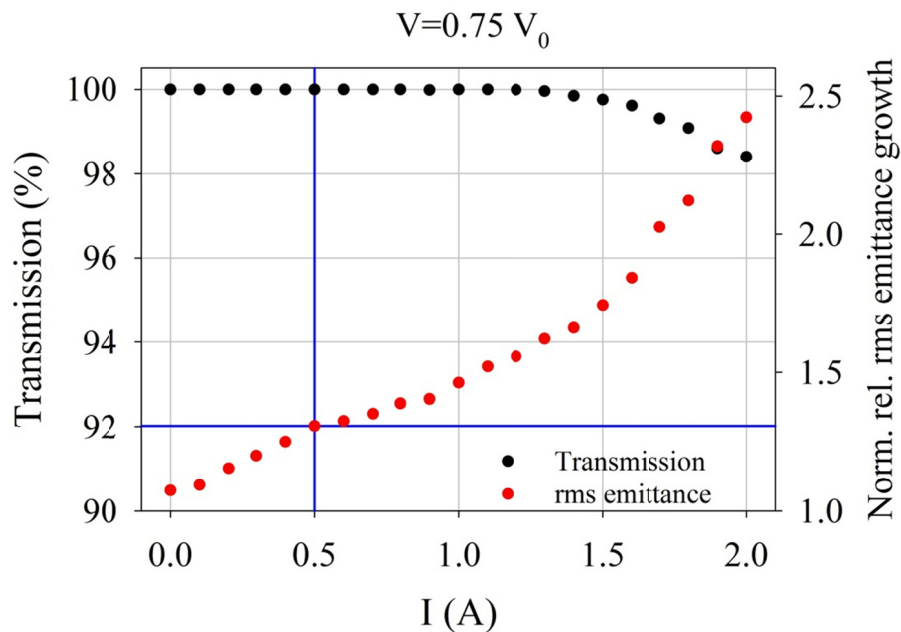


Figure 6.11: The dependence of transmission and normalized relative longitudinal rms-emittance growth on the beam current in case of p – acceleration from 10 – 32.5 MeV within a total length of about 4.9 m.

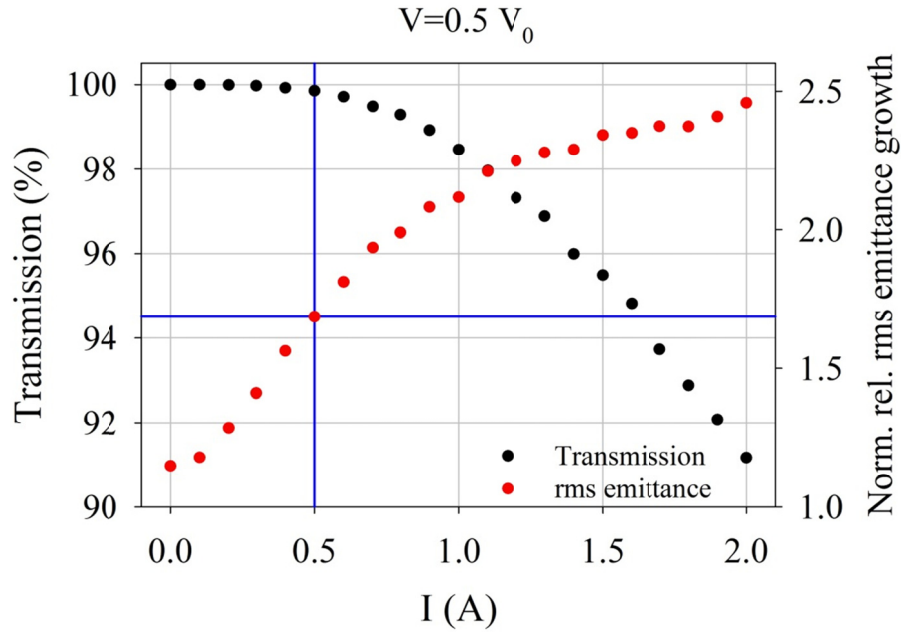


Figure 6.12: The dependence of transmission and normalized relative longitudinal rms-emittance growth on the beam current in case of p – acceleration from 10 – 25 MeV within a total length of about 4.7 m.

Table 6.4: A comparison between different accelerating gradient cases in terms of the transmission and normalized rel. rms emittance growth at different beam current.

Current (A)	Acc. gradient	Transmission (%)	Norm. rel. rms emittance growth
0.0	V_0	100.0	1.16
	$0.75V_0$	100.0	1.07
	$0.5V_0$	100.0	1.15
0.5	V_0	100.0	1.23
	$0.75V_0$	100.0	1.31
	$0.5V_0$	99.8	1.69
1.0	V_0	100.0	1.32
	$0.75V_0$	100.0	1.46
	$0.5V_0$	98.5	2.12

6.3 RF Voltage Level Tolerances

The voltage tolerance $A = \Delta V/V$ was investigated for the CH – DTL in detail. In this study $\Delta V/V$ was varying from -15% to +30% synchronously for all cavities in order to find the

working area of the structure with respect to voltage levels. All rf phase relations between cavities were kept constant.

The rms – emittance values in all planes were calculated at each value of $\Delta V/V$ and compared with the nominal values at $\Delta V/V=0$. It was observed that, the growth in the transverse planes is not much affected by this tolerance in the voltage while the longitudinal emittance stands within acceptable values between $\Delta V/V = -6\%$ to $\Delta V/V = +12\%$. Beyond these limits, the longitudinal emittance values were increased to huge numbers suddenly. These results are summarized in Figures 6.13 – 6.14, where the change in rms – emittance with respect to the nominal value $\Delta V/V = 0$ is displayed.

Besides the change in emittance, the transmission of the particles along the structure was studied with the voltage variation. Within $\Delta V/V = -13\%$ to $\Delta V/V = +20\%$, the loss in particle was less than 10% which still can be accepted. After that, the design cannot stand anymore and more than 50% of the beam will be lost.

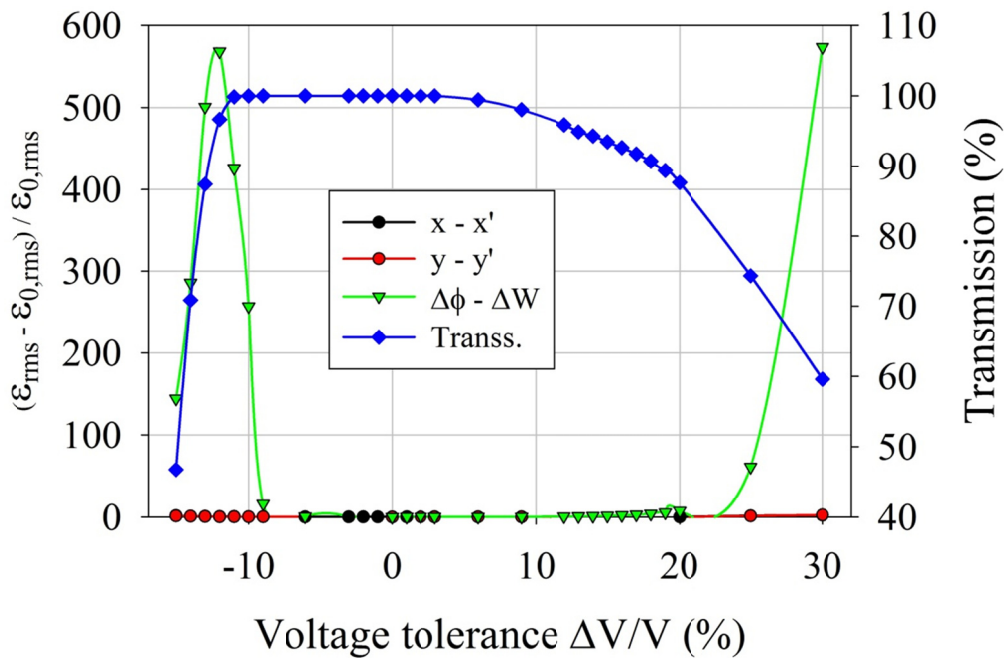


Figure 6.13: The change in rms – emittance with respect to the nominal values due to the voltage variation of the whole linac with rf phases between cavities were kept constant.

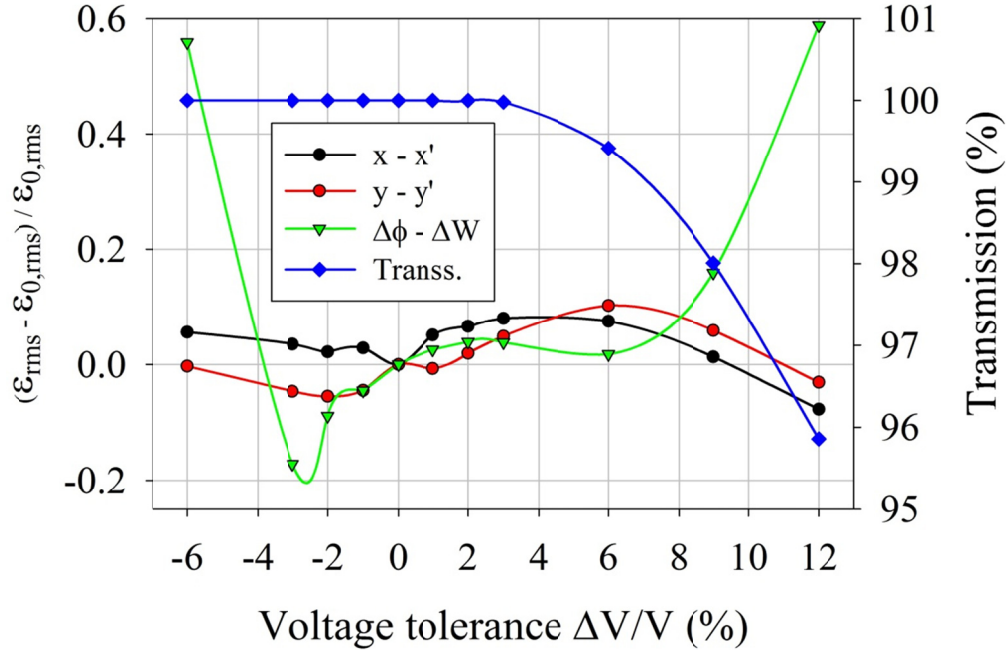


Figure 6.14: Detail of Figure 6.14 for a reduced voltage variation range.

In the following, two cases ($\Delta V/V = -6\%$ and $+6\%$) will be compared to study the beam dynamics in case of voltage variation.

In both cases, the additional emittance growth with respect to $\varepsilon_{rms,0}$ in longitudinal plane is about 60%.

The same input particle distributions in longitudinal and transversal planes were used to investigate both cases. This is the same distribution which is used to study the laser – accelerated case (section 6.1.2).

By comparing the beam envelopes for $\Delta V/V = +6\%$ with $\Delta V/V = -6\%$, one can see that the longitudinal envelope is ending with a big phase width in the -6% case (see Figure 6.15). But the transverse envelopes in case of -6% seem much better than in case of $+6\%$ (Figure 6.16). The last observation is due to the reduced rf defocusing forces at the lower voltage level, where the rf phase are closer to the crest of the wave.

The safety margin in case of -6% is obvious and can be seen clearly, resulting in free beam losses through the structure. This was not the case at $\Delta V/V = +6\%$ where beam envelopes are hit the cavity wall, resulting in a beam loss of about 0.5%.

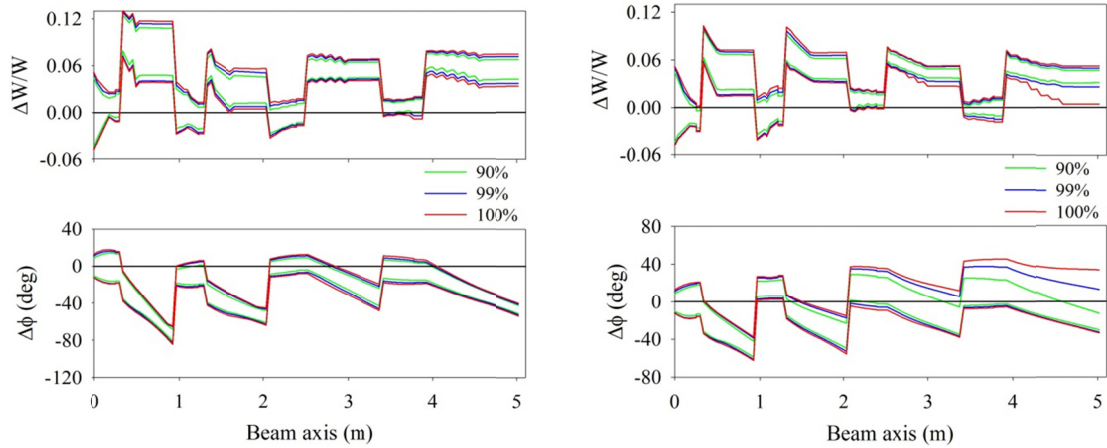


Figure 6.15: Longitudinal 90%, 99% and 100% envelopes for +6% variation in voltage (left) and -6% (right).

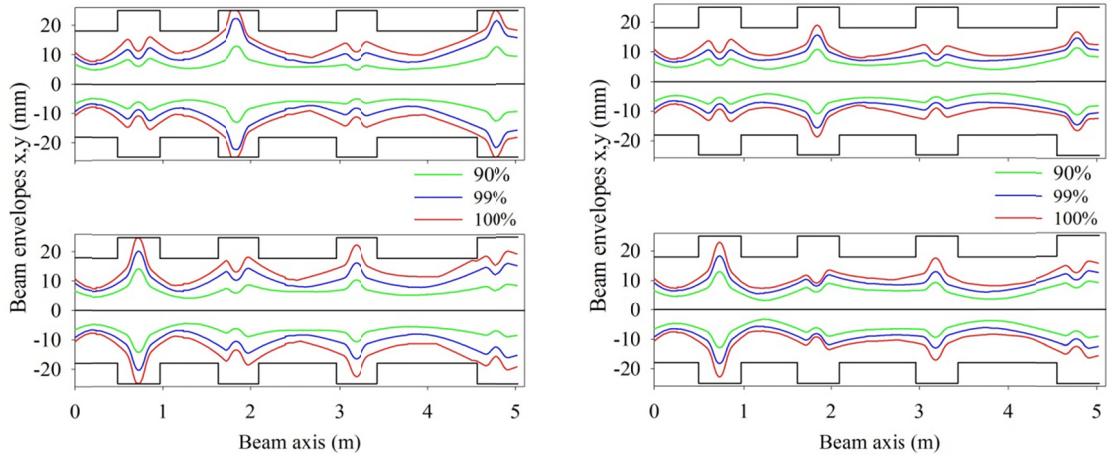


Figure 6.16: Transverse 90%, 99% and 100% envelopes for +6% variation in voltage (left) and -6% (right). Black lines indicate the aperture.

The particle distributions at linac exit in transverse and longitudinal planes are shown in Figure 6.17 for both cases. The input particle distributions for both transverse and longitudinal planes are the same as input in Figure 6.9, left.

These distributions can be still valid for further rf acceleration at acceptable loss rates, as the duty cycle stays very low.

The motion of bunch center for both cases is shown in Figure 6.18.

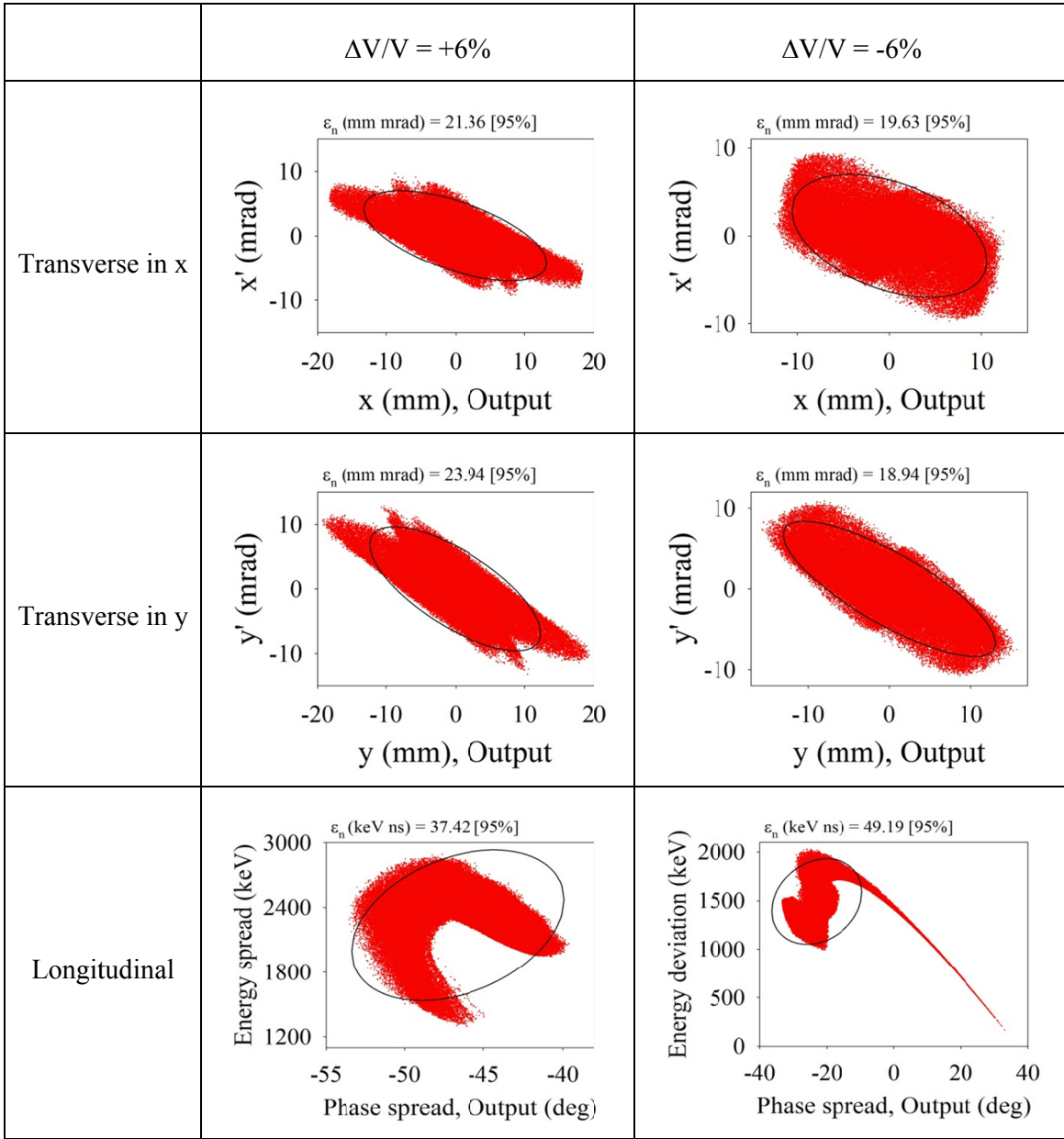


Figure 6.17: Transverse (top and middle) and longitudinal (bottom) particle distribution at linac exit for different voltage variation: (left) $\Delta V/V = +6\%$ and (right) $\Delta V/V = -6\%$.

By the meaning of KONUS beam dynamics, the bunch center is injected with a surplus in energy against the synchronous particle (see Figure 5.19). Because of this extra energy, the bunch center will arrive the next gap when the electric field is not on the maximum and more negative phase, thus reducing energy spread with respect to the synchronous particle.

In the CH – DTL simulation, the bunch center is expected to come with zero energy spread in re – buncher section (as can be seen for nominal case). This means the bunch center should

be end with a negative synchronous phase (design value) with zero energy spread. This is not the case when this is a variation in voltage, where the bunch can gain more or less energy resulting in a shifted in phase and energy spread.

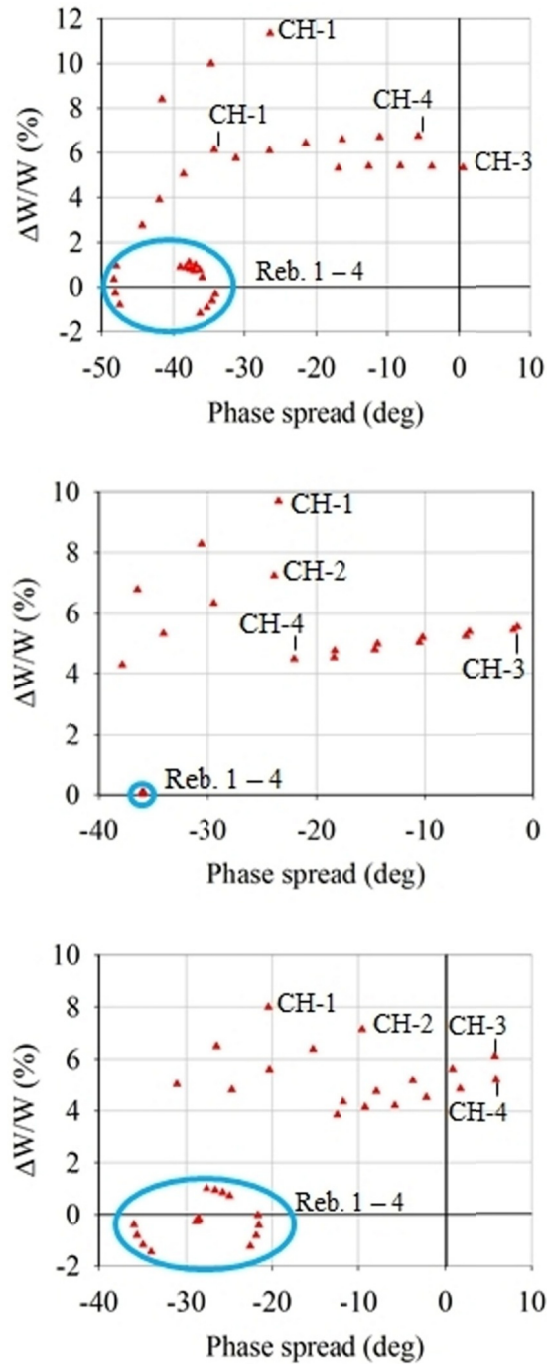


Figure 6.18: Motion of bunch center through CH – DTL for different voltage variation +6% (top) nominal case (middle) and -6% (bottom).

From these simulations one can see that, the design discussed in section 6.1 is quite robust and can stand with acceptable emittance growths and with good transmission values over 95% for the variation of voltage levels from $\Delta V/V = -6\%$ to $\Delta V/V = +12\%$.

6.4 RF Power Budget for a Single Bunch Operation

One great advantage of high current, single bunch passage along the cavity is that the amplifier only has to provide the loss power in the cavity walls. The beam power is provided by the stored energy in the cavity fields, while reducing the field levels only within tolerances.

An estimation of the maximum single bunch proton number can be given in the following way [198]:

$$W = \frac{P_{loss} \cdot Q_0}{\omega}; \quad (6.2)$$

$$P_{loss} = \frac{(N_G T_f U_0)^2}{Z_{eff} \cdot L} \quad (6.3)$$

W = stored field energy, P_{loss} = thermic wall losses, Q_0 = unloaded quality factor, N_G = gap numbers, T_f = the transit time factor, U_0 = averaged gap voltage amplitude along the cavity, Z_{eff} = effective shunt impedance, L = the effective cavity length.

The synchronous beam bunch will absorb cavity energy while passing N_G cells of length $\beta\lambda/2$; the bunch transit time along the cavity corresponds to

$$\tau_c = T \cdot \frac{N_G}{2}; \quad (6.4)$$

with $T = 1/f$, f being the rf frequency in Hz. Assuming an rf phase of 0° in each gap center – that means maximum voltage gain $V_g = V_{0,gap} \cdot T_f$ with $V_{0,gap}$ being the gap voltage amplitude assuming to be constant along the cavity, the energy transfer to the beam bunch with N_p protons along each gap passage corresponds to

$$W_g = N_p \cdot e \cdot V_g; \quad (6.5)$$

The bunch will pass the cavity during a few ten *ns*, where a feedback control will be too slow for compensation. On the other hand, a feed forward loop technique might provide solutions for achieving even higher bunch particle numbers, but is not considered here.

The acceptable voltage drop tolerance *A* caused by the bunch will be in the 1 to 2 percent range.

$$A = \left| \frac{\Delta V_{g,max}}{V_g} \right|; \quad (6.6)$$

This assures in a good approximation an unchanged power input P_l by the feeder line during the bunch passage, additionally the matching condition will be disturbed slightly only.

The time constant τ_m , after which the amplitude shift caused by the beam reaches the limit is given by

$$\tau_m = 2 \cdot \frac{A \cdot W}{P_{b,eff}}; \quad (6.7)$$

$P_{b,eff}$ = the beam extracted rf power. In case of a single bunch passage through a $\beta\lambda/2$ structure it is

$$P_{b,eff} = 2 \cdot T_f \cdot U_0 \cdot \frac{Q_{Bunch}}{T}; \quad (6.8)$$

The bunch particle limit will be exceeded if

$$\tau_m \leq \tau_c; \quad (6.9)$$

The particle limit is given by

$$\frac{\tau_m}{\tau_c} = 1; \quad (6.10)$$

$$\frac{2 \cdot A \cdot W}{T_f \cdot U_0 \cdot Q_{Bunch} \cdot N_G} = 1; \quad (6.11)$$

$$Q_{Bunch} = \frac{2 \cdot A \cdot W}{T_f \cdot U_0 \cdot N_G}; \quad (6.12)$$

As an example, for the first cavity of the proposed linac, the cavity parameters can be estimated by CST – MWS (see table 7.1 in next chapter) to get Q_{Bunch} like follows:

$$L = 0.5 \text{ m}; Z_{eff} = 45 \text{ M}\Omega/\text{m}; N_G = 7 \text{ gaps}; T_f = 0.8, U_0 = 1.0 \text{ MV}; Q_0 = 13289;$$

From equation 6.3, the wall losses result in $P_{loss} = 1.39 \text{ MW}$. Equation 6.2 gives the stored field energy $W = 9.07 \text{ J}$.

With an assumed tolerance value $A = 0.01$ one gets from equation 6.12 a maximum bunch charge of $Q_{Bunch} = 3.24 \times 10^{-8} \text{ C}$, corresponding to a proton number $N_P = 2.02 \times 10^{11}$.

This would correspond to a beam current of 10.5 A with all buckets filled by the same particle number.

The resulting proton number above can be compared with a particle number of 4.3×10^9 in the simulate example in section 6.1.2.

This shows that, the single bunch beam load will not affect the cavity oscillation, as stated above.

One further aspect is the total number of protons arriving at the linac entrance. These particles might cause cavity sparking when hitting the wall. Even cavity de-phasing might occur by a large particle fraction with energies close enough to the accepted energy window. To reduce the risk of sparking, the intense low energy part of the laser generated pulse should be cut at the linac entrance. This will be a subject of intense simulation studies in the next future. Moreover, the inner drift tube contour can be optimized to reduce the secondary particle emission.

The total number of accepted particles with energies above 10.5 MeV is estimated to about 5×10^9 . But they are continuously distributed in rf phase. One main aspect of an rf postacceleration experiment will be the rf operation stability under these beam load conditions.

CHAPTER 7

THE FIRST CAVITY OF THE DEDICATED CH – DTL FOR LASER PROTON ACCELERATION

The investigation of the dedicated CH linac for laser proton acceleration was performed in two steps. In the first one, the LORASR code was used to design the main parameters for the cavities like the number of gaps per cavity, the drift tubes lengths, the voltage value the synchronous phase in each gap and the transit time factor. This process was worked out in detail and the final results were presented in Chapter 6.

In the second step the CST – Microwave Studio software was used to optimize drift tubes, gaps and stems geometries and to tune the electric and magnetic fields distributions inside the cavity.

7.1 Optimization of the First CH – Cavity

In this section, the analysis of the first CH – cavity using CST – MWS [255] will be presented.

The first cavity has a length of 668.4 mm with an inner diameter of 385.9 mm and is operated at 325.2 MHz (Figure 7.1). In this cavity, the proton bunch will be accelerated from 10 to 16.1 MeV with an average accelerating gradient of about 12.6 MV/m.

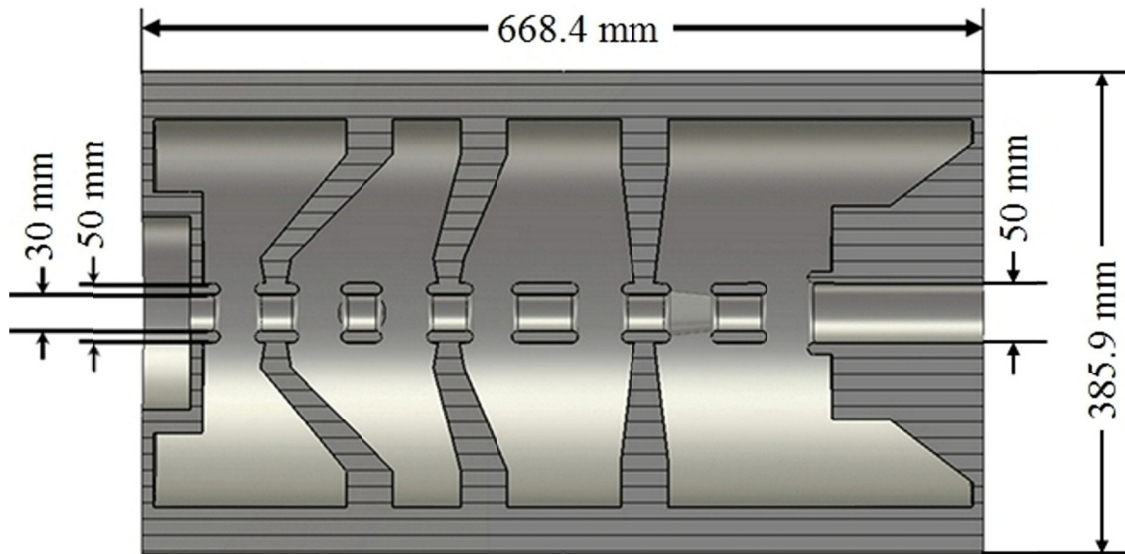


Figure 7.1: Schematic view for the first CH – cavity of the proposed linac.

In the CH – structure, the current flows from the outer cylinder to the drift tubes through the stems in order to generate the axial electric field which is needed for particle acceleration.

The stems are not only responsible for the mechanical stability in the CH – structure, but also they carry of highest current density in the whole structure (Figure 7.2). Because of that their design must be very robust and well cooled by water. On the other hand, close to the beam axis the stems have to be kept slim to reduce the capacitance between neighbored stems.

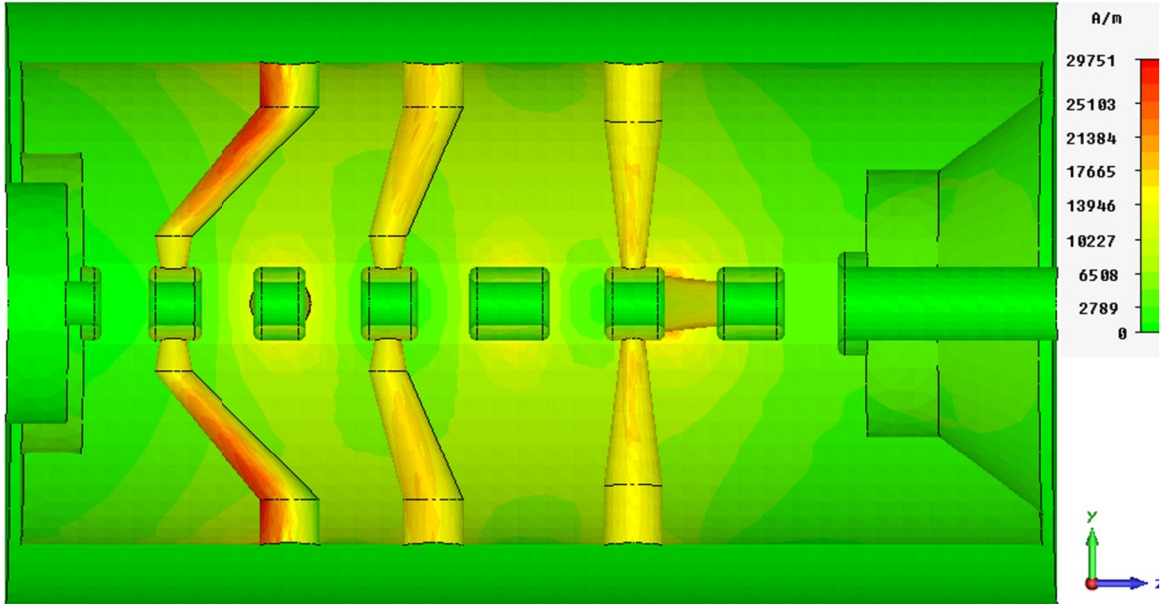


Figure 7.2: A schematic view for the surface current density flowing along the stems. The inclined stems are carrying the highest density because the magnetic field flux is turning transversally into the neighbored quadrants.

Taking into account these criteria, a conical shape has been chosen for the stems where the larger radius is connected with the outer cylinder as can be seen in Figure 7.3. This Figure shows a schematic view of a CH – structure in xy – plane.

The electric and magnetic field distributions across the CH – DTL are shown in Figures 7.4 – 7.6. The magnetic field runs parallel and antiparallel to the beam axis.

For convenience, the aperture radii for all drift tubes were kept at 15 mm, while finally the last tubes of cavity 1 may get larger tubes due to beam dynamics needs.

At the end cell, the magnetic field has a B_ϕ component (see Figure 7.7).

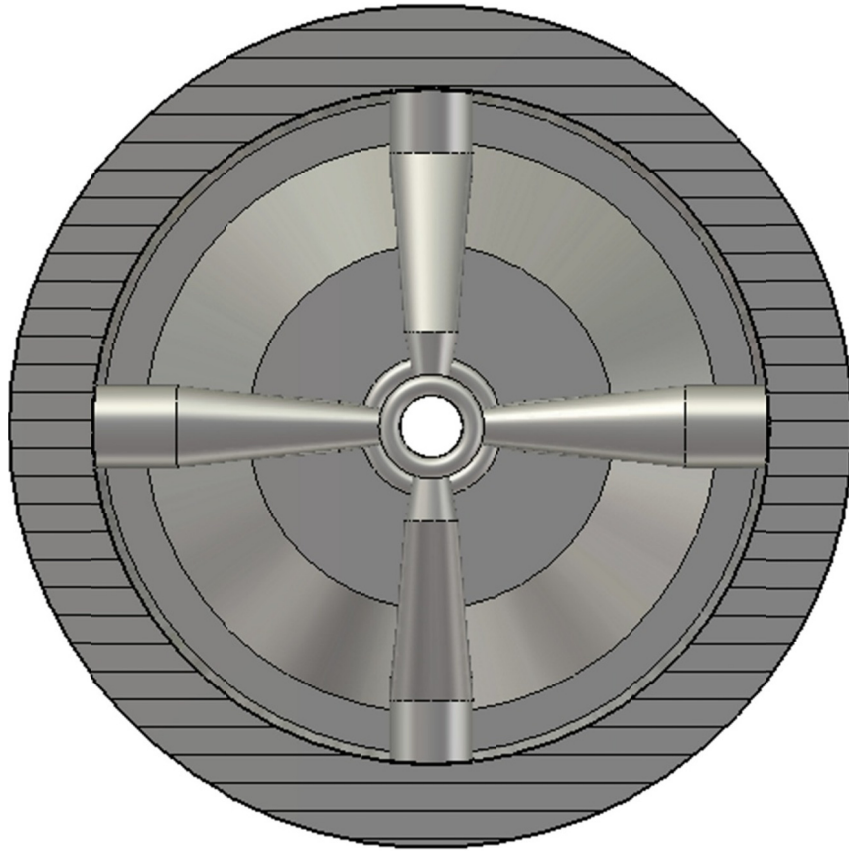


Figure 7.3: A schematic view of a CH – structure in xy – plane. The conical shape for the stems was used in order to have a robust design and make it easy for cooling.

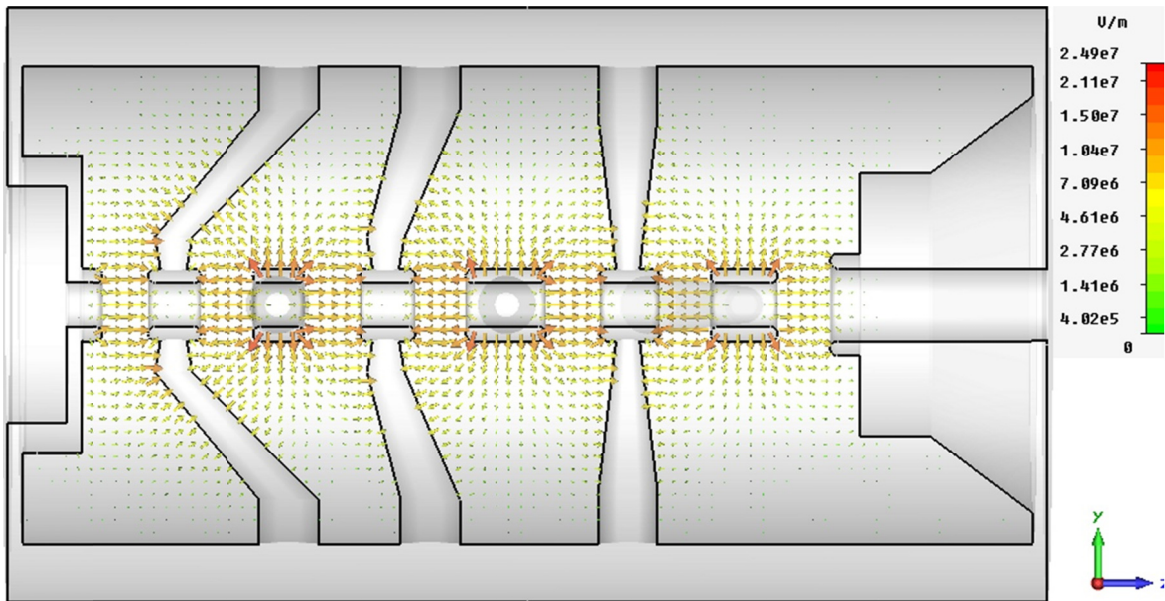


Figure 7.4: The electric field distribution across the CH – DTL. The field is well concentrated at the beam aperture.

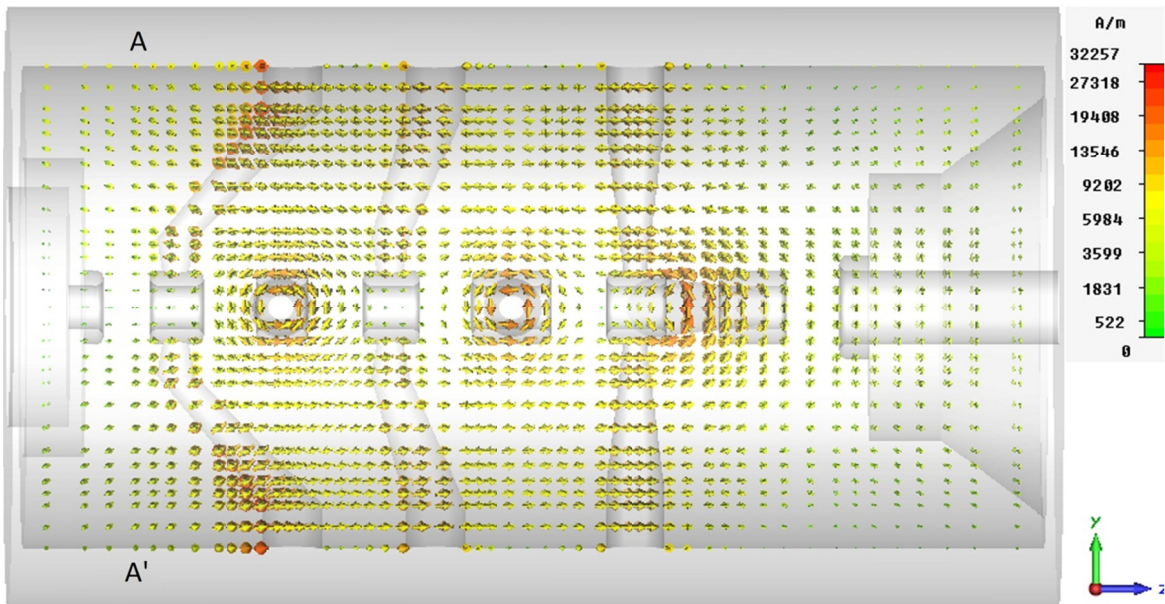


Figure 7.5: The magnetic field distributions across the CH – DTL. The magnetic field runs parallel and antiparallel to the beam axis in the accelerator modules. Due to the current flow in the stems, the magnetic field is oriented locally around each stem.

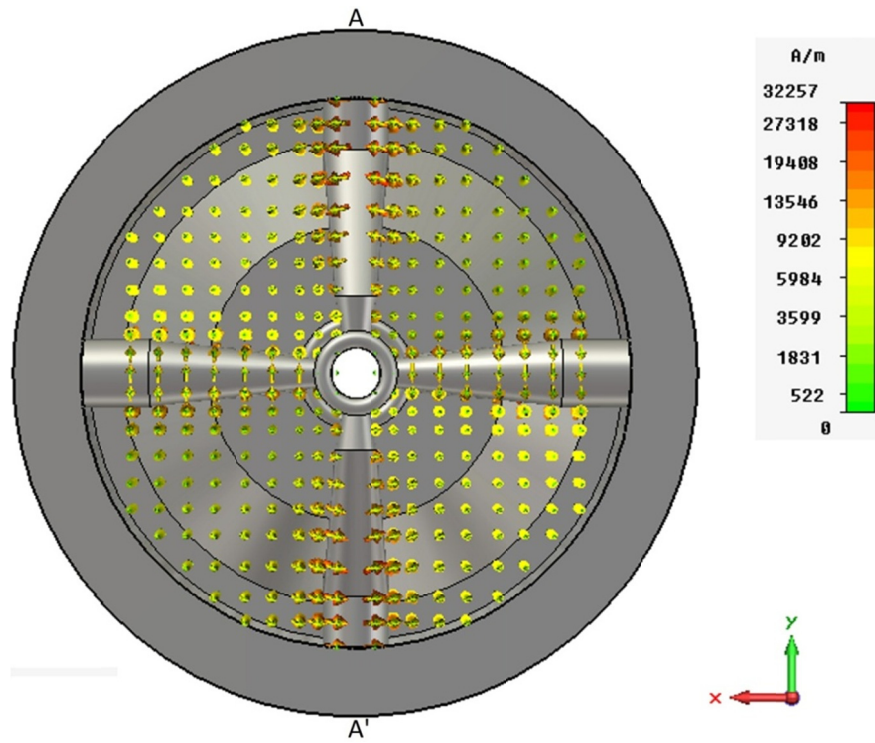


Figure 7.6: The magnetic field distribution in xy – plane, projection $A - A'$ of Figure 7.5.

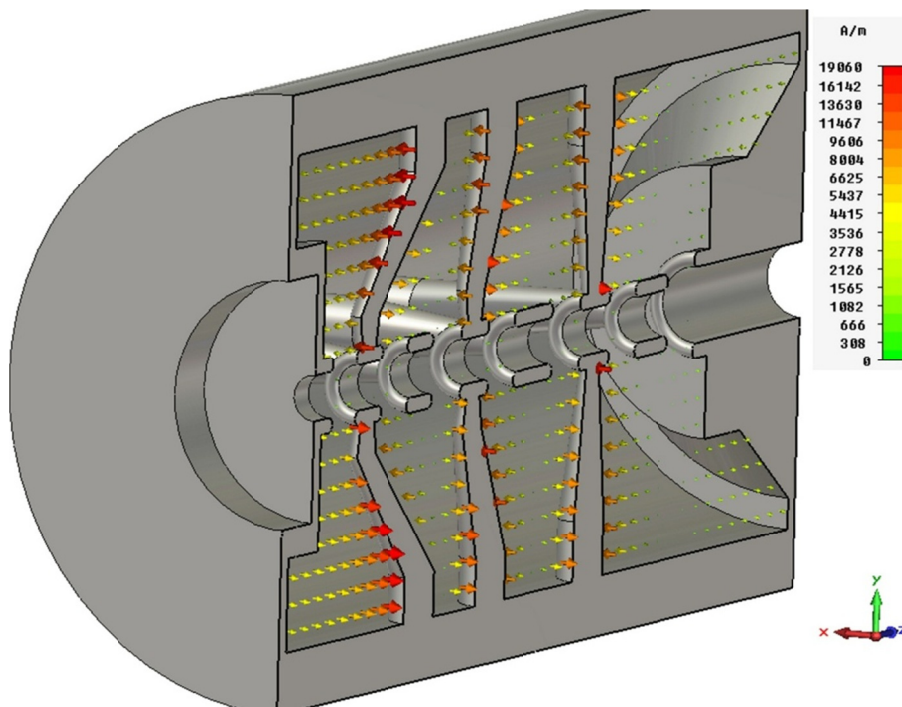


Figure 7.7: The schematic view of the magnetic field around the stems. At the end cell, the magnetic field has a pronounced B_ϕ component.

The on axis electric field distribution as calculated with MWS is shown in Figure 7.8. The corresponding voltage value for this electric field distribution in each gap is calculated accordingly, and the results are compared with the reference values as given from LORASR code (see Figure 7.9).

The electric field is roughly uniform along the central 5 gaps and is reduced in the end gaps. This gives the optimum effective shunt impedance values.

In order to increase the magnetic flux in the end cells, the concept based on inclined stem geometry for the end cells were applied. This choice helps to increase the voltage values in the end gaps.

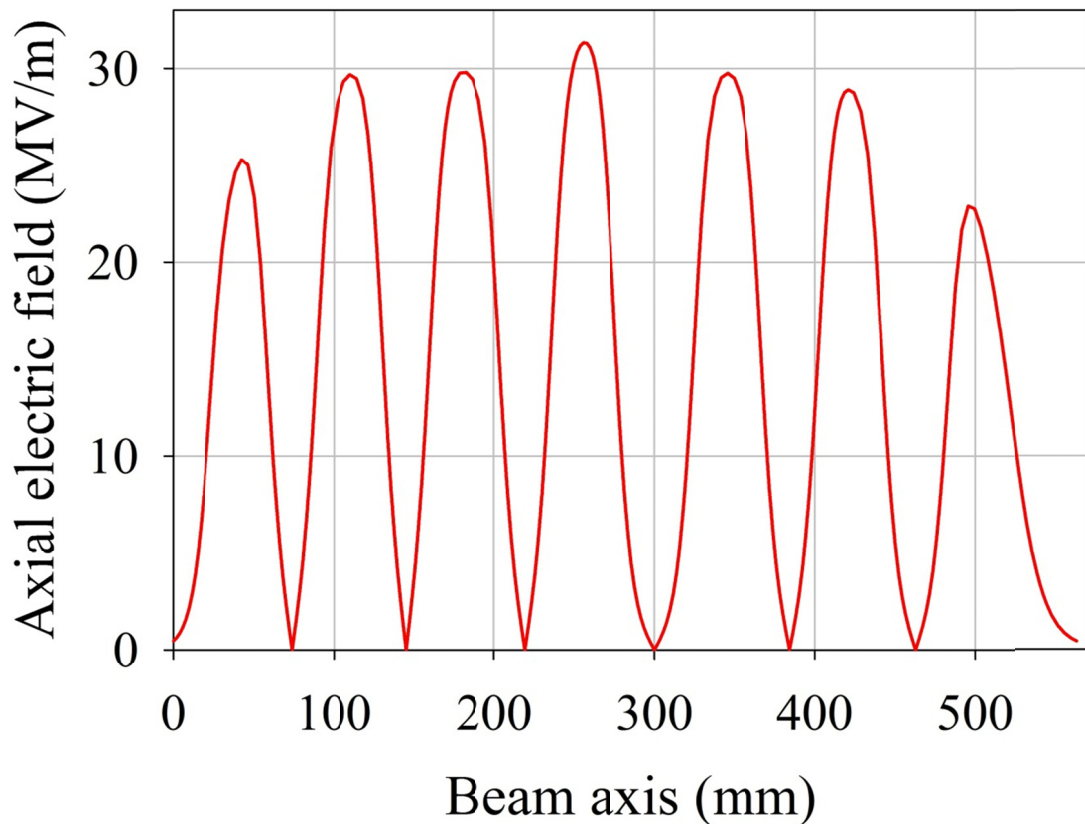


Figure 7.8: The axial electric field distribution as calculated by CST – MWS in all gaps along the beam axis.

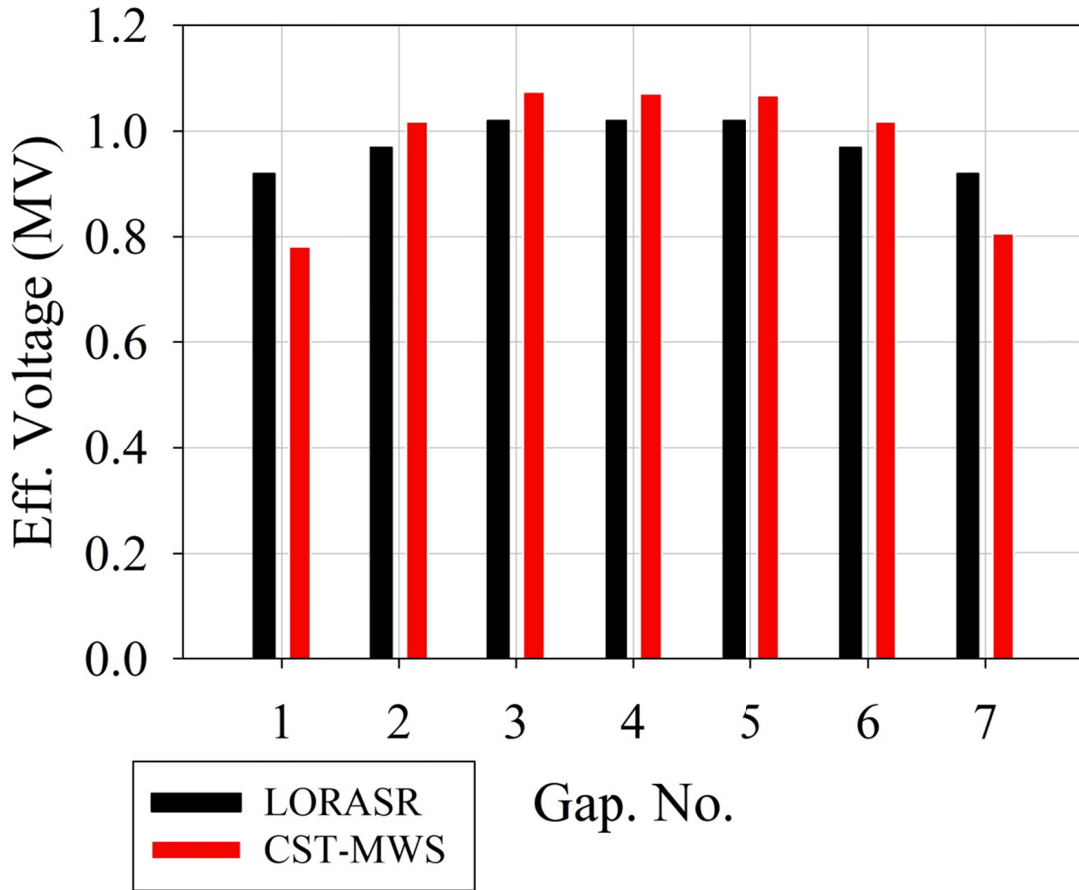


Figure 7.9: A comparison between the corresponding voltage distribution as calculated from the electric field which is given in Figure 7.8 with the reference design values as given from LORASR code.

This concept of inclined stems was applied for the superconducting CH – DTL [250-252] and for the room temperature CH – structure of the FAIR proton injector [76].

It is expected that the electric energy density is localized on the drift tube edges. This can be seen easily in Figure 7.10.

In Figure 7.11, the electric energy density is shown for two examples; the shortest and longest drift tubes (D3 and D5 in Figure 7.15). The maximum surface electric field on D3 (shortest drift tube) is localized on the edges. One can see that these values on the left are somehow higher and distributed on larger area than the right edges. This is because of the inclined stems, where the inclined angle for the stem in front is larger than for the stem behind. This results a higher storage capacity as can be seen in Figure 7.4 qualitatively.

This behavior is still valid in case of D5 (longest drift tube). This drift tube is preceded by an inclined stem and followed by a straight one, which results in higher surface fields at the left side again.

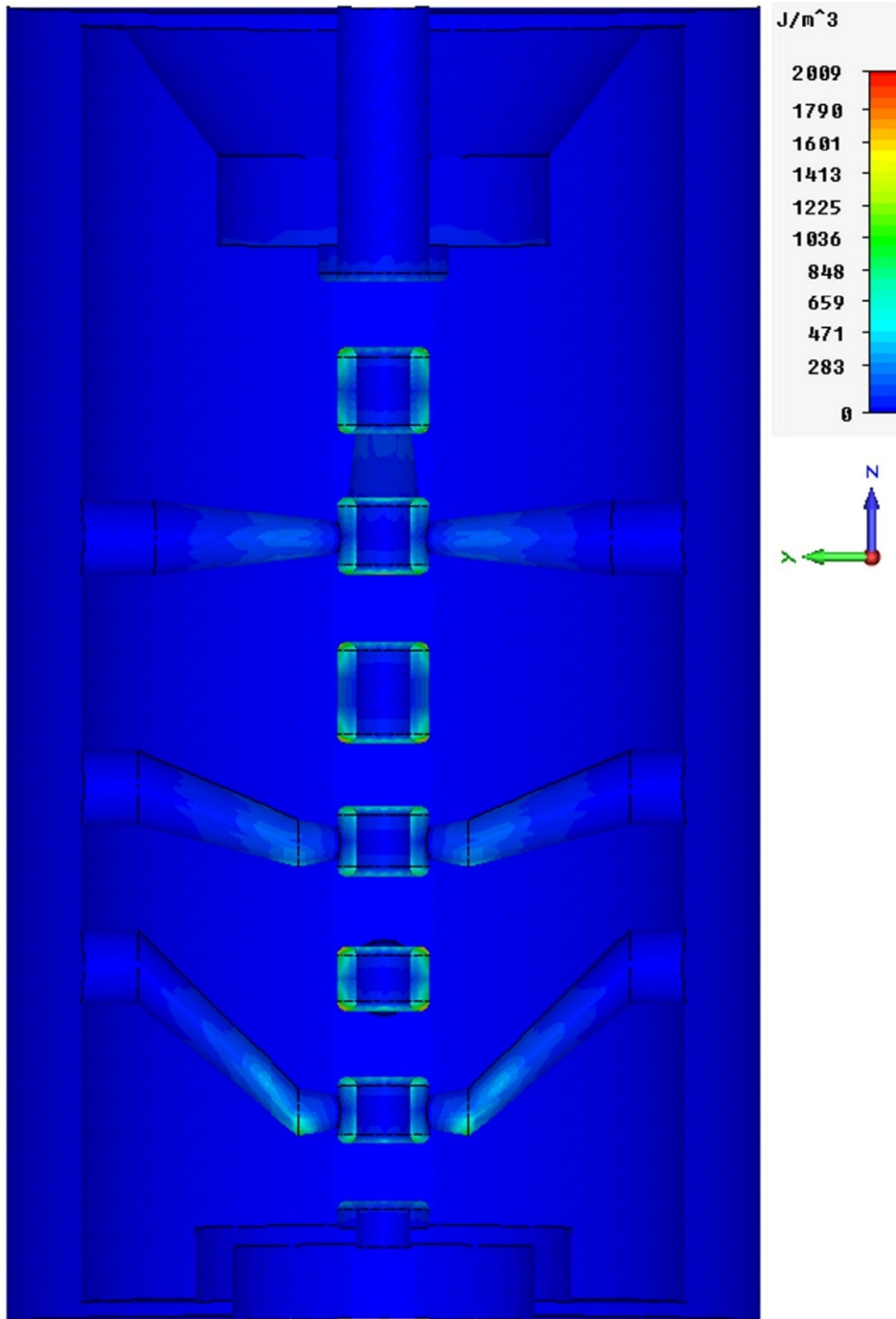


Figure 7.10: The electric energy density inside the cavity which is localized on the drift tube edges.

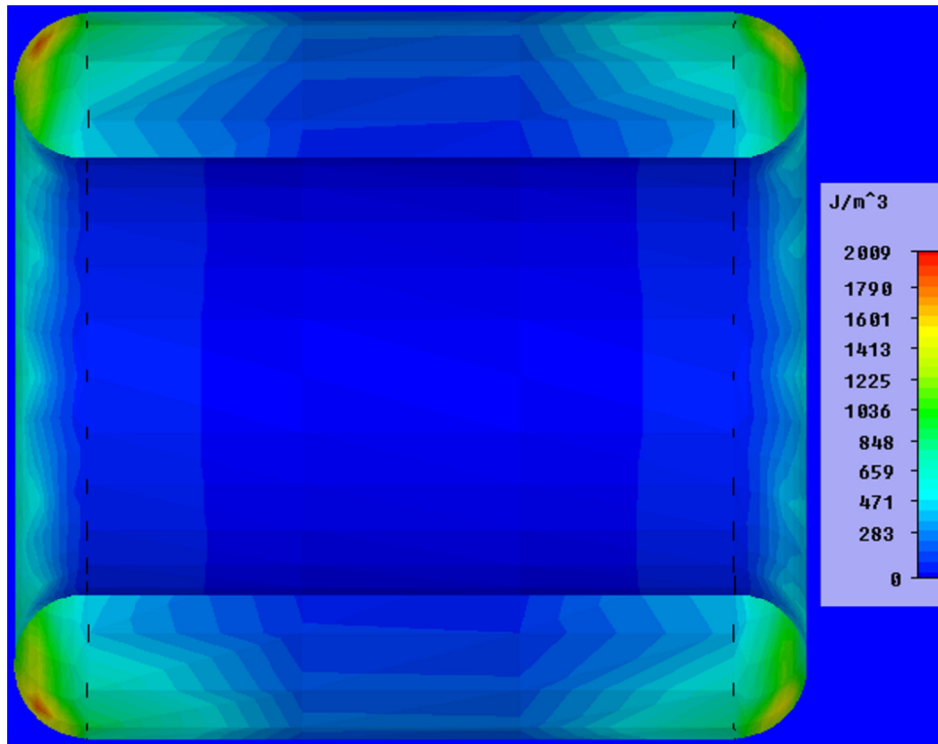
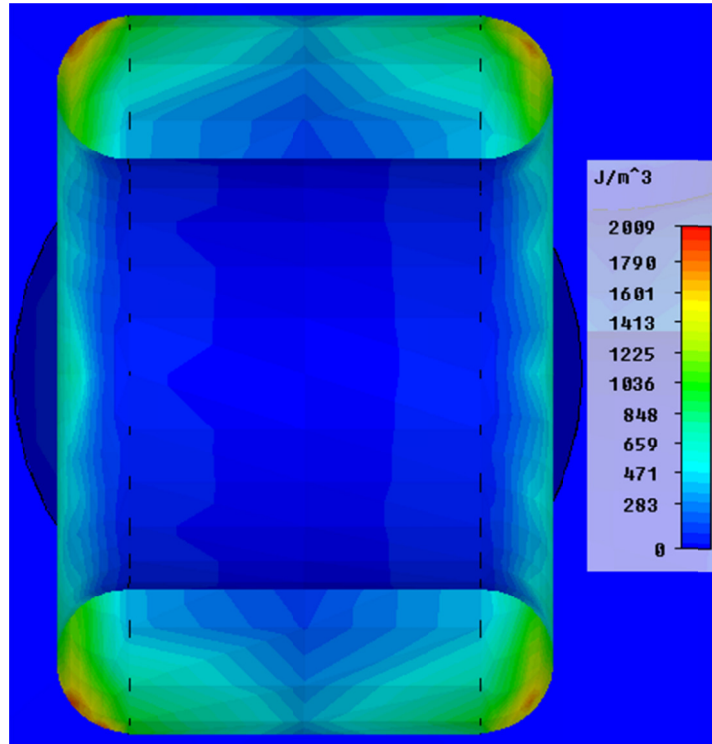


Figure 7.11: The electric energy density distribution for the shortest D3 (up) and longest D5 (down) drift tubes in cavity 1.

As mentioned before the stems carry the highest current density. From Figures 7.12 – 7.13, it can be seen that the highest magnetic field densities are also located on the stem surfaces.

A summary for this study is given in table 7.1 which shows the main parameters of the first CH – cavity for this linac.

Table 7.1: The main characteristic parameters of the first CH – cavity of the dedicated linac for laser accelerated protons.

Number of Gaps	7
Frequency (MHz)	325.2
Energy Range (MeV)	10.05 – 16.09
Power Loss (MW)	1.92
Q_0 – value	13289
Effective Shunt impedance (M Ω /m)	45.7
Accelerating Field Gradient (MV/m)	12.6
Beam Aperture (mm)	30
Outer Drift Tube Diameter (mm)	50
Total Length (mm)	668.4

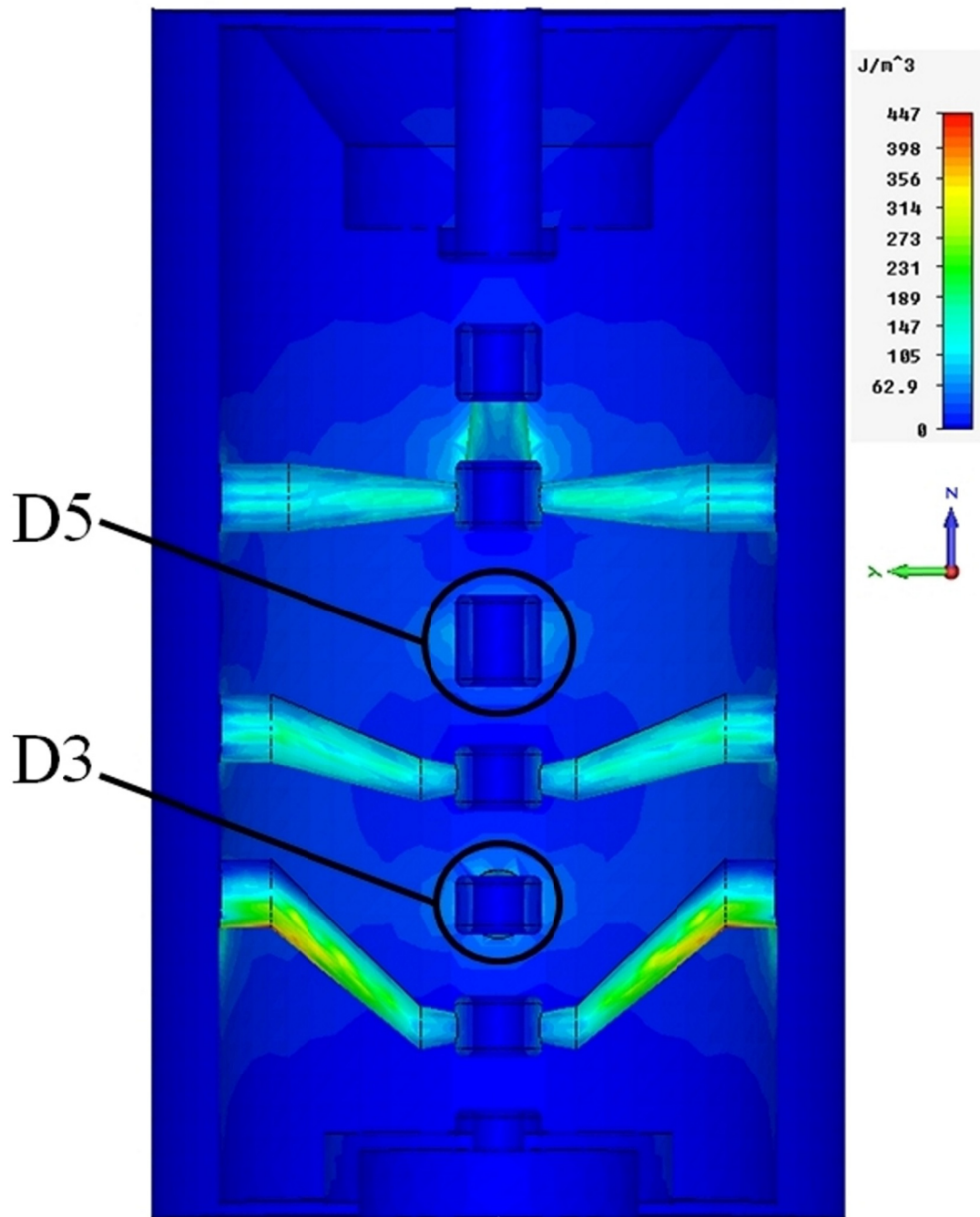


Figure 7.12: The magnetic energy density inside the cavity CH – 1 in yz – plane reflects very well the surface current distribution as shown by Figure 7.2.

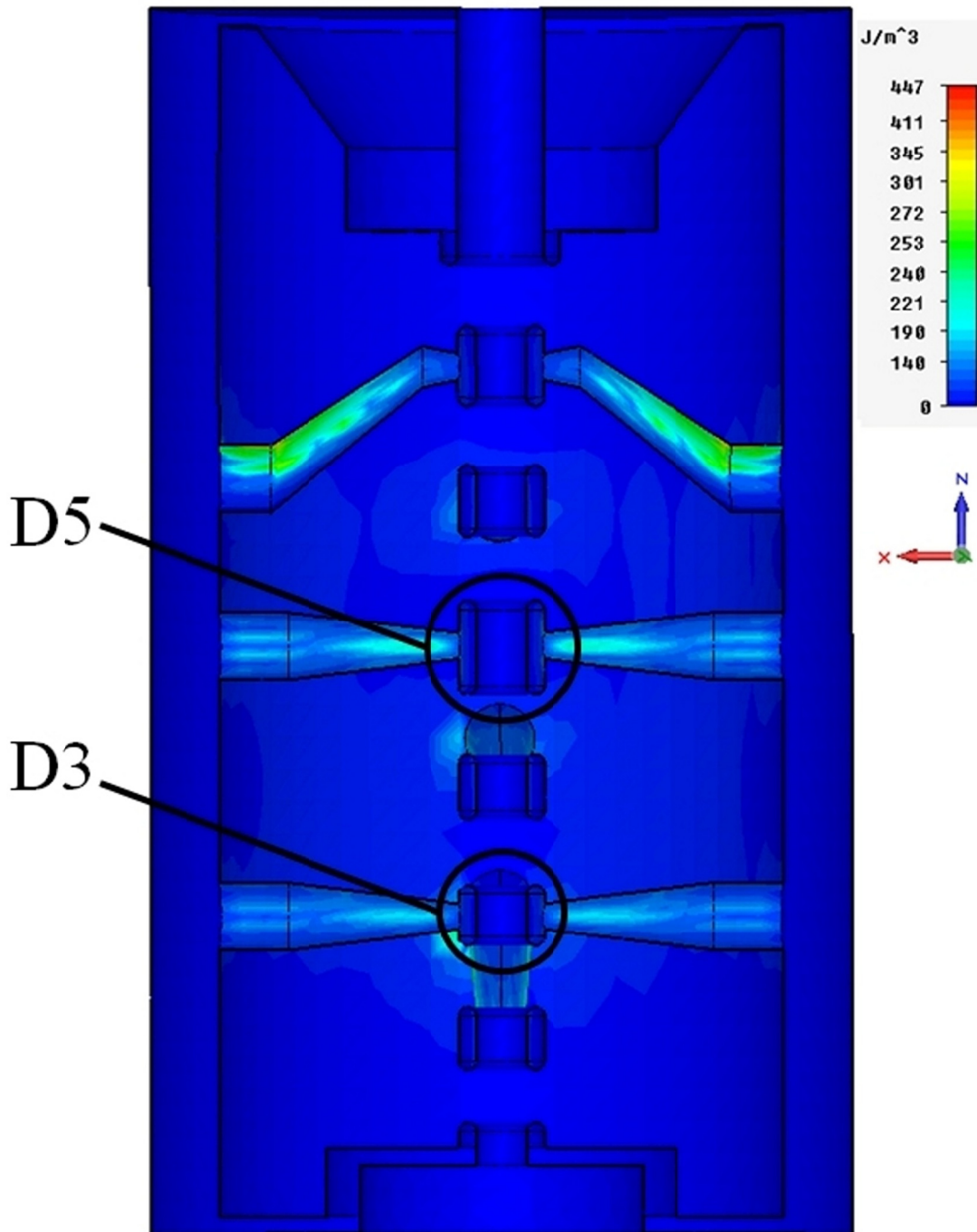


Figure 7.13: The magnetic energy density inside the cavity CH – 1 in xz - plane.

7.2 Surface Field Distribution

In chapter 6 it was mentioned that, high gap voltages of typically 1 MV are applied in order to get a robust longitudinal bunch focusing and to prevent beam losses. The CH – DTL linac discussed in chapter 6 was simulated for 500 mA. As a consequence of strong space charge forces, a high accelerating field gradient of the order 12.6 MV/m is needed.

On the other hand, at high gap voltages the room temperature cavities will experience problems because of electric breakdown (sparking).

Because of no internal focusing elements in this CH – DTL, the adaption of slim drift tubes is possible. This behavior of the drift tubes results in many interesting features like a very high sparking limit when compared with other structures.

For example, the surface electric field in the IH2 cavity of the CERN Lead Ion Linac (LINAC 3) reached about 54 MV/m locally on the drift tubes surfaces (see Figure 7.14) [213, 215]. This value is about 3.5 times higher than the Kilpatrick limit [215].

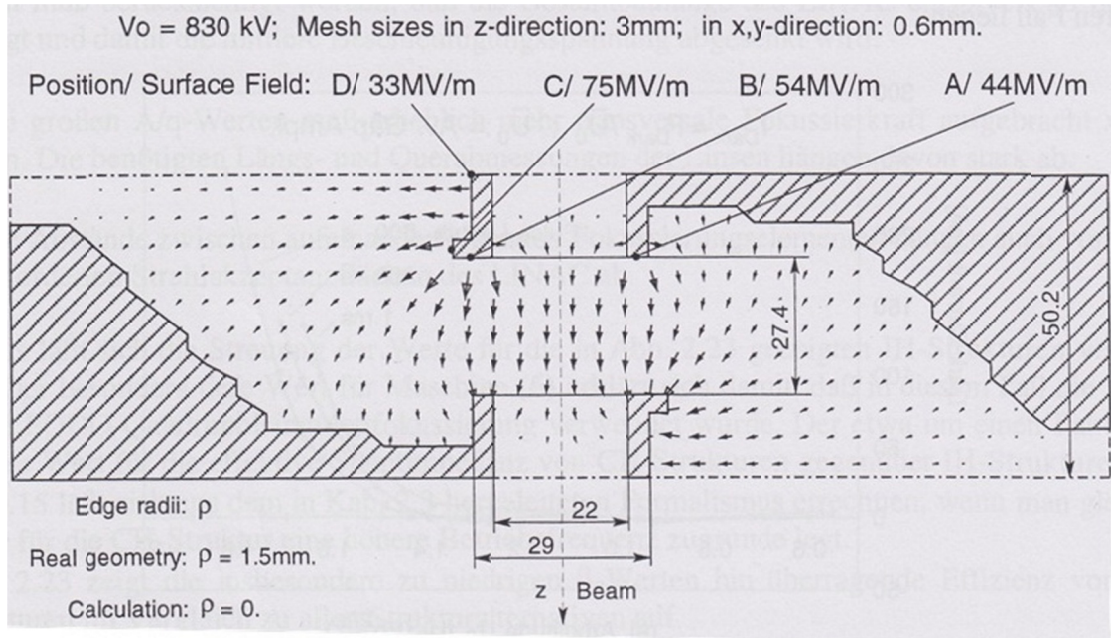


Figure 7.14: Calculated electric field for the gap number 9 in the plane of the stems using MAFIA code. The value of the electric field is given at four representative points on the drift tube surface. The gap reached voltage of 830 kV in high power tests (Courtesy of U. Ratzinger).

The maximum effective accelerating gradient for this cavity was reaching 10.7 MV/m. This corresponds to a 75 MV/m surface electric field spot at the drift tube bulges (see Figure 7.14).

To investigate the surface electric field in the CH – DTL discussed in the previous section, several simulations with CST – MWS had been performed.

The surface field distributions for each tube were calculated and the maximum values are summarized together with the maximum gap voltages in table 7.2.

Figure 7.15 shows the positions for the calculated values in table 7.2.

Table 7.2: A summary for the maximum surface electric fields together with the maximum gap voltage values. The ratio between the surface field value before and after the gap to the gap voltage is shown.

Max. surface electric field on drift tube, E_s (MV/m)		Gap No.	Max. gap electric on axis field, E_g (MV/m)	$E_{s,i}/E_{g,i}$	$E_{s,i+1}/E_{g,i}$
before the gap	after the gap				
36.7	63.7	g1	25.4	1.50	2.51
65.7	94.0	g2	29.7	2.21	3.17
84.2	65.8	g3	29.7	2.84	2.22
74.1	83.9	g4	31.4	2.36	2.67
77.0	83.8	g5	29.7	2.59	2.82
88.1	72.3	g6	29.0	3.04	2.49
70.4	21.8	g7	23.0	3.06	0.95

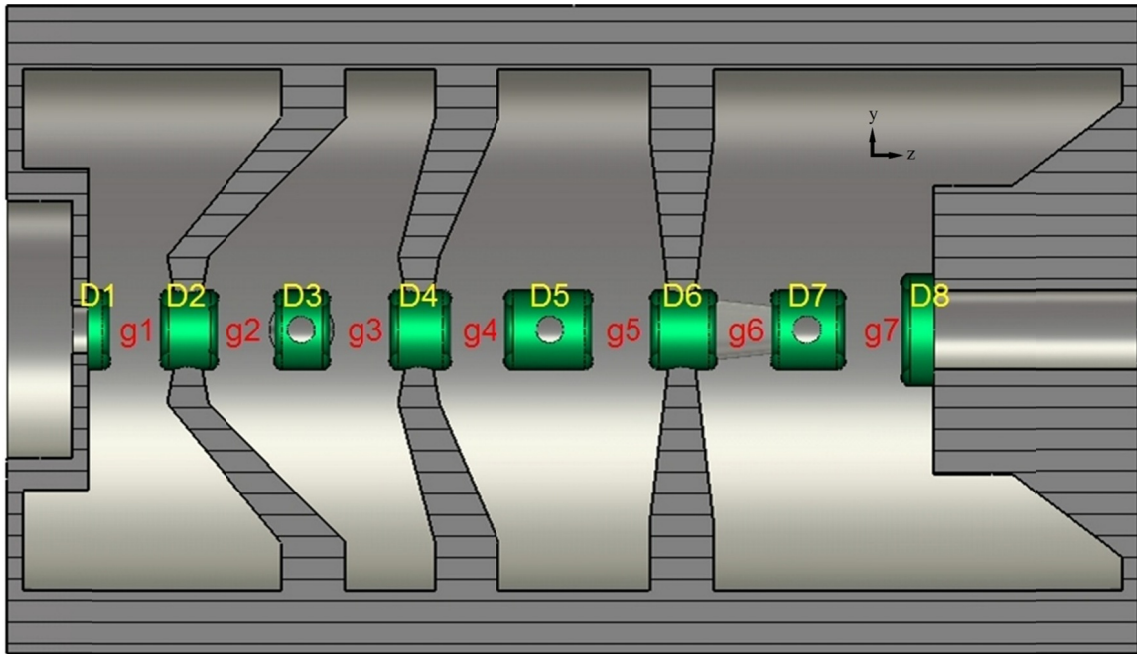


Figure 7.15: A schematic view for the first CH – Cavity showing the corresponding positions for the calculated values in table 7.2.

Figures 7.16 – 7.17 show the off axis electric field distribution passing the maximum surface field values in xz (Figure 7.16) – and yz (Figure 7.17) – planes, respectively. The paths, where these values are calculated, are shown in Figure 7.18.

The maximum values reached 94 MV/m and 88.1 MV/m on third and sixth drift tubes, respectively. The reason to have the maximum surface field on these positions is mainly due

to the inclined stems. In case of straight stems, the surface field distribution is similar to the on axis distribution unless the values are different.

As a consequence, the stems should get a larger straight element close to the drift tubes to reduce that effect.

In the CST – MWS simulations the drift tubes edges are rounded to have realistic geometry. Thus the field values on the surfaces can be taken as a good estimation for the field values in reality.

Another important distribution which is important for the beam dynamics is the electric field distribution along the path 3 which is parallel to the beam axis and displaced radially by the aperture radius (path 3, Figure 7.18). This can be seen in Figure 7.19.

The longitudinal electric field distribution along the path AB in gap number 2 of the CH cavity is shown in Figure 7.20.

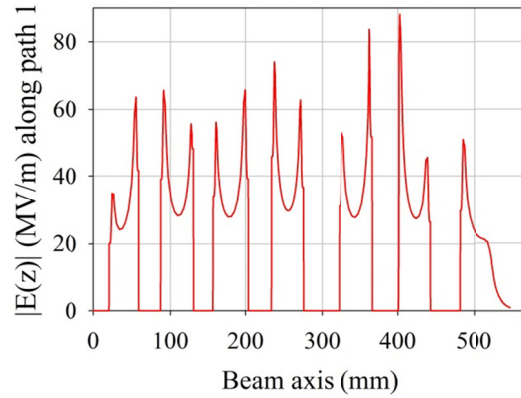


Figure 7.16: Electric field distribution along the curve passing the maximum electric field values on the drift tubes surfaces in xz - plane. This is path 1 as indicated in Figure 7.18. The maximum value is located at the right edge of drift number 6 (D6 in Figure 7.15) and it reached 88.1 MV/m.

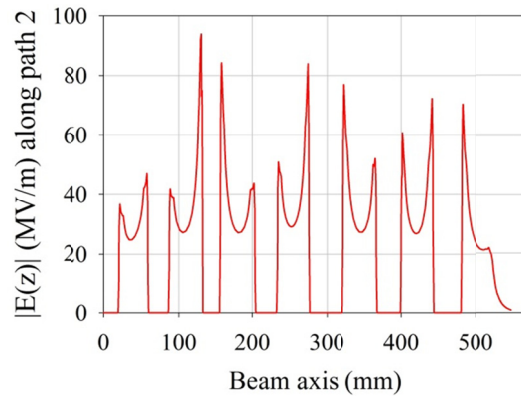


Figure 7.17: Electric field distribution along path 2 as indicated in Figure 7.18. The maximum value is located at the edge of the third drift tube (D3 in Figure 7.15) and it reached 94.0 MV/m.

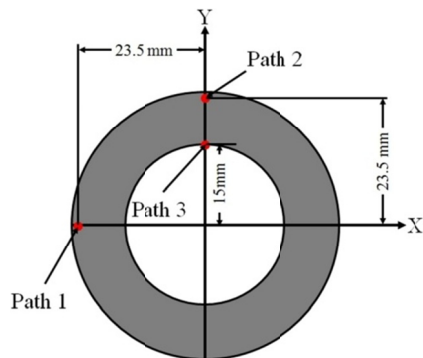


Figure 7.18: The paths used to calculate the surface electric field distribution in xz - plane (path 1), in yz - plane (path 2) and in yz - plane along the path which is parallel to the beam axis at $r = 15$ mm (path 3).

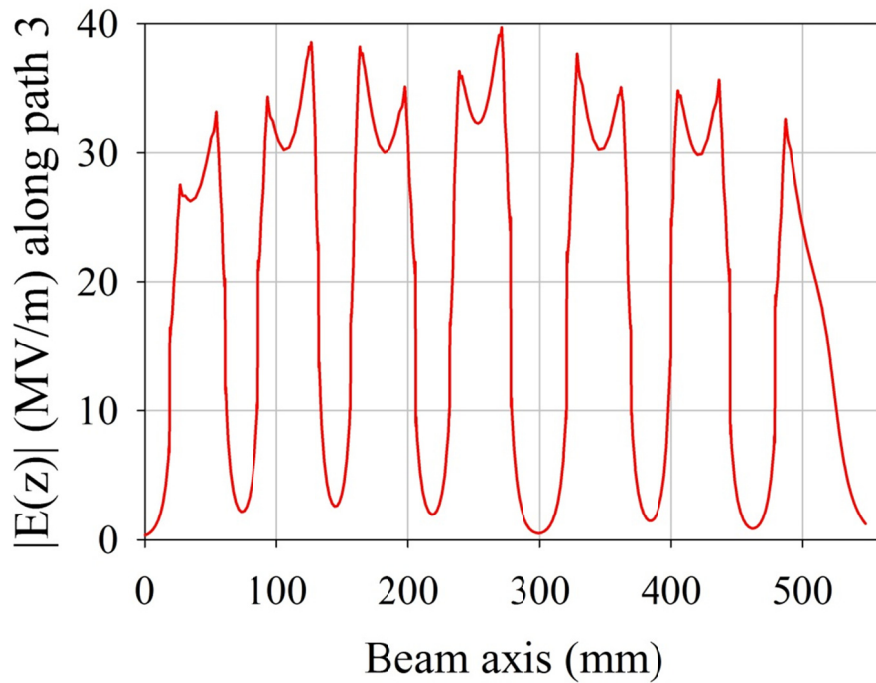


Figure 7.19: Electric field distribution along the line parallel to the beam axis and displaced radially with a distance equal to the inner drift tube radius = 15 mm.

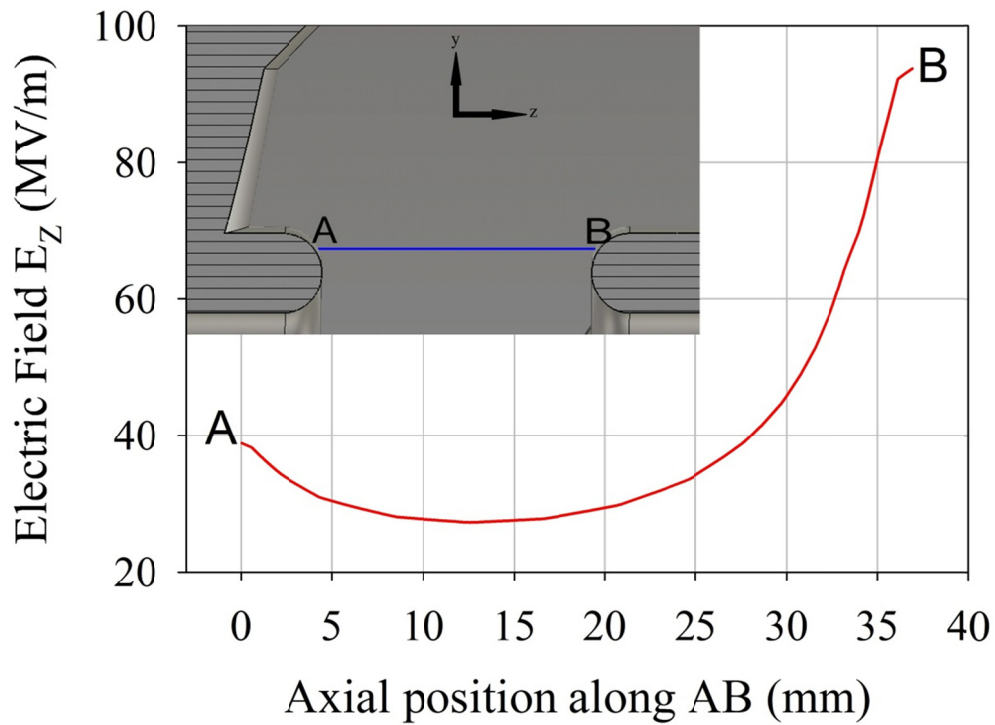


Figure 7.20: Longitudinal electric field distribution along the path AB in gap number 2 of the CH – cavity shown in Figure 7.1.

CHAPTER 8

CONCLUSION AND OUTLOOK

The results of this study show that the matching of laser – accelerated protons into a conventional RF drift tube linac is possible.

Laser driven proton beam sources (TNSA) possess attractive features in terms of energy and proton number per bunch. These interesting features make them attractive to be used as RF linac injectors at energies as high as 10 *MeV* or beyond.

With respect to laser – accelerated beams, the high current capability of the CH – DTL cavity has been investigated. Beam simulations have demonstrated that 10^{10} protons per bunch can be accelerated successfully and loss free along the structure.

The high number of particles per bunch and the feature of delivering single bunches to the experiment are unique. Moreover, the beam power is delivered by the stored energy in the linac cavities and does not cause a demand for larger RF amplifier, while in case of multi bunch acceleration the beam power has to be derived additionally by the RF amplifier.

In section 6.4, it was shown that, the maximum number of protons per bunch that can be accelerated in the first cavity by exploiting about 1% of the stored field energy is 2.02×10^{11} protons. This corresponds to an equivalent beam current of 10.5 A.

The maximum proton number can be compared with a particle number of 4.3×10^9 in the simulated bunch example in section 6.1.2.

One further aspect is the total number of protons arriving at the linac entrance. These particles might cause cavity sparking when hitting the wall. Even cavity de-phasing might occur by a large particle fraction with energies close enough to the accepted energy window. To reduce the risk of sparking, the intense low energy part of the laser generated pulse should be cut at the linac entrance by scrapers. Moreover, the inner drift tube contour can be optimized to reduce the secondary particle emission.

The total number of accepted particles with energies above 10.5 MeV is estimated to about 5×10^9 . But they are continuously distributed in rf phase. One main aspect of an rf post-acceleration experiment will be the rf operation stability under these beam load conditions.

Single bunch proton numbers of around 10^{10} at the linac exit seem within reach. Detailed simulations from the target along the solenoid and down to the linac entrance were presented, applying adapted software. Special care was taken on the time steps, especially close to the target, and on the collective phenomena between electron and proton distributions. The effect of co-moving electrons on the beam dynamics has been investigated in detail.

The resulting emittance values in all three planes are relatively large at linac injection, due to the high phase space density at bunch generation which leads to emittance growth along the transport section.

A CH – linac with high space charge limit and large transverse and longitudinal acceptance was designed to accept a maximum fraction of the laser generated proton bursts. The high particle number per bunch requires a high voltage gain per meter along the linac to get enough longitudinal focusing force. The described example is at the upper technical limit. The voltage can be reduced by up to 50 % with only a minor increase in emittance growth and at beam losses below 0.5 %.

Hence, high voltage gains of the order 1 MV are attractive to minimize the beam losses along the linac. This aspect becomes very important at the low energy end of the rf linac.

Due to well-known transformations of the injected beam emittances along the CH- cavity, it is aimed to derive parameters of the TNSA generated beam by measuring the beam properties behind of the CH- cavity. Different CH operation settings may allow solving this interesting task.

Attractive applications for single bunch operation as delivered naturally by laser driven systems might occur, involving time of flight techniques or the study of secondary reactions at low noise level, for instance.

The time averaged beam current at the linac exit may be increased to more interesting values for certain applications, if advanced laser systems with much higher repetition rates (100 Hz to several kHz) will become available. On the other hand, conventional injectors consisting of an ion source, low energy beam transport LEBT and radiofrequency quadrupole RFQ will be

superior if a high time averaged proton current is needed, as these systems are flexible in the beam pulse structure up to cw operation.

With respect to the linac development it is intended to realize the first cavity of the proposed CH – DTL and to demonstrate the acceleration of a laser generated proton bunch with the LIGHT project.

The first cavity consists of 7 gaps within a total length of about 668 mm. It is operated at 325 MHz and has an effective accelerating field gradient of about 12.6 MV/m.

The study on the surface electric field for this cavity shows, that maximum surface fields of about 94 MV/m and 88 MV/m on the third and sixth drift tubes are reachable, respectively. These values are about 5.2 and 4.9 times greater than the Kilpatrick limit. However, they appear very locally only at the drift tube ends.

Further optimization and development is needed in order to optimize the proposed CH - cavities by using the CST – MicroWave Studio (MWS), and by improving cavity surface preparation techniques. This concept will lead towards intense single proton bunch acceleration far above particle numbers reached so far by conventional accelerator techniques.

This work is connected to the LIGHT project as an advanced option. LIGHT is proposed to produce a controllable compact laser – proton source with controlled energy and divergence, which can be injected into a conventional accelerator. It is a collaboration project including GSI - Helmholtzzentrum für Schwerionenforschung GmbH, Technische Universität Darmstadt, the newly founded Helmholtz-Institute Jena, the Forschungszentrum Dresden-Rossendorf and the Institute for applied Sciences at the University of Frankfurt (UF).

Figure 8.1 contains the CH – cavity which will get beam from PHELIX by rotating the target chamber by 90° counter clockwise. This experiment will allow testing a most direct coupling of the rf linac with the laser source by using only one compact, pulsed magnetic solenoid for matching

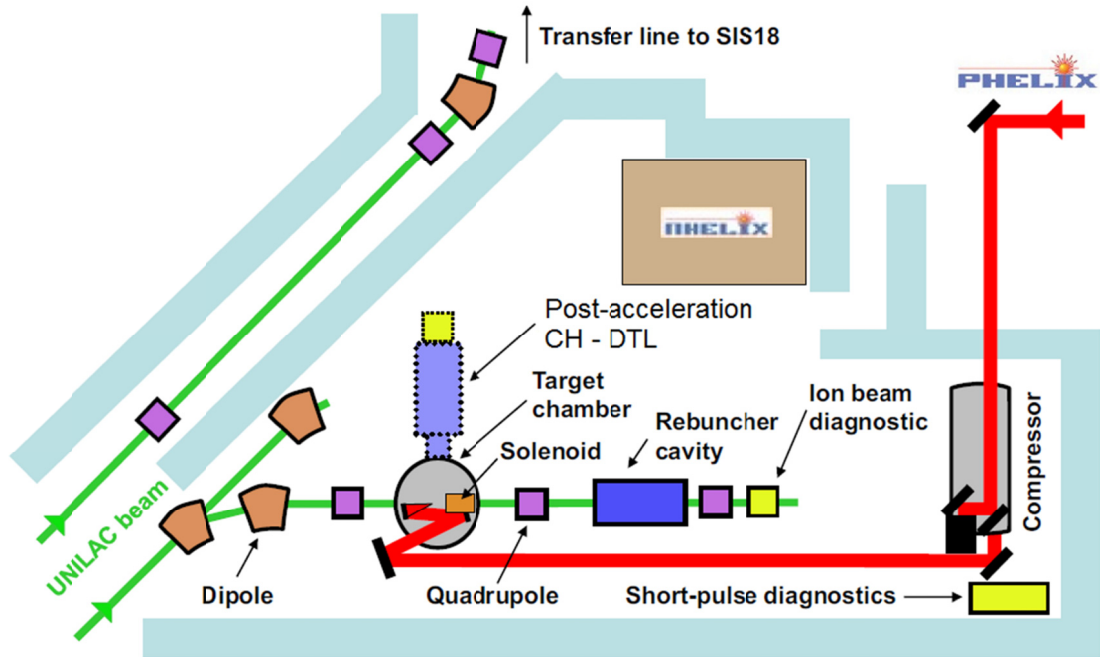


Figure 8.1: Overview of the experimental areas Z4 and Z6 at the GSI Helmholtzzentrum für Schwerionenforschung GmbH. The CH – cavity which will get beam from PHELIX by rotating the target chamber by 90° counter clockwise is indicated (Courtesy of B. Zielbauer).

BIBLIOGRAPHY

- [1] D. A. Edwards and M. J. Syphers. “*An Introduction to the Physics of High Energy Accelerators*”. John Wiley & Sons, Inc., 605 Third Avenue, New York, NY 10158-0012, 1993.
- [2] J.D. Cockcroft and E.T.S. Walton, “*Experiments with high velocity ions*”, *Proced. of Royal Society, Series A* **136**, 619 (1932).
- [3] R. Wideröe, *Arch.fr Elektrotechnik* **21**, 387 (1928).
- [4] E.O. Lawrence and N.E. Edlefsen, “On the Production of High Speed Protons”, *Science* **72**, 376 (1930).
- [5] The Large Hadron Collider, <http://lhc.web.cern.ch/lhc/>.
- [6] A. Maksimchuk, S. Gu, K. Flippo, D. Umstadter, and V.Yu. Bychenkov. Forward Ion Acceleration in Thin Films Driven by a High-Intensity Laser. *Phys. Rev. Lett.* **84**, 4108 (2000).
- [7] E. Clark, K. Krushelnick, M. Zepf, F. Beg, M. Tatarakis, A. Machacek, M. Santala, I. Watts, P. Norreys, and A. Dangor. “*Energetic heavy-Ion and proton generation from ultraintense laser-plasma interactions with solids*”. *Phys. Rev. Lett.* **85**, 1654 (2000).
- [8] R.A. Snavely et al., “*Intense High-Energy Proton Beams from Petawatt-Laser Irradiation of Solids*”, *Phys. Rev. Lett.* **85**, 2945 (2000).
- [9] P. Stephen et al., “*Electron, photon and ion beams from relativistic interaction of Petawatt laser pulses with solid targets*”. *Phys. Plasmas* **7**, 2076 (2000).
- [10] S.C. Wilks, A.B. Langdon, T.E. Cowan, M. Roth, M. Singh, S. Hatchett, M.H. Key, D. Pennington, A. MacKinnon, and R.A. Snavely. “*Energetic proton generation in ultra-intense laser-solid interactions*”. *Phys. Plasmas* **8**, 542 (2001).
- [11] M. Hegelich et al., “*MeV ion jets from short-pulse-laser interaction with thin foils*”. *Phys. Rev. Lett.* **89**, 085002 (2002).
- [12] A. Mackinnon, M. Borghesi, S. Hatchett, M. Key, P. Patel, H. Campbell, A. Schiavi, R. Snavely, S. Wilks, and O. Willi. “*Effect of plasma scale length on multi-MeV proton production by intense laser pulses*”. *Phys. Rev. Lett.* **86**, 1769 (2001).
- [13] M. Roth et al., “*Energetic ions generated by laser pulses: A detailed study on target properties*”. *Phys. Rev. Special Topics - Accelerators and Beams* **5**, 061301 (2002).
- [14] M. Allen, P.K. Patel, A. Mackinnon, D. Price, S. Wilks, and E. Morse. “*Direct experimental evidence of back-surface ion acceleration from laser-irradiated gold foils*”, *Phys. Rev. Lett.* **93**, 265004 (2004).
- [15] Y. Murakami, Y. Kitagawa, Y. Sentoku, M. Mori, R. Kodama, K.A. Tanaka, K. Mima, and T. Yamanaka. “*Observation of proton rear emission and possible gigagauss scale magnetic fields from ultra-intense laser illuminated plastic target*”. *Phys. Plasmas* **8**, 4138 (2001).
- [16] E. Brambrink, J. Schreiber, T. Schlegel, P. Audebert, J. Cobble, J. Fuchs, M. Hegelich,

- and M. Roth. “*Transverse characteristics of short-pulse laser-produced ion beams: a study of the acceleration dynamics*”. Phys. Rev. Lett. **96**, 154801 (2006).
- [17] A. Fews, P. Norreys, F. Beg, A. Bell, A. Dangor, C. Danson, P. Lee and S. Rose, “*Plasma ion emission from high intensity picosecond laser pulse interaction with solid targets*”, Phys. Rev. Lett. **73**, 1801 (1994).
- [18] E. Clark et al., “*Measurements of Energetic Proton Transport through Magnetized Plasma from Intense Laser Interactions with Solids*”, Phys. Rev. Lett. **84**, 670 (2000).
- [19] A. Almomani, M. Droba, U. Ratzinger and I. Hofmann. “*Matching the Laser Generated p – Bunch into a CH – DTL*”, GSI Scientific Report, Plasma-Physics-**22**, p.407 (2009).
- [20] F. Nürnberg et al., “*Radiochromic film imaging spectroscopy of laser – accelerated proton beams*”, Rev. Sci. Inst. **80**, 033301 (2009).
- [21] L. Robson et al., “*Scaling of proton acceleration driven by petawatt-laser-plasma interactions*”. Nature Phys. **3**, 58 (2007).
- [22] M. Roth et. al., “*Proton acceleration experiments and warm dense matter research using high power lasers*”, Plasma Phys. Control. Fusion **51**, 124039 (2009).
- [23] M. Dunne. “*Laser – Driven Particle Accelerators*”, Science **312**, 374 (2006).
- [24] M. Schollmeier et al., “*Laser beam-profile impression and target thickness impact on laser-accelerated protons*”. Phys. Plasmas **15**, 053101 (2008).
- [25] H. Schworer et. al., “*Laser-plasma acceleration of quasi-monoenergetic protons from microstructured targets*”, Nature **439**, 445 (2006).
- [26] B. Hegelich. “*Acceleration of Heavy Ions to MeV/nucleon Energies by Ultrahigh-Intensity Lasers*”, Dissertation, Ludwig-Maximilians-Universität München, 2002.
- [27] M. Kaluza. “*Characterisation of Laser – Accelerated Proton Beams*”, Dissertation, Technischen Universität München, 2004.
- [28] S. Becker. “*Dynamics and Transport of Laser – Accelerated Particle Beams*”, Dissertation, Ludwig-Maximilians-Universität München, 2010.
- [29] R. Jung. “*Laser – Plasma Interaction with Ultra-short Laser Pulses*”, Dissertation, Heinrich-Heine-Universität Düsseldorf, 2007.
- [30] K-U. Amthor. “*Laser Plasma Accelerators for Charged Particles*”, Dissertation, Friedrich-Schiller-Universität Jena, 2006.
- [31] O. Shorokhov. “*Generation and Propagation of Energetic Particles in Relativistic Laser – Matter Interactions*”, Dissertation, Heinrich-Heine-Universität Düsseldorf, 2005.
- [32] M. S. Schollmeier. “*Optimization and Control of Laser – Accelerated Proton Beams*”, Dissertation, Technischen Universität Darmstadt, 2008.
- [33] J. Schreiber. “*Ion Acceleration Driven by High – Intensity Laser Pulses*”, Dissertation, Ludwig-Maximilians-Universität München, 2006.
- [34] F. Nürnberg. “*Laser – Accelerated Proton Beams as a New Particle Source*”, Dissertation, Technischen Universität Darmstadt, 2010.

- [35] M. Amin. “Experimental Control of the beam properties of Laser – Accelerated protons and Carbon Ions”, Dissertation, Heinrich-Heine-Universität Düsseldorf, 2008.
- [36] D. Strickland et al., “*Compression of amplified chirped optical pulses*”. Optics Communication **56**, 219 (1985).
- [37] C. Danson et al., “*Vulcan Petawatt – an ultra-high-intensity interaction facility*”. Nucl. Fusion **44**, S239 (2004).
- [38] Y. Kitagawa et al., “*Prepulse-Free Petawatt Laser for a Fast Ignition*”. IEEE Journal of Quantum Electronics **40**, 281 (2004).
- [39] C. Hernandez-Gomez et al., “*The Vulcan 10 PW OPCPA project*”. Central Laser Facility Annual Report page 210 (2007).
- [40] V. Bagnoud et al., “*Commissioning and early experiments of the PHELIX facility*”. Appl. Phys. B DOI, 10.1007/s00340-009-3855-7 (2009).
- [41] K. Krushelnick et al., “*Ultrahigh-intensity laser-produced plasmas as a compact heavy ion injection source*”. IEEE Transactions on Plasma Science **28**, 1184 (2000).
- [42] F. Pegoraro et. al., “*Generation and Propagation of High Quality Proton Beams Produced by Laser Plasma Interactions*”, Physica Scripta **T107**, 130 (2004).
- [43] J. Fuchs et al., “*Comparison of Laser Ion Acceleration from the Front and Rear Surfaces of Thin Foils*”, Phys. Rev. Lett. **94**, 045004 (2005).
- [44] M. Roth et. al., “*Laser accelerated ions and electrons transport in ultra-intense laser matter interaction*”, Laser and Particle Beams **23**, 95 (2005).
- [45] J. Fuchs et al., “*Laser-Foil Acceleration of High-Energy Proton in Small-Scale Plasma Gradients*”, Phys. Rev. Lett. **99**, 015002 (2007).
- [46] M. Borghesi et. al., “*Laser-accelerated high-energy ions: state of-the-art and applications*”, Journal of Physics: Conference Series **58**, 47-80 (2007).
- [47] M. Nishiuchi et al., “*Efficient production of a collimation MeV proton beam from a polyimide target driven by an intense femtosecond laser pulse*”, Phys. Plasmas **15**, 053104 (2008).
- [48] I. Hofmann, A. Orzhekhovskaya, S. Yaramyshev, I. Alber, K. Harres and M. Roth. “*Laser Accelerated Ions and their Potential for Therapy Accelerators*”, Proc. HIAT09, Venice, Italy, FR-06 (2009).
- [49] T. Tajima and J. Dawson, “*Laser Electron Accelerator*”, Phys. Rev. Lett. **43**, 267 (1992).
- [50] B. Hegelich et al., “*Laser acceleration of quasi-monoenergetic MeV ion beams*”, Nature **439**, 441 (2006).
- [51] I. Hofmann, J. Meyer-ter-Vehn, X. Yan, A. Orzhekhovskaya and S. Yaramyshev. “*Collection and Focusing of Laser Accelerated Ion Beams for Therapy Application*”, Phys. Rev. Special Topics – Accelerators and Beams **14**, 031304 (2011).
- [52] K. Krushelnick et al., “*Energetic proton production from relativistic laser interaction with high density plasmas*”. Phys. Plasmas **7**, 2055 (2000).

- [53] T. Cowan et al., “*Intense electron and proton beams from PetaWatt laser-matter interactions*”. Nucl. Instrum. and Meth. **A 455**, 130 (2000).
- [54] S. Karsch et al. “*Highly-Intensity Laser Induced Ion Acceleration from Heavy-Water Droplets*”, Phys. Rev. Lett. **91**, 015001 (2003).
- [55] Y. Sentoku, K. Mima, P. Kaw and K. Nishikawa. “*Anomalous Resistivity Resulting from MeV – Electron Transport in Overdense Plasma*”, Phys. Rev. Lett. **90**, 155001 (2003).
- [56] T. Cowan et al., “*Ultra-low emittance, high current proton beams produced with a laser-virtual cathode sheath accelerator*”. Nucl. Instrum. and Meth. **A 544**, 277 (2005).
- [57] T. Tajima and G. Mourou, “*Zettawatt-exawatt lasers and their applications in ultrastrong-field physics*”, Phys. Rev. Special Topics – Accelerators and Beams **5**, 031301 (2002).
- [58] G.A. Mourou, T. Tajima and S.V. Bulanov, “*Optics in the relativistic regime*”, Rev. Mod. Phys. **78**, 309 (2006).
- [59] P. Antici, M. Fazi, A. Lombardi, M. Migliorati, L. Palumba, P. Audebert and J. Fuchs. “*Postacceleration of Laser – Generated High Energy Protons through Conventional Accelerator Linacs*”, IEEE Transaction on Plasma Science **36**, 1843 (2008).
- [60] M. Roth et al., “*The generation of high-quality, intense ion beams by ultra-intense lasers*”, Plasma Phys. Control. Fusion **44**, B99 (2002).
- [61] T. Cowan et al., “*Ultralow Emittance, Multi-MeV Proton Beams from a Laser Virtual-Cathode Plasma Accelerator*”, Phys. Rev. Lett. **92**, 204801 (2004).
- [62] M. Borghesi, A.J. Mackinnon, D.H. Campbell, D.G. Hicks, S. Kar, P.K. Patel, D. Price, L. Romagnani, A. Schiavi and O. Willi, “*Multi-MeV Proton Source Investigations in Ultraintense Laser-Foil Interactions*”, Phys. Rev. Lett. **92**, 055003 (2004).
- [63] T. Cowan et al., “*Ultra-low emittance, high current proton beams produced with a laser-virtual cathode sheath accelerator*”, Nucl. Instrum. and Meth. **A 544**, 277 (2005).
- [64] A. Kemp, J. Fuchs, Y. Sentoku, V. Sotnikov, M. Bakeman, P. Antici, and T. Cowan. “*Emittance growth mechanisms for laser-accelerated proton beams*”, Phys. Rev. **E 75**, 056401 (2007).
- [65] B. Hegelich et al., “*Spectral properties of laser-accelerated mid-Z MeV/u ion beams*”, Phys. Plasmas **12**, 056314 (2005).
- [66] A. Schempp. “*RFQ Ion Accelerators*”, Nucl. Instrum. and Meth. **B45**, 302 (1990).
- [67] A. Schempp. “*Overview of Recent RFQ Projects*”, Proc. LINAC08, Victoria, BC, Canada, MO302 (2008).
- [68] S. Yaramyshev, W. Barth, I. Hofmann, A. Orzhekhovskaya and B. Zielbauer. “*Capture and Transport of the Laser Accelerated Ion Beams for the LIGHT project*”, Proc. IPAC11, San Sebastián, Spain, MOODB03 (2011).
- [69] S. Busold et al. “*Laser – Proton Acceleration as Compact Ion Source*”, Proc. PAC11, New York, NY, USA, WEP256 (2011).
- [70] C. Ronsivalle et al. “*Hybrid Schemes for the Post-Acceleration of Laser Generated Protons*”, Proc. IPAC10, Kyoto, Japan, THPD038 (2010).

- [71] A. Almomani, M. Droba, U. Ratzinger and I. Hofmann. “*Matching the Laser Generated p – Bunch into a CH – DTL*”, Protons”, Proc. IPAC10, Kyoto, Japan, THPD035 (2010).
- [72] Project Report. “*LIGHT – Laser Ion Generation, Handling and Transport*”. <https://www.gsi.de/documents/DOC-2010-Nov-36-1.pdf>
- [73] B. Zielbauer et al. “*LIGHT Update: A Laser – Based Ion – Source at Z6*”, GSI Scientific Report, PNI-PP-16, p.421 (2010).
- [74] U. Ratzinger et al. “*A 70 – MeV Proton LINAC for the FAIR Facility Based on CH – Cavities*”, Proc. LINAC06, Knoxville, Tennessee, USA, TH1004 (2006).
- [75] U. Ratzinger and R. Tiede, “*Status of the HIF RF Linac Study Based on H-Mode Cavities*”, Nucl. Instrum. Meth. A **415**, 229 (1998).
- [76] G. Clemente, U. Ratzinger, H. Podlech, L. Groening, R. Brodhage and W. Barth. “*Development of Room Temperature Crossbar-H-mode Cavities for Proton and Ion Acceleration in the Low to Medium Beta Range*”, Phys. Rev. Special Topic – Accelerators and Beams **14**, 110101 (2011).
- [77] F. Nürnberg et al. “*Warp Simulation for Capture and Control of Laser – Accelerated Proton Beams*”, Journal Phys. Conference Series **244**, 022052 (2010).
- [78] K. Harres et al., “*Beam Collimation and Transport of Quasineutral Laser – Accelerated Protons by a Solenoid Field*”, Phys. Plasmas **17**, 023107 (2010).
- [79] M. Schollmeier et al., “*Laser ion acceleration with micro-grooved targets*”, Nucl. Instrum. and Meth. A **577**, 186 (2007).
- [80] K. Flippo et al., “*Increased efficiency of short-pulse laser-generated proton beams from novel flat-top cone targets*”. Phys. Plasmas **15**, 056709 (2008).
- [81] K. Flippo et al., “*Ablation cleaning techniques for high-power short-pulse laser-produced heavy ion targets*”. Proceedings of SPIE 6261, 62612I (2006).
- [82] K. Flippo et al., “*Ultrashort-laser-produced heavy ion generation via target ablation cleaning*”. Journal de Physique IV **133**, 1117 (2006).
- [83] E. Garcia Saiz et al., “*Probing warm dense lithium by inelastic x-ray scattering*”. Nature Phys. **4**, 940 (2008).
- [84] K. Harres et al., “*Development and calibration of a Thomson parabola with microchannel plate for the detection of laser-accelerated MeV ions*”. Rev. Sci. Instrum. **79**, 093306 (2008).
- [85] M. Roth et al., “*Laser accelerated heavy particles – Tailoring of ion beams on a nano-scale*”. Optics Communications **264**, 519 (2006).
- [86] M. Roth et al., “*Laser accelerated ions in ICF research prospects and experiments*”. Plasma Phys. Control. Fusion **47**, 841 (2005).
- [87] An. Tauschwitz, E. Brambrink, J.A. Maruhn, M. Roth, M. Schollmeier, T. Schlegel, and A. Tauschwitz. “*Laser-produced proton beams as a tool for equation-of-state studies of warm dense matter*”. High Energy Density Physics **2**, 16 (2006).
- [88] J. Schreiber, F. Bell, F. Grüner, U. Schramm, M. Geissler, M. Schnürer, S. Ter-Avetisyan, B.M. Hegelich, J. Cobble, E. Brambrink, J. Fuchs, P. Audebert, and D. Habs.

- “Analytical Model for Ion Acceleration by High-Intensity Laser Pulses”. *Phys. Rev. Lett.* **97**, 045005 (2006).
- [89] J. Schreiber et al., “*Pointing of laser-accelerated proton beams*”, *Phys. Plasmas* **13**, 033111 (2006).
- [90] J. Fuchs et al., “*Laser-driven proton scaling laws and new paths towards energy increase*”. *Nature Phys.* **2**, 48 (2006).
- [91] J. Honrubia, M. Kaluza, J. Schreiber, G. Tsakiris and J. Meyer ter Vehn, “*Laser-driven fast-electron transport in preheated foil targets*”, *Phys. Plasmas* **12**, 052708 (2005).
- [92] J.C. Fernández et al., “*Laser-ablation treatment of short-pulse laser targets: Towards an experimental program on energetic-ion interactions with dense plasmas*”, *Laser & Part. Beams* **23**, 267 (2005).
- [93] M. Roth et al., “*Laser accelerated ions and electron transport in ultra-intense laser matter interaction*”, *Laser & Part. Beams* **23**, 95 (2005).
- [94] M. Kaluza, J. Schreiber, M.I.K. Santala, G.D. Tsakiris, K. Eidmann, J. Meyer ter Vehn and K.J. Witte, “*Influence of the Laser Prepulse on Proton Acceleration in Thin-Foil Experiments*”, *Phys. Rev. Lett.* **93**, 045003 (2004).
- [95] J. Schreiber et al “*Source-size measurements and charge distributions of ions accelerated from thin foils irradiated by high-intensity laser pulses*”, *Appl. Phys.* **B 79**, 1041 (2004).
- [96] P. Gibbon and E. Förster. “*Short-Pulse Laser – Plasma Interactions*”, *Plasma Phys. Control. Fusion* **38**, 769 (1996).
- [97] D. Umstadter. “*Relativistic Laser – Plasma Interactions*”, *J. Phys. D: Appl. Phys.* **36**, R151 – R165 (2003).
- [98] L. Romagnani et al., “*Dynamics of electric fields driving the laser acceleration of multi-MeV protons*”. *Phys. Rev. Lett.* **95**, 195001 (2005).
- [99] Y. Sentoku, A.J. Kemp, R. Presura, M.S. Bakeman, and T.E. Cowan. “*Isochoric heating in heterogeneous solid targets with ultrashort laser pulses*”. *Phys. Plasmas* **14**, 122701 (2007).
- [100] P. McKenna et al., “*Lateral electron transport in high-intensity laser-irradiated foils diagnosed by ion emission*”. *Phys. Rev. Lett.* **98**, 145001 (2007).
- [101] E. Esarey, P. Sprangle, and J. Krall. “*Laser acceleration of electrons in vacuum*”. *Phys. Rev. E* **52**, 5443 (1995).
- [102] H. Boot and R. Shersby-Harvie. “*Charged Particles in a Non-uniform Radio-frequency Field*”. *Nature* **180**, 1187 (1957).
- [103] S. Wilks et al. “*Absorption of ultrashort, ultra-intense laser light by solids and overdense plasmas*”. *IEEE Journal of Quantum Electronics* **33**, 1954 (1997).
- [104] D. Bauer et al. “*Relativistic ponderomotive force, Uphill acceleration, and transition to chaos*”. *Phys. Rev. Lett.* **75**, 4622 (1995).
- [105] B. Lamb and G. Morales. “*Ponderomotive Effects in Nonneutral Plasmas*”, *Phys. Fluids* **26**, 3488 (1983).

- [106] G. Morales and Y. Lee. “*Ponderomotive Force Effects in a Nonuniform Plasma*”, Phys. Rev. Lett. **33**, 1016 (1974).
- [107] C. Grebogi and R. Littejohn. “*Relativistic Ponderomotive Hamiltonian*”, Phys. Fluids **27**, 1996 (1984).
- [108] B. Quesnel and P. Mora. “*Theory and Simulation of the Interaction of Ultraintense Laser Pulses with Electrons in Vacuum*”, Phys. Rev. **E 58**, 3719 (1998).
- [109] J. Badziak, S. Glowacz, S. Jablonski, P. Parys, J. Wolowski, H. Hora, J. Krása, L. Láska, and K. Rohlena. “*Production of ultrahigh ion current densities at skin-layer subrelativistic laser plasma interaction*”. Plasma Phys. Control. Fusion **46**, 541 (2004).
- [110] J. Badziak, P. Antici, J. Fuchs, S. Jabłowski, L. Lancia, A. Mancic, P. Parys, M. Rosiński, R. Suchańska, A. Szydłowski, and J. Wołowski. “*Ultrahigh-current proton beams from short-pulse laser-solid interactions*”. J. Phys.: Conf. Ser. **112**, 042040 (2008).
- [111] P. Mora and T. Antonsen. “*Kinetic modeling of intense, short laser pulses propagating in tenuous plasmas*”. Phys. Plasmas **4**, 217 (1997).
- [112] S. Wilks, W. Kruer, M. Tabak, and A. Langdon. “*Absorption of ultra-intense laser pulses*”. Phys. Rev. Lett. **69**, 1383 (1992).
- [113] G. Malka and J. Miquel. “*Experimental Confirmation of Ponderomotive-Force Electrons Produced by an Ultrarelativistic Laser Pulse on a Solid Target*”. Phys. Rev. Lett. **77**, 75 (1996).
- [114] H. Chen and S. Wilks. “*Evidence of enhanced effective hot electron temperatures in ultraintense laser-solid interactions due to reflexing*”. Laser Part. Beams **23**, 411 (2005).
- [115] F. Chen. *Introduction to Plasma Physics*. Plenum Press New York (1974).
- [116] A. Pukhov et al. “*Relativistic magnetic self-channeling of light in near-critical plasma: Three-dimensional particle-in-cell simulation*”. Phys. Rev. Lett. **76**, 3975 (1996).
- [117] M. Borghesi et al. “*Relativistic channeling of a picosecond laser pulse in a near-critical preformed plasma*”. Phys. Rev. Lett. **78**, 879 (1997).
- [118] F. Hartemann, S. Fochs, G. LeSage, N. Luhmann Jr., J. Woodworth, M. Perry, Y. Chen, and A. Kerman. “*Nonlinear ponderomotive scattering of relativistic electrons by an intense laser field at focus*”. Phys. Rev. **E 51**, 4833–4843 (1995).
- [119] D. Meyerhofer. “*High-intensity-laser-electron scattering*”. IEEE Journal of Quantum Electronics **33**, 1935 (1997).
- [120] F. Brandl, G. Pretzler, D. Habs, and E. Fill. “*Cerenkov radiation diagnostics of hot electrons generated by fs-laser interaction with solid targets*”. Europhysics Letters **61**, 632 – 638 (2003).
- [121] C. Moore, J. Knauer, and D. Meyerhofer. “*Observation of the Transition from Thomson to Compton Scattering in Multiphoton Interactions with Low-Energy Electrons*”. Phys. Rev. Lett. **74**, 2439 (1995).
- [122] M. Stoyer et al., “*Nuclear diagnostics for petawatt experiments*”. Rev. Sci. Instrum. **72**, 767 (2001).

- [123] M. Roth et al., “*Intense ion beams accelerated by Petawatt-class Lasers*”. Nucl. Instrum. and Meth. **A 464**, 201 (2001).
- [124] J. Yu et al., “*Hard x-ray emission in high intensity femtosecond lasertarget interaction*”, Phys. Plasmas **6**, 1318 (1999).
- [125] M. Key et al., “*Hot electron production and heating by hot electrons in fast ignitor research*”, Phys. Plasmas **5**, 1966 (1998).
- [126] J. Fuchs et al. “*Laser-driven proton scaling laws and new paths towards energy increase*”. Nature **2,48** (2006).
- [127] A. Robinson et al. “*Radiation pressure acceleration of thin foils with circularly polarized laser pulses*”. New J. Phys. **10**, 013021 (2008).
- [128] A. Henig et al. “*Radiation-Pressure Acceleration of Ion Beams Driven by Circularly Polarized Laser Pulses*”, Phys. Rev. Lett. **103**, 245003 (2009).
- [129] T. Esirkepov, M. Borghesi, S. V. Bulanov, G. Mourou and T. Tajima. “*Highly Efficient Relativistic – Ion Generation in the Laser – Piston Regime*”, Phys. Rev. Lett. **92**, 175003 (2004).
- [130] T. Esirkepov, M. Yamagiwa and T. Tajima. “*Laser Ion – Acceleration Scaling Laws Seen in Multiparametric Particle-In-Cell Simulations*”, Phys. Rev. Lett. **96**, 105001 (2006).
- [131] P. McKenna et al., “*Characterization of proton and heavier ion acceleration in ultrahigh-intensity laser interactions with heated target foils*”. Phys. Rev. **E 70**, 036405 (2004).
- [132] P. Mora. “*Plasma expansion into vacuum*”. Phys. Rev. Lett. **90**, 185002 (2003).
- [133] S. Betti et al. “*Expansion of a finite-size plasma in vacuum*”. Plasma Physics and Controlled Fusion **47**, 521 (2005).
- [134] P. Mora. “*Thin-foil expansion into a vacuum*”. Phys. Rev. **E 72**, 056401 (2005).
- [135] M. Passoni et al. “*Charge separation effects in solid targets and ion acceleration with a two-temperature electron distribution*”. Phys. Rev. **E 69**, 026411 (2004).
- [136] J. Fuchs et al., “*Comparative spectra and efficiencies of ions laser-accelerated forward from the front and rear surfaces of thin solid foils*”. Phys. Plasmas **14**, 053105 (2007).
- [137] P. Mora. “*Collisionless expansion of a Gaussian plasma into a vacuum*”. Phys. Plasmas **12**, 112102 (2005).
- [138] T. Grismayer and P. Mora. “*Influence of a finite initial ion density gradient on plasma expansion into a vacuum*”. Phys. Plasmas **13**, 032103 (2006).
- [139] B. Albright, L. Yin, B. Hegelich, K. Bowers, T. Kwan, and J. Fernández. “*Theory of laser acceleration of light-ion beams from interaction of ultrahigh-intensity lasers with layered targets*”. Phys. Rev. Lett. **97**, 115002 (2006).
- [140] J. Crow, P. Auer, and J. Allen. “*The expansion of a plasma into a vacuum*”. Journal Plasma Physics **14**, 65 – 76 (1975).
- [141] M. Passoni and M. Lontano. “*One-dimensional model of the electrostatic ion*

- acceleration in the ultraintense laser solid interaction*". Laser & Part. Beams **22**, 163 (2004).
- [142] S. Bulanov, T. Esirkepov, J. Koga, T. Tajima, and D. Farina. "Concerning the maximum energy of ions accelerated at the front of a relativistic electron cloud expanding into vacuum". Plasma Physics Reports **30**, 18 (2004).
- [143] A. Maksimchuk et al., "High-energy ion generation by short laser pulses". Plasma Physics Reports **30**, 473 (2004).
- [144] S. Betti, F. Ceccherini, F. Cornolti, and F. Pegoraro. "Expansion of a finite-size plasma in vacuum". Plasma Phys. Control. Fusion **47**, 521 (2005).
- [145] N. Kumar and A. Pukhov. "Self-similar quasineutral expansion of a collisionless plasma with tailored electron temperature profile". Phys. Plasmas **15**, 053103 (2008).
- [146] M. Murakami and M.M. Basko. "Self-similar expansion of finite-size non-quasi-neutral plasmas into vacuum: Relation to the problem of ion acceleration". Phys. Plasmas **13**, 012105 (2006).
- [147] J. Fuchs et al., "Spatial uniformity of laser-accelerated ultrahigh-current MeV electron propagation in metals and insulators". Phys. Rev. Lett. **91**, 255002 (2003).
- [148] Y. Oishi et al., "Measurement of source profile of proton beams generated by ultraintense laser pulses using a Thomson mass spectrometer". Journal Appl. Phys. **97**, 4906 (2005).
- [149] A. Pukhov. "Three-Dimensional Simulations of Ion Acceleration from a Foil Irradiated by a Short-Pulse Laser". Phys. Rev. Lett. **86**, 3562 (2001).
- [150] D. Habs, G. Pretzler, A. Pukhov, and J. Meyer-Ter-Vehn. "Laser acceleration of electrons and ions and intense secondary particle generation". Progress in Particle and Nuclear Physics **46**, 375 (2001).
- [151] J. Fuchs, P. Antici, M. Fazi, A. Lombardi, M. Migliorati, L. Palumbo, and P. Audebert. "Postacceleration of Laser-Generated High Energy Protons Through Conventional Accelerator Linacs". AIP conference proceedings: Laser-Driven Relativistic Plasmas Applied For Science, Industry, and Medicine: The 1st International Symposium, Kyoto (Japan), volume **1024**, 90 (2008).
- [152] S. Nakamura et al., "High-Quality Laser-Produced Proton Beam Realized by the Application of a Synchronous RF Electric Field". J. Appl. Phys. **46**, L717 – L720 (2007).
- [153] H. Haseroth and H. Hora, "Physical mechanism leading to high currents of highly charged ions in laser-driven ion sources", Laser & particle beams **14**, 393 (1996).
- [154] E. Fourkal, B. Shahine, M. Ding, J. Li, T. Tajima, and C. Ma. "Particle in cell simulation of laser-accelerated proton beams for radiation therapy". Med. Phys. **29**, 2788 (2002).
- [155] S. Bulanov and V. Khoroshkov. "Feasibility of using laser ion accelerators in proton therapy". Plasma Physics Reports **28**, 453 – 456 (2002).
- [156] S. Bulanov et al., "Accelerating protons to therapeutic energies with ultraintense, ultra-clean, and ultrashort laser pulses". Med. Phys. **35**, 1770–6 (2008).

- [157] M. Murakami et al., “Radiotherapy using a laser proton accelerator”. arXiv: 0804.3826v1 (2008).
- [158] D. Schulz-Ertner et al. “Results of carbon ion radiotherapy in 152 patients”. Int. J. Radiation Oncology Biol. Phys. **58**, 631 (2004).
- [159] I. Spencer et al., “Laser generation of proton beams for the production of short-lived positron emitting radioisotopes”. Nucl. Instrum. and Meth. **B 183**, 449 (2001).
- [160] M. Santala et al., “Production of radioactive nuclides by energetic protons generated from intense laser-plasma interactions”. Appl. Phys. Lett. **78**, 19 (2001).
- [161] K. Nemoto, A. Maksimchuk, S. Banerjee, K. Flippo, G. Mourou, D. Umstadter, and V.Yu. Bychenkov. “Laser-triggered ion acceleration and table top isotope production”. Appl. Phys. Lett. **78**, 595 (2001).
- [162] K.. Ledingham et al., “High power laser production of short-lived isotopes for positron emission tomography”. J. Phys. D: Appl. Phys. **37**, 2341 (2004).
- [163] S. Fritzler, V. Malka, G. Grillon, J. Rousseau, F. Burgy, E. Lefebvre, E. d’Humières, P. McKenna, and K. Ledingham. “Proton beams generated with high-intensity lasers: Applications to medical isotope production”. Appl. Phys. Lett. **83**, 3039 (2003).
- [164] V. Malka, “Practicability of protontherapy using compact laser systems”, Med. Phys. **31**, 1587 (2004).
- [165] S. Bulanov, H. Daido, T. Esirkepov, V. Khoroshkov, J. Koga, K. Nishihara, F. Pegoraro, T. Tajima and M. Yamagiwa, “Feasibility of using laser ion accelerators in proton therapy”, The Physics of Ionized Gases: 22nd Summer School and International Symposium on the Physics of Ionized Gases, ed. by L. Hadzievski, T. Grozdanov, and N. Bibic, AIP Conf. Proc. No. **740** (AIP, New York) 414 (2004).
- [166] M. Nishiuchi et al. “Laser – Driven Proton Accelerator for Medical Application”, Proc. IPAC10, Kyoto, Japan, MOPEA013 (2010).
- [167] P. Patel et al. “Isochoric Heating of Solid-Density Matter with an Ultrafast Proton Beam”. Phys. Rev. Lett. **91**, 125004 (2003).
- [168] B. Remington, D. Arnett, R. Darke and H. Takabe. “Modeling Astrophysical Phenomena in the Laboratory with Intense Lasers”, Science **284**, 1488 (1999).
- [169] D. Bailey, D. Townsend, P. Valk and M. Maisey. “Positron Emission Tomography: Basic Sciences”, Springer – Verlag London Limited 2005.
- [170] H.Eickoff, R. Bää, A. Dolinski, Th. Haberer, B. Schlitt, P. Spiller and U. Weinrichl. “HICAT – The German Hospital – Based Light Ion Cancer Therapy Project”, Proc. PAC03, Portland, Oregon, USA, FOAA002 (2003).
- [171] P. McKenna et al. “Demonstration of fusion-evaporation and direct-interaction nuclear reactions using high-intensity laser-plasma-accelerated ion beams”. Phys. Rev. Lett. **91**, 075006 (2003).
- [172] M. Temporal et al. “Numerical study of fast ignition of ablatively imploded deuterium-tritium fusion capsules by ultra-intense proton beams”. Phys. Plasmas **9**, 3098 (2002).
- [173] S. Atzeni et al. “A first analysis of fast ignition of precompressed ICF fuel by laser-

- accelerated protons*". Nuclear Fusion **42**, L1 (2002).
- [174] M. Roth et al., "Fast ignition by intense laser-accelerated proton beams". Phys. Rev. Lett. **86**, 436 (2001).
- [175] V.Yu Bychenkov, W. Rozmus, A. Maksimchuk, D. Umstadter, and C.E. Capjack. "Fast Ignitor Concept with Light Ions". Plasma Physics Reports **27**, 1017 (2001).
- [176] M. Roth, B. Becker-de Mos, R. Bock, S. Borneis, H. Brandt, C. Bruske, and J. Caird. "PHELIX: a petawatt high-energy laser for heavy ion experiments". Proc. SPIE 4424, 78 (2001).
- [177] P. Neumayer et al., "Status of PHELIX laser and first experiments". Laser & Part. Beams **23**, 385–389 (2005).
- [178] Gafchromic dosimetry films International Specialty Products, 1361 Alps Road Wayne NJ 07470. <http://www.ispcorp.com/products/dosimetry/content/gafchromic>. Aug. 2006.
- [179] M. D. Perry and G. Mourou. "Terawatt to Petawatt Subpicosecond Lasers", Science **264**, 917 (1994).
- [180] S. Mangles et al., "Monoenergetic beams of relativistic electrons from intense laser-plasma interactions". Nature **431**, 535–8 (2004).
- [181] E. Fourkal et al. "Particle selection for laser-accelerated proton therapy feasibility study". Med. Phys. **30**, 1660 (2003).
- [182] K. Nakajima et al. "Recent Results of Laser-Plasma Electron Beam Acceleration Experiments at JAERIAPRC". 31st EPS Conference on Plasma Phys. ECA 28G, O–1.30 (2004).
- [183] S. Irvine et al. "Ultra-compact 180° magnetic spectrometer for intermediate energy electron measurement". Meas. Sci. Technol. **17**, 2455 (2006).
- [184] J. J. Thomson. "Rays of positive electricity". Philos. Mag. **21** (122), 225 (1911).
- [185] A. Szydlowski et al. "Application of solid-state nuclear track detectors of the CR-39/PM-355 type for measurements of energetic protons emitted from plasma produced by an ultra-intense laser". Radiation Measurements **44**, 881 (2009).
- [186] F. Nürnberg et al. "RCF imaging spectroscopy of laser-accelerated proton beams at Vulcan Petawatt". Central Laser Facility Annual Report page **49** (2008).
- [187] F. Nürnberg et al. "Transverse emittance of laser-accelerated proton beams". Proceedings of the XXX ECLIM 2008 pages EC–18, p34 (2009).
- [188] S. Hauf et al. "Research and Development on the Geant4 Radioactive Decay Physics". DPG Frühjahrstagung, Bonn EP14.1, Astrophysics III (2010).
- [189] N. Klassen, L. van der Zwan, and J. Cygler. "GafChromic MD-55: Investigated as a precision dosimeter". Med. Phys. **24**, 1924 – 1934 (1997).
- [190] ISP -International Specialty Products, Wayne, New Jersey, USA. "Radiochromic film types HD-810, HS, MD-55, MD-V2-55 are trademarks of ISP corporation". Website, June (2008). Available online at http://online1.ispcorp.com/_layouts/Gafchromic/index.html (2008).

- [191] W. McLaughlin, M. Al-Sheikhly, D. Lewis, A. Kovács, and L. Wojnárovits. “*Radiochromic solid-state polymerization reaction*”, chapter 11, 152 – 166. ACS Symposium Series, edited by R.L. Clough and S.W. Shalaby. American Chemical Society, 620 edition (1996).
- [192] D. Hey, M. Key, A. Mackinnon, A. MacPhee, P. Patel, R. Freeman, L. Van Woerkom, and C. Castaneda. “*Use of GafChromic film to diagnose laser generated proton beams*”. Rev. Sci. Instrum. **79**, 053501 (2008).
- [193] Grey wedge #T4110cc, Stouffer Graphic Arts, Mishawaka, IN 46544, USA; 41 steps from optical density 1 to 4. <http://www.stouffer.net> (2008).
- [194] SRIM2006 -The Stopping and Range of Ions in Matter, ©1984-2006, James F. Ziegler. <http://www.srim.org>. August 2006.
- [195] M. Schollmeier et al., “*Controlled Transport and Focusing of Laser-Accelerated Protons with Miniature Magnetic Devices*”. Phys. Rev. Lett. **101**, 055004 (2008).
- [196] A. Almomani, M. Droba, U. Ratzinger and I. Hofmann. “*Matching a Laser Driven Proton Injector to a CH – Drift tube Linacs*”, Proc. IPAC11, San Sebastián, Spain, WEPS033 (2011).
- [197] A. Almomani, M. Droba, U. Ratzinger and I. Hofmann. “*Focusing the Laser Generated p- Bunch by a Magnetic Solenoid*”, FAIR-2010-1 Report, October 2010, AC-04, 24 (2010).
- [198] A. Almomani, M. Droba, U. Ratzinger and I. Hofmann, “*Matching the Laser Generated p- bunch into a Drift Tube Linac of the CH – Type*”, Phys. Rev. Special Topics – Accelerator and Beams **15**, 051302 (2012).
- [199] M. Droba, Private Communication.
- [200] J. M. Dawson. “*Particle Simulation of Plasmas*”, Rev. Mod. Phys. **55**, 403 (1983).
- [201] M. Wang and T. Sheu. “*An Element-by-element BICGSTAB Iterative Method for Three – Dimensional Steady Navier-Stokes Equations*”, J. Computational and Applied Mathematics **79**, 147 (1997).
- [202] T. J. Stuchi. “*Symplectic Integrators Revisited*”, Braz. J. Phys. **32**, No. 4 (2002).
- [203] The Center for Scientific Computing (CSC) of the Goethe University Frankfurt am Main. <http://csc.uni-frankfurt.de>
- [204] S. Jr. Humphries. “*Principles of Charged Particle Acceleration*”. John Wiley and Sons University of New Mexico, Department of Electrical and Computer Engineering, Albuquerque, New Mexico, USA 1999.
- [205] I. M. Kapchinsky and V.V. Vladimírsky. “*Limitations of Proton Beam Current in a Strong Focusing Linear Accelerator with the Beam Space Charge*”, Proceeding of the conference on High Energy Accelerators and Instrumentation, CERN, p. 274 (1959).
- [206] M. Reiser. “*Theory and Design of Charged Particle Beams*” WILEY-VCH Verlag GmbH & Co. KGaA, Weinheim, Germany 2008.
- [207] A. Almomani, M. Droba, U. Ratzinger and I. Hofmann. “*Space Charge Effect on the Beam Dynamics of p – Bunch Generated by Laser*”, GSI Scientific Report, PHN-AC-

RD-56, p. 317 (2010).

- [208] T. Wangler. “RF Linear Accelerators”. WILCY-VCH Verlag GmbH & Co. KGaA, Weinheim, Germany, 2008.
- [209] U. Ratzinger. “*The IH Structure – a New Approach to the Fusion RF Linac*”, IL NUOVO CIMENTO, **106 A**, 1583 (1993).
- [210] U. Ratzinger. “*H-Type Linac Structures*”, CERN Accelerator School on RF Engineering, May 2000, Seeheim, Germany, p. 351 (2000).
- [211] C. Zhang. “*Linac Design for Intense Hadron Beams*”, Dissertation, Johan Wolfgang Goethe Universität, 2009.
- [212] H. Podlech, U. Ratzinger, H. Klein, C. Commenda, H. Liebermann and A. Sauer. “*Superconducting CH Structure*”, Phys. Rev. Special Topics – Accelerators and Beams **10**, 080101 (2007).
- [213] U. Ratzinger. Habilitationsschrift. “*Effiziente Hochfrequenz-Linearbeschleuniger für leichte und schwere Ionen*”, Frankfurt University, Germany (1998).
- [214] G. Clemente. “*The Room Temperature CH – DTL and its Application for the FAIR Proton Injector*”, Dissertation, J. W. Goethe Universität Frankfurt am Main, 2007.
- [215] J. Broere, H. Kugler, M. Vretenar, U. Ratzinger and B. Krietenstein. “*High Power Conditioning of the 202 MHz IH Tank 2 at the CERN LINAC3*”, Proc. LINAC98, Chicago, Illinois, USA, TH4004 (1998).
- [216] J. Blewett, “*Linear Accelerator Injector for Proton Synchrotrons*”, CERN Symposium 1956, p. 162 (1956).
- [217] E. Nolte et al., “*The Munich Heavy Ion Postaccelerator*”, Nucl. Instrum. and Meth., **158**, 311 (1979).
- [218] U. Ratzinger, “*High Current IH Structures*”, Proc. EPAC94, London, UK, vol.1, P.264 (1994).
- [219] U. Ratzinger, “*RNB-specific linac development*”, Nuclear Physics A 701 (2002) 641c/646c
- [220] H. Haseroth, “*Pb Injector at CERN*”, Proc. LINAC 96, Geneva, Switzerland, TU201 (1996).
- [221] O. Kester, et al., “*Status of the REX-ISOLDE LINAC*”, Proc. LINAC98, Chicago, Illinois, USA, TH4021 (1998).
- [222] www.cnao.it
- [223] A. Schempp, U. Ratzinger, R. Tiede and C. Zhang “*RFQ and IH Accelerators for the new EBIS Injector at BNL*”, Proc. PAC07, Albuquerque, New Mexico, USA, TUPAN021 (2007).
- [224] L.P. Chao et al., “*The Frankfurt Neutron Source at the Stern-Gerlach-Zentrum (FRANZ)*” Proc. EPAC06, , Edinburg, Scotland, TUPLS082 (2006).
- [225] T. Shannon et al., “*IFMIF International Fusion Materials Irradiation Facility: A High Intensity Deuteron Beam Application*” Proc. EPAC98, Stockholm, Sweden, pp. 231

(1998).

- [226] www.fzk.de/eurotrans/
- [227] H. Podlech. “Development of Room Temperature and Superconducting CH – Structures”, Proc. LINAC04, Lübeck, Germany, MO302 (2004).
- [228] G. Amendola et al., “A Heavy Ion Linac for the CERN Accelerator Complex”, Proc. EPAC92, Berlin, Germany, p. 536 (1992).
- [229] U. Ratzinger, E. Nolte, R. Geier, N. Gärtner and H. Morinaga. “The UpGraded Munich Linear Heavy Ion Postaccelerator”, Proc. PAC87, Washington, D.C., USA, p.367 (1987).
- [230] U. Ratzinger. “The New High Current Ion Accelerator at GSI and Perspectives for LINAC Design Based on H – Mode Cavities”, Proc. EPAC00, Vienna, Austria, p. 98 (2000).
- [231] N. Angert et al., “Commissioning and First Operation Experience of the New Heavy Ion Injector of the UNILAC”, Proc. EPAC92, Berlin, Germany, p. 167 (1992).
- [232] W. Henning et al., “An International Accelerator Facility for Beams of Ions and Antiprotons”, GSI Darmstadt, 2001, www.gsi.de/GSI-Future/cdr/.
- [233] M. Steck. “Status of the FAIR Project”, Proc. COOL09, Lanzhou, China, THM1MCIO01 (2009).
- [234] L. Groening et al. “The 70 MeV Proton LINAC for the Facility for Antiproton and Ion Research FAIR”, Proc. LINAC06, Knoxville, Tennessee, USA, MOP061 (2006).
- [235] G. Clemente, H. Podlech, U. Ratzinger, R. Tiede and S. Minaev. “HIPPI-Relevant Activities at IAP-Frankfurt on the Development of the Room Temperature CH-DTL Second Report”, CARE-Report-2008-014-HIPPI (2008).
- [236] G. Clemente et al., “The FAIR Proton Linac: The First LINAC Based on a Room Temperature CH-DTL”, Proc. HB2010, Morschach, Switzerland, MOPD26 (2010).
- [237] L. Groening et al., “The 70 MeV Proton LINAC for the Facility for Antiproton and Ion Research FAIR”, Proc. LINAC06, Knoxville, Tennessee, USA, MOP061 (2006).
- [238] G. Clemente, L. Groening, U. Ratzinger, R. Tiede and S. Minaev. “Beam Dynamics Layout and Loss Studies for the FAIR p – Injector”, Proc. EPAC08, Genoa, Italy, WEPP079 (2008).
- [239] R. Brodhage, U. Ratzinger, H. Podlech, S. Minaev, R. Tiede, G. Clemente and L. Groening. “Prototype Construction of a Coupled CH-DTL Proton LINAC for FAIR”, Proc. PAC09, Vancouver, BC, Canada, FR5REP060 (2009).
- [240] R. Brodhage, U. Ratzinger, H. Podlech, G. Clemente and L. Groening. “Development and Measurements on a Coupled CH Proton LINAC for FAIR”, Proc. IPAC10, Kyoto, Japan, MOPD031 (2010).
- [241] R. Tiede, G. Clemente, H. Podlech, U. Ratzinger, A. Sauer and S. Minaev. “LORASR Code Development”, Proc. EPAC06, Edinburgh, Scotland, WEPCH118 (2006).
- [242] <http://nuklear-server.ka.fzk.de/eurotrans/>

- [243] <http://www.frascati.enea.it/ifmif>.
- [244] K. Shepard. “*The RIA Driver LINAC*”, Proc. LINAC02, Gyenogju, Korea, TH301 (2002).
- [245] T. Junquera et al., “*High Intensity LINAC Driver for the SPIRAL-2 Project: Design of Superconducting 88 MHz Quarter Wave Resonator (Beta 0.12), Power Couplers and Cryomodules*”, Proc. EPAC04, Lucerne, Switzerland, TUPLT058 (2004).
- [246] D. Barni. “*Status of the TRASCO Project*”, the Workshop on RF Superconductivity, Tsukuba, Japan, p. 337 (2001).
- [247] F. Dziuba et al., “*Development of Superconducting Crossbar-H-mode Cavities for Proton and Ion Accelerators*”, Phys. Rev. Special Topics – Accelerator and Beams **13**, 041302 (2010).
- [248] S. Minaev, U. Ratzinger, H. Podlech, M. Busch and W. Barth. “*Superconducting Energy Variable Heavy Ion Linac with constant β , Multicell Cavities of CH-type*”, Phys. Rev. Special Topics – Accelerator and Beams **12**, 120101 (2009).
- [249] H. Podlech, H. Liebermann, A. Sauer and U. Ratzinger, “*Development of Superconducting CH-Structures for Low and Medium Beta Beams*”. Proceed. of the ICFA-HB04, Bensheim, Germany, September 18-22 2004.
- [250] H. Podlech, M. Amberg, A. Bechtold, M. Busch, F. Dziuba, H. Klein and U. Ratzinger, “*New Cavity Shape Developments for Low Beta Applications*”, Proc. SRF2009, Berlin, Germany, THOAAU06 (2009).
- [251] M. Busch, U. Ratzinger, H. Podlech and F. Dziuba, “*Progress in Superconducting CH – Cavity Development*”, Proc. SRF2009, Berlin, Germany, THPPO016 (2009).
- [252] F. Dziuba, H. Podlech, M. Busch, U. Ratzinger, C. Zhang and H. Klein, “*Development of Superconducting CH – Cavities for the EUROTRANS Linac*”, Proc. SRF2009, Berlin, Germany, THPPO017 (2009).
- [253] M. Lindmayer and H. Mosebach. “*Quenching of High – TC – Superconductors and Current Limitation – Numerical Simulations and Experiments*”, IEEE Transactions on Applied Superconductivity **7**, 1029 (1997).
- [254] P. Antici, M. Migliorati, A. Mostacci, L. Picardi, L. Palumbo and C. Ronsivalle, “*A compact post-acceleration Scheme for Laser – generated Protons*”, Physics of Plasmas **18**, 073103 (2011).
- [255] CST MICROWAVE STUDIO, <http://www.cst.com>.

List of Figures

Figure 1.1: Development in laser – focused power density and laser power (left axis) and corresponding maximum ion energies (right axis) during the years. The solid black curve is taken from Tajima and Mourou [57-58]. This trend should be corrected (red line) because the threshold 1 PW laser intensity was not overcome since the first realization at Lawrence Livermore Laboratory. The yellow rectangle shows the current TNSA – regime (Courtesy of J. Schreiber) 2

Figure 1.2: Dependence of differential particle yield (left) and half opening angle (right) from the proton energy at TNSA experiments with PHELIX (Courtesy of M. Roth and V. Bagnoud)..... 4

Figure 2.1: Scheme of the interaction between the laser and solid target. The laser pulse with focal spot radius r_L hits a target of thickness d resulting in a pre-plasma on the target front side. The laser propagates through the plasma until it reaches a position where the electrons have its critical density n_c . At that density the plasma has a zero refractive index and the laser will be reflected (Courtesy of J. Schreiber) 13

Figure 2.2: Scheme of the Target Normal Sheath Acceleration TNSA mechanism. The laser pulse is focused on the front side of the target and interacts with the pre-plasma generated by unavoidable laser pre-pulse. The laser energy is converted to the plasma electrons resulting in electrons with kinetic energy in MeV – range. These electrons are accelerated and transported through the solid target and it reaches the rear side and some of them can escape leaving the target positively charged. The charge separation between the electron sheath and the target will form a huge electrostatic field of order TV/m which is high enough to ionize the atoms at the target rear side and accelerate the protons (ions) to energies in MeV – range 16

Figure 2.3: Dependence of differential particle yield (left) and half opening angle (right) on proton energy generated in PHELIX laser experiments (Courtesy of M. Roth and V. Bagnoud) 18

Figure 2.4: The laser – accelerated proton envelopes for different proton energies. This sketch is showing the dependence of source size and envelope divergence at proton energies generated by laser. For increasing proton energy the generated proton source radius and the divergence is decreasing..... 18

Figure 2.5: The proton loses its energy uniformly in the matter up to the point of the Bragg peak where the proton comes to rest. In the isochronic heating, the target is located in the plateau region which leads to an almost uniform temperature 20

Figure 3.1: Experimental setup for the laser – proton acceleration at PHELIX (Courtesy of Kunt Harres, the same as shown in ref. 78)..... 23

Figure 3.2: Schematic for the PHELIX laser facility and the accelerator chain in GSI 24

Figure 3.3: Schematic of the PHELIX laser system (Courtesy of V.Bagnoud)..... 24

Figure 3.4: Schematic for the Chirped Pulse Amplification (CPA) process..... 25

Figure 3.5: Layer configuration of Radiochromic film of types MD-55, HD-810 and HS. The color codes in Figure 3.5 and table 3.2 are identical	26
Figure 3.6: Calibration curves for the deposited energy versus the optical density for the radiochromic film types HD-810, MD-55 and HS. [PhD thesis of F. Nürnberg ref 34].....	28
Figure 3.7: The proton energy deposited per unit length in radiochromic film type HD-810 for four different initial energies as calculated with SRIM 2006 (the Stopping and Range of Ions in Matter). The marked areas from left to right are correspondence to different layers in RCF from left to right: gelatin coating (dark yellow), sensitive layer (blue) and polyester (dark gray)	28
Figure 3.8: Intensity distribution of the laser focal spot focused by a parabola mirror. The full width at half maximum (FWHM) dimensions of the spot are $10\mu\text{m} \times 10\mu\text{m}$	29
Figure 3.9: Radiochromic film stack (three films of HD-810 type followed by another three films of MD-55 type) exposed by a laser – accelerated proton beam at PHELIX experiment. A gold target of thickness $10\mu\text{m}$ was exposed to a laser intensity of about 10^{19} W/cm^2 resulting in protons with 10.6 MeV maximum energy. The stack was positioned 31 mm behind of the target. The energy value on the top right of each film corresponds to the proton Bragg peak energy.....	30
Figure 3.10: Screenshot of the graphical user interface running in MATLAB program for the reconstruction of the proton spectrum written by the working group of M. Roth from Institut für Kernphysik, Technische Universität Darmstadt (Courtesy of S. Busold)	31
Figure 3.11: The dependence of the half opening angular divergence of the PHELIX proton beam on the proton energy	31
Figure 3.12: The calculated energy deposited of the measured data in the RCF stack (Courtesy of S. Busold)	33
Figure 3.13: Dependence of differential particle yield on energy for PHELIX experiment by solving the integral in equation 3.2 numerically using equation 3.3.....	33
Figure 4.1: A schematic view of the laser target and the focusing solenoid. The geometrical parameters of the solenoid were indicated.	37
Figure 4.2: Longitudinal (left) and transverse (right) components of the solenoidal field along the axis for different radii in cm; the geometric length of the solenoid (cyan lines) as well as the target position (brown line) are marked.....	38
Figure 4.3: Spherical aberration. The lens focuses the particles far from the axis more strongly than the particles near the axis.....	39
Figure 4.4: Chromatic aberration. The lens focuses the particles with higher energies less than the particles with lower energies.....	39
Figure 4.5: Output rms – emittance values in $x - x'$ versus $\Delta p/p$ (left) output to the input rms – emittance ratio in $x - x'$ versus $\Delta p/p$ (right) at different opening angles, 210 mm behind of the target.....	41

Figure 4.6: Input and output distributions in $x - x'$ for different opening angle with $\Delta p/p = 0\%$	42
Figure 4.7: Input and output distributions in $x - x'$ for different momentum spreads $\Delta p/p$ with 90 mrad opening angle	43
Figure 4.8: The evolution of $x - x'$ distribution for $x' = 180$ mrad and $\Delta p/p = 0\%$ at different positions. The $s -$ shaped deformation at the last position is mainly due to the spherical aberration.....	44
Figure 4.9: Canonical (red) and mechanical (black) emittance evolutions on the $z -$ axis for $\Delta p/p = 0\%$. The smooth growth in the canonical emittance is an impact of the spherical effect. Both evolutions are ended at the same values where the magnetic field is reduced down to less than 1 % The geometric length of the solenoid (blue lines) is marked.....	45
Figure 4.10: The beam envelopes of proton beam in x for different opening angles at $\Delta p/p = 0\%$ (left) and for different momentum spreads at $\alpha = \pm 45$ mrad (right), the geometrical length of the solenoid is marked in cyan lines	46
Figure 4.11: Protons spectrum measured at PHELIX experiments. The proton number per unit energy is showing an exponential by decreasing curve. 10^{10} protons can be detected in the energy band of $10 \text{ MeV} \pm 0.5 \text{ MeV}$ (Courtesy of M. Roth and V. Bagnoud, [40]).....	47
Figure 4.12: Input and output distribution in $x - x'$ at the target positions (left) and after the Coulomb explosion at $z = 1.6$ mm (right).....	48
Figure 4.13: Input and output energy spread distributions in the proton bunch at the target position (red) and after the Coulomb explosion at $z = 1.6$ mm (black).....	49
Figure 4.14: The relation between the bunch diameters in x (or y) and z at different positions. The non - linear behavior around $z = 0$ is mainly due to the Coulomb explosion. Starting conditions like given in table 4.1 and mirror effects of the target are not included..	49
Figure 4.15: The ratio of bunch widths $\Delta x/\Delta z$ at different z positions. The initial ellipsoid distribution was expanded longitudinally more than transversally due to the bigger space charge forces in z and it becomes a sphere after the end of Coulomb's explosion.....	50
Figure 4.16: The proton bunch at different positions, where the initial bunch at $z = 0$ is expanding in all directions especially in $z -$ direction where it is about 22 time larger finally	50
Figure 4.17: Bunch shapes in $x-z$ projection at different positions along the beam axis. Additionally, the beam envelopes with their correlated proton energies at the last position are color coded. The dashed dark green lines show the geometrical length of the solenoid	51
Figure 4.18: Output distribution in $x - x'$ of the proton bunch at the last position which is extended from $z = 16.3$ cm to $z = 25.2$ cm (see Figure 4.16).....	52
Figure 4.19: Schematic view of the laser target, the focusing solenoid and the drift to the rf linac. The longitudinal axis is marked in mm and in ps time of flight for a 10 MeV on axis proton. Additionally, the range of LASIN and LORASR code based simulations in space charge case (protons with the co-moving electrons) are indicated.....	53

Figure 4.20: The evolution of a neutralized bunch propagating along z – axis towards the magnetic solenoid. The bunch starts with 100 % neutralization between protons and electrons. The impact of the magnetic field on the electron is much bigger than on protons. The magnetic field level at the starting point was more than 6 T, reaching a maximum 18 T in the solenoid	54
Figure 4.21: The measured energy deposition of protons in RCF films compared with the calculations using equation $\int (dN(E')/dE) \times E_{\text{loss}}(E')dE'$ (left). The fit shows the number of protons per energy interval. Equation $dN/dE = (N_0/\sqrt{2Ek_B T}) \times \exp(-\sqrt{2E/k_B T})$ was used to get the plot on the right [PhD thesis of F. Nürnberg ref. 34]	56
Figure 4.22: Proton beam parameters of the PHELIX data used in the LASIN simulations where the blue dots (■) are referring to the experimental data and (—) is the fitted function [PhD thesis of F. Nürnberg ref. 34]	56
Figure 4.23: The $x - y$ – (left) and $x - x'$ – (right) projections of the 10 MeV \pm 0.5 MeV fraction of a simulated proton pulse after 10 ps; $\epsilon_{\text{rms}} = 6.56 \text{ mm} \cdot \text{mrad}$	57
Figure 4.24: Transversal density profile distribution of the macroparticle from Figure 4.23, left	57
Figure 4.25: $z - x$ projection of the particle distributions after 25 ps. The action of the magnetic solenoid fringing field is seen already	58
Figure 4.26: Potential curves in transversal (left) and longitudinal (right) directions at three different positions along z . At $t = 40 \text{ ps}$, the space charge potential is reaching a maximum.	58
Figure 4.27: Detail of the potential curve (from Figure 4.26) after 17.5 ps in the longitudinal direction. The plasma oscillation has a higher potential fluctuation at lower z – positions, where the simulated particle density reaches its maximum	59
Figure 4.28: Time evolution of the electron energy distribution at different time steps. The right picture has different scaling	59
Figure 4.29: Proton (red) and electron (blue) distribution in z - x plane after 460 ps. Electrons are accelerated axially by their own potential. The detail AB containing the whole proton distribution is shown in detail (right). The green marked area corresponds to the protons with 10 MeV \pm 0.5 MeV	60
Figure 4.30: The $x - x'$ phase space projection of the transported proton spectrum with 10 MeV \pm 5 MeV at 460 ps.....	61
Figure 4.31: Transversal proton distribution for the energy band 10 MeV \pm 0.5 MeV after 460 ps	61
Figure 4.32: Proton distribution $x - x'$ for the energy band 10 MeV \pm 0.5 MeV after 460 ps. The local influence of co-moving on axis electrons is seen at $ x < 0.5 \text{ mm}$	62
Figure 4.33: Proton spectral distribution development within the first 460 ps. The shape is changing mainly at low energy end	62

Figure 4.34: (Left) $z - x$ proton pulse distribution after solenoid and followed by a 6 cm drift. The low energy part is near to the focal spot. (Right) $x - x'$ distribution for the same propagation time $t = 3.4$ ns. Green marked area corresponds to the energy of interest (see also Figure 6.6 for more detailed view)..... 64

Figure 4.35: Longitudinal particle distribution of laser generated protons 60 mm behind the solenoid with energies $10 \text{ MeV} \pm 5 \text{ MeV}$ (left). Green marked area corresponds to protons within energy of interest $10 \text{ MeV} \pm 0.5 \text{ MeV}$, which is shown in detail at right. The red marked area corresponds to the accepted particle distribution fall within the CH – DTL acceptance and used for post-acceleration study. The vertical axis of right picture has different unit..... 64

Figure 5.1: Basic block diagram of an RF linear accelerator showing its main components 65

Figure 5.2: Schematic of the geometry (left) and the electric field distribution (right) for an accelerating gap. The length L is standing for the gap effective length where the field distribution is confined within $\pm L/2$ as shown in right of the Figure 66

Figure 5.3: Beam bunches in an RF linac for efficient acceleration. The bunches are separated longitudinally by one or more RF periods 67

Figure 5.4: Longitudinal focusing is providing by choosing the right phase of the synchronous particle relative to the accelerating wave crest. The synchronous phase point is the stable point because particles arrive earlier than the synchronous particle gain less energy and particles arrive later will gain more energy 70

Figure 5.5: Accelerating field lines in an accelerating gap. The off-axis particles in the gap experience radial forces. These forces work like focusing forces in the first half of the gap and as defocusing forces in the second half..... 70

Figure 5.6: A series of accelerating cells describing the longitudinal motion. These cells are consisting of drift tubes separated by accelerating gaps..... 71

Figure 5.7: At the top, the accelerating electric field E_z is shown as a function of the phase ϕ ; the synchronous phase ϕ_s is shown as a negative value. Thus, the longitudinal potential V_ϕ has its minimum at $\phi = \phi_s$ as shown in the bottom. The particle trajectories in the longitudinal phase space are shown in the middle. Here, the separatrix is dividing the motion in the longitudinal phase space into a stable (inside the separatrix) and unstable (outside the separatrix) area..... 73

Figure 5.8: Effective shunt impedance for different rf structures including the transit time factor T and the synchronous phase ϕ_s as a function of the particle velocity $\beta = v/c$. The black horizontal bars represent some existing IH-DTLs and the red bars represent the expected shunt impedance of the rt CH cavities for the GSI-FAIR 70 MeV, 70 mA proton linac (Courtesy of U. Ratzinger and R. Tiede)..... 77

Figure 5.9: A scheme of the H-DTL, showing the separated function principle KONUS – beam dynamics with respect to acceleration and beam focusing 78

Figure 5.10: The H – mode structure family. The main direction of the magnetic RF field is oriented parallel or antiparallel with respect to the beam axis [209]	78
Figure 5.11: Scheme of an Interdigital H-mode structure (IH) showing the electric field lines in red and the magnetic field lines in blue (Courtesy of R. Tiede)	79
Figure 5.12: IH – DTL for the CERN LINAC 3 lead injector showing a detail of the electric and magnetic field distributions inside the cavity [209]	80
Figure 5.13: Scheme of a Crossbar H-mode structure (CH) showing the electric field lines in red and the magnetic field lines in blue (Courtesy of R. Tiede)	81
Figure 5.14: Schematic for the accelerator chain in GSI and FAIR facility [213]	81
Figure 5.15: 3D view on the second coupled CH – cavity for the FAIR proton injector. This cavity consists of 27 gaps within two sections coupled by a triplet quadrupole and accelerates the proton beam from 11.7 to 24.3 MeV within 2.8 m inner length (Courtesy of R. Brodhage)	82
Figure 5.16: Particle trajectories in longitudinal phase space at different values of synchronous phase $\phi_s = -30^\circ$ (a), -90° (b) and 0° (c) (Courtesy of R. Tiede).....	84
Figure 5.17: Comparison of the longitudinal particle motion at two synchronous phase values; a negative synchronous phase (left) and zero synchronous phase (right). The accelerating field is shown as a cosine function of the phase (a), the longitudinal potential well (b) and the longitudinal phase – space trajectories are shown in (c) [212].....	85
Figure 5.18: Flowchart of single particle motion in the longitudinal phase space for $\phi_s = 0$. Stable area in longitudinal phase space which can be used by KONUS is marked with dark arrows [212]	85
Figure 5.19: Schematic of the KONUS period showing its main sections; focusing magnetic lenses, rebuncher section with a negative synchronous phase and main acceleration section with a zero synchronous phase. On the top, the bunch motions in phase space reflecting the KONUS beam dynamics [212].....	86
Figure 5.20: The beam envelopes in longitudinal (a) and transversal (b) planes along the IH-DTL cavity of GSI HLI injector. The plots reflect the KONUS beam dynamics (Courtesy of R. Tiede).....	87
Figure 5.21: Superconducting CH – DTL (Courtesy of U. Ratzinger)	88
Figure 5.22: Dependence of the measured quality factor – Q_0 for the superconducting CH – DTL on the accelerating field gradient E_a (Courtesy of H. Podlech)	89
Figure 6.1: 3D view on the proposed CH- DTL consisting of four RF- cavities separated by triplet quadrupoles. In front of the first cavity, the pulsed solenoid is located and the distance between the end edge of the solenoid and the center of the first gap is 103 mm.....	92
Figure 6.2: Simulated effective gap voltage along the CH structure, the voltage near the quadrupoles is minimized	93
Figure 6.3: Normalized relative rms- emittance growth for the matched case.....	96

Figure 6.4: Transverse (left) and longitudinal (right) 90%, 99% and 100% envelopes at 500 mA beam current. $\Delta W/W$ and $\Delta\phi$ – plots are showing detail of the KONUS – beam dynamics design. Black lines in the left plot indicate the aperture.....	96
Figure 6.5: Transverse (top and middle) and longitudinal (bottom) particle distributions at entrance and exit of the CH-DTL section at 500 mA equivalent beam current. The input and output energies of the CH – DTL were 10 MeV and 40 MeV, respectively. Normalized emittance values are relevant for the plotted 95% ellipses	97
Figure 6.6: Laser generated particle distribution in transversal (left) and longitudinal (right) planes at the DTL – entrance within an energy range $10 \text{ MeV} \pm 0.5 \text{ MeV}$ in green (identical with Figure 3.37, right). The red 72% subsets of the particle distribution fall within the transverse CH – DTL acceptance area and are used for DTL beam dynamics simulations	98
Figure 6.7: Normalized relative rms- emittance growths rates along the linac for the laser generated proton case.....	99
Figure 6.8: Transverse (left) and longitudinal (right) 90%, 99% and 100% beam envelopes starting at 6 cm behind of the solenoid. Black lines in the left plot indicate the aperture	100
Figure 6.9: Transverse (top and middle) and longitudinal (bottom) particle distributions at entrance (6 cm behind the solenoid) and exit of the CH-DTL structure. The input and output energies of the CH – DTL were 10 MeV and 40 MeV, respectively. Normalized emittance values are relevant for the plotted 95% ellipses.....	101
Figure 6.10: The dependence of transmission and normalized relative longitudinal rms-emittance growth on the beam current in case of acceleration the proton bunch from 10 – 40 MeV within a total length of about 5.1 m (nominal case).....	103
Figure 6.11: The dependence of transmission and normalized relative longitudinal rms-emittance growth on the beam current in case of p – acceleration from 10 – 32.5 MeV within a total length of about 4.9 m.....	103
Figure 6.12: The dependence of transmission and normalized relative longitudinal rms-emittance growth on the beam current in case of p – acceleration from 10 – 25 MeV within a total length of about 4.7 m.....	104
Figure 6.13: The change in rms – emittance with respect to the nominal values due to the voltage variation of the whole linac with rf phases between cavities were kept constant	105
Figure 6.14: Detail of Figure 6.14 for a reduced voltage variation range.....	106
Figure 6.15: Longitudinal 90%, 99% and 100% envelopes for +6% variations in voltage (left) and -6% (right).....	107
Figure 6.16: Transverse 90%, 99% and 100% envelopes for +6% variations in voltage (left) and -6% (right). Black lines indicate the aperture	107
Figure 6.17: Transverse (top and middle) and longitudinal (bottom) particle distribution at linac exit for different voltage variation: (left) $\Delta V/V = +6\%$ and (right) $\Delta V/V = -6\%$	108

Figure 6.18: Motion of bunch center through CH – DTL for different voltage variation +6% (top) nominal case (middle) and -6% (bottom).....	109
Figure 7.1: Schematic view for the first CH – cavity in the proposed linac	113
Figure 7.2: A schematic view for the surface current density flowing along the stems. The inclined stems are carrying the highest density because the magnetic field flux is turning transversely into the neighbored quadrants	114
Figure 7.3: A schematic view of a CH – structure in xy – plane. The canonical shape for the stems was used in order to have a robust design and make it easy for cooling	115
Figure 7.4: The electric field distribution across the CH – DTL. The field is well concentrated at the beam aperture	116
Figure 7.5: The magnetic field distributions across the CH – DTL. The magnetic field runs parallel and antiparallel to the beam axis in the accelerator modules. Due to the current flow in the stems, the magnetic field is oriented locally around each stem.....	116
Figure 7.6: The magnetic field distribution in xy – plane, projection A – A' of Figure 7.5.	117
Figure 7.7: The schematic view of the magnetic field around the stems. At the end cell, the magnetic field has a pronounced B_{ϕ} component	117
Figure 7.8: The axial electric field distribution as calculated by CST – MWS in all gaps along the beam axis	118
Figure 7.9: A comparison between the corresponding voltage distribution as calculated from the electric field which is given in Figure 7.8 with the reference design values as given from LORASR code	119
Figure 7.10: The electric energy density inside the cavity which is localized on the drift tubes edges.....	120
Figure 7.11: The electric energy density distribution for the shortest D3 (up) and longest D5 (down) drift tubes in the cavity 1	121
Figure 7.12: The magnetic energy density inside the cavity CH-1 in yz – plane reflects very well the surface current distribution as shown in Figure 7.2.....	123
Figure 7.13: The magnetic energy density inside the cavity CH-1 in xz - plane	124
Figure 7.14: Calculated electric field for the gap number 9 in the plane of the stems using MAFIA code. The value of the electric field is given at four representative points on the drift tube surface. The gap reached voltage of 830 kV in high power tests (Courtesy of U. Ratzinger, [212]).....	125
Figure 7.15: A schematic view for the first CH – Cavity showing the corresponding positions for the calculated values in table 7.2	126
Figure 7.16: Electric field distribution along the curve passing the maximum electric field values on the drift tubes surfaces in xz - plane. This is path 1 as indicated in Figure 7.18. The maximum value is located at the right edge of the drift number 6 (D6 in Figure 7.15) and it reached 88.1 MV/m.....	128

Figure 7.17: Electric field distribution along path 2 as indicated in Figure 7.18. The maximum value is located at the edge of the third drift tube (D3 in Figure 7.15) and it reached 94.0 MV/m..... **128**

Figure 7.18: The paths used to calculate the surface electric field distribution in xz – plane (path 1), in yz – plane (path 2) and in yz – plane along the path which is parallel to the beam axis at $r = 15$ mm (path 3)..... **128**

Figure 7.19: Electric field distribution along the line parallel to the beam axis and displaced radially with a distance equal to the inner drift tube radius = 15 mm..... **129**

Figure 7.20: Longitudinal electric field distribution along the path AB in gap number 2 of the CH – cavity shown in Figure 7.1 **129**

Figure 8.1: Overview of the experimental areas Z4 and Z6 at the GSI Helmholtzzentrum für Schwerionenforschung GmbH. The CH – cavity which will get beam from PHELIX by rotating the target chamber by 90° counter clockwise is indicated (Courtesy of B. Zielbauer) **134**

List of Tables

<i>Table 3.1: Present operational parameters of the PHELIX laser system for the pulses and for short pulses operations</i>	25
<i>Table 3.2: Chemical composition and density of Gafchromic Radiochromic films</i>	27
<i>Table 4.1: Starting conditions of the proton bunch at the target position</i>	47
<i>Table 5.1: A comparison between Alvarez drift tube linac and H – type DTL.....</i>	76
<i>Table 5.2: The main parameters of the second CH cavity of the FAIR proton injector.....</i>	82
<i>Table 6.1: A summary for each cell period structure in all cavities of the CH – DTL</i>	94
<i>Table 6.2: Normalized rms- emittance values for the input and output distribution with 500 mA beam current.....</i>	95
<i>Table 6.3: Normalized rms- emittance values for the input and output distribution for the laser accelerated case (216 mA equivalent beam current).....</i>	98
<i>Table 6.4: A comparison between different accelerating gradient cases in terms of the transmission and normalized rel. rms emittance growth at different beam current.....</i>	104
<i>Table 7.1: The main characteristic parameters of the first CH – cavity of the dedicated linac for the laser accelerated protons</i>	122
<i>Table 7.2: A summary for the maximum surface electric field together with the maximum gap voltage values. The ratio between the surface field value before and after the gap to the gap voltage is shown.....</i>	126

ACKNOWLEDGEMENT

First, I would like to thank in particular my advisor Prof. Dr. Ulrich Ratzinger for all the hope he has put on me, before I thought I could do my research at all. It has been an honor to be one of his PhD students. During my stay in IAP – Frankfurt University, he has helped me to see life and science in their full depth, and taught me how to appreciate the good scientific work that helps other researchers. I appreciate all his contributions of time, ideas and funding to make my study experience productive and stimulating. The joy and enthusiasm he has for his research was motivated for me, even during hard days in the doctoral study pursuit. I am also thankful for the excellent example he has provided as a successful physicist and professor. Also, I want to thank him very much for helping me for translation of the Zusammenfassung.

I am so thankful to Prof. Dr. Ingo Hofmann who had assisted me in the beginning to get this PhD position at IAP – Frankfurt University. Also, I appreciate for his helpful advices, suggestions, scientific discussions and remarks through my study here. It was great honor for me to work with him.

Special thanks go to Dr. Martin Droba for the fruitful discussions through this work and for giving outstanding scientific supervision in simulation techniques. His code – LASIN, which was written especially for this study, was quite necessary to perform the first part of simulations in this work. Without you here, this works cannot be done properly.

I would like to thank my colleagues in LINAC group at IAP for their assistant and helping me to use the CST – MicroWave Studio program. Especially, I want to express my thankful for Prof. Dr. Holger Podlech, Robert Brodhage, Dominik Mäder and Marco Busch.

I want to acknowledge my colleagues and friends at IAP (also those of you who already left) for their fast and competent response to any scientific, technical or computer problems.

My worm thanks are due to Dr. Rodelf Tiede for his valuable advices and friendly help. His extensive discussion about LORASR code and his patient advices on technical programming questions about the simulation procedure have been very helpful for this study.

I warmly thank Dr. Giuliano Franchetti and Dr. Gianluigi Clemente from GSI for their valuable advices, friendly help, supporting and worthy discussions in many topics.

I deeply grateful to Prof. Dr. Ahmad Alkhateeb at Yarmaouk University in Jordan. He had taught me several courses in bachelor and master studies and also he assists me to get contact with the people here in Germany.

I wish to express my warm and sincere thanks to the people in HGS –HIRE: Prof. Dr. Harald Appelshäuser, Prof. Dr. Henner Büsching, Dr. Gerhard Burau, Dr. Sasch Vogel, Mrs. Helena Dos Santos, Mrs. Sylke Schneider and Mrs. Johanna Dilley. Through my participation in this program, I had attended several scientific and soft skill courses which help me and improve my way of researching through my PhD study. Also, I would like to thank HGS – HIRE program for their financial supporting to attend conferences and workshops.

Also, I would like to thank the people in HIC for FAIR for their funding support of this work and for giving me one of their scholarships.

I would like to thank the CERN accelerator school people especially Dr. Roger Bailey and Mrs. Barbara Strasser for giving me a grant to join one of their courses.

Special thanks for Mrs. Tanja Harji for her help in a lot of things related to my work and also for my stay her in Germany. Without her, it would not have been possible for me to concentrate on my thesis.

I would like to appreciate the close and fruitful collaboration with the members of PHELIX laser facility and our collaborators in LIGHT project (GSI, Technische Universität Darmstadt, Helmholtz Institute Jena and Forschungszentrum Dresden – Rossendorf).

Also, I like to thank Prof. Dr. Markus Roth and his group especially Dr. Frank Nürnberg, Dr. Kunt Harres, Simon Busold and Oliver Deppert for their kind collaboration, helpful discussion and for showing me the way of analyzing the experimental data.

I want to acknowledge Prof. Dr. Markus Roth and Dr. Abel Blažević for giving me the chance to join them in a PHELIX experimental run.

My warm and sincere thanks are going to the members of physics department at Yarmouk University where I did my B.Sc and M.Sc study. Especially, I would like to thank Prof. Dr. Nihad Yusuf, Dr. Anas Ababneh and Prof. Dr. Ahmad Salem.

I am also grateful for my friends Husam Al-Omari, Youssef Al-Hayek, Mohammad Obeidat, Omar Nusair, Mohammad Daradkeh and Mahmoud Al-Omari for their support and nice moments we had spent together here in Germany or even in Jordan.

It was a pleasure to share the first year of my doctoral study with wonderful people like Yuancun Nie and Zihui Li my first office mates. I want to thank both of them a lot.

I also want to thank other people I met here in Germany for the wonderful friendship they offered me.

A special acknowledgment belongs to my family for keeping me highly motivated to go through many difficulties in my study (Bachelor, Master and PhD) and for teaching me to never give up. Special sincere thanks for my lovely parents (Mohammad and Fathia) who raised me with a love of science and supported me in all my pursuits. Dad and Mom thank you a lot for your love, encouragement and support.

Also, I would like to acknowledge my parents in law (Mahmoud and Amira) who always supported and motivated me through my study. Their hidden assistant was one of the reasons for my success during the doctoral study. I want to appreciate their encouragement which gave me enormous energy to work and study.

I owe my lovely thanks to my wife Suha. Without her encouragement and understanding it would have been impossible for me to finish this work. Suha, without you I would be a very different person today, it would have been certainly much harder to finish a PhD. Still today, learning to love you and to receive your love which makes me a better person. Special thanks for you to be always there for me during the last years.

Frankfurt am Main

Ali Almomani

CURRICULUM VITAE

Ali Almomani, MSc.



1- PERSONAL DATA:

Date of Birth: October 25th, 1983.
Place of Birth: Irbid, Jordan.
Nationality: Jordanian.
Marital Status: Married.
Address (Business): Institute for Applied Physics, Goethe-Universität Frankfurt
Max-von-Laue Str. 1
60438 Frankfurt am Main, Germany
Phone (Business): +496979847441
Mobile (Private): +491637182624
E-mail: a.almomani@iap.uni-frankfurt.de

2- EDUCATION:

September 1995 – August 2000: Secondary School in Ajloun, Jordan.
September 2000 – August 2001: General Secondary Education Examination in Ajloun, Jordan
(Tawjehe Certificate)
September 2001 – January 2005: Bachelor in Physics (GPA: 92.3%) at Yarmouk University, Irbid –
Jordan
February 2005 – May 2008: Master in Physics (GPA: 94.1%) at Yarmouk University, Irbid –
Jordan
October 2008 – April 2009: Guest Scientist in Accelerator and Beam Physics at Institute for
Applied Physics (IAP), Goethe Universität, Frankfurt am Main,
Germany.
April 2009 – till present: Ph.D. Student in Accelerator Physics at IAP – Goethe Universität,
Frankfurt am Main, Stipendium by HIC for FAIR and F&E
Frankfurt / GSI (Disputation date: July 15, 2012).

3- TITLE OF THESIS:

- M.Sc.: “Gamma Radiation Measurements and Dose Rate Calculations of Soil Samples within and around Ras Muneef, Jordan”.
Supervisor: Dr. Anas Ababneh. Physics Department, Yarmouk University, Irbid, Jordan.
- Ph.D.: “RF Acceleration of Intense Laser Generated Proton Bunches”.
Supervisor: Prof. Dr. Ulrich Ratzinger, Institute for Applied Physics (IAP) – Goethe
Universität, Frankfurt am Main, Germany.

4- HONORS AND AWARDS:

- Placed on the Honor list of the Dean of the Faculty of Science Seven Times (September 2001 – February 2004), Yarmouk University, Irbid, Jordan.
- The award of first place student of the BSc. Physics class, Yarmouk University, Irbid Jordan (2004).
- Teaching Assistantship, Yarmouk University, Irbid, Jordan. (February 2004 – September 2007).
- The award of first place student of the MSc. Physics class, Yarmouk University, Irbid Jordan (2008).
- A guest scientist in Accelerator and Beam Physics, Institute for Applied Physics, J.W. Goethe-University in Frankfurt am Main (October 15th, 2008 – April 15th, 2009).
- A scholarship from Frankfurt University for PhD. study (April 2009 – till now).
- Student Grant to attend the First Particle Accelerator Conference (IPAC 10), Kyoto, Japan, May 23 - 28, 2010.
- A scholarship to attend the CERN accelerator school on “High Power Hadron Machines”, Bilbao, Spain, 24.05.2011 – 02.06.2011.

5-TEACHING EXPERIENCES:

- Teaching assistant, Physics Department, Yarmouk University, Irbid Jordan. (February 2004 – September 2006).
- Part Time Lecturer, Physics Department, Yarmouk University, Irbid, Jordan. (September 2006 – August 2008).

6- RESEARCH EXPERIENCES:

- Research Assistant in the Project “Gamma Ray Activity Concentrations and the Associate Annual Dose Equivalent in Soil and Food Stuffs in the Northern Jordan”. Funded by the Deanship of Graduate Students (Project No. 11/2007) with Dr. Ababneh, A. Physics Department, Yarmouk University, Irbid, Jordan. (2007 – 2008).
- Installing various Nuclear Instrument: Gamma Spectroscopy, Alpha Spectroscopy, Coincidence Summing experiments (at Jordan University of Science and Technology), NaI(Tl) detectors.
- Good knowledge of using Gamma – ray spectroscopy, Alpha spectroscopy and NaI (TI) detectors.
- Good knowledge in sample preparation of Alpha spectroscopy detector.
- Longitudinal and Transverse Coupling Impedance, Analytical Theoretical Physics and Waves in Plasma with Prof. Dr. Ahmed Al-Khateeb and Prof. Dr. Nabil Laham, Yarmouk University, Irbid, Jordan.
- Work as a scientist in accelerator and beam physics at the Institute for Applied Physics of the J. W. Goethe-University in Frankfurt am Main (October 15th, 2008 – till now).
- Good knowledge of using LORASR code of beam dynamics, CST – MWS program, TRACE-3D code of beam envelope and SRIM code.

8- CONFERENCES, WORKSHOPS AND SCIENTIFIC MEETINGS:

- 1- 4th Symposium on Use of Nuclear Techniques in Environmental studies (13 -15 September 2004, Yarmouk University, Irbid, Jordan).
- 2- 5th Symposium on Use of Nuclear Techniques in Environmental studies (12 – 14 September 2005, Yarmouk University, Irbid, Jordan).
- 3- 6th Symposium on Use of Nuclear Techniques in Environmental studies (4 – 6 September 2006, Yarmouk University, Irbid, Jordan).
- 4- 7th Symposium on Use of Nuclear Techniques in Environmental studies (3 – 5 September 2007, Yarmouk University, Irbid, Jordan) (Talk).
- 5- Workshop "HICforFAIR", Haus Bergkranz, Riezlern, March 08- 14, 2009 (Talk).
- 6- Workshop "HICforFAIR", Haus Bergkranz, Riezlern, March 07- 13, 2010 (Talk).
- 7- DPG conference, Bonn, Germany, March 15 - 19, 2010 (Poster).
- 8- The First International Particle Accelerator Conference (IPAC 10), Kyoto, Japan, May 22 - 29, 2010 (Poster).
- 9- Workshop " Milestones and Perspectives of the Projected Test Stand to Capture and Transport Laser-Accelerated Proton Beams", GSI Darmstadt, 06.08.2010 (Talk).
- 10- HGS-HIRE Participant Seminar, GSI, Darmstadt, 15.12.2010 (Talk).
- 11- Workshop "HICforFAIR", Haus Bergkranz, Riezlern, March 06- 12, 2011 (Talk).
- 12- DPG conference, Münster, Germany, March 21 - 25, 2011 (Talk).
- 13- CERN Accelerator School on "High Power Hadron Machines", Bilbao, Spain, 24.05 – 02.06. 2011.
- 14- The Second International Particle Accelerator Conference (IPAC 11), San Sebastián, Spain, September 04 – 09, 2011 (Poster).
- 15- HGS-HIRE Graduate Day, Königstein – Taunus, Germany, 27 – 28.10.2011 (Talk).
- 16- Workshop "LIGHT Collaboration Meeting 2011", GSI, Darmstadt, 03.11.2011 (Talk).
- 17- Workshop "HICforFAIR", Haus Bergkranz, Riezlern, March 11- 17, 2012 (Talk).

9- TALKS:

- 1- "Gamma Radiation Measurements and Dose Rate Calculations of Soil Samples within and around Ras Muneef- Jordan", 7th Symposium on Use of Nuclear Techniques in Environmental studies, September 3 -5, 2007, Irbid, Jordan.
- 2- "Matching of a Laser Generated Ion Beam into a CH-Cavity" given at Workshop on HICforFAIR, Haus Bergkranz, Riezlern, March 09, 2009.
- 3- "Matching the Laser Generated p- Bunch into a CH- DTL", Workshop on HICforFAIR "Current Problems of Accelerators and Plasma Physics", Haus Bergkranz, Riezlern, March 10, 2010.
- 4- "Matching the Laser Generated p- Bunch into a CH- DTL, Status and perspectives" Workshop " Milestones and Perspectives of the Projected Test Stand to Capture and Transport Laser-Accelerated Proton Beams", LIGHT collaboration, GSI Darmstadt, 06.08.2010.
- 5- "RF Acceleration of Intense Laser Generated Proton Bunches", HGS – HIRE Participant Seminar, GSI, Darmstadt, 15.12.2010.
- 6- "TNSA – A New Particle Source", Workshop on HICforFAIR "Current Problems of Accelerators and Plasma Physics", Haus Bergkranz, Riezlern, March 08, 2011.
- 7- "Transporting Laser - Accelerated Protons by a Pulsed Solenoid to a CH- DTL", DPG conference, Münster, March 23, 2011.

- 8- "RF Acceleration of Intense Laser Generated Proton Bunch by CH – Drift Tube Linac", HGS-HIRE Graduate Day, Königstein – Taunus, 28.10.2011 (Invited).
- 9- "Matching the Laser Generated p – Bunch into a CH – DTL, New Linac Desing", Workshop on "LIGHT Collaboration Meeting 2011", GSI, Darmstadt, 03.11.2011.
- 10- "TNSA – A New Particle Source for Conventional Accelerators", Freitagseminar, IAP, Frankfurt University, 20.01.2012 (Invited).

9- PUBLICATIONS:

- 1- "Matching the laser Generated P- Bunch into a CH – DTL", **A. Almomani**, M. Droba, U. Ratzinger and I. Hofmann, **GSI Scientific Report** 2009 (Plasma – Physics – 22), p. 407 (2009).
- 2- "Focusing the Generated p- Bunch by a Magnetic Solenoid", **A. Almomai**, M. Droba, U. Ratzinger and I. Hofmann, **Annual Report of the High Energy Density Physics Community at FAIR**, p.24 (2010).
- 3- "Matching the laser Generated p- Bunch into a CH - DTL", **A. Almomai**, M. Droba, U. Ratzinger and I. Hofmann, **Proceeding of IPAC 10**, Kyoto, Japan, THPD035, p. 4355 (2010).
- 4- "Space Charge Effect on the Beam Dynamics of p- Bunch Generated by Laser", **A. Almomai**, M. Droba, U. Ratzinger and I. Hofmann, **GSI Scientific Report** 2010, PHN–ACC–RD–56, p. 317 (2010).
- 5- "LIGHT Update: A laser – based ion – source at Z6", B. Zielbauer, **A. Almomani**, V. Bagnoud, A. Blazevic, C. Brabetz, S. Busold, O. Deppert, H. Eickhoff, S. Götter³, O. Kester, T. Merz-Mantwill, F. Nürnberg, M. Roth and T. Stöhlker, **GSI Scientific Report**, PNI-PP-16, p. 421 (2010).
- 6- "Matching a Laser Driven Proton Injector to a CH – Drift Tube Linacs", **A. Almomani**, M. Droba, U. Ratzinger and I. Hofmann, **Proceeding of IPAC 11**, San Sebastián, Spain, WEPS033, p. 2556 (2011).
- 7- "Laser – Proton Acceleration as Compact Ion Source", S. Busold, **A. Almomani**, V. Bagnoud, W. Barth, A. Blazevic, O. Boine-Frankenheim, C. Brabetz, T. Burris-Mog, T. Cowan, O. Deppert, M. Droba, P. Forck, A. Gopal, K. Harres, T.Herrmannsdoerfer, S. Herzer, G. Hoffmeister, I. Hoffmann, O. Jäckel, M. Joost, M.Kaluza, O. Kester, F. Nürnberg, A. Orzhakovskaya, U. Ratzinger, M. Roth, T.Stöhlker, A. Tauschwitz, W. Vinzenz, S. Yaramishev, B. Zielbauer, **Proceeding of PAC11**, New York, NY, USA, WEP256, p. 1960 (2011).
- 8- "Code development: Implementation of compensation electrons for space charge dominated beams", M. Droba, **A. Almomani**, O. Meusel, D. Noll, U. Ratzinger, J. Wagner and C. Wiesner, **GSI Scientific Report** 2011 (Submitted).
- 9- "Distribution of Natural and Anthropogenic Radionuclides in Heavy Rainfall Areas in Jordan", Anas Ababneh, **Ali Almomani**, Abedalmajeid Alyassin and Zaid Ababneh, **Radiation Protection Dosimetry**, doi: 10.1093/rpd/ncr371, p. 1-9 (2011).
- 10- "Matching the Laser Generated p- Bunch into a Drift Tube Linac of the CH - type", **A. Almomani**, M. Droba, U. Ratzinger and I. Hofmann, **Phys. Rev. Special Topics – Accelerator and Beams**, **15**, 051302 (2012).

10- COMPUTER SKILLS

- Windows Operating System.
- C++, FORTRAN Programming Language (Basic).
- CorelDraw, Origin, Mathematica, SigmaPlot, ImageJ, Viso, Microsoft Office.
- Experience in running several codes like LORASR code, TRACE-3D code, SRIM code, CST – MICROWAVE STUDIO Program.

11- LANGUAGE SKILLS

- Arabic: Native
- English: Very good

12- REFERENCES

- 1- Prof. Dr. Ulrich Ratzinger (U.Ratzinger@iap.uni-frankfurt.de)
IAP, Frankfurt University, Max-von-Laue Str. 1, 60438 Frankfurt am Main, Germany.
- 2- Prof. Dr. Ingo Hofmann (I.Hofmann@gsi.de)
GSI, Planckstr. 1, 64291 Darmstadt, Germany.
- 3- Prof. Dr. Ahmad Al-khateeb (helga@yu.edu.jo) or (a.alkhateeb@gsi.de)
Physics Department, Yarmouk University, 21163 Irbid – Jordan.
- 4- Dr. Anas Ababneh (ababneha@yu.edu.jo)
Physics Department, Yarmouk University, 21163 Irbid – Jordan.
- 5- Prof. Dr. Nihad Yusuf (nihadyusuf@yu.edu.jo)
Physics Department, Yarmouk University, 21163 Irbid – Jordan.
- 6- Prof. Dr. Sami Mahmood (s.mahmood@ju.edu.jo)
Physics Department, University of Jordan, Amman – Jordan.
- 7- Dr. Mohammad Sheboul (msheboul@yu.edu.jo)
Physics Department, Yarmouk University, 21163 Irbid – Jordan.

